

Spectrally selective tin oxide and indium oxide coatings

Han Haitjema

TR diss
1770

405507

207 9244

TA diss 1770

Spectrally selective tin oxide and indium oxide coatings

Spectrally selective tin oxide and indium oxide coatings

Proefschrift



ter verkrijging van de graad van doctor
aan de Technische Universiteit Delft,
op gezag van de Rector Magnificus,
prof. drs. P.A. Schenck, in het openbaar
te verdedigen ten overstaan van een
commissie door het College van Dekanen
daartoe aangewezen, op
23 november 1989 te 14.00 uur
door

Han Haitjema

geboren te Ommen
natuurkundig doctorandus

**TR diss
1770**

Dit proefschrift is goedgekeurd door de promotor
prof. ir. C.J. Hoogendoorn

Acknowledgement

This investigation in the program of the Foundation for Fundamental Research on Matter (FOM) has been supported (in part) by the Netherlands Technology Foundation (STW).

Voor Margreeth en Saskia

CIP-GEGEVENS KONINKLIJKE BIBLIOTHEEK, DEN HAAG

Haitjema, Han

Spectrally selective tin oxide and indium oxide coatings /

Han Haitjema ; [ill. by the author]. - [S.l. : s.n.]. - Ill.

Proefschrift Delft. - Met lit. opg. - Met samenvatting in het Nederlands.

ISBN 90-9003138-3

SISO 644.8 UDC 620.1:620.91(043.3)

Trefw.: spectraal selectieve absorbers / coatings /

optische materiaaleigenschappen.

CONTENTS

1. General Introduction	1
1.1 Photothermal solar energy conversion	1
1.2 Overview of spectrally selective surfaces	4
1.2.1 Intrinsic absorbers	5
1.2.2 Optical trapping	5
1.2.3 Coating/metal tandem	5
1.2.3.1 Semiconductor/metal tandem	5
1.2.3.2 Particulate coatings	6
1.2.4 Multilayer thin films	6
1.2.5 Transparent heat reflector/absorber tandem	7
1.3 Transparent, heat reflecting and conducting coatings	7
1.4 Motivations and objectives	9
1.5 Outline of the thesis	11
2. Spectrally selective properties of transparent conductors	13
2.1 Radiation quantities	13
2.1.1 Absorptance	13
2.1.2 Emittance	15
2.1.3 Reflectance and transmittance	16
2.1.4 Relations between radiation quantities: Kirchhoff's law	17
2.2 Thin film optics	18
2.2.1 Wave propagation through an absorbing medium	18
2.2.2 Reflection and transmission at a plane interface	19
2.2.3 Reflection and transmission by planar structures	21
2.2.4 Extension to anisotropic layers	23
2.2.5 Extension to the case of $d \gg \lambda$	24
2.2.6 Modelling of surface roughness	25
2.3 The Drude theory	27
2.4 Scattering mechanisms	33
2.4.1 Ionized impurity scattering	33
2.4.2 Neutral impurity scattering	39
2.4.3 Lattice scattering	39
2.4.3.1 Scattering by acoustical phonons	39
2.4.3.2 Scattering by longitudinal optical phonons	39

2.4.4	Grain boundary scattering	40
2.4.5	Other scattering mechanisms	43
2.4.6	Combining different scattering mechanisms	44
2.5	The free electron density	44
2.6	Model calculations on hypothetical coatings	46
2.6.1	Normal reflectance	47
2.6.2	Solar absorptance	49
2.6.3	Angle dependent reflectance	51
2.6.4	Angle dependent emittance	53
2.6.5	Hemispherical emittance	53
2.6.5.1	Minimum theoretical emittance	53
2.6.5.2	Temperature dependence of ϵ_h	55
2.7	Methods for improving the solar absorptance	55
3.	Experimental methods for characterizing spectrally selective coatings	59
3.1	Determination of spectral specular reflectance and emittance	59
3.2	Determination of the spectral near-normal hemispherical reflectance and transmittance	62
3.2.1	Determination of the near-normal hemispherical spectral reflectance in the 1.8-20 μm spectral region	62
3.2.1.1	The integrating sphere	64
3.2.1.2	The monochromator	65
3.2.1.3	Error analysis and an example of a measurement	67
3.2.2	Determination of the near-normal spectral reflectance and transmittance in the 0.3-2.5 μm spectral region	67
3.3	Determination of solar absorptance and thermal emittance	70
3.3.1	Determination from the near-normal hemispherical reflectance spectrum	70
3.3.2	Determination of the total directional emittance	70
3.4	Determination of the electrical properties	73
3.4.1	Experimental set-up	73
3.4.2	Measuring method	75
3.4.3	Error discussion	77
3.4.4	Example of a measurement	78
3.5	Ellipsometry	80
3.5.1	Introduction	80
3.5.2	Experimental set-up	81
3.5.3	Measuring method	82
3.5.4	Determination of statistical errors	83
3.6	Other experimental techniques used	83

4. Methods for determining optical constants and coating thickness	85
4.1 The Reflection-Transmission method	85
4.2 The envelope method	87
4.3 Application of a Kramers-Kronig relation to the reflectance spectrum	89
4.4 Ellipsometry	95
4.5 Determination of the coating thickness	102
4.5.1 The extrema method	102
4.5.2 The step method	103
4.6 Conclusions	104
5. The spray-pyrolysis coating process	105
5.1 Introduction	105
5.2 The spraying equipment	105
5.3 Film formation by spray pyrolysis	105
5.4 The process parameters	109
5.4.1 Droplet size	109
5.4.2 Substrate temperature	109
5.4.3 Chemical solutions used	111
5.4.4 The gas and liquid flow in the spraying process	112
5.5 Film growth	113
5.6 Sample preparation and reproducibility	115
6. Tin dioxide coatings	117
6.1 Introduction	117
6.2 General properties of tin oxide (SnO_2)	117
6.3 Physical effects of fluorine doping	121
6.3.1 Preparation conditions	121
6.3.2 Infrared optical properties	121
6.3.3 Comparison of optical and electrical properties	123
6.3.4 Temperature dependence of electrical properties	125
6.3.4.1 The free electron density	126
6.3.4.2 The mobility	127
6.3.5 X-ray diffraction measurements	132
6.3.6 Elemental composition	134
6.3.7 Optical properties near the fundamental band-gap	136
6.4 Coating thickness effects	140
6.4.1 Spraying conditions	140
6.4.2 Optical properties	140
6.4.3 Electrical properties	141

6.4.4	Comparison of electrical and optical properties	143
6.4.5	X-Ray diffraction measurements	143
6.4.6	Elemental composition	145
6.4.7	Scanning Electron Micrographs	145
6.5	Influence of process parameters	146
6.5.1	Influence of the substrate temperature	146
6.5.1.1	Electrical and optical properties	146
6.5.1.2	X-Ray diffraction measurements	149
6.5.1.3	Elemental composition	151
6.5.1.4	Scanning Electron Micrographs	152
6.5.1.5	Other substrate/solution combinations	153
6.5.1.6	Effect of spraying time	154
6.5.1.7	Optimum temperature found in the literature	155
6.5.2	Influence of the carrier gas	155
6.5.3	Influence of the droplet size	156
6.6	Annealing	157
6.6.1	Electrical and optical properties	159
6.6.2	Temperature dependence of electrical properties	160
6.6.3	Structural properties	161
6.6.4	Comparison with literature	161
6.7	Ageing	162
6.7.1	Electrical and optical properties	163
6.7.2	X-ray diffraction measurements and elemental composition	166
6.8	Determination of anisotropy and inhomogeneity with ellipsometry	166
6.8.1	Results at $\lambda = 632.8$ nm	167
6.8.1.1	Coating thickness and refractive index	167
6.8.1.2	Anisotropy	168
6.8.1.3	Inhomogeneity	168
6.8.2	Results at $\lambda = 1523$ nm	169
6.8.2.1	Coating thickness and refractive index	169
6.8.2.2	Anisotropy	169
6.8.2.3	Inhomogeneity	171
6.9	Effects of lattice resonances	173
6.10	General discussion	178
6.10.1	Model for the optical properties	178
6.10.2	Relations between the electrical and structural properties	181

6.10.2.1	The free electron density	181
6.10.2.2	The mobility	184
6.11	Conclusions for application in solar collectors	186
6.11.1	The solar absorptance	187
6.11.2	Coating with lowest emittance obtained	187
7.	Indiumoxide coatings	189
7.1	General properties of indiumoxide (In_2O_3)	189
7.2	Effects of tin doping	189
7.3	Annealing effects	191
7.3.1	Electrical and optical properties	191
7.3.2	Tin concentration and free electron density	193
7.3.3	Temperature dependence of electrical properties	195
7.3.3.1	Electron density	196
7.3.3.2	Mobility	199
7.4	Coating thickness effects	201
7.4.1	Preparation conditions	201
7.4.2	Optical and electrical properties	201
7.4.3	X-ray diffraction measurements	203
7.4.4	Scanning electron micrographs	204
7.5	Influence of the substrate temperature	204
7.6	Best coating obtained	205
7.7	Final discussion	206
8.	Concluding remarks	207
8.1	Theoretical investigations	207
8.2	Characterization methods	207
8.3	The spray pyrolysis coating process	208
8.4	Results on SnO_2 coatings	209
8.5	Results on In_2O_3 coatings	211
8.6	Final conclusions	211
	Principal symbols	213
	References	217
	Summary	227
	Samenvatting	233
	Curriculum vitae	239
	Nawoord	241

1. GENERAL INTRODUCTION

This introductory chapter starts with a brief introduction into the concept of spectral selectivity in solar energy conversion. After this, an overview of existing selective surfaces is given, the possible applications of tin oxide and indium oxide coatings are mentioned and a short discussion of the motivations for this research is given. The chapter concludes with a short outline of the thesis.

1.1 Photothermal solar energy conversion

At present, the fossile fuels such as oil, coal and gas, are the most commonly used sources of energy. The still increasing use of these fuels will cause large environmental problems, which already appear nowadays in the form of an increasing CO₂ content of the atmosphere and acid rain. The somewhat cleaner fuel, gas, will be depleted in the not-too-distant future. Therefore one must be prepared to supply a large portion of the world energy needs by other means. One of the alternatives is to make a direct use of the incoming solar energy.

Various conversion processes can be applied to convert solar radiation into a usable form of energy. The most important processes are the conversion into electricity, called photovoltaic conversion, and the conversion into heat, which is called photothermal conversion. Here, we will restrict ourselves to the photothermal conversion process.

Figure 1.1 depicts the basic design of a typical thermal solar collector, the flat plate collector. The instantaneous heat current density q_u which is delivered by the collector can be expressed as (Duffie and Beckman, 1980):

$$\begin{array}{ccc}
 \boxed{\text{absorbed}} & \boxed{\text{thermal radiant}} & \boxed{\text{conduction and}} \\
 \boxed{\text{solar energy}} & \boxed{\text{heat loss}} & \boxed{\text{convection heat loss}} \\
 | & | & | \\
 q_u = \alpha_a \tau_c E_s & - \frac{\sigma (T_a^4 - T_c^4)}{\epsilon_a^{-1} + \epsilon_c^{-1} - 1} & - h (T_a - T_c)
 \end{array} \quad (1.1)$$

where: α_a = solar absorptance of the absorber
 ϵ_a, ϵ_c = thermal emittance of the absorber and cover respectively
 τ_c = solar transmittance of the cover

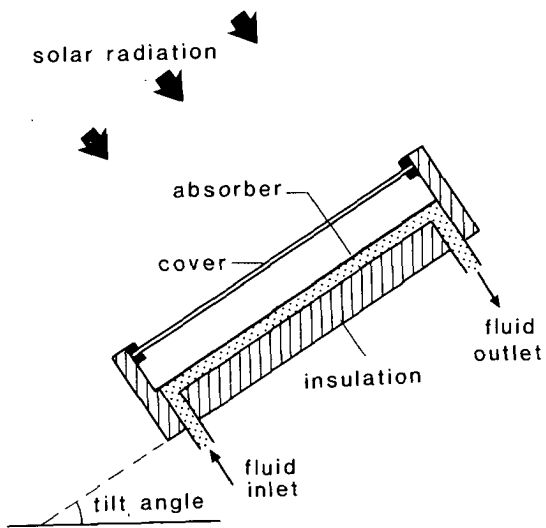


Figure 1.1 Cross section of a simple tilted flat plate collector

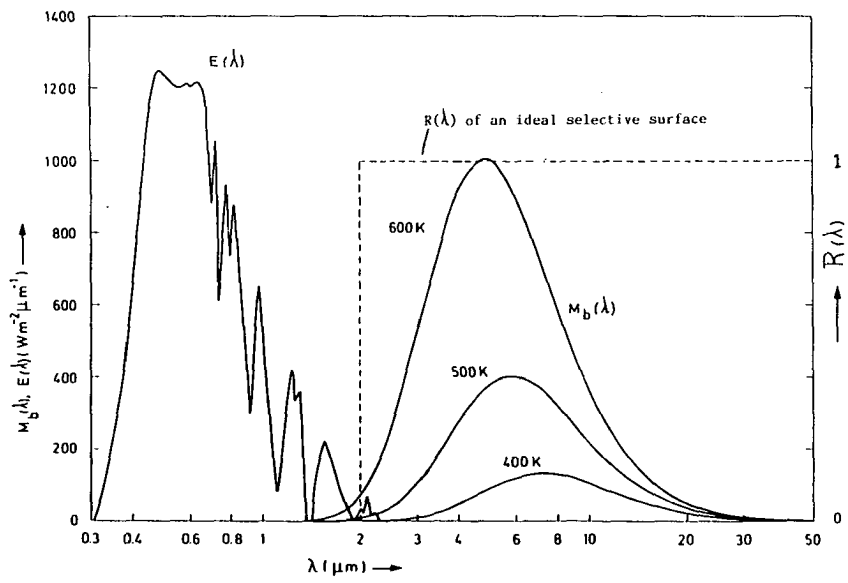


Figure 1.2 The spectral energy distribution of solar irradiance $E(\lambda)$ at sea level and of a black body with different surface temperatures

- σ = Stefan-Boltzmann constant
- T_a, T_c = absolute temperatures of absorber and cover respectively
- E_s = solar irradiance
- h = heat loss coefficient due to conduction and convection

The collector instantaneous efficiency η , which is defined as $\eta = q_u/E_s$, should be as high as possible for an optimum collector performance. The collector performance can be optimized by reducing the thermal radiant heat losses. From (1.1) it follows that this can be achieved in two ways: by reducing the absorber emittance ϵ_a while maintaining a high solar absorptance ($\alpha_a \approx 1$), and by reducing the cover emittance ϵ_c while maintaining a high solar transmittance of the cover ($\tau_c \approx 1$). Since the spectral distributions of the solar irradiance $E(\lambda)$ and the blackbody radiant exitance $M_b(\lambda, T)$ have their main contributions in different wavelength ranges as long as T_a is not too high, these demands can be met by requiring that the spectral reflectance of the absorber $R(\lambda) \approx 0$ at wavelengths shorter than a cut-off wavelength λ_c and $R(\lambda) \approx 1$ at longer wavelengths. This is illustrated in figure 1.2. In this figure it is shown that for an opaque absorber surface with a spectral reflectance as sketched in the figure the solar absorptance $\alpha_a \approx 1$ and the thermal emittance $\epsilon_a \approx 0$ (because $\epsilon(\lambda) = \alpha(\lambda)$ according to Kirchhoff's law). A surface with these properties is called a spectrally selective absorbing surface or a selective absorber.

In the case that the collector efficiency is to be optimized by the properties of the transparent cover it is, apart from the required $R(\lambda)$, also required that $\tau_c(\lambda) \approx 1$ for $\lambda < \lambda_c$. Since $\alpha(\lambda) + R(\lambda) + \tau(\lambda) = 1$, this additional requirement is identical with $\alpha(\lambda) \approx 0$ for both the solar and the thermal spectrum. A cover with such properties is called a spectrally selective transmitting cover or a selective cover.

To illustrate the improvement in collector performance obtained by making use of spectrally selective absorbing surfaces, typical values for η are depicted in figure 1.3 for some different values of α_a , ϵ_a and h . The values of α_a and ϵ_a are typical for black paint and two different selective surfaces respectively. The used value of h ($h = 3 \text{ W/m}^2\text{K}$) is typical for an air-filled collector (Linthorst, 1985). Also a curve for $h = 0$ is drawn, which represents the hypothetical situation that the heat loss coefficient is eliminated, e.g. by using an evacuated system. In the calculations (1.1) is used, and ϵ_a and h are assumed to be temperature independent.

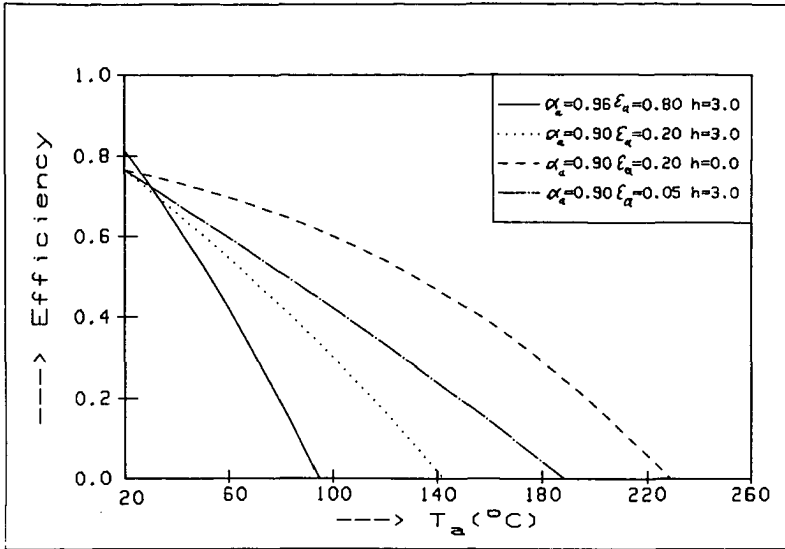


Figure 1.3 Collector efficiency η as a function of the absorber temperature T_a for different selective surfaces

Other parameters taken are $E_s = 0.8 \text{ kW/m}^2$ (about the maximum value obtained at the earth's surface), $\epsilon_c = 0.84$, $\tau_c = 0.85$ (typical values for glass) and the cover temperature is taken as $20 \text{ }^\circ\text{C}$.

Figure 1.3 shows that at a high collector temperature the emittance determines the collector efficiency while at a low collector temperature α_a is the decisive factor with regard to the efficiency. The figure also shows that to achieve a large absorber temperature connected with a large efficiency, also the conduction and convection heat loss coefficient must be suppressed. A more extensive analysis of the effect of a selective surface on the performance of a solar collector has been given by Tal-Tatlo and Zvirin (1988).

1.2 Overview of spectrally selective surfaces

The use of spectrally selective surfaces for solar collectors was introduced by Tabor (1956). Since that time many kinds of surfaces have been developed. Extensive overviews can be found in literature (Lampert, 1979; Seraphin, 1979; Agnihotri, 1981). Solar selectivity can be obtained by a variety of methods. These techniques are outlined in the next sections with a few examples of surfaces that have been investigated. References are given as far as they are not given in the three references just mentioned.

1.2.1 Intrinsic absorbers

There are a few materials which exhibit a reasonable selective behavior without necessary modifications. Examples of these materials are Hafnium Carbide (HfC), semiconductor Cu_2S and metallic tungsten (W). A selective transmitting material is lathanum hexaboride (LaB_6), which transmits 85% in the visible and reflects 90% in the infrared spectral region. The spectrally selective properties of these materials are moderate, so they are not used in practice.

1.2.2 Optical trapping

A common technique used to obtain optical trapping of energy or wavelength discrimination is surface roughening. It is possible to produce a surface which appears rough and absorbing to visible wavelengths while appearing mirror like in the infrared. Nearly ideal surfaces have been produced by chemical vapor deposition (CVD) of Rhenium which results in a dendritic structure. Surfaces of this kind based on Tungsten dendrites or on nickel dendrites on aluminium have a solar absorptance in the 0.95-0.99 range and a thermal emittance between 0.2 and 0.7.

1.2.3 Coating/metal tandem

This kind of a selective surface consists of a solar absorbing coating on a poorly emitting metal substrate. The coating is either thin enough to have little influence on the low thermal emittance of the metal substrate or is transparent for thermal radiation. The coatings used are mostly of the semiconductor type. Often the absorptance is further enlarged by introducing small metal particles in the coating. In this case the coating is called a particulate coating. The semiconductor- and the particulate coatings are discussed separately below, but the division is not very sharp.

1.2.3.1 Semiconductor/metal tandems

If a metal is covered with a semiconductor film then the semiconductor will absorb solar radiation, while in the infrared the tandem will act like a poorly emitting metal due to the high transparency of the semiconductor in this region. The simplest absorber of this type is an oxidized metal. Examples are oxidized stainless steel, oxidized titanium and oxidized copper. There are numerous semiconductor/metal combinations: e.g. PbS on

aluminium, CuO on aluminium and WO_3 on Nickel. The major disadvantage of most surfaces of this type is the deterioration of the properties when temperatures larger than 200 °C are applied to the surfaces.

1.2.3.2 Particulate coatings

Coatings of this type consist of complicated dispersions of metallic or semiconductor particles in dielectric or conductive matrices. They are based on two different mechanisms of absorption: optical trapping as discussed in the previous section and resonant scattering. Resonant scattering deals with both the size and optical properties of the particles and surrounding media. The Mie effect and the Maxwell-Garnet theory predict high forward scattering from particles smaller than 0.1 of the wavelength of the incident radiation.

Selective surfaces of this type are black chrome (Cr/Cr₂O₃), black cobalt (CoO/Co₃O₄) (Kruidhof, 1979), black nickel (Ni/ZnS) (Kumar, 1983), black zinc oxide (Zn/ZnO) (van der Ley, 1978) and nickel carbide (Ni/C) (Sikkens, 1982). Also cermets (ceramic/metal), such as MgO/Au, Al₂O₃/Fe (Sella, 1987), SiO/Cr (Thomas, 1987), MgF₂/Sn, MgF₂/Ni (Köhl, 1987), and selective paints (e.g. PbS particles imbedded in a silicon paint) can be classified into this type of materials. Of these coatings, the first three mentioned are probably the most important with a solar absorptance of about 0.96 and a thermal emittance of about 0.08 at room temperature. Sometimes coatings are applied to rough substrates to achieve a higher absorptance by optical trapping (section 1.2.2) (see e.g. Vogelzang (1983) for the case of nickel carbide coatings on rough copper substrates).

1.2.4 Multilayer thin films

Multilayer thin films known as interference stacks are dielectric-metal combinations which act like a selective filter for energy absorption. The desired effect of an interference stack is to trap energy between semi-transparent metal, dielectric and metal alterations. Particular wavelengths of solar energy are absorbed by multiple reflection in the dielectric-metal layers, while other wavelengths not corresponding to the absorption frequency are reflected. Some examples are : alternate coatings of ZnS/NiS, Ag/Al₂O₃, Ag/CuS and Mo/Al₂O₃. The disadvantage with most multilayer coatings is that they are fairly expensive to fabricate.

1.2.6 Transparent heat reflector/absorber tandem

The principle of this type is the reverse of the semiconductor/metal tandem. In this case the top layer reflects heat and transmits solar radiation. The solar radiation is absorbed in the bottom absorber surface. Examples of this type are: a tin-doped In_2O_3 coating on a silicon substrate, a fluorine-doped SnO_2 coating on pigmented aluminium oxide (Roos, 1986) and a fluorine-doped SnO_2 coating on black enameled steel. The best properties of the last mentioned coatings are: a thermal emittance ϵ_h of 0.15 and a solar absorptance of 0.91 (Simonis, 1987). These types of coatings are called transparent conductors as they are both visually transparent and electrically conducting; the heat-reflecting property is connected with the electrical conductivity of the semiconductor. In principle, any transparent conductor can be taken as the heat-reflecting top layer. A short outline of the principles and properties of transparent conductors is given in the next section.

1.3 Transparent, heat reflecting and conducting coatings

The simultaneous occurrence of high optical transparency in the visible region and high conductivity is not possible in an intrinsic stoichiometric material. The only way to obtain good transparent conductors is to create electron degeneracy in a wide bandgap (>3 eV) oxide by introducing oxygen vacancies and/or appropriate dopants.

The most commonly used transparent conductors are tin oxide (SnO_2), doped with antimony or fluorine, indium oxide (In_2O_3), doped with tin (known as ITO, Indium Tin Oxide), zinc oxide (ZnO), doped with indium or aluminium and Cadmiumstannate (Cd_2SnO_4), which needs no doping. Various other doped oxides could be applicable, but have been less intensively investigated. Among these are cadmium oxide (CdO), Bismuth oxide (Bi_2O_3), Titanium oxide (TiO_2) and Molybdenum oxide (MoO_3).

Coatings of the oxides first mentioned have been produced by a large number of techniques, ranging from elaborate and expensive (sputtering, chemical vapor deposition) to easy and cheap (spray pyrolysis). Doped tin oxide has probably the best mechanical and chemical properties (hardness, wear resistance and stability at high temperatures); the highest conductivity and heat-reflection can be obtained with indium oxide and cadmiumstannate coatings. Cadmiumstannate coatings are not widely used because of the high toxicity of cadmium; the use of indium oxide coatings on a large scale is hampered by the high indium price, which is about as high

Table 1.1 Survey of applications of transparent conductive coatings

Application	Property exploited	Coatings used
Photovoltaic solar cells:		
1. Semiconductor/Insulator/ Semiconductor (SIS) cells	UV-absorption/ visual transmittance	$\text{In}_2\text{O}_3:\text{Sn}$, SnO_2 , ZnO , MoO_3
2. Heterojunction solar cells	solar transmittance/ conductivity	$\text{SnO}_2:\text{F}$, $\text{In}_2\text{O}_3:\text{Sn}$
3. Antireflection coating for solar cells	solar transmittance/ refractive index ≈ 2	SnO_2
Spectrally selective coating on solar collector	low solar reflectance/ low thermal emittance	$\text{SnO}_2:\text{F}$, $\text{In}_2\text{O}_3:\text{Sn}$
Double-glazed windows	solar transmittance/ low thermal emittance	$\text{SnO}_2:\text{F}$
Anti-frost coating on car window	visual transmittance/ low thermal emittance	$\text{SnO}_2:\text{F}$
Sodium lamp	visual transmittance/ heat reflectance	$\text{SnO}_2:\text{F}$, $\text{SnO}_2:\text{Sb}$, $\text{In}_2\text{O}_3:\text{Sn}$
Opto-electronic devices (CID's, CCD's)	visual transmittance/ conductivity	$\text{SnO}_2:\text{Sb}$, $\text{In}_2\text{O}_3:\text{Sn}$
Heating element on automobile, aeroplane and ship windows.	visual transmittance/ conductivity	SnO_2 , $\text{SnO}_2:\text{F}$, $\text{SnO}_2:\text{Sb}$
Microwave shielding	visual transmittance/ microwave reflectance	$\text{SnO}_2:\text{F}$
FET-transistors	semiconductor	SnO_2
Hot-end coating on bottles	mechanical stability	SnO_2
Gas sensors, Smoke sensors	chemical instability at high temperatures	SnO_2 , ZnO

as the silver price.

A strong impulse to the research on these coatings was given by the use of a tin oxide coating to enhance the efficiency of sodium lamps (Groth and Kauer, 1964). Transparent conductors have many other applications. Most of the known applications are summarized in table 1.1. Although each application has specific demands, most of them require high visual transparency, high conductivity and a low thermal emittance. The mechanical stability of tin oxide is so high, that it is even used to enhance the strength of bottles. This property is also of importance for some of the other applications, especially for the use as a spectrally selective coating. Most of the applications have been mentioned by Chopra (1983) and de Waal (1981). A specific discussion of the use of transparent conductive coatings for automotive applications has been given by Granqvist (1988).

For the applications which require only a visual transmittance (up to $0.7 \mu\text{m}$) combined with a low thermal emittance, also a thin metal coating ($\sim 20 \text{ nm}$ aluminium or silver) between two thin oxide coatings (SnO_2 or TiO_2) can be applied. This type of coating can have a high visual transmittance, a high solar reflectance (for $\lambda > 0.7 \mu\text{m}$) and a lower thermal emittance than can be obtained with transparent conductors. These coatings are produced by magnetron sputtering on window pane on a large scale (Gainsbury, 1988). As these coatings fall outside the scope of this thesis, they will not be discussed here further.

1.4 Motivations and objectives

In the past, in the Delft heat transfer group investigations have been carried out on the conduction and convection losses (Linthorst, 1985) and the thermal radiant heat loss (van der Ley, 1979) of solar collectors. A conclusion of the latter is that a fluorine-doped tin oxide coating applied on an absorbing substrate forms an attractive spectrally selective coating. The further investigations have been carried out in close cooperation with the TPD (Institute for applied physics TNO-TH). The coatings are produced by spray pyrolysis (spraying a tin solution on a hot substrate). In an optimized process the solar absorptance is 0.91 and the lowest thermal emittance which has been achieved is about 0.15. This coating is primarily designed for low-temperature solar collectors with an operating temperature of about 80°C . When a stagnation occurs in the cooling system of the collector, the temperature may rise up to 200°C and the spectrally selective layer must be able to withstand this temperature for many hours.

The main advantage of tin oxide over most other spectrally selective coatings is its high mechanical, chemical and thermal stability. The coating properties hardly change when a temperature up to 250 °C is applied in vacuum, and in air the coating is stable for temperatures up to 400 °C. This means that the stagnation temperature is no problem for tin oxide coatings and the coatings can also be used for collectors operating between 100 °C and 200 °C. The most commonly used selective surfaces, black chrome and black cobalt, have a lower ϵ (about 0.08) and a higher α (about 0.96), but are more expensive than tin oxide. Moreover these coatings are chemically and mechanically less stable.

The largest disadvantage of a tin oxide coating is its moderate emittance and it would be of great importance if a method could be found in which a lower emittance can be obtained. Therefore a good insight in the relations between the electrical, structural, morphological and spectrally selective properties of the coating should be achieved. From this insight possibly an answer can be given to the question what structural and morphological properties a coating should have to have optimum spectrally selective properties, and what limits can be achieved for the thermal emittance and the solar absorptance. As all properties depend on the production parameters, attention must be paid to the spraying process to vary the coating properties in a controlled way, as well as to get insight in this process as to optimize it.

To find a solution to these problems the research described in this thesis has been carried out. Primarily tin oxide coatings have been subject to various investigations. Indium oxide coatings have been investigated because of the interesting properties of these coatings and also to enable a comparison between the physical principles which determine the properties of these two transparent conductors. As a low thermal emittance is related to a high conductivity, this research is of interest for most of the applications mentioned in table 1.1. Parts of the results as presented in this thesis have been published elsewhere (Haitjema, 1986, 1987, 1988, 1989; Elich, 1989).

1.5 Outline of the thesis

After this introduction, in chapter 2 first the definitions of the various radiation quantities are given. This theoretical chapter further gives the thin film optics used, the Drude model which relates electrical and optical properties, the various scattering mechanisms which might limit the conductivity in the coatings and a model for the free electron density in a degenerate semiconductor. Finally, model calculations on hypothetical coatings, based on the former sections, are given.

Chapter 3 is dedicated to some of the measuring techniques which have been used to determine the coating properties. These techniques include spectrophotometry, Hall-effect determinations, ellipsometry, and the determination of the angle-dependent thermal emittance. The determinations which have been carried out for us by other groups (e.g. X-ray diffraction and electron microprobe analysis) are briefly discussed.

In chapter 4 the various methods in which the optical constants and the thickness of the coatings have been determined are given and mutually compared. Knowledge of the optical constants is essential when the coatings are to be modeled physically.

Chapter 5 describes the pyrolysis process with which the coatings have been produced. Also the chemical solutions which have been used in the spray pyrolysis process are described.

The results on tin oxide coatings are given in chapter 6. These results include the effects of fluorine doping, coating thickness and the process parameters. At the end of the chapter these results are summarized in a model for the optical properties and in a discussion on the relation between the structural and electrical properties.

Chapter 7 gives the results obtained for indium oxide coatings. The effects of tin doping, annealing and the coating thickness are determined and compared to the results found in chapter 6 for tin oxide coatings.

The thesis is concluded with a summary of the main theoretical and experimental results and conclusions in chapter 8.

2. SPECTRALLY SELECTIVE PROPERTIES OF TRANSPARENT CONDUCTORS

In this chapter the spectrally selective properties of transparent conductors, such as tin oxide (SnO_2) and indium oxide (In_2O_3) will be treated theoretically. First the different radiation quantities which characterize a spectrally selective surface are defined in section 2.1. In section 2.2 the thin film optics which is needed for calculations on the optical properties of substrate-coating systems is given. The Drude-theory, which is used as the basic theory describing the spectral selectivity in a general sense, is discussed in section 2.3. In section 2.4 some scattering mechanisms which may limit the conductivity, and consequently the infrared reflectance, in a transparent conductor are discussed.

In section 2.5 model calculations on a hypothetical coating-substrate system are presented, based on the theory given in sections 2.1-2.4. Two methods for improving the solar absorptance of a coating, i.e. roughing the upper surface and applying an anti-reflection coating on the upper surface, is treated theoretically in section 2.6.

2.1 Radiation quantities

When radiation is incident on a surface, part of this radiation will be absorbed, transmitted and reflected. In this section the quantities 'absorptance', 'reflectance' and 'emittance' are defined. In the given definitions, the textbook of Siegel and Howell (1972) has closely been followed. Analogous summaries are given in the theses of van der Ley (1979), Sikkens (1980) and van Heereveld (1987).

2.1.1 Absorptance

The *directional spectral absorptance* of a surface is defined as the absorbed fraction of the radiation (of wavelength λ from the direction (θ_1, ϕ_1) and of polarization state p) incident on that surface. This is illustrated in figure 2.1 where θ_1 is the polar angle and ϕ_1 is the azimuthal angle of incidence. The radiation is incident on the x-y plane, where the z-axis is normal to the surface. In equation form it is:

$$\alpha(\theta_1, \phi_1, \lambda, p) = \frac{I_a(\theta_1, \phi_1, \lambda, p)}{I_i(\theta_1, \phi_1, \lambda, p)} \quad (2.1)$$

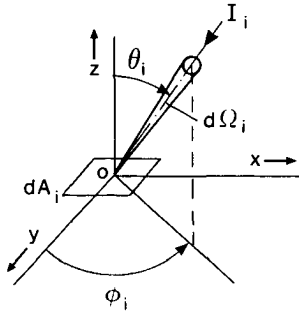


Figure 2.1 Picture of the parameters used in the definition of the absorptance. The surface of the absorbing medium is in the x-y plane.

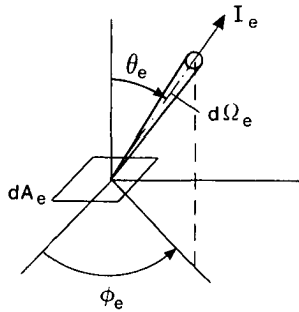


Figure 2.2 Picture of the parameters used in the definition of the emittance, analogous to figure 2.2

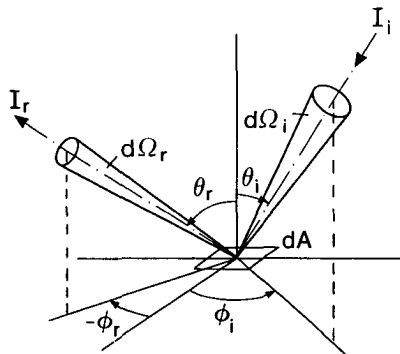


Figure 2.3 Picture of the parameters used in the definition of the bidirectional reflectance

Here the subscript 'i' stands for 'incident' and 'a' for 'absorbed'. The radiant intensity I_i is defined for an infinitesimal wavelength interval $d\lambda$, a surface area dA_i in the x-y plane and a pencil of solid angle $d\Omega_i$. For the sake of simplicity, we will neglect polarization effects and omit the p-dependence in the further definitions. Integration of $\alpha(\theta_i, \phi_i, \lambda)$ over the wavelength distribution of $I_i(\theta_i, \phi_i, \lambda)$ gives the *directional total absorptance*:

$$\alpha(\theta_i, \phi_i) = \frac{\int_0^{\infty} \alpha(\theta_i, \phi_i, \lambda) I_i(\theta_i, \phi_i, \lambda) d\lambda}{\int_0^{\infty} I_i(\theta_i, \phi_i, \lambda) d\lambda} \quad (2.2)$$

Where solar radiation is involved, I_i can be replaced by E with E as the solar radiation incident on a surface. A characteristic value of a solar absorber used in a solar collector is the *normal solar absorptance*:

$$\alpha_{s, \perp} = \frac{\int_0^{\infty} \alpha_{\perp}(\lambda) E(\lambda) d\lambda}{\int_0^{\infty} E(\lambda) d\lambda} \quad (2.3)$$

where the *normal spectral absorptance* $\alpha_{\perp}(\lambda)$ is the directional spectral absorptance for $\theta_i = 0$ (the ϕ dependence disappears for symmetry reasons).

2.1.2 Emittance

The emittance of a surface is directly related to its temperature. The *directional spectral emittance* of a surface with temperature T is given by (see figure 2.2):

$$\varepsilon(\theta_e, \phi_e, \lambda, T) = \frac{I_e(\theta_e, \phi_e, \lambda, T)}{I_b(\lambda, T)} \quad (2.4)$$

where $I_e(\theta_e, \phi_e, \lambda, T)$ is the emitted spectral radiant intensity defined for an infinitesimal wavelength interval $d\lambda$, a surface area dA_e and a pencil of solid angle $d\Omega_e$. The subscript 'e' stands for 'emitted'. $I_b(\lambda, T)$ is the spectral radiant intensity for a black body. It is related to the Planck radiation distribution law $M_b(\lambda, T)$ by $I_b = M_b(\lambda, T) d\Omega_e d\cos\phi$. Some spectral curves of M_b are drawn in figure 1.2. Integration of $\varepsilon(\theta_e, \phi_e, \lambda, T)$

over the wavelength distribution of $M_b(\lambda, T)$ gives the *directional total emittance*:

$$\epsilon(\theta_e, \phi_e, T) = \frac{\int_0^{\infty} \epsilon(\theta_e, \phi_e, \lambda, T) M_b(\lambda, T) d\lambda}{\int_0^{\infty} M_b(\lambda, T) d\lambda} \quad (2.5)$$

The *normal total emittance* $\epsilon_{\perp}(T)$ is defined as the directional total emittance normal to the surface, so $\theta_e = 0$ in eqn. (2.5). The *hemispherical total emittance* is the directional total emittance integrated over a hemisphere:

$$\epsilon_h(T) = (2\pi)^{-1} \int_0^{2\pi} \int_0^{\pi} \epsilon(\theta_e, \phi_e, T) \sin(\theta_e) \cos(\theta_e) d\theta_e d\phi_e \quad (2.6)$$

This quantity is normally used to characterize a spectrally selective surface, together with $\alpha_{s,1}$.

2.1.3 Reflectance and transmittance

The most general definition of a reflection quantity is the *bidirectional spectral reflectance* (see figure 2.3):

$$R(\theta_r, \phi_r, \theta_i, \phi_i, \lambda) = \frac{I_r(\theta_r, \phi_r, \lambda)}{I_i(\theta_i, \phi_i, \lambda)} \quad (2.7)$$

where the radiant intensity I_i of the incoming radiation is defined for an infinitesimal wavelength interval $d\lambda$, a surface area dA and a pencil of solid angle $d\Omega_i$. The radiant intensity of the reflected radiation I_r is defined for an infinitesimal wavelength interval $d\lambda$, a surface area dA and a pencil of solid angle $d\Omega_r$. The *specular spectral reflectance* is defined as the part of the incoming radiation which is reflected specularly:

$$R_s(\theta_i, \phi_i, \lambda) = \frac{I_r(\theta_i, \phi_i - \pi, \lambda)}{I_i(\theta_i, \phi_i, \lambda)} \quad (2.8)$$

This is reduced to the *normal specular spectral reflectance* when the incident radiation is normal to the surface ($\theta_i = 0$). The part of the incoming radiation which is reflected from the surface, indifferent in

which direction, is called the *directional hemispherical spectral reflectance* and is obtained by integrating the bidirectional spectral reflectance over a hemisphere:

$$R_h(\theta_i, \phi_i, \lambda) = (2\pi)^{-1} \int_0^{2\pi} \int_0^\pi R(\theta_i, \phi_i, \theta_r, \phi_r, T) \sin(\theta_r) \cos(\theta_r) d\theta_r d\phi_r \quad (2.9)$$

The *normal hemispherical spectral reflectance* $R_\perp(\lambda)$ is defined as the directional hemispherical spectral at normal incidence, so $\theta_i = 0$ in eqn. (2.9).

The transmission quantities can be defined analogously if θ_r and ψ_r are replaced by θ_t and ψ_t with $\pi/2 \leq \theta_t \leq \pi$. In the numerator of equation (2.8) θ_i must be replaced by $(\theta_i + \pi)$ to obtain the *straight-on going spectral transmittance*.

2.1.4 Relations between radiation quantities: Kirchhoff's law

When a surface having a temperature T is in thermodynamical equilibrium the relation between the absorptance and emittance of a surface is given by Kirchhoff's law:

$$\epsilon(\theta, \phi, \lambda, T) = \alpha(\theta, \phi, \lambda, T) \quad (2.10)$$

For an opaque body (transmittance $\underline{T}=0$) the directional hemispherical spectral reflectance can be related to the directional spectral absorptance (as $\alpha + R + \underline{T} = 0$ due to energy conservation) :

$$\alpha(\theta, \phi, \lambda, T) = 1 - R(\theta, \phi, \lambda, T) \quad (2.11)$$

Combining equations (2.10) and (2.11) gives a relation between the directional spectral emittance and the directional hemispherical spectral reflectance:

$$\epsilon(\theta, \phi, \lambda, T) = 1 - R(\theta, \phi, \lambda, T) \quad (2.12)$$

Similar relations hold for the directional total properties and for the hemispherical spectral properties. By determining the normal-hemispherical spectral reflectance spectrum of an opaque surface, both the normal solar absorptance and the normal total emittance can be derived using equations (2.3), (2.5), (2.11) and (2.12).

2.2 Thin film optics

The optics of thin film structures is discussed extensively in various textbooks (e.g. Heavens, 1965; Azzam and Bashara, 1977). In this section a recapitulation of the theory is given as far as it is used in ensuing sections.

2.2.1 Wave propagation through an absorbing medium

The optical properties of an isotropic medium are fully described by a complex refractive index $n(\lambda)$. To illustrate the concept of a complex refractive index, the propagation of an electromagnetic plane wave through an absorbing medium is discussed.

The electric field \vec{E} of a linearly polarized, monochromatic plane wave, travelling along the z-axis, can be described by:

$$\vec{E} = \begin{pmatrix} E_x \\ E_y \end{pmatrix} e^{i(\omega t - \tilde{\kappa}z)} \quad (2.13)$$

with E_x and E_y being the two transversal components of \vec{E} , ω is the circular frequency, t is the time, z is the z-axis coordinate, i is the complex number for which $i^2 = -1$ holds and $\tilde{\kappa}$ is the complex wavenumber which follows from the Maxwell equations and is given by:

$$\tilde{\kappa} = \frac{\omega}{c} \sqrt{\mu \tilde{\epsilon}} \quad (2.14)$$

with c the phase velocity, μ the magnetic permeability and $\tilde{\epsilon}$ the complex relative dielectric permittivity. μ can usually be put equal to unity at optical frequencies. The complex dielectric constant $\tilde{\epsilon}$ describes the response of the medium to the driving field \vec{E} yielding the electric displacement \vec{D} :

$$\vec{D} = \epsilon_0 \tilde{\epsilon} \vec{E} \quad (2.15)$$

where ϵ_0 is the permittivity of free space. The complex refractive index is written as $n = n - ik$, where n is the real part of the refractive index and k is the extinction coefficient. n is defined as the complex root of $\tilde{\epsilon}$, so:

$$\tilde{\epsilon} = \epsilon_r - i\epsilon_c = (n - ik)^2 = n^2 \quad (2.16)$$

Equation (2.13) can now be written as:

$$\vec{E} = \begin{pmatrix} E_x \\ E_y \end{pmatrix} e^{i(\omega t - \frac{\omega}{c}nz)} e^{-\frac{\omega}{c}kz} \quad (2.17)$$

This means that the wave travels along the z-axis with phase velocity $v = c/n$. The intensity $I = |\vec{E}|^2$ is z-dependent with:

$$I(z) = I(0) \exp\left(-2kz\frac{\omega}{c}\right) = I(0) e^{-az} \quad (2.18)$$

Here a is called the absorption coefficient, which is sometimes used instead of k as a measure of the attenuation of the intensity of a plane wave. The characteristic depth at which the intensity is reduced to $1/e$ of its initial value is called the skin depth and is given by:

$$\delta = a^{-1} = \frac{c}{k\omega} = \frac{\lambda}{4\pi k} \quad (2.19)$$

where λ is the vacuum wavelength. According to Kirchoff's law this is also the characteristic depth at which thermal radiation with wavelength λ which is emitted normal from the surface is generated.

2.2.2 Reflection and transmission at a plane interface

In figure 2.4 the beam trajectories are sketched for a wave incident on a plane interface between two media having a real refractive index n_1 and n_2 respectively.

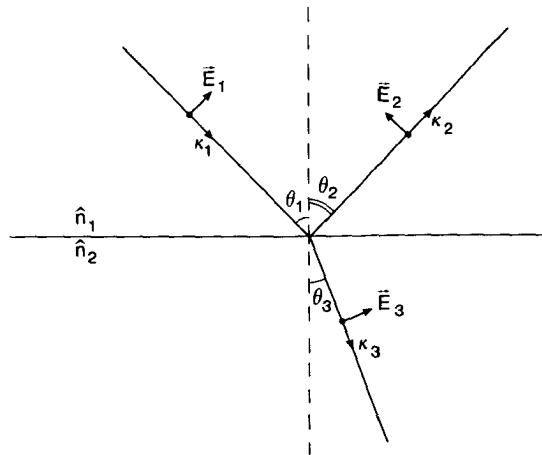


Figure 2.4 Reflection and refraction at a plane interface

The condition that the phase of the three waves must be the same at the interface gives:

$$\kappa_1 \sin(\theta_1) = \kappa_2 \sin(\theta_2) = \kappa_3 \sin(\theta_3) \quad (2.20)$$

with $\kappa_1 = \kappa_3$ this gives $\theta_1 = \theta_3$ (specular reflection), and:

$$\frac{\sin(\theta_1)}{\sin(\theta_2)} = \frac{n_1}{n_2} \quad (2.21)$$

which is Snell's law. The amplitudes of the transmitted and reflected vectors in terms of those of the incident vectors are derived by applying the continuity conditions for the Maxwell equations at the interface and lead to the Fresnel-coefficients for the reflected (r) and transmitted (t) amplitudes (Jackson, 1975):

$$r_s = \frac{E_{3s}}{E_{1s}} = \frac{n_1 \cos(\theta_1) - n_2 \cos(\theta_2)}{n_1 \cos(\theta_1) + n_2 \cos(\theta_2)} \quad (2.22)$$

$$r_p = \frac{E_{3p}}{E_{1p}} = \frac{n_1 \cos(\theta_2) - n_2 \cos(\theta_1)}{n_1 \cos(\theta_2) + n_2 \cos(\theta_1)} \quad (2.23)$$

$$t_s = \frac{E_{2s}}{E_{1s}} = \frac{2n_1 \cos(\theta_1)}{n_1 \cos(\theta_1) + n_2 \cos(\theta_2)} \quad (2.24)$$

$$t_p = \frac{E_{2p}}{E_{1p}} = \frac{2n_1 \cos(\theta_1)}{n_1 \cos(\theta_2) + n_2 \cos(\theta_1)} \quad (2.25)$$

Where the 's' subscript denotes the component of \vec{E} perpendicular to the surface and the 'p' subscript denotes the \vec{E} component parallel to the interface. θ_2 can be eliminated in the equations (2.22-2.25) using Snell's law:

$$\cos(\theta_2) = \frac{(n_2^2 - n_1^2 \sin^2(\theta_1))^{1/2}}{n_2} \quad (2.26)$$

Although originally derived for real angles θ_1 and refractive indices n_1 , equations (2.22-2.26) also hold for complex n_1 and $\tilde{\theta}_1$ (Heavens, 1965). If medium 1 is assumed to be vacuum ($n_1 = 1$), the reflectance at normal incidence becomes:

$$R = |r_p r_p^*| = |r_s r_s^*| = \left| \frac{n_2 - 1}{n_2 + 1} \right|^2 = \frac{(n_2 - 1)^2 + k_2^2}{(n_2 + 1)^2 + k_2^2} \quad (2.27)$$

2.2.3 Reflection and transmission by isotropic stratified planar structures

Usually a spectrally selective material is applied as a thin coating on a substrate. To describe such a system it is necessary to extend the theory given in section 2.2.2 to the case of a stratified planar structure. The electric field resulting from a system consisting of m layers on a substrate as sketched in figure 2.5, can be written as (Azzam and Bashara, 1977):

$$\begin{pmatrix} E_0^+ \\ E_0^- \end{pmatrix} = \prod_{j=0}^m \mathbb{U}_{j,j+1} \mathbb{L}_{j+1} \begin{pmatrix} E_{m+1}^+ \\ 0 \end{pmatrix} \quad (2.28)$$

In equation (2.28), $\mathbb{U}_{j,j+1}$ and \mathbb{L}_{j+1} are the scattering matrices for the transition through an interface from medium j to medium $j+1$ between two media and for the propagation through medium $j+1$ respectively. E_0^+ and E_0^- denote the complex amplitude of the forward and backward travelling plane wave.

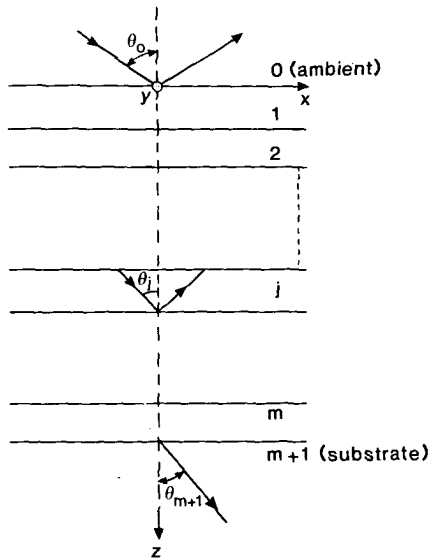


Figure 2.5 Sketch of a system of m layers on a substrate

\mathbb{L} is given by:

$$\mathbb{L}_{j,j+1} = \frac{1}{t_{j,j+1}} \begin{bmatrix} 1 & r_{j,j+1} \\ r_{j,j+1} & 1 \end{bmatrix} \quad (2.29)$$

with r and t the Fresnel coefficients defined in (2.22-2.25). \mathbb{L} is given by:

$$\mathbb{L}_j = \begin{bmatrix} e^{i\tilde{\beta}} & 0 \\ 0 & e^{-i\tilde{\beta}} \end{bmatrix} \quad (2.30)$$

with $\tilde{\beta}$ being the complex phase shift which is:

$$\tilde{\beta} = \frac{2\pi n_j d_j}{\lambda} \frac{(n_j^2 - n_0^2 \sin^2(\theta_0))^{1/2}}{n_j} \quad (2.31)$$

where d_j is the thickness of layer no j and λ is the vacuum wavelength. When the matrix multiplications are carried out, equation (2.28) can be rewritten as:

$$\begin{pmatrix} E_0^+ \\ E_0^- \end{pmatrix} = \begin{bmatrix} S_{11} & S_{12} \\ S_{21} & S_{22} \end{bmatrix} \begin{pmatrix} E_{m+1}^+ \\ 0 \end{pmatrix} \quad (2.32)$$

The complex reflection- and transmission coefficients are obtained from:

$$r = \frac{E_0^-}{E_0^+} = \frac{S_{21}}{S_{11}} \quad (2.33)$$

and

$$t = \frac{E_{m+1}^+}{E_0^+} = \frac{1}{S_{11}} \quad (2.34)$$

Equations (2.28-2.34) can be used for both p and s polarization. Finally, the reflectance R and the transmittance T are obtained from $R = |r r^*|$ and $T = |t t^*|$ respectively.

2.2.4 Extension to anisotropic layers

The formalism as given in sections 2.2.2 and 2.2.3 can be extended to the case of anisotropic layers. As the SnO_2 and In_2O_3 coatings have grown in the z-direction, perpendicular to the substrate, it can be assumed that a possible anisotropy will be restricted to the z-direction relative to the x-y plane. A coating with this property is called an uniaxial anisotropic film.

In figure 2.6 the light trajectories are sketched for a system consisting of two uniaxially anisotropic layers on a substrate. The complex refractive index in the x-y plane is denoted by the subscript 'o' (ordinary), and the refractive index in the z-direction is denoted by the subscript 'e' (extraordinary). The Fresnel reflection coefficients for the transition between layer i and layer i+1 are:

$$r_{p,j,j+1} = \frac{n_{j+1,o} n_{j+1,e} (n_{j,e}^2 - n_0^2 \sin^2(\theta_0))^{1/2} - n_{j,o} n_{j,e} (n_{j+1,e}^2 - n_0^2 \sin^2(\theta_0))^{1/2}}{n_{j+1,o} n_{j+1,e} (n_{j,e}^2 - n_0^2 \sin^2(\theta_0))^{1/2} + n_{j,o} n_{j,e} (n_{j+1,e}^2 - n_0^2 \sin^2(\theta_0))^{1/2}} \quad (2.35)$$

and:

$$r_{s,j,j+1} = \frac{(n_{j,o}^2 - n_0^2 \sin^2(\theta_0))^{1/2} - (n_{j+1,o}^2 - n_0^2 \sin^2(\theta_0))^{1/2}}{(n_{j,o}^2 - n_0^2 \sin^2(\theta_0))^{1/2} + (n_{j+1,o}^2 - n_0^2 \sin^2(\theta_0))^{1/2}} \quad (2.36)$$

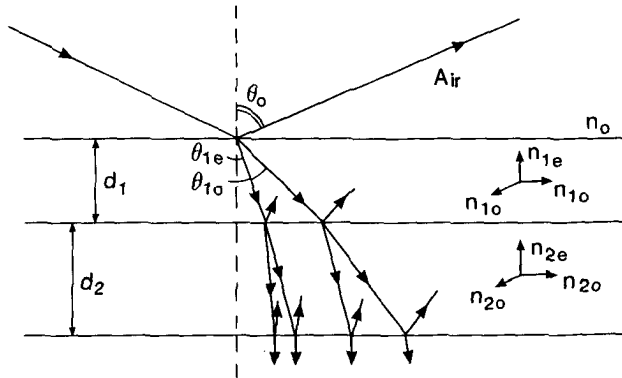


Figure 2.6 Sketch of the beam trajectories of a system consisting of two uniaxially anisotropic layers on a substrate

The phase shift $\tilde{\beta}$ is different for p and s polarized light:

$$\tilde{\beta}_{p_j} = \frac{2\pi d_j}{\lambda} \frac{n_{j,o}}{n_{j,e}} (n_{j,e}^2 - n_o^2 \sin^2(\theta_o))^{1/2} \quad (2.37)$$

$$\tilde{\beta}_{s_j} = \frac{2\pi d_j}{\lambda} (n_{j,o}^2 - n_o^2 \sin^2(\theta_o))^{1/2} \quad (2.38)$$

Equations (2.35-2.38) have been derived following the method given by Schopper (1952). The equations for the isotropic case are easily retained by equating the 'o' and 'e' components.

2.2.5 Extension to the case of $d \gg \lambda$

It is important to include the reflection from the backside of the substrate in the formalism described in sections 2.1.2-2.1.4. As the substrate thickness is usually a few millimeters while the wavelength is of the order of one micron, this leads to the situation that $d \gg \lambda$, which needs special precautions, as will be illustrated below.

Consider again the scattering matrix S as defined in (2.32). The transition through the substrate can be incorporated explicitly by:

$$S = \begin{bmatrix} A_{11} & A_{12} \\ A_{21} & A_{22} \end{bmatrix} \begin{bmatrix} e^{i\tilde{\beta}} & 0 \\ 0 & e^{-i\tilde{\beta}} \end{bmatrix} \begin{bmatrix} 1 & r \\ r & 1 \end{bmatrix} \frac{1}{t} \quad (2.39)$$

here $\tilde{\beta}$ is the phase shift through the substrate, r and t are the Fresnel coefficients at the substrate/air interface and the matrix A is the scattering matrix resulting from the coating system on the substrate. So the matrix elements A_{ij} are arbitrary complex numbers. For the calculation of the reflectance and transmittance it is necessary to calculate $S_{11} S_{11}^*$ and $S_{21} S_{21}^*$ (see equations (2.33) and (2.34)). For $S_{21} S_{21}^*$ this gives:

$$S_{21} S_{21}^* = (t t^*)^{-1} \left[A_{21} A_{21}^* \exp(4\pi kd/\lambda) + A_{22} A_{22}^* r r^* \exp(-4\pi kd/\lambda) + \operatorname{Re}(A_{22} A_{21}^* r) 2 \cos(4\pi nd/\lambda) + \operatorname{Im}(A_{22} A_{21}^* r) 2 \sin(4\pi nd/\lambda) \right] \quad (2.40)$$

where n and k are the real and complex part respectively of the substrate refractive index. d is the substrate thickness. For $S_{11} S_{11}^*$ a similar

expression is valid. From equation (2.40) it can be observed that, as for a glass substrate $d/\lambda \approx 4 \cdot 10^3$, a slight non-parallelism of both substrate sides, a very small error in the determination of d or a very small bandwidth of the light with center wavelength λ , will cause the sine- and the cosine term in equation (2.40) to be undetermined.

In practice these terms will always be undetermined and R and T must be averaged over all possible values of $\cos(4\pi nd/\lambda)$ and $\sin(4\pi nd/\lambda)$. This requires the solution of an integral of the form:

$$R, T = (2\pi)^{-1} \int_0^{2\pi} \frac{a + b \sin(\psi) + c \cos(\psi)}{d + e \sin(\psi) + f \cos(\psi)} d\psi \quad (2.41)$$

with a, b, c, d, e and f constants. As analytical integration of (2.41) is very tedious, in practice R and T are calculated for $(4\pi nd/\lambda) = 0, \frac{1}{4}\pi, \dots, \frac{7}{4}\pi$ and the results are averaged to obtain the final value.

2.2.6 Modelling of surface roughness

A rough surface between two media with dielectric constants ϵ_1 and ϵ_2 is schematically drawn in figure 2.7a. It is assumed that the surface roughness height $h(z)$ can be described by a Gaussian profile with a standard deviation σ . The effective dielectric constant in the z -direction can be written as (Szczyrbowski, 1985):

$$\epsilon(z) = \epsilon_1 + \left(\frac{\epsilon_2 - \epsilon_1}{2} \right) \left(1 + \operatorname{erf} \left(\frac{z}{a} \right) \right) \quad (2.42)$$

with erf being the error function:

$$\operatorname{erf} \left(\frac{z}{a} \right) = \frac{2}{\sqrt{\pi}} \int_{-\infty}^{z/a} \exp(-q^2) dq \quad (2.43)$$

and $a = \sqrt{2} \sigma$. For the calculation of reflectance and transmittance of a rough interface, in principle the dielectric constant profile of equation (2.42) can be simulated with a large number of thin films. To limit the amount of calculus needed, we make a drastic approximation by describing the surface roughness by only one film between regions 1 and 2. This film has an effective dielectric constant of $(\epsilon_1 + \epsilon_2)/2$. This is equivalent to using the effective medium theory of Bruggeman (1935) for the effective dielectric constant of a mixture of two materials with a volume fraction of

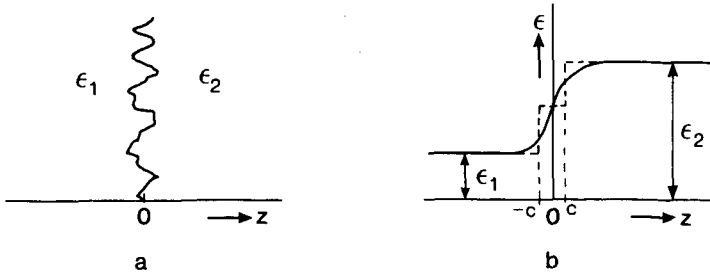


Figure 2.7 a: sketch of a rough interface between media with dielectric constants ϵ_1 and ϵ_2 respectively.
 b: sketch of the effective dielectric constant and the approximation of the roughness by a single coating (---)

0.5 each. The model can be written as:

$$\begin{aligned}
 \epsilon_m(z) &= \epsilon_1 & \text{for } z < -c \\
 \epsilon_m(z) &= 0.5 (\epsilon_1 + \epsilon_2) & \text{for } -c < z < c \\
 \epsilon_m(z) &= \epsilon_2 & \text{for } z > c
 \end{aligned} \tag{2.44}$$

This is sketched in figure 2.7b. A measure for the error in $\epsilon(z)$ made in this approximation is:

$$\Delta\epsilon = \left(\frac{\epsilon_2 - \epsilon_1}{2} \right) \int_{-\infty}^{\infty} \left(1 + \operatorname{erf}\left(\frac{z}{a}\right) - \epsilon_m(z) \right) dz \tag{2.45}$$

This integral has a minimum when the error function has a value of 0.50. This gives the thickness of the coating with which the roughness can be simulated best. The relation between c and σ is for this case:

$$c = \sigma \sqrt{2} \operatorname{erf}^{-1}(0.50) \approx 0.67 \sigma \tag{2.46}$$

So the thickness of the coating which simulates the surface roughness best is: $d_s = 2c \approx 1.34 \sigma$.

The approximation of simulating the surface roughness by one or a number of specularly reflecting coatings is only valid if the correlation length of the surface roughness is much smaller than the wavelength of the light used. Also the condition $\lambda \gg d_s$ must be valid. As usually $d_s \approx 20$ nm in our films and we expect that the correlation length will have the same magnitude, these conditions will be fulfilled in our coatings as

wavelengths $\lambda > 300$ nm are used. When these conditions are not fulfilled the problem becomes much more complicated (see e.g. van Heereveld, 1988).

2.3 The Drude theory

In this section an elementary recapitulation of the Drude model is given. A more comprehensive derivation, based on the solution of the Boltzmann transport equation, leads with some approximations to the same result and can be found in the literature (Ashcroft and Mermin, 1976; Wilson, 1965).

The equation of motion for a free electron which is acted on by an electric field $E(x, t)$ is:

$$m \left[\ddot{\vec{x}} + \gamma \dot{\vec{x}} \right] = e \vec{E}(x, t) \quad (2.47)$$

where γ is the attenuation factor. If the field varies harmonically in time with frequency ω as $e^{-i\omega t}$, the solution is:

$$\dot{\vec{x}} = \frac{e}{m} \frac{\vec{E}(x, t)}{(\omega^2 - i\omega\gamma)} \quad (2.48)$$

So the contribution to the dipole moment of n_- electrons is:

$$\vec{P} = n_- e \dot{\vec{x}} = \frac{n_- e^2}{m} \frac{\vec{E}(x, t)}{(\omega^2 - i\omega\gamma)} \quad (2.49)$$

The dielectric susceptibility χ is in general defined by:

$$\vec{P} = \epsilon_0 \chi \vec{E} \quad (2.50)$$

Equation (2.49) gives the polarizability of the free electrons only. When also other effects contribute to the polarizability, these effects are superimposed. Together with the definition of the dielectric constant ϵ which is defined in terms of \vec{E} and \vec{P} from:

$$\vec{D} = \epsilon_0 \vec{E} + \vec{P} = \epsilon \epsilon_0 \vec{E} \quad (2.51)$$

, where \vec{D} is the dielectric displacement, it follows that the dielectric constant can in general be written as:

$$\epsilon = 1 + \chi_{VE} + \chi_{FC} + \chi_{PH} + \dots \quad (2.52)$$

with: χ_{VE} : contribution from valence electrons
 χ_{FC} : contribution from free carriers
 χ_{PH} : contribution from polar phonons

We assume that χ_{VE} is the same for all wavelengths, and define $\epsilon_{\infty} \equiv 1 + \chi_{VE}$. χ_{PH} and other possible contributions are neglected for the moment; in chapter 6 an expressions for χ_{PH} is given.

Equation (2.52) can now be written as:

$$\epsilon(\omega) = \epsilon_{\infty} - \frac{n_- e^2}{m} \cdot \frac{1}{(\omega^2 - i\omega\gamma)} \quad (2.53)$$

When considering free electrons in a crystal lattice the effect must be taken into account that an electron in a periodic potential is accelerated relative to the lattice in an applied electric field as if the mass of the electron were equal to an effective mass m_{eff} which is defined as:

$$m_{eff}^{-1} = \hbar^{-2} \frac{d^2\psi}{dk^2} \quad (2.54)$$

where $d^2\psi/dk^2$ denotes the band bending of the conduction band, \underline{k} is the electron wavevector and \hbar is Planck's constant h divided by 2π . This means that in equation (2.53) m must be replaced by m_{eff} to be valid in a periodic crystal lattice. Finally equation (2.53) can be rewritten as:

$$\epsilon(\omega) = (n-ik)^2 = \epsilon_{\infty} \left[1 - \frac{\omega_p^2}{\omega^2 + \gamma^2} - i \frac{\omega_p^2 (\gamma/\omega)}{\omega^2 + \gamma^2} \right] \quad (2.55)$$

where ω_p is the plasma circular frequency given by:

$$\omega_p = \left(\frac{n_- e^2}{\epsilon_0 \epsilon_{\infty} m_{eff}} \right)^{1/2} \quad (2.56)$$

From the Maxwell equations a relation can be derived which defines the relative permittivity in terms of a complex resistivity $\tilde{\rho}$ (Jackson, 1975):

$$\epsilon(\omega) = \epsilon_{\infty} - \frac{i}{\epsilon_0 \omega \tilde{\rho}(\omega)} \quad (2.57)$$

Combining equations (2.55) and (2.57) gives an alternative formulation of the Drude theory:

$$\tilde{\rho}(\omega) = \frac{\gamma + i\omega}{\epsilon_0 \epsilon_\infty \omega_p^2} \quad (2.58)$$

The real part of $\tilde{\rho}(\omega)$ for $\omega \rightarrow 0$ is also defined as $\rho = (n_e e \mu)^{-1}$, with μ the electrical mobility. Combining this with equation (2.58) gives a relation between μ and γ :

$$\gamma = \frac{e}{m_{\text{eff}} \mu} \quad (2.59)$$

The mobility μ is defined as the drift velocity of the conduction electrons in a material per unit of applied electric field. This quantity is related to the average relaxation time $\langle \tau \rangle$, where $\langle \tau \rangle$ is the mean time between successive collisions of an electron, by $\langle \tau \rangle = \gamma^{-1}$ and (2.59). Equations (2.59) and (2.56) give, via equation (2.55), a relation between the optical constants n and k and the electrical properties n_e and μ .

To get some insight in the wavelength dependent reflective properties of materials which behave according to the Drude model given by equation (2.55), some limiting cases are considered.

1. high frequency (low wavelength) limit: $\omega > \omega_p, \gamma$.

For this case equation (2.55) can be approximated by:

$$\epsilon(\omega) \approx \epsilon_\infty \left[1 - \left(\frac{\omega_p}{\omega} \right)^2 - i \frac{\omega_p^2 \gamma}{\omega^3} \right] \quad (2.60)$$

This gives for the refractive index n and the extinction coefficient k :

$$n(\omega) \approx \epsilon_\infty^{1/2} \left[1 - \left(\frac{\omega_p}{\omega} \right)^2 \right]^{1/2} \quad \text{and} \quad k(\omega) \approx \epsilon_\infty^{1/2} \left[\frac{\omega_p^2 \gamma}{2 \omega^3} \right] \quad (2.61)$$

This means that for increasing frequency (decreasing wavelength) the material becomes more transparent ($k \rightarrow 0$) with a refractive index which approaches ϵ_∞ .

2. low frequency (high wavelength) limit: $\omega < \omega_p, \gamma$.

For this case equation (2.55) can be approximated by:

$$\epsilon(\omega) \approx \epsilon_{\infty} \left[1 - \left(\frac{\omega_p}{\gamma} \right)^2 - i \frac{\omega_p^2}{\omega \gamma} \right] \quad (2.62)$$

This gives for the refractive index n and the extinction coefficient k :

$$n(\omega) \approx k(\omega) \approx \omega_p \sqrt{\frac{\epsilon_{\infty}}{2 \omega \gamma}} \quad (2.63)$$

As n and k are much larger than unity, the normal reflectance, using equation (2.27), can be approximated by:

$$R(\omega) = \frac{(n(\omega)-1)^2 + k(\omega)^2}{(n(\omega)+1)^2 + k(\omega)^2} \approx 1 - \frac{2}{k(\omega)} = 1 - 2 (2\rho\omega\epsilon_0)^{1/2} \quad (2.64)$$

This equation is known as the Hagen-Rubens relation. The reflectance will approach unity with decreasing circular frequency (increasing wavelength) and with decreasing resistivity of the material.

The behaviour of $n(\lambda)$ and $k(\lambda)$ in the intermediate region $\lambda_p < \lambda < \lambda_{\gamma}$, where λ_p and λ_{γ} are defined as: $\lambda_p \equiv 2\pi c/\omega_p$ and $\lambda_{\gamma} \equiv 2\pi c/\gamma$, is illustrated in figure 2.8. In this figure curves of $n(\lambda)$ and $k(\lambda)$ are drawn for $\epsilon_{\infty} = 4$, $\lambda_p = 1$ and $2 \mu\text{m}$ and $\lambda_{\gamma} = 5 \mu\text{m}$.

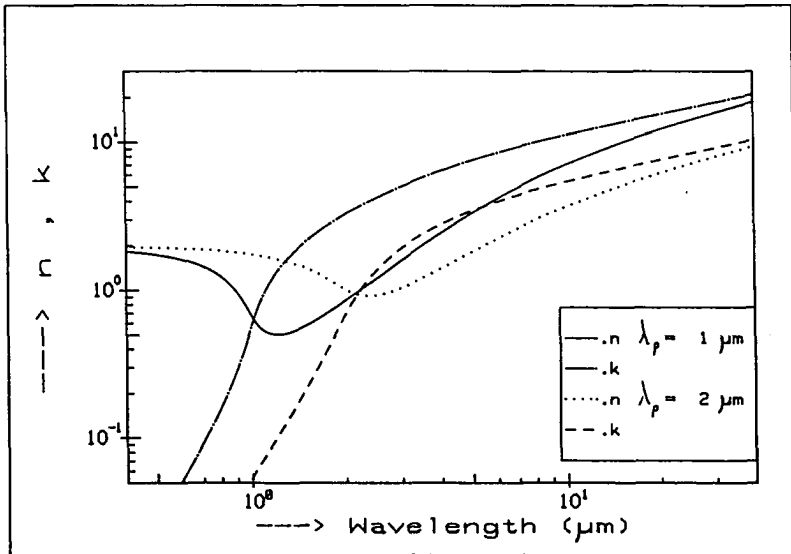


Figure 2.8 Refractive index n and extinction coefficient k as a function of wavelength according to the Drude model for 2 values of λ_p .

It is observed that $n(\lambda)$ reaches a minimum at $\lambda \approx \lambda_p$, and $k(\lambda)$ decreases rapidly for $\lambda < \lambda_p$. Also the high- and low wavelength behaviour of n and k , as discussed above, can be observed in the figure.

Before discussing the properties of materials which obey the Drude theory in more detail, we note that the three parameters ω_p , ω and γ in equation (2.55) can be reduced to two by defining a plasma frequency ω'_p slightly different from equation (2.56) (Groth and Kauer, 1965):

$$\omega'_p = \left(\frac{n_e e^2}{\epsilon_0 \epsilon_\infty m_{\text{eff}}} - \gamma^2 \right)^{1/2} = (\omega_p^2 - \gamma^2)^{1/2} \quad (2.65)$$

Equation (2.55) can be rewritten as:

$$\epsilon(\omega) = \epsilon_\infty \left[1 - \frac{1 + \left(\frac{\gamma}{\omega'_p}\right)^2}{\left(\frac{\omega}{\omega'_p}\right)^2 + \left(\frac{\gamma}{\omega'_p}\right)^2} - i \frac{\frac{\gamma}{\omega'_p} \left(1 + \left(\frac{\gamma}{\omega'_p}\right)^2\right)}{\frac{\omega}{\omega'_p} \left[\left(\frac{\omega}{\omega'_p}\right)^2 + \left(\frac{\gamma}{\omega'_p}\right)^2\right]} \right] \quad (2.66)$$

So equation (2.55) is rewritten in terms of (γ/ω'_p) and (ω/ω'_p) . Equation (2.66) can only be used if $\gamma < \omega_p$. If $\gamma > \omega_p$ another plasma frequency ω'' can be defined by:

$$\omega'' = (\gamma^2 - \omega_p^2)^{1/2} \quad (2.67)$$

For this case equation (2.55) can be rewritten as:

$$\epsilon(\omega) = \epsilon_\infty \left[1 - \frac{1 - \left(\frac{\gamma}{\omega''}\right)^2}{\left(\frac{\omega}{\omega''}\right)^2 + \left(\frac{\gamma}{\omega''}\right)^2} - i \frac{\frac{\gamma}{\omega''} \left(1 - \left(\frac{\gamma}{\omega''}\right)^2\right)}{\frac{\omega}{\omega''} \left[\left(\frac{\omega}{\omega''}\right)^2 + \left(\frac{\gamma}{\omega''}\right)^2\right]} \right] \quad (2.68)$$

We now consider the normal reflective properties of a semi-infinite medium behaving according to the Drude theory. In figure 2.9 the normal reflectance curves, calculated from (2.66), (2.16) and (2.27), are given for different $\lambda'_p/\lambda_\gamma$ ratio's as a function of λ/λ'_p . For ϵ_∞ a value of 4 has been taken. In figure 2.10 the reflectance curves calculated analogously for different $\lambda''_p/\lambda_\gamma$ ratio's as a function of λ/λ''_p are given.

In these figures it is observed that the spectrally selective properties become very poor when $\lambda_\gamma < \lambda_p$. The ideal spectrally selective behaviour is approximated best when $\lambda'_p/\lambda_\gamma$ is as small as possible.

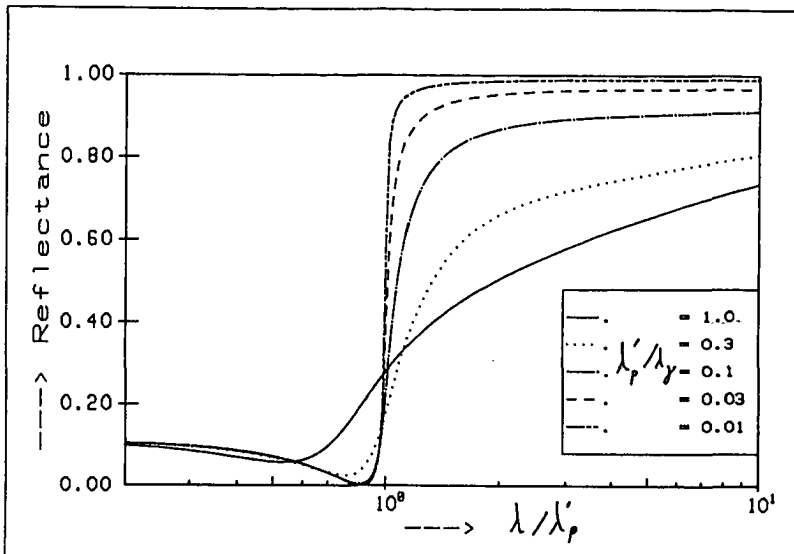


Figure 2.9 Reflectance as a function of the parameter λ/λ'_p for different values of $\lambda'_p/\lambda_\gamma$.

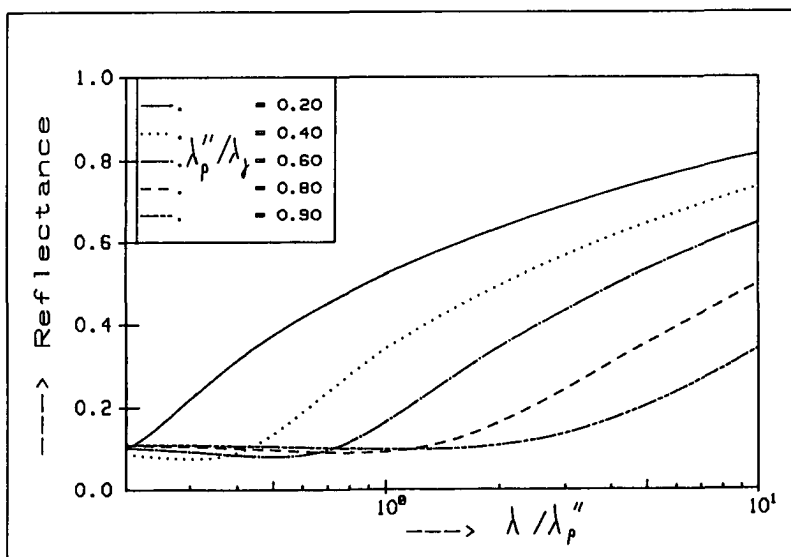


Figure 2.10 Reflectance as a function of the parameter λ/λ''_p for different values of $\lambda''_p/\lambda_\gamma$.

As for this case $\lambda_p \approx \lambda'_p$ we find that, in electrical quantities, the quotient

$$\frac{\lambda}{\lambda_p} = \mu \sqrt{\frac{m_{eff} n}{\epsilon_\infty \epsilon_0}} \quad (2.69)$$

must be as large as possible. When the value of λ_p is fixed, the resulting condition is that the product $m_{eff} \mu$ (see equation (2.59)) must be as large as possible. The reflectance for $\lambda < \lambda_p$ can be diminished by putting $\epsilon_\infty = 1$. This is valid for a free electron plasma, of which the spectrally selective properties have been treated theoretically by Sikkens (1981). The mobility μ , which should be as high as possible for optimum spectrally selective behaviour, will be limited by the various scattering mechanisms which are operative in real materials. The mechanisms which can be expected to be important in our transparent conductors are subject of the next section.

2.4 Scattering mechanisms

In this section some scattering mechanisms are discussed which might affect the mobility in doped tin oxide and indium oxide coatings. These mechanisms include scattering by ionized impurities, neutral impurities, longitudinal optical and acoustical phonons and grain boundaries.

2.4.1 Ionized impurity scattering

The scattering against ionized impurities will always be present in doped tin oxide and indium oxide coatings as ions are necessary to have free electrons. A theory which rests upon the equivalence of Joule heat and energy loss of electrons in a medium has been given by Gerlach and Grosse (1977). In this treatment the ionized impurities are treated as scattering centers with a Coulomb potential. The relaxation frequency γ in 2.58 is taken both complex and frequency dependent ($\tilde{\gamma}(\omega) = \gamma_r(\omega) + i \gamma_c(\omega)$):

$$\tilde{\rho}(\omega) = \frac{\gamma_r(\omega) + i (\gamma_c(\omega) + \omega)}{\epsilon_0 \epsilon_\infty \omega_p^2} \quad (2.70)$$

According to the Gerlach-Grosse theory the dynamic resistivity due to ionized impurity scattering can be written as:

$$\tilde{\rho}(\omega) = i \frac{Z^2 N_1}{6\pi^2 \epsilon_0 n_0^2 \omega} \int_0^\infty k^2 \left((\tilde{\epsilon}(\underline{k}, \omega))^{-1} - (\tilde{\epsilon}(\underline{k}, 0))^{-1} \right) dk + i \frac{\omega}{\epsilon_0 \epsilon_\infty \omega_p^2} \quad (2.71)$$

where N_1 is the ion density, Z is the charge of the impurities and $\tilde{\epsilon}(\underline{k}, \omega)$ is the dielectric function of the free-electron gas which depends on the frequency ω and on the electron wavevector \underline{k} . Following the treatment as given by Hamberg and Granqvist (1986-2,3), we take the longitudinal part of the dielectric function $\tilde{\epsilon}(\underline{k}, \omega)$ as given by Linhard (1954), with a correction for electron exchange and -correlation according to the Singwi-Sjölander theory (Singwi, 1968; Vashista, 1972). For a degenerate electron gas (where the Fermi energy is much larger than the thermal electron energy), this gives:

$$\epsilon(\underline{k}, \omega) = \epsilon_\infty + \frac{3\epsilon_\infty^2 \omega^2}{k^2 v_F^2} \left(1 - G(\underline{k}) \right) (F_1 + i F_2) \quad (2.72)$$

with:

$$F_1 = \frac{1}{2} + \frac{1}{8z} \left[1 - (z-u)^2 \right] \ln \left| \frac{z-u+1}{z-u-1} \right| + \frac{1}{8z} \left[1 - (z+u)^2 \right] \ln \left| \frac{z+u+1}{z+u-1} \right| \quad (2.73)$$

and:

$$F_2 = \begin{cases} \frac{\pi}{2} u & \text{for } z+u < 1 \\ \frac{\pi}{8z} \left[1 - (z-u)^2 \right] & \text{for } |z-u| \leq 1 \leq |z+u| \\ 0 & \text{for } |z-u| > 1 \end{cases} \quad (2.74)$$

with : $z = k/2k_F$

$u = |\omega|/k v_F$

$v_F = \hbar k_F / m_{\text{eff}}$: the electron Fermi velocity

$k_F = (3\pi^2 n_0)^{1/3}$: the electron Fermi wavenumber

The function $G(\underline{k})$ is the correction to the Linhard dielectric function as given by Singwi and Sjölander and can be approximated by:

$$G(\underline{k}) = A_1 \left\{ 1 - \exp[-A_2 (k/k_F)^2] \right\} \quad (2.75)$$

A_1 and A_2 are dependent on the parameter r_s^* , which is given by:

$$r_s^* = \frac{3}{4\pi n_- a_0^*} \quad (2.76)$$

Here a_0^* denotes the effective Bohr radius given by:

$$a_0^* = \frac{h^2 \epsilon_0 \epsilon_s}{\pi e^2 m_{eff}} \quad (2.77)$$

where ϵ_s is the static dielectric constant. We have approximated the tabulated values of $A_1(r_s^*)$ and $A_2(r_s^*)$ (Vashista, 1972) by:

$$\left. \begin{aligned} A_1(r_s^*) &= 0.598 + 0.124 r_s^* \\ A_2(r_s^*) &= 0.393 - 0.029 r_s^* \end{aligned} \right\} \quad (2.78)$$

The integral in equation (2.71) has been calculated numerically with the trapezium rule, taking 2000 steps for $\underline{k} < k_F$ and 500 steps for $k_F < \underline{k} < 6k_F$ for each value of λ ($= 2\pi c/\omega$). It has been checked that the contribution to the integral is negligible for $\underline{k} > 6k_F$.

Calculations have been made with fixed parameters $\epsilon_\infty = 4$ and $\epsilon_s = 10$, which is applicable to both SnO_2 and In_2O_3 . The real part of $\tilde{\rho}(\lambda)$, $\rho_r(\lambda)$, calculated as described above, is given as a function of λ with n_- and m_{eff} as varied parameters in figures 2.11 and 2.12. In these figures the dependence of $\rho_r(\lambda)$ on m_{eff} and n_- can be observed. The characteristic behaviour of $\rho_r(\lambda)$ observed in both figures is: for $\lambda \leq 0.7 \lambda_p$, $\rho_r(\lambda)$ follows a power law: $\rho_r(\lambda) \sim \lambda^{1.7}$ and for $\lambda \geq 0.7 \lambda_p$, $\rho_r(\lambda)$ is constant. This means that the Drude theory, with a wavelength-independent γ , is valid for $\lambda \geq 0.7 \lambda_p$ but not for $\lambda \leq 0.7 \lambda_p$.

The complex part of $\tilde{\rho}(\lambda)$, $\rho_c(\lambda)$, differs little from $(\lambda_p^2 / (2\pi c \epsilon_0 \epsilon_\infty \lambda))$, the value which is predicted by the Drude theory. The deviations which occur for $\lambda \approx \lambda_p$ can be illustrated by defining a wavelength dependent plasma wavelength:

$$\lambda_p(\lambda) = 2\pi c \epsilon_0 \epsilon_\infty \rho_c(\lambda) \lambda \quad (2.79)$$

The $\lambda_p(\lambda)$ thus defined has been calculated for a material with $n_- = 3.344 \cdot 10^{26} / \text{m}^3$, $m_{eff} = 0.30 m_e$ and $\epsilon_\infty = 4$, which gives $\lambda_p = 2 \mu\text{m}$ according to equation (2.56).

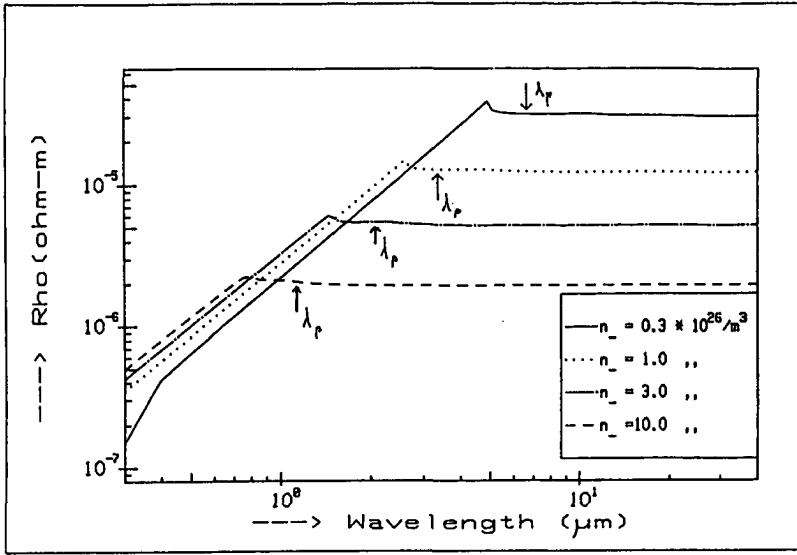


Figure 2.11 The real part of the complex resistivity as a function of wavelength for $m_{\text{eff}} = 0.3 m_e$ and different values of n_- . The plasma wavelengths are also indicated in the figure.

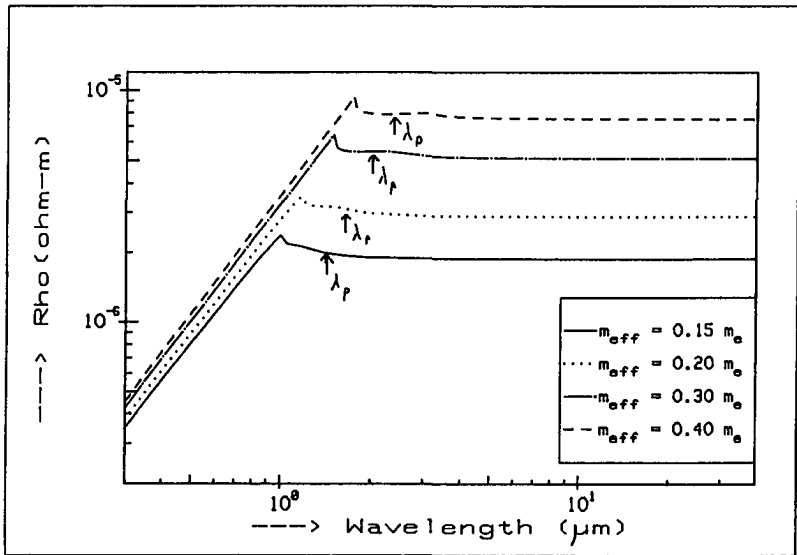


Figure 2.12 The real part of the complex resistivity as a function of wavelength for $n_- = 3 \cdot 10^{26} / \text{m}^3$ and different values of m_{eff} . The plasma wavelengths are also indicated in the figure.

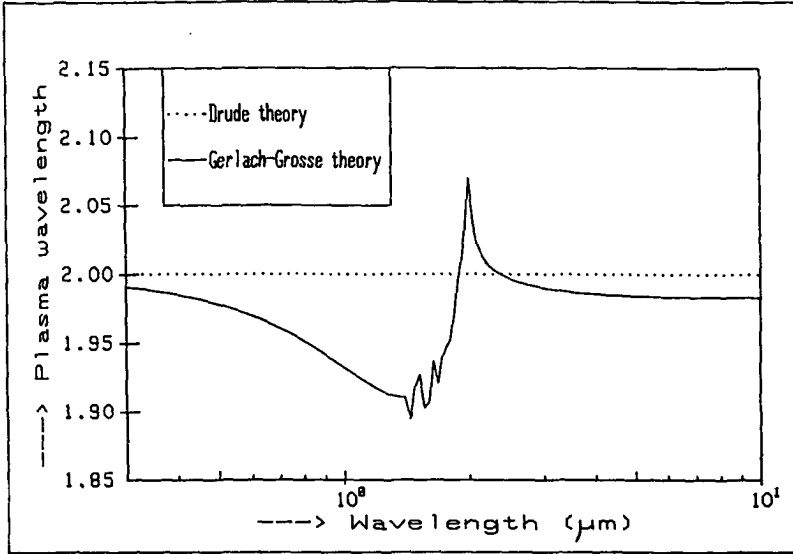


Figure 2.13 The plasma wavelength $\lambda_p(\lambda)$ as defined by (2.79) as a function of wavelength.

Figure 2.13 gives $\lambda_p(\lambda)$ calculated from equations (2.79) and (2.72). In this figure it is shown that the maximum deviation from the wavelength-independent value is at about $0.7\lambda_p$ and is about 5%. The oscillations in the curve for $0.7\lambda_p < \lambda < 0.9\lambda_p$ are due to errors in the numerical evaluation of equation (2.72), as for these wavelengths the function F_1 (2.74) changes sign very rapidly for $z-u \approx 1$.

The constant value of $\rho_r(\lambda)$ for $\lambda \rightarrow \infty$ implies that the DC-mobility μ has a maximum value due to ionized impurity scattering. This maximum value is given by:

$$\mu_{\max} = (n_- e \rho_r(\lambda \rightarrow \infty))^{-1} \quad (2.80)$$

The calculated maximum mobility is given as a function of the electron density in figure 2.14 and as a function of the effective mass in 2.15. In these figures it can be observed that μ_{\max} is weakly dependent on n_- and strongly dependent on m_{eff} . This implies that the product $\mu_{\max} \cdot m_{\text{eff}}$ increases with a decreasing effective mass.

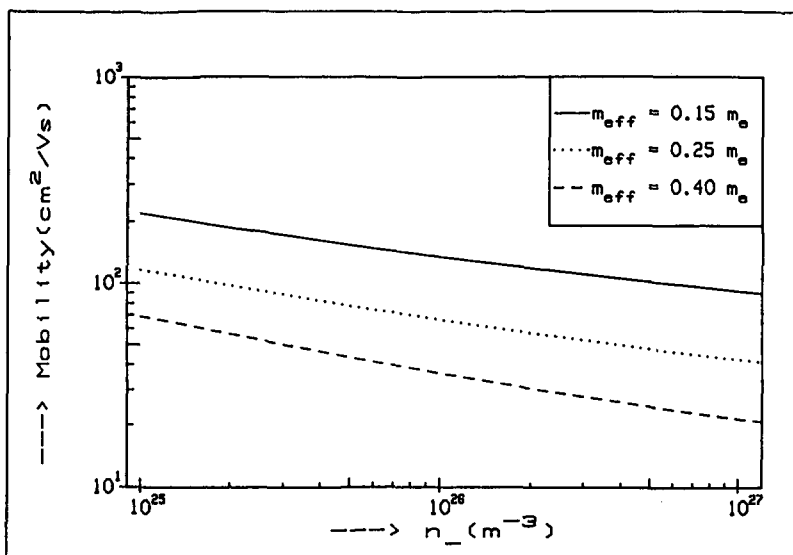


Figure 2.14 Maximum mobility due to ionized impurity scattering as a function of the electron density for different values of m_{eff} .

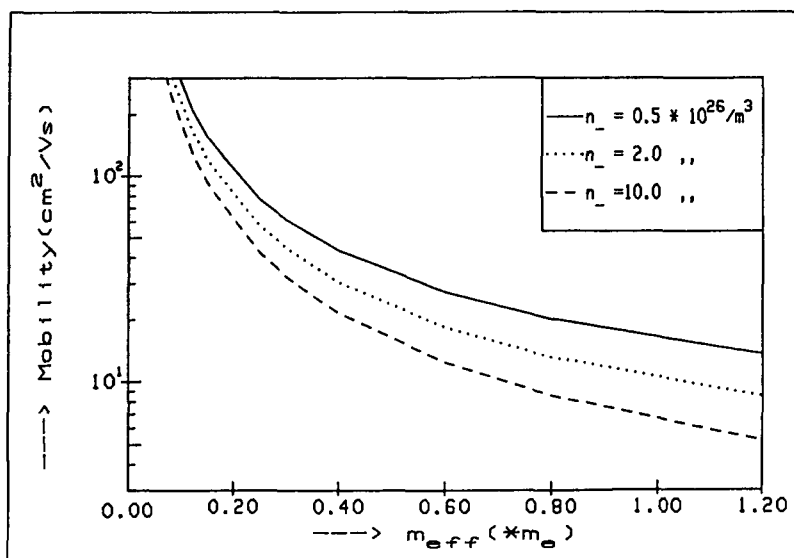


Figure 2.15 Maximum mobility due to ionized impurity scattering as a function of the effective mass for different values of n_{-} .

2.4.2 Neutral impurity scattering

The maximum mobility due to scattering of electrons against neutral impurities, such as interstitial oxygen atoms, is, according to Erginsoy (1950), given by:

$$\mu_n = \frac{\pi^2 m_{eff} e^3}{10 \epsilon_0 \epsilon_s N_n h^3} \quad (2.81)$$

with N_n the density of neutral impurities. For $N_n = 1 \cdot 10^{25}/m^3$, $m_{eff} = 0.3m_e$ and $\epsilon_s = 10$ a mobility of $\mu_n = 4.3 \text{ cm}^2/\text{Vs}$ is found.

2.4.3 Lattice scattering

2.4.3.1 Scattering by acoustical phonons

For degenerate electron statistics the mobility due to acoustical phonons can be approximated for high and low temperatures T by:

$$\begin{aligned} \mu_{la} &\sim T^{-1} && \text{for } T \gg \theta_R \\ \mu_{la} &\sim T^{-5} && \text{for } T \ll \theta_R \end{aligned} \quad (2.82)$$

Here θ_R is a characteristic temperature of the solid's lattice resistivity in the same way as the Debye temperature θ_D is characteristic of a solid's lattice specific heat. The characteristic temperature θ_R should be about equal to the Debye temperature θ_D , but is not necessarily the same. An equation which has proved to be valid moderately well for most metals, also in the $T \approx \theta_R$ region (Meaden, 1965), is given by the Grüneisen-Bloch relation, which can be written as:

$$\mu_{la} = \left(\frac{c_{la}}{\theta_R} \cdot \left(\frac{T}{\theta_R} \right)^5 \int_0^{\theta_R/T} \frac{z^2 dz}{(e^z - 1)(1 - e^{-z})} \right)^{-1} \quad (2.83)$$

where c_{la} is a constant. In the high and low temperature limit, equation (2.83) reduces to (2.82).

2.4.3.2 The scattering by longitudinal optical phonons

The scattering by longitudinal optical phonons has been described by Howarth and Sondheimer (1953) and has been used by Koch (1963) to interpret

the dependence of the conductivity of SnO_2 coatings on the electron density. The dependence of the mobility on the temperature can be written as:

$$\mu_{10} = c_{10} T \sinh^2\left(\frac{\theta_{10}}{2T}\right) \quad (2.84)$$

where θ_{10} is a characteristic temperature and c_{10} a constant which depends on m_{eff} and n_- :

$$c_{10} \sim m_{\text{eff}}^{-11/6} n_-^{1/3} \quad (2.85)$$

For high and low temperatures, equation (2.84) reduces to:

$$\begin{aligned} \mu_{10} &\sim T^{-1} && \text{for } T \gg \theta_{10} \\ \mu_{10} &\sim T \exp(\theta_{10}/T) && \text{for } T \ll \theta_{10} \end{aligned} \quad (2.86)$$

This is essential the same behaviour as predicted for acoustical phonons by equation (2.82); in both cases $\mu \sim T^{-1}$ for high temperatures, and the influence of phonon scattering rapidly decreases ($\mu \rightarrow \infty$) at low temperatures.

2.4.4 Grain boundary scattering

The tin oxide and indium oxide coatings investigated are polycrystalline. This means that they consist of crystallites separated by irregular formed grain boundaries. In these grain boundaries many dangling bonds will be present, so electrons will be trapped in these regions thus giving rise to a potential barrier between the grains.

The theory of scattering by grain boundaries has been reviewed by Orton and Powell (1980). The model used in this review is that the grains in the polycrystalline material are represented by cubic grains with edges d_1 , separated by intergranular regions from the neighbour cubes at a distance d_2 (see figure 2.16). The overall grain size is $d_g = d_1 + d_2$. When the grain boundaries are assumed to affect the electron mobility only, and not the Hall coefficient which is used to determine the electron density, two conditions must be met. The first condition is:

$$\ell = v_F \langle \tau \rangle < d_g \quad (2.87)$$

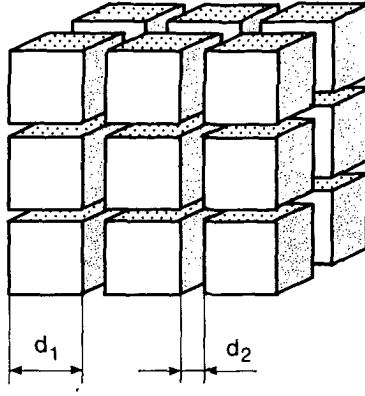


Figure 2.16 Model of the grain structure in a polycrystalline film.

Here ℓ is the electron free range, v_f is the electron Fermi velocity and $\langle \tau \rangle$ is the average time between two collisions of electrons in the grains. The other condition is that the density of the trapped electrons in the grain boundary, n_t (m^{-2}), is such that:

$$n_t < n_- \cdot d_g \quad (2.88)$$

When the intergrain region is treated as a back-to back Schottky barrier, and current flows between grains by thermionic emission, the mobility due to the scattering against grain boundaries can be written as:

$$\mu_{gb} = \mu_0 \exp(-\phi_b / k_B T) \quad (2.89)$$

with:

$$\mu_0 = \frac{e d_g}{(8\pi k_B T m_{eff})^{1/2}} \quad (2.90)$$

and:

$$\phi_b = \frac{e^2 n_t^2}{8\epsilon_s n_-} \quad (2.91)$$

where k_B is Boltzmann's constant. If the conditions (2.87) and (2.88) are not fulfilled, a relation like (2.89) holds for both μ_{gb} and n_- as derived from the measured Hall coefficient. In the treatment given above, it has been assumed that the current between the grains is determined by thermal field emission. However, in the theory of grain boundary scattering, a separation is made between thermal field emission and electron tunneling

(Roth and Williams, 1981). The criterion, as given by Roth and Williams, for a current dominated by tunneling, is that a specific parameter E_{00} is much larger than $k_B T$. E_{00} is given in electron volts by:

$$E_{00} = 0.185 \left(\frac{n_-}{m_{\text{eff}} \epsilon_s} \right)^{1/2} \text{ eV} \quad (2.92)$$

where m_{eff} is given in units of m_e and n_- in units of $10^{26}/\text{m}^3$. For a slightly doped SnO_2 or In_2O_3 coating we take $m_{\text{eff}} = 0.25$, $n_- = 0.3$ and $\epsilon_s = 10$ in (2.92). With these values we find that $E_{00} = 0.064$ eV, which is larger than $k_B T$ for $T < 740$ K. This means that for moderately and heavily doped coatings, one always has to deal with scattering dominated by electron tunneling between the grains. Though no satisfactory analytical model exists for grain boundary scattering dominated by electron tunneling, often an expression is used which has a form like equation (2.89):

$$\mu_{\text{gb}} = c_{\text{gb}} T^{-1/2} \exp(-\phi_p/k_B T) \quad (2.93)$$

where c_{gb} is a constant and ϕ_p is a pseudo activation energy which decreases with decreasing temperature. This last point makes equation (2.93) a weak base to conclude from a measured $\mu(T)$ whether grainboundary scattering occurs or not. Nevertheless, some authors (Shanthi, 1980-2; Islam and Hakim, 1986) measure $\mu(T)$ in a limited temperature range, apply (2.89) instead of (2.93) and sometimes even derive d_g and n_t from (2.90) and (2.91). Equations (2.89) and (2.93) are also unsatisfactory because the limit $\phi_p \rightarrow 0$ does not imply that the influence of grain boundary scattering disappears ($\mu_{\text{gb}} \rightarrow \infty$).

We note that equation (2.89) has been derived using Maxwell-Boltzmann statistics for the electron energy distribution. For the case of a degenerate electron gas, which will be the case for doped SnO_2 and In_2O_3 coatings, the Fermi-Dirac distribution law must be used. By using the Richardson-Dushman equation (Alonso, 1975) for the current which flows between two grains, equation (2.89) changes into:

$$\mu_{\text{gb}} = c_{\text{gb}} T^{-1} \exp(-\phi_b/k_B T) \quad (2.94)$$

where c_{gb} is a constant and ϕ_b is the activation energy.

An alternative approach to the problem of grain boundary scattering has recently been given by Warkusz (1988), who treats the grain boundaries as quantummechanical potential barriers. Warkusz concludes that the conductivity decreases rapidly when the electron energy becomes less than the potential barrier height when the barrier width (the intergranular region d_2) is larger than 2 Å.

It should be noted that, as long as $\ell < d_1$, grain boundary scattering will affect the electrical rather than the optical and radiation properties. This is because it can be expected that the radiation properties are mainly determined by the bulk of the material, while the electrical properties are determined by the grain boundaries, which make up only a small volume fraction of the material. This implies that for this case the optical properties cannot be easily connected to the electrical properties.

2.4.5 Other scattering mechanisms

As outlined in the review paper by Gerlach and Grosse (1977), the real part of $\tilde{\rho}(\lambda)$, $\rho_r(\lambda)$, follows a power law for $\lambda < \lambda_p$:

$$\rho_r(\lambda) \sim \lambda^s \tag{2.95}$$

where s takes on different values depending on the scattering mechanism. Table 2.1, based on Gerlach and Grosse (1977), summarizes the exponents applicable to different scattering mechanisms.

Table 2.1 Exponents s in the real part of the dynamic resistivity for different scattering mechanisms

scattering mechanism	s
Ionized impurity	3/2
Dislocation:	
Charged monopole line	2
Charged dipole line	1
Neutral impurity	-1/2
Acoustic phonons:	
Deformation potential coupling	-1/2
Piezoelectric coupling	1/2
Optical phonons	1/2

In this table, $s = 3/2$ is given for ionized impurity scattering which is slightly different from the value $s = 1.7$ which is found in section 2.4.1. This difference is due to the correction which has been made to the Linhard potential in equation (2.75).

2.4.6 Combining different scattering mechanisms

When the electron damping is influenced by different scattering mechanisms simultaneously, the effective relaxation time $\tau = \gamma^{-1}$ is (Blatt, 1968):

$$\tau_{\text{eff}} \leq \left(\sum_i \tau_i^{-1} \right)^{-1} \quad (2.96)$$

With τ_i the characteristic relaxation time from the different scattering mechanisms. Equation (2.96) is known as Matthiessens' rule. The equality in (2.96) is valid when the scattering mechanisms do not influence each other. If it is also assumed that the effective mass is the same for the different scattering mechanisms, (2.96) can be rewritten as:

$$\mu_{\text{eff}} \leq \left(\sum_i \mu_i^{-1} \right)^{-1} \quad (2.97)$$

2.5 The electron density

Pure SnO_2 and In_2O_3 single crystals are insulators with a band gap of about 4 eV. The intrinsic free electron density at room temperature of a material with a band gap of 4 eV is about $10^{-9}/\text{m}^3$. However, even undoped SnO_2 coatings have a free electron density of about $10^{25}/\text{m}^3$ at room temperature. This high electron density is caused by deviations from the ideal single crystal structure. These deviations might be, for example:

- oxygen vacancies
- interstitial atoms
- dislocations

The free electron density can be further enlarged by doping the coating. To calculate the free electron density resulting from a given amount of donor atoms, we adopt a simplified model for which the derivation of the properties is given by Blakemore (1962). It is assumed that all free electrons originate from N_d donor atoms and are at one donor level E_d from the conduction band. For this case the free electron density is given by:

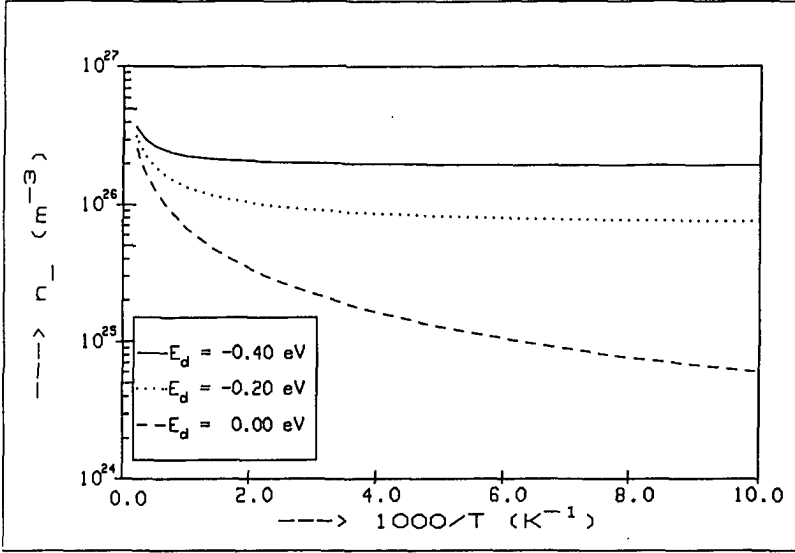


Figure 2.17 Electron density as a function of inverse temperature for different values of the donor energy level

$$n_- = N_c \frac{\mathcal{F}_{1/2}(\eta)}{\Gamma(3/2)} = \frac{N_d}{1 + \beta^{-1} \exp(\eta - \epsilon_d)} \quad (2.98)$$

with: $\epsilon_d = E_d/k_B T$: the dimensionless donor energy

$\eta = \phi_F/k_B T$: the dimensionless Fermi level

β^{-1} : the spin degeneracy factor: for one free electron for each ionized donor atom β can be put 1/2

$\mathcal{F}_{1/2}(\eta)$: the Fermi-Dirac integral of order 1/2

N_c is the quantum concentration given by:

$$N_c = 2 \left(\frac{2\pi m_{eff} k_B T}{h^2} \right)^{3/2} \quad (2.99)$$

For a given N_d , E_d , T and m_{eff} , η is found iteratively by searching a value for η which equals the middle and right hand part of equation (2.98). Once η is known, n_- can easily be calculated from (2.98). As an example we give n_- as a function of the inverse temperature in figure 2.17, for three

values of N_d and one value of N_d ($10^{27}/m^3$) and m_{eff} ($0.30m_e$). In this figure it is observed that n_- is temperature dependent, even when $E_d=0$, and that the temperature dependence becomes weaker when E_d is negative, which means that the donor energy level is in the conduction band. One can also observe that the temperature dependence is different from the classical case ($\eta \ll 1$), as in that case a $\ln n_-$ versus T^{-1} plot gives a straight line.

2.6 Model calculations on hypothetical coatings

In this section model calculations on hypothetical are presented. The model consists of a single solar transparent coating on an absorbing substrate. The substrate is assumed to be an 'ideal' type of black enamel: the optical constants are equal to those of glass, but the radiation passing the coating/substrate interface is assumed to be absorbed totally in the substrate. This means that in the spectral region where the substrate would be transparent, the extinction coefficient is much smaller than unity, but is large enough to absorb the solar radiation within a part of a millimeter. The glass optical constants have been taken from literature (Rubin, 1985).

For the coating optical constants a modified Drude model is used. The parameter ϵ_∞ is fixed ($\epsilon_\infty = 4$); the remaining parameters are: the plasma wavelength λ_p , the relaxation wavelength λ_γ and the coating thickness d . For $\lambda > 0.7\lambda_p$ the complex resistivity is calculated from the Drude model (equation (2.55)). For $\lambda < 0.7\lambda_p$, $\rho_r(\lambda)$ is modified according to the theory of ionized impurity scattering (see section 2.4.1):

$$\tilde{\rho}(\lambda) = \left(\frac{\lambda}{0.7\lambda_p} \right)^{1.7} \frac{\lambda_p^2}{2\pi c \epsilon_0 \epsilon_\infty \lambda_\gamma} - i \frac{\lambda_p^2}{2\pi c \epsilon_0 \epsilon_\infty \lambda} \quad (2.100)$$

and the optical constants are calculated using equations (2.100), (2.57) and (2.16). The reflectance of the coating-substrate system is calculated with the matrix method as described in section 2.2. The reflectance of unpolarized light is calculated, i.e. the calculation is performed for s- and p-polarized light and the results are averaged:

$$R(\lambda, \lambda_p, \lambda_\gamma, d, \theta) = 0.5 \left(R_s(\lambda, \lambda_p, \lambda_\gamma, d, \theta) + R_p(\lambda, \lambda_p, \lambda_\gamma, d, \theta) \right) \quad (2.101)$$

The normal solar absorptance is obtained from equations (2.3) and (2.11). For the solar spectrum we have taken a recently published spectrum for a solar zenith angle of 60° (Justus and Paris, 1987). The integrals in equation (2.3) are evaluated numerically from $\lambda = 0.3 \mu\text{m}$ to $\lambda = 2.3 \mu\text{m}$ in about 100 steps. Regarding the choice of $E(\lambda)$ it is noted that the choice of the solar spectrum turns out not to be very critical for the calculation of $\alpha_{s,\perp}$ (van der Ley and Hoogendoorn, 1977).

The directional total emittance is obtained from equations (2.12) and (2.5). The integrals in equation (2.5) are integrated numerically from $\lambda = 0.3$ to $\lambda = 100 \mu\text{m}$ in about 300 steps. The hemispherical total emittance $\epsilon_h(T)$ is obtained using equation (2.6) in the following way:

$$\epsilon_h(T) = 2 \int_0^{\pi/2} \epsilon(\theta, T) \sin(\theta) \cos(\theta) d\theta = \int_0^1 \epsilon(\theta, T) d \sin^2(\theta) \quad (2.102)$$

The integral in (2.102) is evaluated numerically from the calculation of $\epsilon(\theta, T)$ for $\theta = 0^\circ, 20^\circ, 30^\circ, 40^\circ, 50^\circ, 60^\circ, 70^\circ, 75^\circ, 80^\circ, 83^\circ, 86^\circ$ and 89° . For $\theta = 90^\circ$, $\epsilon(\theta, T)$ is taken equal to zero.

It is noted that the correction made in the Drude model by equation (2.100) only affects R slightly for $\lambda < \lambda_p$. For the cases we have made calculations for, the effect on ϵ_h was never noticeable and the effect on α never exceeded 0.3%.

2.6.1 Normal reflectance

The normal reflectance of the coating-substrate system with variation in the parameters λ_p , λ_γ and d , is given in figures 2.18, 2.19 and 2.20 respectively.

Figure 2.18 shows the normal reflectance for a coating of $0.5 \mu\text{m}$ thickness and $\lambda_\gamma = 15 \mu\text{m}$. The plasma wavelength λ_p has the values 1, 2 and $4 \mu\text{m}$. In the figure it is shown that the reflection edge shifts with λ_p , and the reflectance for $\lambda > \lambda_p$ rises more steeply for decreasing λ_p . This is in accordance with figure 2.9, when considering that $\omega'_p \approx \omega_p$ in equations (2.65-2.66).

Figure 2.19 shows the normal reflectance for a $0.5 \mu\text{m}$ coating with $\lambda_p = 2 \mu\text{m}$. The relaxation wavelength λ_γ has the values 2, 5, 10 and $30 \mu\text{m}$. In this figure it is shown that the reflection edge remains at about $\lambda = 2 \mu\text{m}$, while the steepness of the reflection edge increases with increasing λ_γ , which can also be observed in figure 2.9.

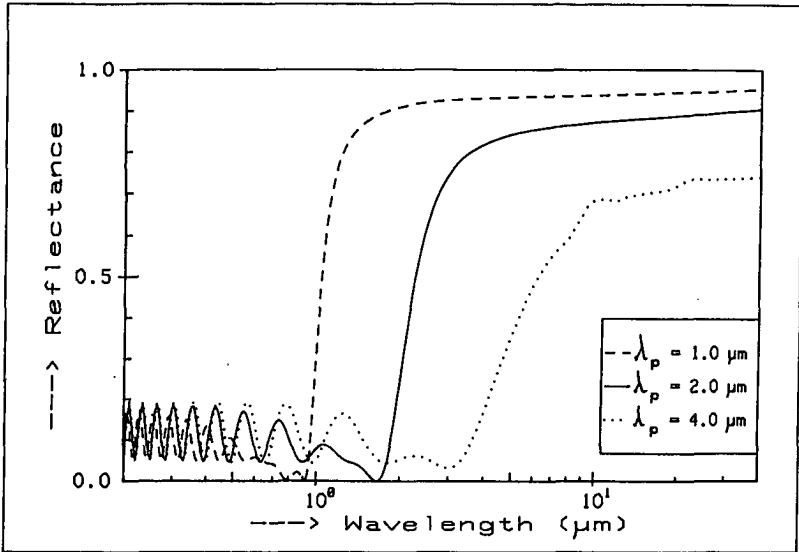


Figure 2.18 Normal reflectance for a 0.5 μm coating with $\lambda_\gamma = 15 \mu\text{m}$ and $\lambda_p = 1, 2$ and $4 \mu\text{m}$.

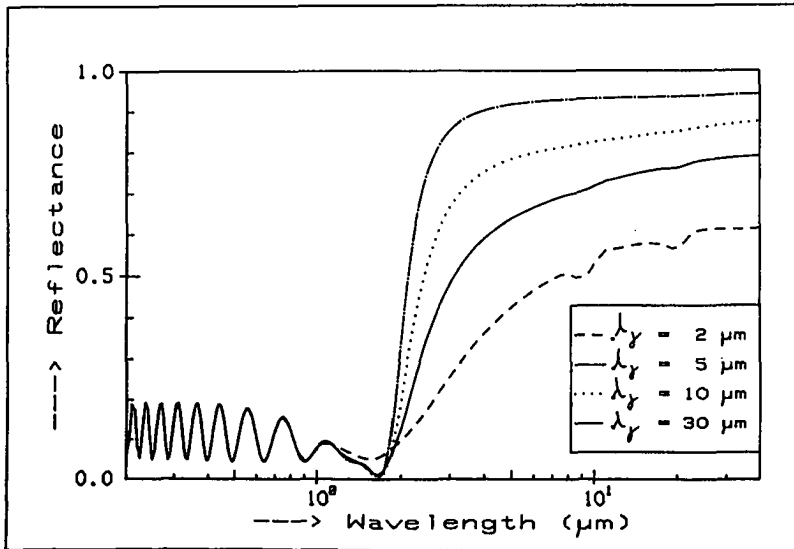


Figure 2.19 Normal reflectance for a 0.5 μm coating with $\lambda_p = 2 \mu\text{m}$ and $\lambda_\gamma = 2, 5, 10$ and $30 \mu\text{m}$.

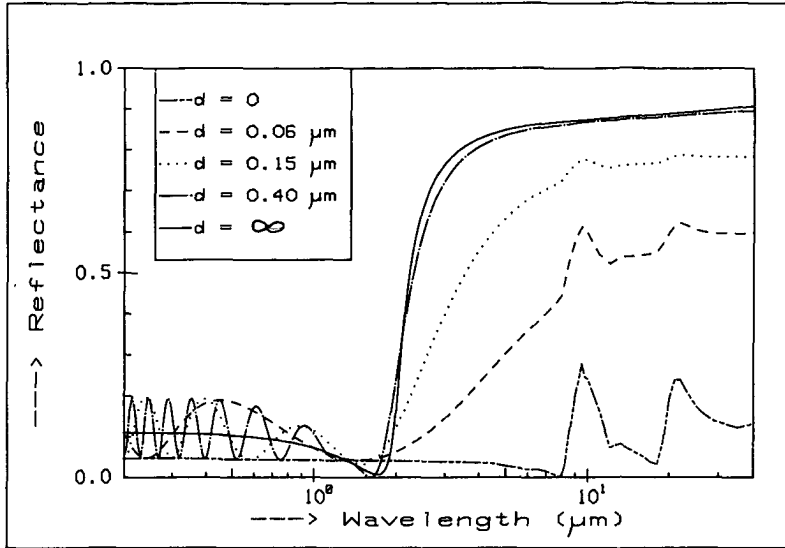


Figure 2.20 Normal reflectance for a coating with $\lambda_p = 2 \mu\text{m}$ and $\lambda_\gamma = 15 \mu\text{m}$. The thickness is 0, 0.06, 0.15, 0.40 μm and ∞ .

The thickness dependence of the reflectance of a coating with $\lambda_p = 2 \mu\text{m}$ and $\lambda_\gamma = 15 \mu\text{m}$ is shown in figure 2.20. In this figure the calculated curves are shown for zero, 0.06 μm , 0.15 μm , 0.40 μm and 'infinite' thickness. In this figure it can be observed that the infrared reflectance will hardly increase if the coating is made thicker than about 0.40 μm .

2.6.2 Solar absorptance

The solar absorptance $\alpha_{s,\perp}$ is given as a function of the coating thickness in figure 2.21. In this figure it is observed that $\alpha_{s,\perp}$ is about constant for $d > 0.13 \mu\text{m}$. The absorption minimum at $d = 0.065 \mu\text{m}$ is due to the reflectance maximum which coincides with the solar maximum at $\lambda \approx 0.4 \mu\text{m}$ (see also figure 2.20). For coatings being thick enough to have a reasonable infrared reflectance (see figure 2.20), the thickness hardly influences the solar absorptance.

The influence of λ_p on the solar absorptance has been calculated for a coating thickness of 0.5 μm for two cases: in the first case the plasma wavelength has been varied while keeping the DC-resistivity $\rho_r (\omega \rightarrow 0)$ constant: $\lambda_p^2 \cdot \lambda_\gamma^{-1} = 0.26$.

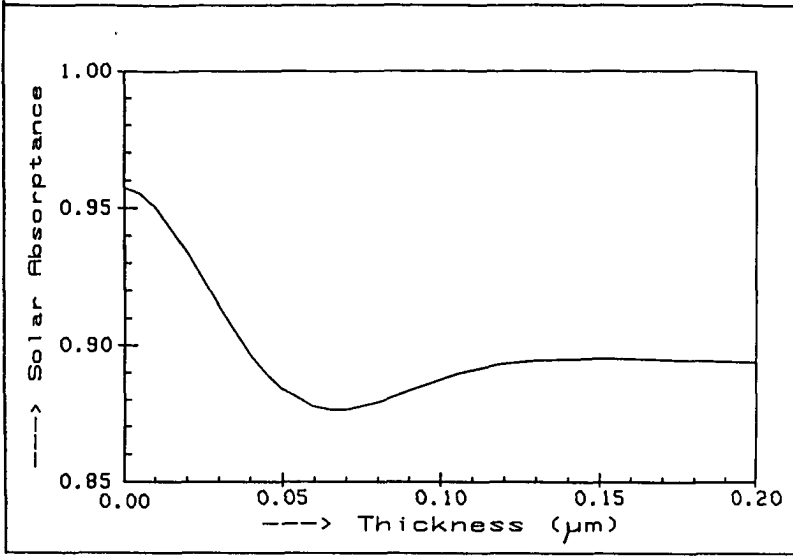


Figure 2.21 Solar absorbance as a function of coating thickness for a coating with $\lambda_p = 2 \mu\text{m}$ and $\lambda_\gamma = 15 \mu\text{m}$

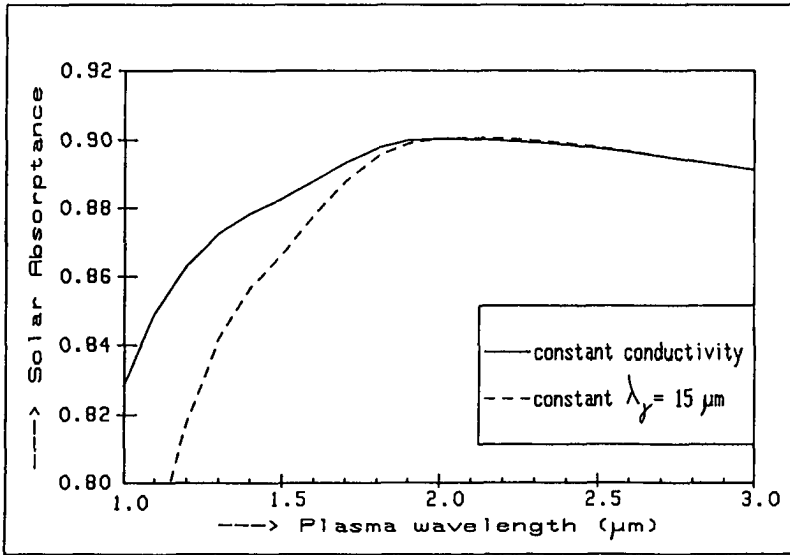


Figure 2.22 Solar absorbance as a function of λ_p for the case of a constant conductivity: $\lambda_p^2 \cdot \lambda_\gamma^{-1} = 0.26$ and for a constant $\lambda_\gamma = 15 \mu\text{m}$.

This means that for decreasing λ_p the reflection edge becomes less steep, but the far infrared reflectance remains the same (see also equation (2.64)). In the second case λ_γ has been kept constant ($\lambda_\gamma = 15 \mu\text{m}$) as in figure 2.18. The results are presented in figure 2.22. In this figure it is observed that for $\lambda_p = 2 \mu\text{m}$ the solar absorptance is even higher than for $\lambda_p > 2.2 \mu\text{m}$, due to the reflectance minimum at $\lambda \approx \lambda_p$. The solar absorptance decreases rapidly for $\lambda_p < 1.7 \mu\text{m}$ for both cases. Variation of λ_p and λ_γ for other thicknesses larger than $0.2 \mu\text{m}$ gave equal results, as can be expected from figure 2.21. Methods for increasing the solar absorptance are given in section 2.7.

2.6.3 Angle dependent reflectance

The reflectance spectrum for a $0.5 \mu\text{m}$ coating with $\lambda_p = 2 \mu\text{m}$ and $\lambda_\gamma = 15 \mu\text{m}$ is given for different angles of incidence θ in figure 2.23. In this figure it is observed that the reflectance changes little for $\theta < 60^\circ$. The reflectance at $\lambda < \lambda_p$ increases rapidly for $\theta > 60^\circ$, while the reflectance at $\lambda > \lambda_p$ decreases somewhat with increasing angle of incidence. The latter property changes for a poorly infrared reflecting coating, as is illustrated in the next section.

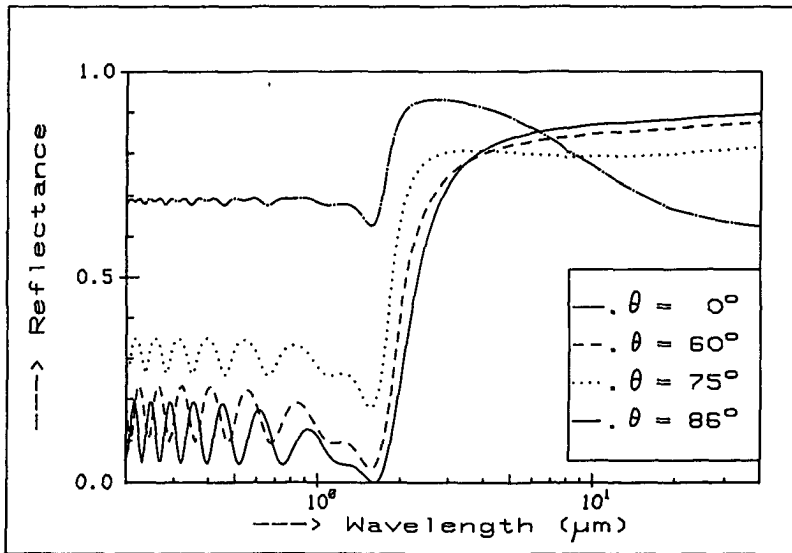


Figure 2.23 Spectral reflectance for a $0.5 \mu\text{m}$ coating with $\lambda_p = 2 \mu\text{m}$ and $\lambda_\gamma = 15 \mu\text{m}$ for different angles of incidence.

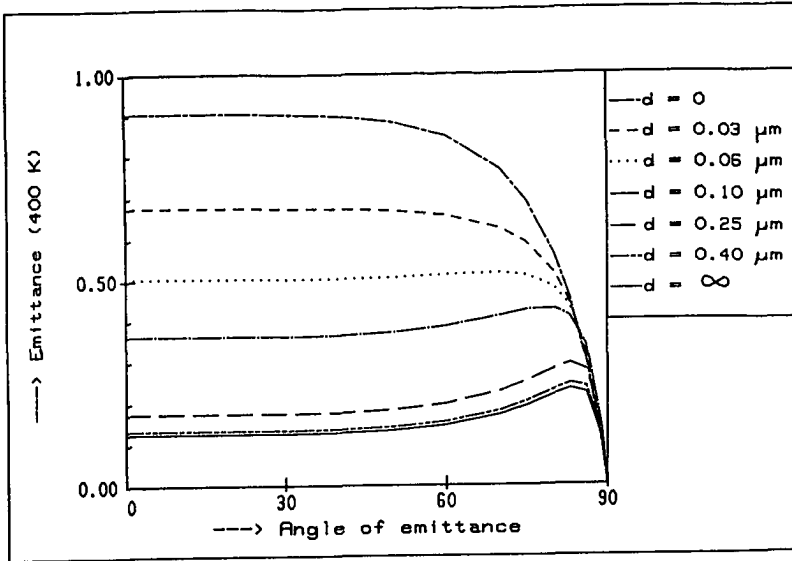


Figure 2.24 Angular emittance for a coating with $\lambda_p = 2 \mu\text{m}$ and $\lambda_\gamma = 15 \mu\text{m}$ for different coating thicknesses.

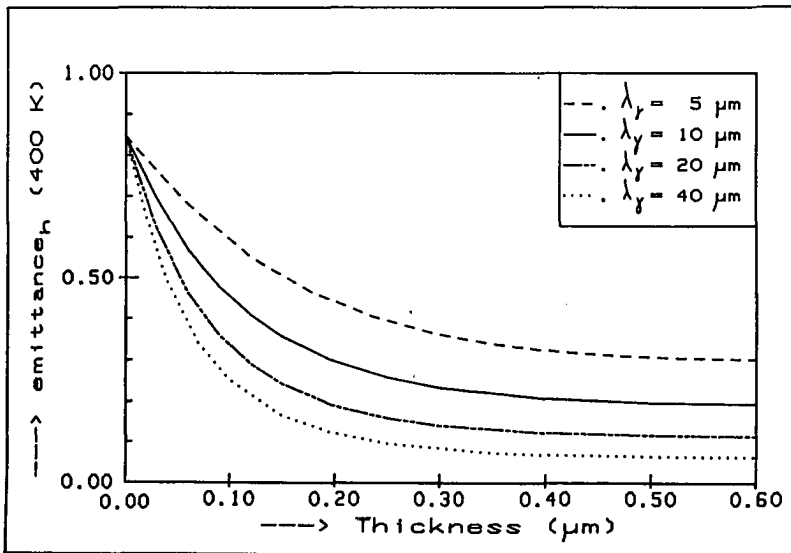


Figure 2.25 Hemispherical emittance as a function of coating thickness for a coating with $\lambda_p = 2 \mu\text{m}$ and $\lambda_\gamma = 5, 10, 20$ and $40 \mu\text{m}$.

2.6.4 Angle dependent emittance

The angle dependent emittance for $T = 400$ K of a coating with $\lambda_p = 2 \mu\text{m}$ and $\lambda_\gamma = 15 \mu\text{m}$ is given for different thicknesses in figure 2.24. In this figure one observes that for thin coatings (high emittance) the emittance decreases with the angle of emittance, while for thicker coatings (low emittance) the emittance increases with the angle of emittance.

This is in accordance with the general rule that $\epsilon_h < \epsilon_\perp$ for dielectrics (with a high emittance) and $\epsilon_h > \epsilon_\perp$ for metals (with a low emittance). In the metallic limit, the ratio $\epsilon_h/\epsilon_\perp$ is 1.327 (Sievers, 1978). In the example just given we find for the case of $0.40 \mu\text{m}$ coating thickness: $\epsilon_h/\epsilon_\perp = 0.1540/0.1362 = 1.131$ which is apparently less. This difference is due to a higher plasma wavelength in our coatings relative to most metals, where the plasma wavelength is in the UV-region due to the high free electron density. Therefore the conductivity is lower and the emittance is higher which makes the $\epsilon_h/\epsilon_\perp$ ratio smaller than for an ideal metal at $T=0$ K. It is also noted that the absolute emittance for $\theta > 85^\circ$ is about the same for all cases. This increases the $\epsilon_h/\epsilon_\perp$ ratio for materials with a lower value for ϵ_\perp .

2.6.5 Hemispherical emittance

The hemispherical emittance at 400 K has been calculated for $\lambda_p = 2 \mu\text{m}$ as a function of coating thickness for different values of λ_γ . The results are given in figure 2.25. In this figure it is observed that ϵ_h remains about constant for $d > 0.5 \mu\text{m}$ in all cases, which is to be expected regarding figures 2.24 and 2.20.

2.6.5.1 Minimum theoretical emittance

It is important to know the lowest possible emittance for a transparent conductor with $\epsilon_\infty = 4$ and $\lambda_p \approx 2 \mu\text{m}$. To calculate the minimum emittance we have proceeded as follows: for a given m_{eff} , n_- has been calculated so that $\lambda_p = 2 \mu\text{m}$ using equation (2.56). The corresponding maximum value for μ is calculated from equation (2.80). This gives a maximum for λ_γ with equation (2.59).

The result of this calculation is shown for a coating of 'infinite' thickness in figure 2.26. In this figure the calculation for $\lambda_p = 1.8 \mu\text{m}$ is also shown. These calculations will hold approximately for coatings with $d > 0.4 \mu\text{m}$. The sensitivity of this calculation for the only remaining parameter, ϵ_∞ , is low.

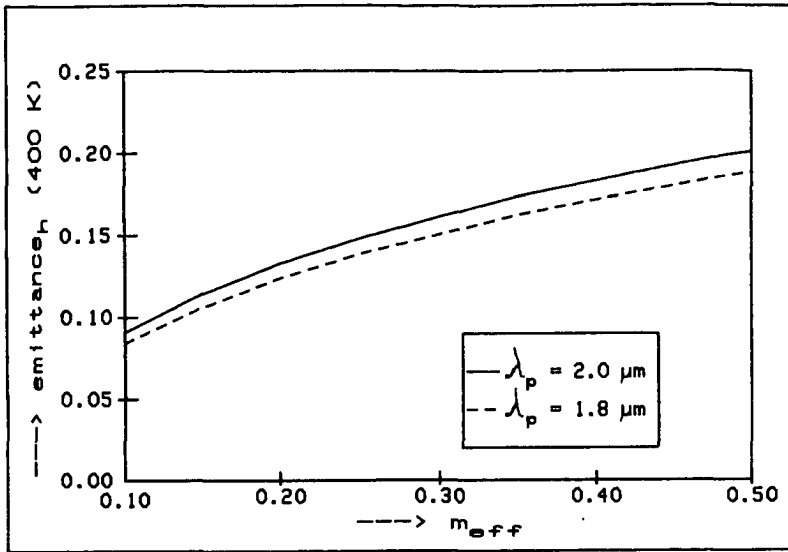


Figure 2.26 Minimum emittance as a function of m_{eff} calculated for $\lambda_p = 2$ and $1.8 \mu\text{m}$.

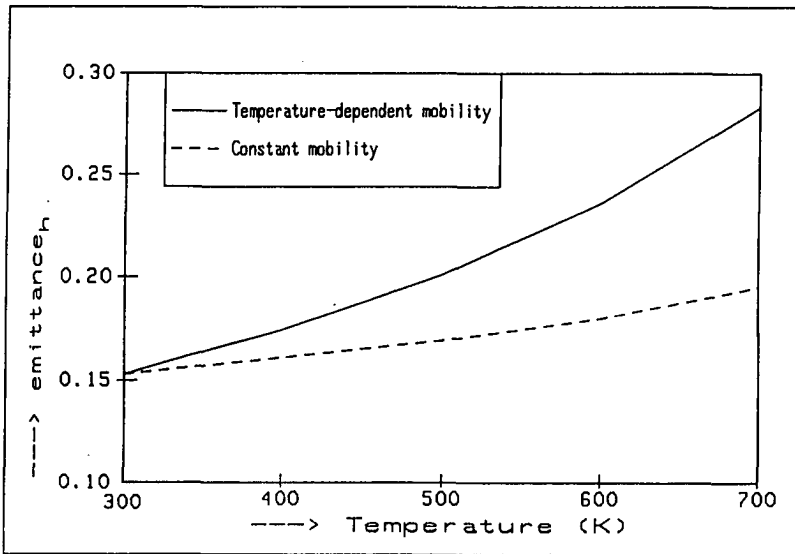


Figure 2.27 Emittance as a function of the temperature for a constant mobility and for a mobility which decreases with temperature

Figure 2.25 shows that it is advantageous to have a material with a low m_{eff} to have a low theoretical ϵ_h . An other advantage of a material with a low m_{eff} is that little doping is needed to obtain a given λ_p . As the lowest reported values for m_{eff} are about $0.15 m_e$ for SnO_2 (see chapter 6), one should not expect to obtain a lower value than $\epsilon_h \approx 0.12$ while maintaining a high solar absorptance.

2.6.5.2 Temperature dependence of ϵ_h

The emittance of a material may be temperature dependent due to three possible causes:

1. Change of the Planck spectrum $M_b(\lambda, T)$ with temperature.
2. Reversible change of the material properties which affect the wavelength dependence of the reflectance with the temperature.
3. Irreversible change of the material properties due to annealing or aging at high temperatures.

The first cause will always take place by definition. In the case of a material behaving according to the Drude theory, the second cause occurs when either ϵ_∞ , m_{eff} , μ or n_- are temperature dependent. As an example the calculations have been performed for a $0.5 \mu\text{m}$ coating with $m_{eff} = 0.30$ and $n_- = 3.337$. This gives $\lambda_p = 2 \mu\text{m}$ and a maximum mobility $\mu_{max} = 40 \text{ cm}^2/\text{Vs}$, so $\lambda_\gamma = 12.9 \mu\text{m}$. When it is assumed that these parameters are constant, only the first cause determines the temperature dependence of ϵ_h . The temperature dependence for this case is illustrated in figure 2.27. In this figure also a curve is drawn for the case that μ decreases with $0.04 \text{ cm}^2/\text{VsK}$ with temperature for $T > 300 \text{ K}$. This is about the value which is found due to phonon scattering in SnO_2 (see chapter 6). Figure 2.27 shows that the shift of the Planck spectrum has little effect on the emittance for $T < 700 \text{ K}$. A decrease of the mobility with temperature together with the shift of the Planck spectrum affects the hemispherical total emittance more drastically.

2.7 Methods for improving the solar absorptance

For transparent conductors on a black substrate the solar absorptance is limited mainly by the reflectance of the coating in the solar region, which is mainly governed by ϵ_∞ . As discussed in section 2.6.2, the maximum solar absorptance which can be achieved using a single coating is about 0.91.

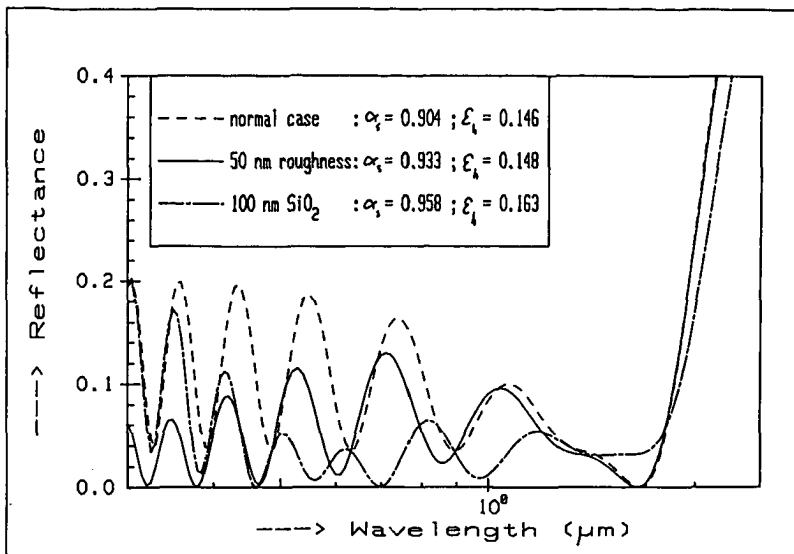


Figure 2.28 Spectral reflectance for a coating with $\lambda_p = 2 \mu\text{m}$ and $\lambda_g = 15 \mu\text{m}$, the same coating with 50 nm roughness and the same coating covered with a 100 nm quartz coating.

Here two methods are discussed in which the solar absorptance can be enhanced: roughening the upper surface and applying an anti- reflection coating on the spectrally selective coating.

Both methods rest upon the general principle that the reflectance of a surface can be minimized by an anti-reflection (a.r.) coating with a refractive index n_{ar} of (Heavens, 1965):

$$n_{ar} = (n_{\text{surface}} \cdot n_{\text{air}})^{1/2} \quad (2.103)$$

When $\epsilon_{\infty} = 4$, we have $n_{ar} = \sqrt{2} \approx 1.41$. The refractive index of a coating which simulates the surface roughness is $n_{\sigma} = (0.5(\epsilon_{\infty} + 1))^{1/2}$ (cf equation (2.44)) which gives $n_{\sigma} \approx 1.58$, which is fairly close to n_{ar} . A surface roughness can either be achieved by producing a coating consisting of large crystallites or by grinding the coating with very fine-grained grinding powder. To stay within the limits of the validity of simulating the surface roughness by a single coating (mentioned at the end of section 2.2.6), the thickness of the coating simulating the surface roughness has not been taken larger than 50 nm.

It has been found that the solar absorptance increases with the surface roughness. For the case of a $0.5 \mu\text{m}$ coating with $\lambda_p = 2 \mu\text{m}$ and $\lambda_\gamma = 15 \mu\text{m}$, the solar absorptance $\alpha_s = 0.904$ and the emittance $\epsilon_h = 0.146$. When it is assumed that the surface of this coating is roughened 50 nm, i.e. we have a surface roughness thickness of 50 nm and a $0.45 \mu\text{m}$ spectrally selective coating, we have $\alpha_s = 0.933$ and $\epsilon_h = 0.148$. This is a good improvement of α_s without affecting ϵ_h significantly. The effect on an air-filled flat plate collector operating at 80°C , using equation (1.1), is that the efficiency rises from 46 % to 48.5 %.

The effect of an anti-reflection coating has been calculated for the case of quartz (SiO_2) with $n \approx 1.47$, as quartz coatings can be produced in a cheap way on large areas by the sol-gel process (Pettit and Brinker, 1986). The complex refractive index in the thermal infrared region has been calculated from measurements of the reflectance and transmittance of a piece of quartz, using the R-T-method combined with a Kramers-Kronig analysis as is described in chapter 4.

The quartz a.r.-coating thickness for which a maximum solar absorptance is found is 102 nm, where α_s increases from $\alpha_s = 0.904$ to $\alpha_s = 0.958$. The emittance, however, increases from 0.146 to 0.163. So it depends of the relative importance of α_s and ϵ_h for a certain application whether or not it is favourable to apply an anti-reflection coating, and if so, what the optimum thickness is. For the example of an air-filled flat plate collector at an operating temperature of 80°C the optimum a.r. coating thickness is 98 nm; the collector efficiency for this case is 49.8%.

The results mentioned above are illustrated in figure 2.28, where the normal reflectance spectrum is given for $0.3 \mu\text{m} < \lambda < 2.5 \mu\text{m}$ for the case of a single spectrally selective coating, a coating with 50 nm surface roughness and a coating covered with a 100 nm quartz coating.

3. EXPERIMENTAL METHODS FOR CHARACTERIZING SPECTRALLY SELECTIVE COATINGS

In this chapter the methods which have been used to characterize the SnO_2 and In_2O_3 coatings are treated. The first two sections, 3.1 and 3.2, deal with the determination of the spectral transmission and reflection properties. Section 3.3 deals with the two essential properties regarding the spectral selectivity: the solar absorptance and the thermal emittance. Section 3.4 deals with the measurement of the electrical properties: the resistivity and the Hall coefficient, from which the free electron density n and the DC mobility μ_{DC} can be derived. Ellipsometry, a technique which has been used to derive further information on the optical properties of the coatings, is discussed in section 3.5. In section 3.6 the methods with which the structural and morphological properties of the coatings have been determined are discussed briefly. This discussion is brief because these determinations have been carried out for us in other groups.

3.1 Determination of spectral specular reflectance and transmittance

The determination of the specular and hemispherical reflectance and transmittance has been carried out by two spectrophotometers, which are owned by the TPD (Institute for Applied Physics TNO-TH). In the 220 - 2500 nm spectral range a Perkin Elmer Lambda 9 double beam spectrophotometer is used. An outline of its specifications is given in table 3.1. The near-normal specular reflectance is measured with a specular reflectance unit in the sample beam. An optical scheme of the unit is given in figure 3.1. To obtain a specular reflectance spectrum the spectral range is scanned three times:

1. a first time with a reference material with a known reflectance $R_{\text{ref}}(\lambda)$ in the sample position. For this reference a reflectance standard of the US National Bureau of Standards is used (NBS standard reference material no 2023). The obtained spectrum is called $I_{\text{ref}}(\lambda)$.
2. a second time with the sample to be measured in position. The obtained spectrum is called $I_{\text{sample}}(\lambda)$.
3. a third time with no sample in position. The obtained spectrum is called $I_0(\lambda)$. It is assumed that this spectrum measures the residual radiation which passes the reflectance unit and amplifier offsets in the spectrophotometer, which influence I_{ref} and I_{sample} equally in an absolute way.

Table 3.1 Specifications of the Perkin-Elmer Lambda 9 spectrophotometer equipped with an integrating sphere

<u>Wavelength:</u>	
usable range:	220 - 2500 nm
inaccuracy :	0.8 nm at maximum
bandwidth :	maximum 5 nm for $\lambda < 860$ nm 20 nm for $\lambda > 860$ nm
<u>Intensity measurement at 100% Reflectance or Transmittance</u>	
stray radiation :	< 0.002%
inaccuracy :	0.07 %
alinerarity :	0.1% for $\lambda < 860$ nm 0.6% for $\lambda > 860$ nm
noise level :	0.03% for $\lambda < 860$ nm, bandwidth = 5 nm 0.10% for $\lambda \approx 1500$ nm, bandwidth = 20 nm 4% for $\lambda = 2500$ nm, bandwidth = 20 nm

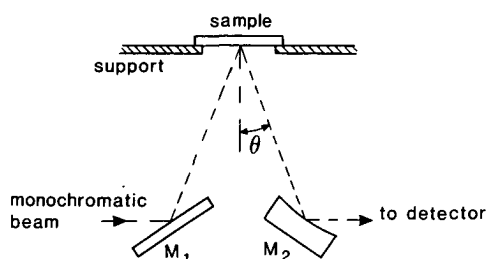


Figure 3.1 Schematic diagram of the specular reflectance unit

From the three spectra the reflectance spectrum $R_{\text{sample}}(\lambda)$ is calculated from:

$$R_{\text{sample}}(\lambda) = \frac{I_{\text{sample}}(\lambda) - I_0(\lambda)}{I_{\text{ref}}(\lambda) - I_0(\lambda)} \cdot R_{\text{ref}}(\lambda) \quad (3.1)$$

The collection of spectra from the spectrophotometer and the computation of e.g. (3.1) is facilitated by a Perkin-Elmer 3600 data station. The accuracy of the reflectance obtained in this way is determined to a large extent by the error in the reflectance of the reference material, which is about 0.5 %. The absolute error in a determination of R_{sample} , ΔR , can be estimated as a combination of the photometric inaccuracy and the reference inaccuracy:

$$(\Delta R)^2 = (0.003)^2 + (0.005 R_{\text{sample}})^2 \quad (3.2)$$

The normal straight-on going transmittance is determined in an analogous way by measuring:

1. $I_{\text{ref}}(\lambda)$ with no sample in the sample beam.
2. $I_{\text{sample}}(\lambda)$ with the sample positioned in the sample beam.
3. $I_0(\lambda)$ with the sample beam blocked.

The transmittance $T_0(\lambda)$ is calculated from:

$$T_{\text{sample}}(\lambda) = \frac{I_{\text{sample}}(\lambda) - I_0(\lambda)}{I_{\text{ref}}(\lambda) - I_0(\lambda)} \quad (3.3)$$

As the reference transmittance ($T_{\text{ref}} \equiv 1$) contains no error, the error in $T_{\text{sample}}(\lambda)$ will only be determined by the spectrophotometric inaccuracy, which causes an error of about 0.003 at minimum, dependent on the spectral range (see table 3.1).

For the determination of the specular reflectance in the thermal infrared spectral region ($\lambda = 2.5\text{-}50 \mu\text{m}$), a Perkin-Elmer 883 Infrared Spectrophotometer has been used. An outline of its specifications is given in table 3.2. The determination of the specular reflectance is analogous to the determination in the visible-near infrared spectral region. As a reference material an evaporated gold sample is used, of which the reflectance is assumed to be 0.985 ± 0.007 in the spectral region (Drummeter, 1964). The inaccuracy due to the detector noise in the $2.5\text{-}40 \mu\text{m}$ spectral region is higher than in the case of the Lambda 9, so the error in a determination of $R_{\text{sample}}(\lambda)$ changes accordingly.

Table 3.2 Specifications of the Perkin Elmer 883 Infrared Spectrophotometer

<u>Wavelength</u>	
usable range:	2.5 - 40 μm (4000 - 250 cm^{-1})
inaccuracy	: 2.5 nm at $\lambda = 2.5 \mu\text{m}$
	0.4 μm at $\lambda = 40 \mu\text{m}$
bandwidth	: 5.5 cm^{-1} at maximum
<u>Intensity measurements at 100% Reflectance</u>	
stray radiation	: < 0.04%
inaccuracy	: < 0.5 %
alinenarity	: < 0.2%
noise level	: < 0.2% for $\lambda < 20 \mu\text{m}$ at maximum bandwidth
	< 1 % for $\lambda < 40 \mu\text{m}$ at maximum bandwidth

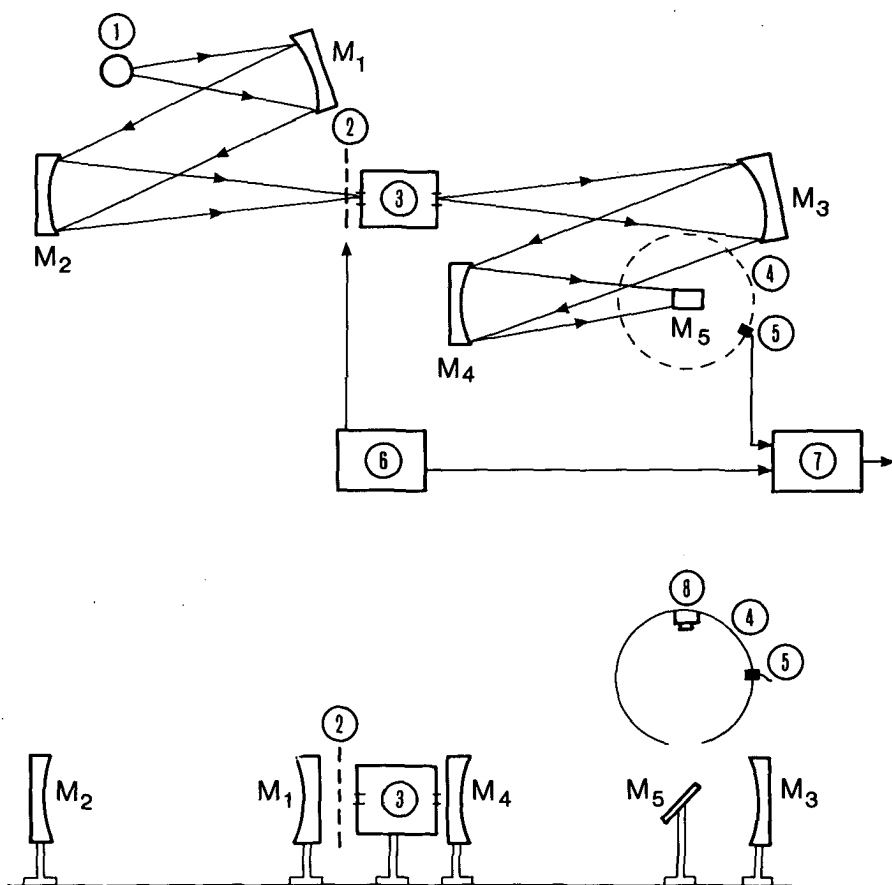
For wavelengths larger than 40 μm the detector noise increases rapidly and no accurate measurements can be performed. Determinations of the transmittance have not been carried out with this apparatus as the glass-like substrates on which the coatings have been applied are opaque for $\lambda > 3 \mu\text{m}$.

3.2 Determination of the spectral near-normal-hemispherical reflectance and transmittance

The near-normal-hemispherical spectral transmittance and reflectance are determined by the Perkin-Elmer Lambda 9 in the visible and near infrared region. The near-normal-hemispherical spectral reflectance in the thermal infrared region is determined with an own-built apparatus which is discussed first.

3.2.1 Determination of the near-normal-hemispherical spectral reflectance in the 1.8 - 20 μm spectral region.

The set-up for the determination of the near-normal-hemispherical reflectance in the thermal infrared spectral region is shown in figure 3.2. It consists of an infrared source (Optitron wire heater glower) which is heated up to about 1200 $^{\circ}\text{C}$. The source is focused by two mirrors on the entrance slit of the monochromator (Oriel grating monochromator model 7240). The monochromatic beam leaving the exit slit of the monochromator is focused on the sample which reflects the beam into the integrating sphere.



- | | |
|-----------------------|----------------------|
| 1. Infrared Source | 5. Golay detector |
| 2. Chopper | 6. Chopper steering |
| 3. Monochromator | 7. Lock-in amplifier |
| 4. Integrating sphere | 8. Sample holder |
| | M1..5 : Mirrors |

Figure 3.2 Schematic diagram of the equipment used for determining the near-normal-hemispherical reflectance.

The light intensity inside the sphere is measured with a Golay detector (Cathodeon IR-50). The output signal of the detector is amplified by a lock-in amplifier (PAR 186A) which is synchronized with an optical chopper

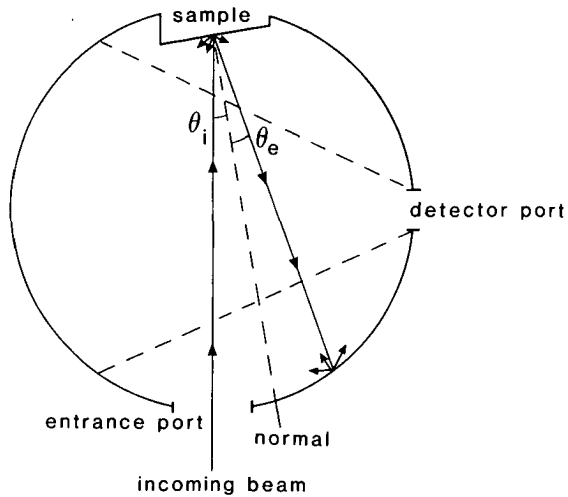


Figure 3.3 Positioning of sample and detector inside the integrating sphere

(Scitec instruments). This chopper chops the beam entering the monochromator with a frequency of about 15 Hz. The steering of the monochromator and the data collection is carried out with a HP 85 desk computer and a HP 3479A data acquisition unit. Two parts of this set-up: the integrating sphere and the monochromator are considered in more detail in the next two sections 3.2.1.1 and 3.2.1.2. The error analysis and an example of a measurement is given in section 3.2.1.3.

3.2.1.1 The integrating sphere

The positioning of the detector and the sample inside the integrating sphere is sketched in figure 3.3. The sphere diameter is 100 nm. The sphere wall has been roughed with grinding paper and has been supplied with a vacuum evaporated gold coating to obtain a diffusely, highly reflecting sphere wall. Van der Ley (1979) has shown that, for the given sphere geometry, the light intensity inside the sphere as measured by the detector, can be written as:

$$I_{\text{sample}} = c_{\text{sph}} \cdot (R_{\text{sp}} + C_e R_d) \quad (3.4)$$

Where c_{sph} is a constant, R_{sp} is the specular reflectance component, R_d is the diffuse reflectance component and C_e is a correction factor due to the non-idealness of the sphere. For the sphere geometry as sketched in figure 3.3, C_e is given by:

$$C_e = 1 - \frac{A_e}{A_w} \cos \theta_1 \quad (3.5)$$

Where A_e is the entrance port area and A_w is the inner wall area of the sphere. In our case we have $C_e \approx 0.95$. In equations (3.4) and (3.5) it is assumed that the sphere is perfectly diffusely reflecting. It is also assumed that the sample reflectance is composed of a purely specular component and a purely diffuse component which is isotropic in space.

As the spectrally selective coating we deal with are mainly specularly reflecting with a small or with a negligible diffuse component in most cases, it may be assumed that the deviation from unity of C_e will hardly influence the detector response on a given sample.

Equation (3.1) can be used to determine the near-normal-hemispherical reflectance R_{sample} when intensity spectra are made with the sample in position (I_{sample}), the gold sample in position (I_{ref}) and with the sample holder removed from the sphere (I_0). The coating-substrate system which is measured must be opaque, as the sample is mounted on the sample holder with paste (Schaffner heat transfer compound). This will cause unwanted reflections into the sphere if the sample is transparent.

3.2.1.2 The monochromator

The monochromator is an Óriel type 7240 grating monochromator. To cover the 1.5-20 μm spectral region, four different gratings with each a different blaze wavelength are used. The blaze wavelength is the wavelength which is reflected with the highest intensity from the grating. Order filters are used to eliminate the overlap of the high orders of small wavelengths with the low order of higher wavelengths.

The wavelength regions which can be scanned are given together with the grating-type and order filter combination in table 3.3. The bandwidth can be adjusted with the entrance and exit slit of the monochromator. We have taken a slitwidth of 2 mm as a compromise between a large bandwidth and a low signal/noise ratio of the detector. The bandwidth corresponding to a slitwidth of 2 mm is also given in table 3.3.

Table 3.3 Combinations of grating and filter in the monochromator. The wavelength bandwidth at 2 mm slitwidth is also indicated.

Blaze-wavelength of grating (μm)	Order filter (Oriel)	Wavelength range (μm)	Bandwidth (μm)
2	18	1.8 - 2.8	0.052
4	27	2.8 - 4.0	0.104
4	38	4.0 - 5.6	0.104
8	38	5.6 - 6.5	0.208
8	60	6.5 - 9.0	0.208
8	90	9.0 - 10.0	0.208
12	110	10.0 - 20.0	0.312

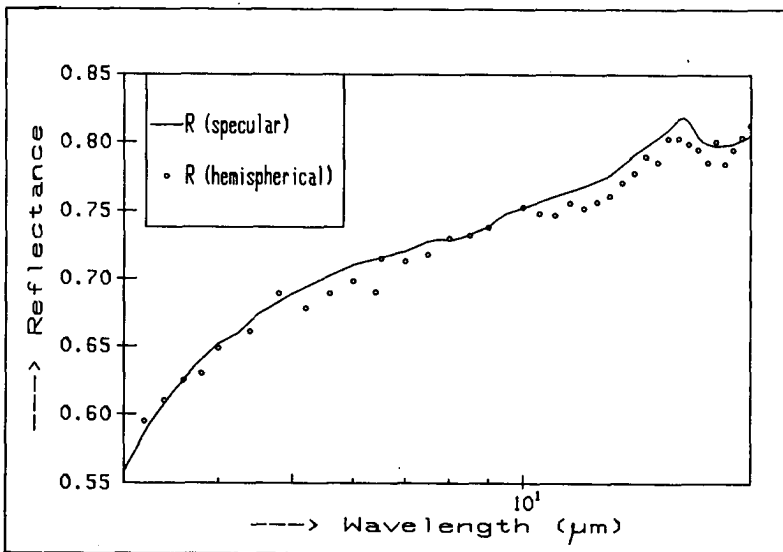


Figure 3.4 Near-normal specular reflectance and near-normal hemispherical reflectance of a SnO_2 coating in the 3 - 20 μm spectral region

3.2.1.3 Error analysis and an example of a measurement

The statistical errors are mainly due to the detector noise. This error is about 0.5% in the spectral region up to 15 μm when measuring the gold reference sample. For $\lambda > 15 \mu\text{m}$ this error increases up to about 10% at $\lambda = 20 \mu\text{m}$. The error due to variations in the infrared source temperature are less than 0.3% as has been checked by recording the detector output for a long time and by recording the infrared source temperature with a Pt-RhPt thermocouple.

The systematic errors are more hard to establish. In general one can state that the error which is caused by the imperfectness of the sphere (see equation 3.4) will be diminished when the reflectance of the reference sample has the same angular distribution as the sample which is to be measured. The error due to stray light will be less than 0.2%. As the reflectance spectra of our samples do not contain sharp peaks, the errors caused by the bandwidth of the wavelength will be negligible. The detector alinearity is 1% at maximum. The remaining error sources are the error in the reflectance of the reference sample, which is estimated to be 0.7% and an error caused by the non-diffuseness of the sphere wall.

As an example the near-normal hemispherical reflectance of sample no 187, a 0.5 μm F-doped SnO_2 coating on glass, and the near-normal specular reflectance, measured as discussed in section 3.1, are given in figure 3.4. In this figure it is observed that the near-normal-hemispherical reflectance and the near-normal specular reflectance are nearly the same. However, when considering this figure in more detail, it is observed that the near-normal-hemispherical reflectance is systematically lower than the specular reflectance, while in principle the reverse should hold. As the same reference sample has been used in both measurements, this is not due to a difference in the reference sample. The explanation of the difference must be an imperfection of the sphere, which causes an alinearity in the measured reflectance, or an alinearity in the detector. However, the error is not too large, about 1%, if it is assumed that the sample and the reference are both only reflecting specularly.

3.2.2 Determination of the near-normal-hemispherical reflectance and transmittance in the 0.3-2.5 μm spectral region

The near-normal-hemispherical radiation properties in the 0.3-2.5 μm spectral region are determined with the Perkin-Elmer Lambda 9 equipped with

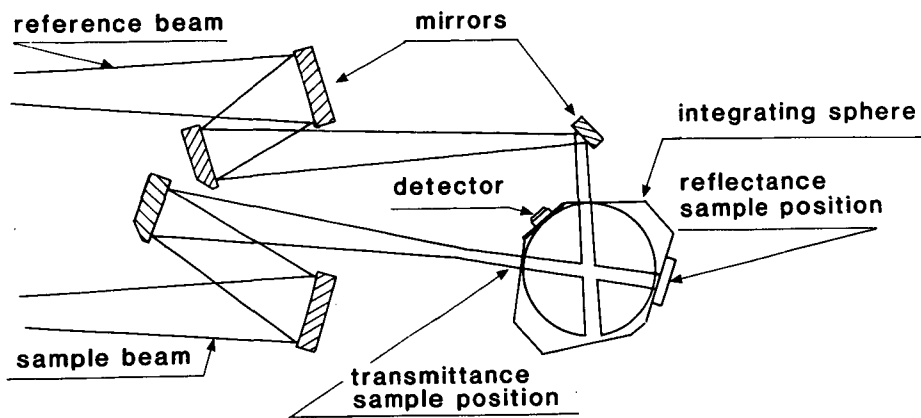


Figure 3.5 Optical scheme of the integrating sphere attachment of the Perkin-Elmer Lambda 9 spectrophotometer

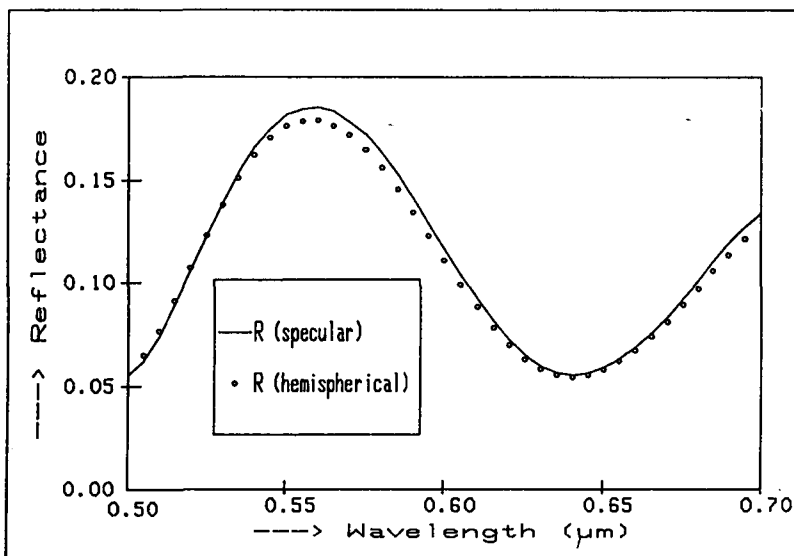


Figure 3.6 Near-normal specular reflectance and near-normal hemispherical reflectance of a SnO_2 coating in the 0.5 - 0.7 μm spectral region

an integrating sphere attachment. The optical scheme of the integrating sphere attachment is given in figure 3.5. For determining the near-normal hemispherical reflectance the sample is put at the sample position in the integrating sphere. At this position the reference sample is put for the reference measurement and the sample is removed to carry out a 'zero' measurement.

The sphere is coated with Ba_2SO_4 which is known to have a high (>99%) diffuse reflectance at visible and near infrared wavelengths. As the sphere geometry is, apart from an additional reference beam port, basically the same as in section 3.2.1, equation (3.6) is also valid here. The correction term C_e is calculated here from:

$$C_e = 1 - \frac{A_e + A_r}{A_w} \cos \theta \quad (3.7)$$

with A_e , A_r and A_w being the sample-beam port, reference beam port and the total sphere wall area respectively. For this case $C_e \approx 0.975$. The error analysis is similar as given in section 3.1, except for the integrating sphere effects which are discussed in section 3.2.1.

The normal-hemispherical transmittance is measured by putting the sample at the entrance beam port. In this case the reflectance port is covered with a Ba_2SO_4 sample. The error analysis is similar to the near-normal-hemispherical reflectance measurement, but it must be kept in mind that for this case the reference sample is air, with $T_{ref} \equiv 1$ and transmitting purely normal-normal.

As an example the near-normal-specular and the near-normal-hemispherical reflectance of sample 187 in the 0.5-0.7 μm spectral region are given in figure 3.6. In this figure it is observed that the near-normal-specular reflectance and the near-normal-hemispherical reflectance are nearly the same, but the near-normal-hemispherical reflectance is again measured systematically lower. As the same reference sample and the same detection system have been used for the two determinations this difference must be due to some integrating sphere effect. At the interference maximum at $\lambda \approx 0.56 \mu\text{m}$ the absolute error is 0.006, which is not a big problem, however this systematic error is much larger than the statistical error caused by the detector noise.

3.3 Determination of solar absorptance and thermal emittance

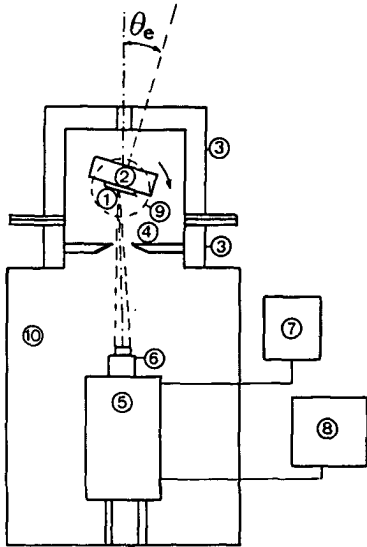
3.3.1 Determination from the near-normal-hemispherical reflectance spectrum

The normal solar absorptance and the normal thermal emittance can be obtained from the near-normal-hemispherical reflectance spectrum, using $\alpha_{\perp}(\lambda) = 1 - R_{\perp,h}(\lambda)$ in equation (2.3) and $\epsilon_{\perp}(\lambda) = 1 - R_{\perp,h}(\lambda)$ in equation (2.5). The errors caused by the numerical integration in equations (2.3) and (2.5), and by the statistical errors in $R(\lambda)$, will be smaller than the systematic errors in $R(\lambda)$ which are discussed in section 3.2. This means that when the normal solar absorptance and the normal total emittance are derived from the near-normal-hemispherical reflectance spectrum, an absolute error of 0.01 must be taken into account.

3.3.2 Determination of the directional total emittance

For the determination of the directional total emittance an apparatus is used which has been developed and described by van der Ley (1979). To this apparatus some small amendments have been made. The equipment is schematically sketched in figure 3.7. The sample is attached to a heating box with a heat transfer compound. This box is turnable around an axis which is positioned along the sample surface and through the center. The angle θ is adjustable between -90° and 90° with a rotating disc. The temperature of the upper surface of the heating box is controlled with a Shimaden type SR10 PiD temperature controller between 0°C and 400°C . The heating box is surrounded by a black-painted cooled jacket, to create a 'black body' with a constant temperature around the sample. The temperatures of the heating box and the cooling jacket are measured with two Heraeus Pt 100 platinum resistance thermometers, type FKG 1030.6. To avoid condensation when the jacket is cooled down to about 5°C and to avoid water vapour absorption, dry air (dried with silicagel) is blown into the outer big box. The detector (Heimann type KT14) consists of a lens, an electronic chopper, a bolometer and an amplifier. The lens is an a.r. coated Germanium lens with which a round spot with only 4 mm diameter on the sample is observed by the detector. The detector is spectrally sensitive from 2 to 20 μm . The output current is between 0 and 20 mA and is detected by a Shimaden type SR1100 digital indicator.

The angular total emittance of the sample at temperature T_s is derived from the apparent sample temperature T_x as observed by the detector, the real sample temperature T_s and the wall temperature T_w . Under some



1. Sample position
2. Heating unit
3. Water cooled jacket
4. Water cooled diaphragm
5. Bolometer
6. Detector head with lens
7. Voltage supply
8. Current indicator
9. Graduated, rotating disc
10. Outer house filled with dry air
11. PiD Temperature controller

Figure 3.7 Schematic lay-out of the apparatus for determining the total angular emittance.

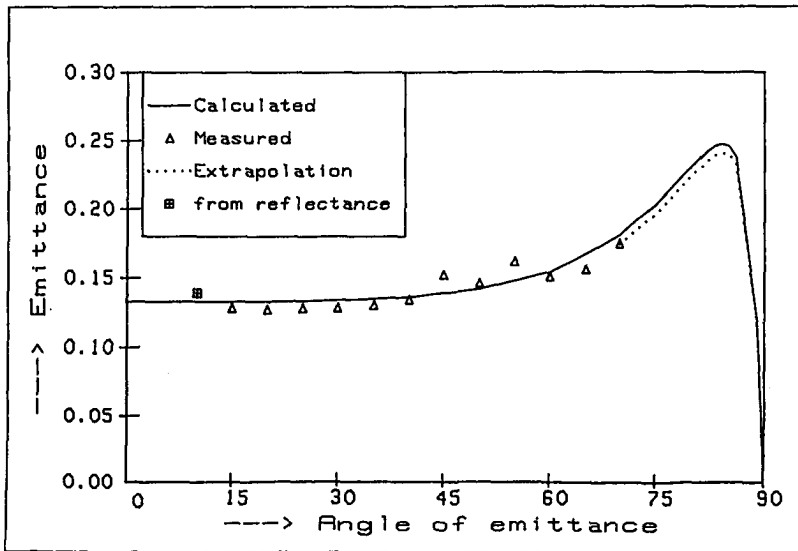
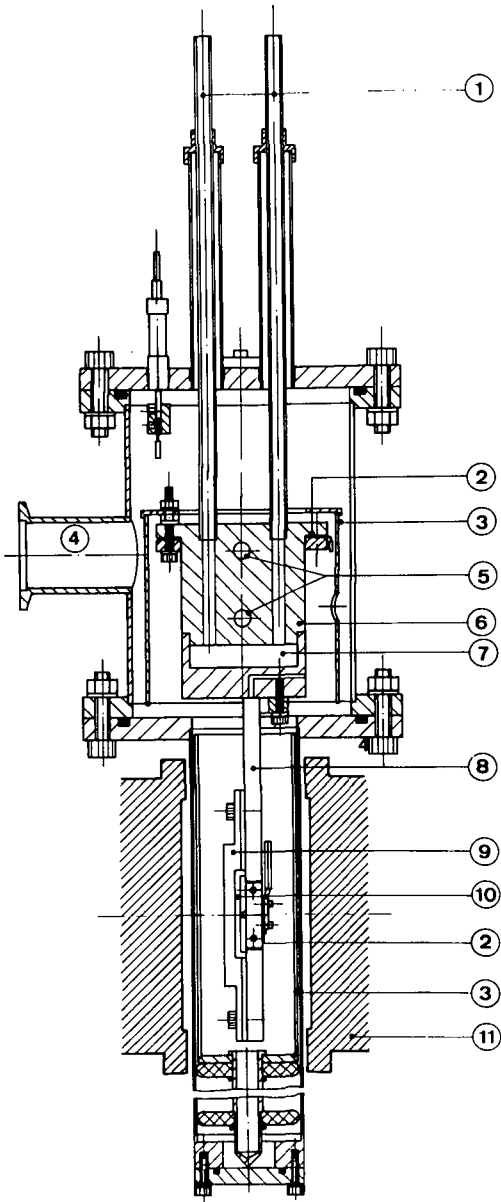


Figure 3.8 Total angular emittance of a SnO_2 coating



1. Liquid nitrogen inlet
2. Pt 100 resistance thermometer
3. Radiation shield
4. Vacuum/gas inlet
5. Heating elements
6. Cooling/heating block
7. Liquid nitrogen reservoir
8. Cooling/heating fin
9. Bridge with electrical contacts
10. Sample position
11. Magnet

Figure 3.9 Schematic view of the cryostat used for determining the electrical properties at different temperatures

assumptions it can be shown that:

$$\epsilon(\theta, T_s) = \frac{T_x^4 - T_w^4}{T_s^4 - T_w^4} \quad (3.8)$$

The assumptions under which equation (3.8) is valid and the error sources in the apparatus and in the measuring method have been discussed by van der Ley (1979) and are partly discussed here at the hand of an example.

As an example the measured angular emittance at 120 °C of sample 298, a 0.62 μm , F-doped SnO_2 coating on pyrex, is given in figure 3.8. A calculated curve has been drawn on the basis of the measured electrical properties at this temperature (see next section) using the Drude theory with $m_{\text{eff}} = 0.25$ (cf section 2.6.4). A point calculated from the near-normal specular reflectance spectrum, with the method described in section 3.3.1, is also shown in the figure. In this calculation a correction has been made for the fact that the reflectance is measured at room temperature, while the emittance is measured at 120 °C.

In the measured $\epsilon(\theta)$ values some deviating points are observed between $\theta = 45^\circ$ and 55° . These deviations can be explained by wall-reflections of the heating unit. An extrapolation for $\theta > 70^\circ$ has been made using the Drude theory, with λ_y fitted to give the measured emittance for $15^\circ < \theta < 40^\circ$. The total hemispherical emittance, calculated from equation (2.102), is 0.145 when the measurements for $\theta = 45^\circ$ and 55° are skipped and $\epsilon(\theta)$ is taken constant for $\theta < 15^\circ$. The value derived from the Drude theory is 0.151. Also the measured emittance at $\theta = 15^\circ$ (0.128) is lower than the value derived from the reflectance spectrum (0.138). This is most probably due to a lower coating temperature than measured at the heating unit. From this it can be concluded that the total angular emittance can be determined for $15^\circ \leq \theta \leq 70^\circ$ with an absolute accuracy of about 0.01.

3.4 Determination of the electrical properties

3.4.1 Experimental set-up

To determine the electrical parameters, viz. the mobility μ and the free carrier density n_- , and their temperature dependence in the temperature range from 80 to 600 K, a cryostat has been used. The cryostat is schematically drawn in figure 3.9. The ambient of the sample can be vacuum, or a gas like air, hydrogen or oxygen.

The sample holder is mounted under a cylinder which can be cooled by liquid nitrogen and heated by heating elements. The temperature of the

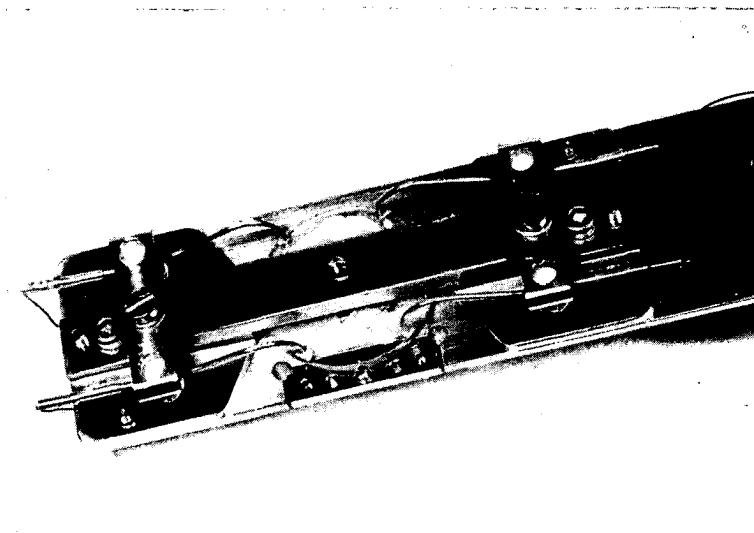


Figure 3.10 Photograph of the sample holder showing the positioning of the sample and the contacts

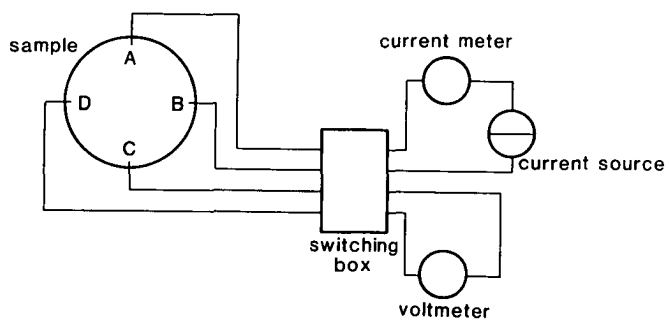


Figure 3.11 Scheme of the electrical measurements

cylinder is measured with a Pt-100 platinum resistance thermometer and controlled with a PID temperature controller. The temperature of the sample holder in height of the sample position is measured with a second Pt-100 element. With this system a stable sample temperature can be maintained within 0.1 K.

The electrical contacts on the sample have a configuration which enables measurements of the resistivity and Hall-effect using the van der Pauw method (van der Pauw, 1958-1,2). Figure 3.10 shows a photograph of the sample holder. The samples are circular shaped with a diameter of 28 mm. Heat transfer compound is used for a good heat contact between sample and holder. For the electrical contacts several wire materials, also combined with a silver paint between the wire and the sample surface have been tested. The most stable and reproducible voltages have been obtained with 1mm diameter platinum wires which are pressed elastically on the sample surface without using silver paint.

3.4.2 Measuring method

The scheme for the electrical measurements following van der Pauw (1958-2) is given in figure 3.11. The basic idea is that a current flows between two contacts and the voltage difference is measured between the other two. A resistance $R_{AB,CD}$ can be defined by:

$$R_{AB,CD} = \frac{V_{CD}}{I_{AB}} \quad (3.9)$$

With I_{AB} the current flowing from contact A to B and V_{CD} the voltage difference measured between contacts C and D. Analogously the resistance $R_{BC,DA}$ is defined as the voltage between contacts D and A divided by the current which flows between contacts B and C. The DC-resistivity of a coating is calculated from:

$$\rho_{DC} = \frac{\pi d}{\ln(2)} \left(R_{AB,CD} + R_{BC,DA} \right) f \left(R_{AB,CD} / R_{BC,DA} \right) \quad (3.10)$$

with d the coating thickness and f a correction factor which makes equation (3.10) applicable for an arbitrary sample shape, when $R_{AB,CD}$ and $R_{BC,DA}$ are not equal. For f the following transcendental equation holds:

$$f(x) = \frac{\ln 2}{\ln \left(2 \cosh \left(\frac{x-1}{x+1} \right) \cdot \frac{1}{f(x)} \right)} \quad (3.11)$$

This equation is solved numerically for $f(x)$ by successive approximations, starting with $f(x) = 1$. For our circular shaped samples with the contacts put in symmetrical positions, $f(x)$ is close to unity in most cases.

When measuring with a magnetic field B which is directed normal to the sample a resistance difference can be defined:

$$\Delta R_{AC,BD} = \frac{V_{BD, \text{without field}} - V_{BD, \text{with magnetic field}}}{I_{AC}} \quad (3.12)$$

The Hall-coefficient R_H is calculated from:

$$R_H = \frac{d}{B} \Delta R_{AC,BD} \quad (3.13)$$

Because the Hall voltages are rather small, it is necessary to eliminate offset and drift effects to obtain accurate values. First the signal-noise ratio is increased with a factor of two by reversing the magnetic field instead of putting it on and off. Further measurements are carried out with reversion of the current and interchanging of the current and voltage contacts. For one determination of R_H , a series of determinations of $\Delta R_{AC,BD}$, $\Delta R_{CA,BD}$, $\Delta R_{DB,AC}$ and $\Delta R_{BD,AC}$ is made while the magnetic field is reversed in fixed time intervals. As an ultimate value the average is taken. The statistical error is usually in the 0.1%-1% range. Combining the measurements as described also eliminates the thermoelectric voltage imposed by a thermal gradient over the sample as well as the Righi-Leduc effect, the Nernst effect and the Nernst-Ettinghausen effect (Wieder, 1979). When measuring the specific resistivity, a measurement with reversed current is also carried out and these results are averaged before using equation (3.10). The free electron density can be calculated from:

$$n_- = \frac{r}{R_H e} \quad (3.14)$$

with e the electron charge and r the Hall scattering factor. The Hall scattering factor depends on both the scattering mechanism and the

degeneracy of the free electron statistics. For a non-degenerate electron statistics, r can have a value between 1.13 for acoustical phonon scattering and 1.9 for ionized impurity scattering. For a degenerate electron statistics r approaches unity, independent of the scattering mechanism (Putley, 1968). As doped SnO_2 and In_2O_3 coatings have a moderately to highly degenerate electron statistics, r is taken equal to unity in the calculation of n_- from equation (3.14). The mobility μ is calculated from:

$$\mu = (n_- e \rho_{DC})^{-1} = \frac{R_H}{r \cdot \rho_{DC}} \quad (3.15)$$

This mobility is called the drift mobility, which in principle is different from the Hall mobility which is defined as $\mu_H = R_H / \rho_{DC}$. As it is assumed that $r=1$, the difference between drift- and Hall mobility will be further neglected.

3.4.3 Error discussion

In the determination of n_- and μ as described in the previous section some systematical errors may occur which will be discussed here shortly.

a. Contact geometry

In section 3.4.2 it has been assumed that the contacts are infinitely small in size and placed exactly at the sample edge. For deviations from this ideal case, equations have been derived by van der Pauw (1958-1,2). For the case of 4 contacts having 1 mm diameter, put at about 1 mm from the coating edge, the error in the Hall coefficient is estimated to be $(18 \pm 3)\%$ and the error in the resistivity is $(1 \pm 0.3)\%$. This means that, when using equations (3.14) and (3.15), n_- will be estimated systematically about 18 % too high and μ about 17 % too low. For this can easily be corrected, but the remaining systematical errors in n_- and μ are still about 3 % due to the uncertainty of the correction for the Hall coefficient.

b. Magnetic field

The magnetic field strength is determined with a Hall-probe (RFL model 750A) which has an inaccuracy of 1.5%. The repeatability of the Hall probe as well as the repeatability of the magnetic field are much better. This means that only the systematical error of 1.5% remains in the determination of n_- and μ .

c. Coating thickness

As will be discussed in chapter 4, the error in the coating thickness determination is about 1%. This implies an error of 1% in n_- which is systematic when measurements of one sample as a function of temperature are carried out, and a statistical error of 1% when different samples are mutually compared.

d. Inhomogeneity

If the coating is inhomogeneous in the direction perpendicular to the coating surface (the z-direction), then in general n_- and μ will be mainly determined by the sub-layer having the highest conductivity. If the sub-layers of which a coating is built up are sequentially removed or added, then the z-dependent carrier concentration $n_-(z)$ and mobility $\mu(z)$ can be derived.

As derived by Wieder (1976), the z-dependent conductivity is given by:

$$\sigma(z) = \frac{d}{dz} (\sigma_s) \quad (3.16)$$

with σ_s being the sheet conductivity given by $\sigma_s = d/\rho$. The electron density is given by:

$$n_-(z) = \frac{\sigma^2(z)}{e \left(\frac{d}{dz} (R_{H,s} \sigma_s^2) \right)} \quad (3.17)$$

where $R_{H,s}$ is the sheet Hall constant given by $R_{H,s} = R_H/d$. The mobility is given by:

$$\mu_H(z) = \frac{1}{\sigma(z)} \frac{d}{dz} \left(R_{H,s} \sigma_s^2 \right) \quad (3.18)$$

The experimental procedure consists of sequentially removing or adding incremental thickness layers, measuring σ_s and $R_{H,s}$, and evaluating $n_-(z)$ and $\mu(z)$ by reducing the derivatives in equations (3.15-3.17) to differentials.

3.4.4 Example of a measurement

As an example the measurements on sample no 138, a 72 nm SnO_2 coating on glass, are given. The measured values of $n_-(T)$ are plotted in figure 3.12. The figure shows that n_- rises about 15% when the temperature is

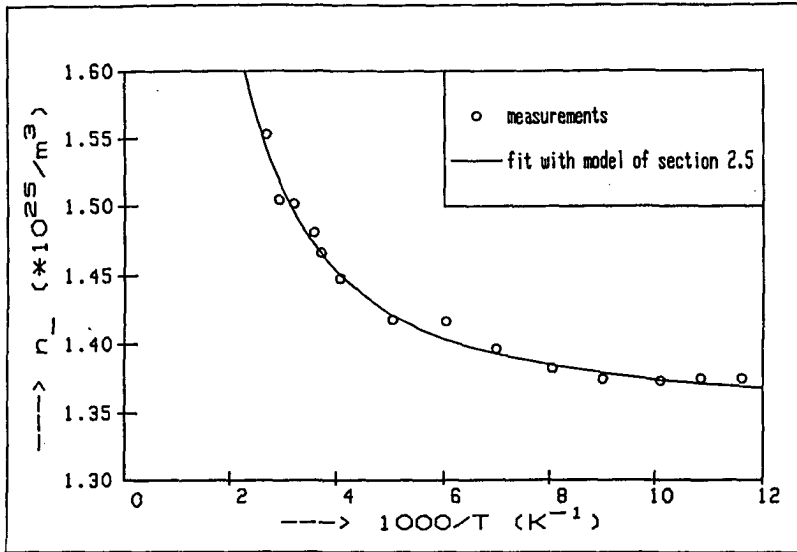


Figure 3.12 Measurements of n_- of a sample as a function of the inverse temperature. The fit to the model of section 2.5 is also shown.

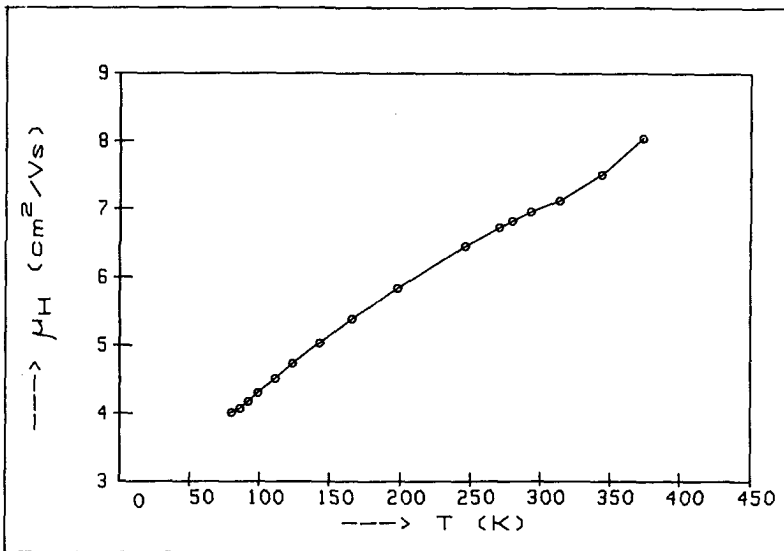


Figure 3.13 Example of a measurement of the mobility as a function of temperature

increased from 80 K to about 400 K. In the figure also the fit made with the model as described in section 2.5 is shown. The parameters, found from a least-squares fit of the parameters E_d and N_d in equation (2.98) to the measured data, are: $E_d = -0.070$ eV and $N_d = 4.06 \cdot 10^{25}/m^3$. The effective mass has been taken to be $0.30 m_e$. As the fit describes the measurements very well, it is used to calculate n_- at any temperature, so it is only necessary to measure the resistivity ρ to obtain the mobility μ from equation (3.15). As measuring the resistivity only is much less elaborate than measuring the Hall coefficient, $\rho(T)$ can be measured at many different temperatures and μ is calculated from equation (3.15), where the fit through the $n_-(T)$ values is used, derived from the measurements of $n_-(T)$ at much less different temperatures.

The result for μ for sample no 138 is given in figure 3.13. In this example $\mu(T)$ has not been determined at more temperatures than $n_-(T)$. The figure shows a monotonous increase of $\mu(T)$ with the temperature. It is noted that the systematical errors may shift the $n_-(T)$ and $\mu(T)$ curves a few percent, but the shape of these curves can be determined very accurately, with statistical fluctuations in $n_-(T)$ and $\mu(T)$ of less than 0.5 %.

3.5 Ellipsometry

3.5.1 Introduction

Ellipsometry has been used to obtain information on the optical constants, the coating thickness and on deviations from the ideal smooth, homogeneous, isotropic film model. Ellipsometry is a collective name for a number of techniques dealing with the measurement and interpretation of the change in the polarization state of a polarized beam of radiation which is reflected from a surface in terms of the optical properties of the reflecting surface.

A change in the polarization state due to reflection at a surface is specified by the change in the relative amplitude and the change in the relative phase after reflection. This can be expressed in terms of the complex amplitude-reflectance ratio, which can be written as:

$$\frac{r_p}{r_s} = \tan(\Psi) \exp(i\Delta) \quad (3.19)$$

where r_p and r_s are the amplitude reflectance for light polarized parallel to the reflecting surface and perpendicular to this direction respectively

(see also section 2.2.2). The ellipsometric angles Δ and Ψ are the quantities which are determined in an ellipsometric measurement. In the next sections the experimental set-up and the measuring method we have used are discussed.

3.5.2 Experimental set-up

A Rudolph Research 200 E ellipsometer is used which can be used in the 0.3-3 μm spectral range. The optical scheme of the Polarizer-Compensator-Sample-Analyzer (PCSA) system is given in figure 3.14. Three light sources are used: a 6 mW Hughes He-Ne laser which gives a collimated beam with $\lambda = 632.8 \text{ nm}$, a Melles Griot 1 mW IR-He-Ne laser with $\lambda = 1523 \text{ nm}$, and a quartz halogen source which gives a continuous spectrum in the 0.3-3 μm spectral range. To obtain circularly polarized light from the linearly polarized laser beams, mica $\frac{1}{4}\lambda$ -retarders are used. For the wavelength selection when using the the halogen source, interference filters are used with center wavelengths between 400 and 2400 nm with about 0.01λ bandwidth in 100 nm steps. By proper alignment the angle of incidence θ can be adjusted within 0.02° .

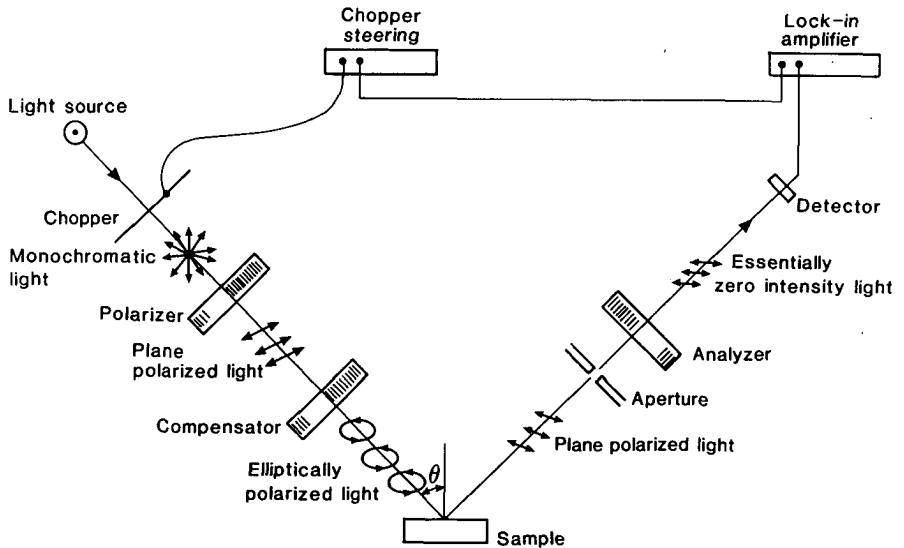


Figure 3.14 Schematic lay-out of the ellipsometer arrangement

The polarizer and analyzer consist of a Glan-Thompson prism mounted in a graduated circle which allows a read-out of the polarizer/analyzer angle within 0.01° . The compensator is a Babinet-Soleil compensator which can be adjusted to give $\frac{1}{4}\pi$ retardation at any wavelength up to 3000 nm. The detector is an EG&G HUV-1000 B silicon detector/amplifier combination for the 400-1100 nm spectral range. In the 1200-2400 nm spectral range a Hughes PbS detector is used with a SBRC-A400 pre-amplifier. The light beam is chopped with about 360 Hz. For the synchronous amplification of the detector signal a PAR model 5104 Lock-in amplifier is used.

3.5.3 Measuring method

The ellipsometer is used as a null-ellipsometer, which means that the compensator angle C is put at $+45^\circ$ or -45° and the polarizer angle P and the analyzer angle A are adjusted so that a minimum intensity is detected by the detection system. At $C = 45^\circ$ there are two combinations of A and P which give an intensity minimum, just like at $C = -45^\circ$. The relation between the combination of C, A and P for which a minimum intensity is obtained, and the corresponding values of Δ and Ψ , are given in table 3.4. The ellipsometric angles are measured in the four zones at about 7, in some cases up to 17 angles of incidence θ between 30° and 75° . By taking the average of the measurements in the four zones, all systematic errors which could arise from component imperfections are eliminated.

Table 3.5 Relation between the Polarizer (P), compensator (C) and analyzer (A) extinction values and the ellipsometric angles Δ and Ψ

zone no	C	P	A	Δ	Ψ
1	$-\frac{\pi}{4}$	$\frac{1}{2}(\Delta_1 - \frac{\pi}{2})$	Ψ_1	$2(P_1 + \frac{\pi}{4})$	A_1
2	$\frac{\pi}{4}$	$\frac{1}{2}(\frac{3}{2}\pi - \Delta_2)$	Ψ_2	$2(\frac{3}{4}\pi - P_2)$	A_2
3	$-\frac{\pi}{4}$	$\frac{1}{2}(\Delta_3 - \frac{3}{2}\pi)$	$-\Psi_3$	$2(P_3 + \frac{3}{4}\pi)$	$-A_3$
4	$\frac{\pi}{4}$	$\frac{1}{2}(\frac{\pi}{2} - \Delta_4)$	$-\Psi_4$	$2(\frac{\pi}{4} - P_4)$	$-A_4$

3.5.4 Determination of statistical errors

An estimate for the statistical errors in Δ and Ψ can be made after correcting the data for the errors caused by the zero- and first order component imperfections.

The zero order errors, these are the differences between the A, P and C scale readings and the real values, are determined according to the method described by McCrackin (1963). The first order imperfections (e.g. a retardation of the compensator which deviates from $\frac{1}{4}\pi$) are deduced from the average of the three two-zone residues and the six four-zone residues determined from measurements at different angles of incidence as described in the textbook of Azzam and Bashara (1977). After these corrections the standard deviation in the average for the corrected Δ and Ψ give the errors $\delta\Delta'$ and $\delta\Psi'$. The error in θ is incorporated in the errors in Δ ($\delta\Delta$) and Ψ ($\delta\Psi$) in the following way:

$$\delta\Delta = (\delta\Delta'^2 + \left(\frac{\partial\Delta}{\partial\theta} \delta\theta \right)^2)^{1/2} \quad (3.20)$$

$$\delta\Psi = (\delta\Psi'^2 + \left(\frac{\partial\Psi}{\partial\theta} \delta\theta \right)^2)^{1/2} \quad (3.21)$$

The values of $\frac{\partial\Delta}{\partial\theta}$ and $\frac{\partial\Psi}{\partial\theta}$ are estimated from the measurements of Δ and Ψ at different angles of incidence θ . For the error $\delta\Psi'$ we usually find a value in the $0.01 - 0.10^\circ$ range when the laser light sources are used, and a value in the $0.10 - 0.50^\circ$ range when the quartz halogen source with an interference filter is used. The error in Δ , $\delta\Delta'$, is usually about twice the value of $\delta\Psi'$.

3.6 Other experimental techniques used

The crystal structure of the coatings has been investigated using an Enraf-Nonius Diffractis 583 stabilized X-ray generator and a Philips PW 1050 X-ray powder diffractometer of the Solid State group. $\text{CuK}\alpha$ -radiation is used and the diffractograms are taken using continuous scanning. An example of a diffractogram of a SnO_2 coating is given in figure 3.15. From the diffraction peaks two parameters are derived: the peak intensity, defined as the peak height times the peak width at half the peak height, and the average grain size which is derived from the peak width using the Debye-Scherrer equation.

The elemental composition of the coatings has been determined with a Jeol JXA 733 Electron probe X-ray microanalyzer of the Metallurgy section and the Submicron Technology Center. The electron beam energy has been reduced to 6 keV to obtain a penetration depth of about 150 nm in which the composition is measured. As a reference material for Sn and O, a SnO_2 standard has been used, for In a metallic In standard has been used and for F a CaF_2 standard has been used. In the calculation of the elemental composition matrix effects have been taken into account.

Scanning Electron Micrography (SEM) has been used to study the structural properties, using a Jeol scanning electron microscope of the Submicron Technology Center. A thin gold coating has been deposited on the sample surface to enhance the contrast. With this method a maximum magnification factor of 80,000 has been obtained.

Further analyses have been carried out using Rutherford Backscattering (RBS) at the Utrecht university and X-ray photoelectron spectroscopy (ESCA) at the Twente university, but as these measurements did not add information to what was already known of the coatings, the results are not used in this thesis and these techniques are not described here further.

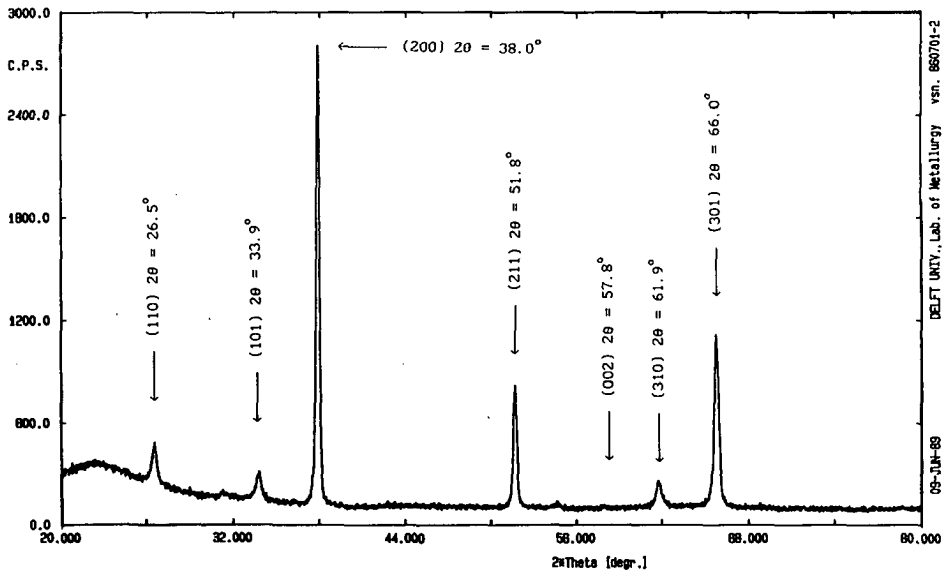


Figure 3.15 Example of a diffractogram of a SnO_2 coating. The indicated line positions are of SnO_2 .

4. METHODS FOR DETERMINING OPTICAL CONSTANTS AND COATING THICKNESS

A homogeneous, isotropic material is at a wavelength λ optically fully characterized by its complex refractive index $n(\lambda) = n(\lambda) - ik(\lambda)$ (see section 2.2.1). When at a certain wavelength the optical constants n and k are known, the transmittance and reflectance for that wavelength can be calculated straightforward for each angle of incidence, polarization state and thickness of the material (see section 2.2). In this chapter the methods which have been used to do the reverse: to derive the optical constants from reflection and transmission quantities, are described. Knowledge of the optical constants is essential to model the properties of transparent conducting coatings, e.g. to check the validity of the Drude model (see section 2.3).

4.1 The Reflection-Transmission method

The Reflection-Transmission method, generally referred to as the R-T method, uses the measured normal reflectance and transmittance of a coating-substrate system to calculate the optical constants. The calculation is iterative: for one wavelength, knowing the substrate thickness, the substrate optical constants and the coating thickness, n and k are iterated to values for which the calculated reflectance and transmittance (using the matrix formalism of section 2.2.2) equal the measured values. The method can also be used to determine the substrate optical constants by determining the reflectance and transmittance of a bare substrate and fitting the substrate optical constants to obtain the measured reflectance and transmittance.

The R-T method has been described by Nilsson (1968). Its advantages are its relatively simplicity in measurement and calculation. Its disadvantages are the occurrence of different possible combinations of n and k for one set of R , T values (at one wavelength, coating thickness d etc.), and sometimes a large uncertainty in n and k due to a small uncertainty in R , T or d . This is illustrated in figure 4.1, which is taken from Hjortsberg (1981). In this figure it can be observed that the determination of k will be more accurate than that of n . Hjortsberg has shown that when $n \approx k+1$, the absolute error in n may be as large as 0.5.

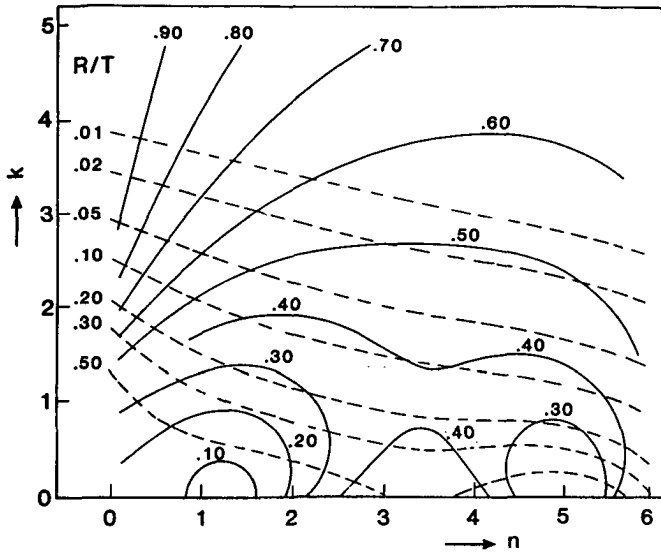


Figure 4.1 Plot of the contours of constant normal transmittance T and reflectance R . The dimensionless coating thickness is 0.1λ . The substrate refractive index is 1.5 . After Hjortsberg (1981).

In the case of transparent conducting coatings this problem can partly be overcome, as for these coatings a reflectance minimum is observed where $n = k+1$. So at this wavelength n can accurately be determined from the value of k .

We have extended the method to enable also the calculation of the coating thickness d and the surface roughness d_σ from spectral data in the interference region. In this region the variation of R and T with the wavelength is due to interference effects rather than to a change in optical constants. So in a small wavelength area, measurements of R and T at N different wavelengths within this area can be used to calculate the optical constants n and k , the thickness d and the surface roughness d_σ . The surface roughness has been modeled with a single layer as described in section 2.2.6. The iteration procedure consists of fitting the calculated reflectances and transmittances as well as possible to the measured ones, i.e. it consists of minimizing the function :

$$X^2 = \sum_{i=1}^N \left(\frac{R_c(n, k, d, d_\sigma, \lambda_i) - R_m(\lambda_i)}{\Delta R_m} \right)^2 + \left(\frac{T_c(n, k, d, d_\sigma, \lambda_i) - T_m(\lambda_i)}{\Delta T_m} \right)^2 \quad (4.1)$$

where: N is the number of different wavelengths

d , d_σ are the thickness and the surface roughness respectively

R_m , T_m are the measured reflectance and transmittance

R_c , T_c are the calculated reflectance and transmittance

ΔR_m , ΔT_m are the experimental errors in R_m and T_m

This is the standard chi-square method for fitting parameters in a model to measurements. The minimization is carried out numerically using the Marquard algorithm and the error in the parameters is derived from the second derivative matrix in the minimum. For further details we refer to a standard textbook (Bevington, 1969), which has closely been followed.

As an example we give the near-normal specular transmittance and reflectance in the 320-2500 nm spectral region of sample no 187, a F-doped SnO_2 coating on a 2mm pyrex substrate, in figure 4.2. From the reflectance and transmittance measurements at six wavelengths between 530 and 580 nm the film thickness and the surface roughness are determined with the above-mentioned method resulting in $d = 525 \pm 10$ nm and $d_\sigma = 20 \pm 5$ nm. These values are fixed to enable the calculation of n and k at single wavelengths between 320 and 2500 nm. As in these calculations two parameters (n and k) are fitted to two measured values (R and T), the minimum of X^2 in equation (4.1) should become zero. The resulting values for n and k are given in figure 4.3. In the spectral regions 0.88-1.0 μm and 1.3-1.5 μm no values are given as no solution was found, i.e. X^2 could not be made zero. The error in k ranges from about 0.001 at $\lambda = 500$ nm to about 0.02 at $\lambda = 2.5$ μm . The error in n is about 0.04 for $\lambda < 0.8$ μm and $\lambda > 1.5$ μm . For 0.8 $\mu\text{m} < \lambda < 1.5$ μm the error in n is about 0.20. This means that with this method the determination of k is far superior to that of n . For $1.0 < n < 1.5$ the determination of n is even hardly possible.

4.2 The envelope method

In the envelope method the interference minima and maxima of R and T are considered as continuous functions of the wavelength. This gives four independent functions which are called $R_{\min}(\lambda)$, $R_{\max}(\lambda)$, $T_{\min}(\lambda)$ and $T_{\max}(\lambda)$. Under certain conditions, from these four functions four coating parameters can be obtained for a coating with a known thickness, which has a surface roughness and which is homogeneous in k , but inhomogeneous in n . The parameters are: n_1 , the refractive index near the coating/air interface; n_2 , the refractive index near the coating/substrate interface; d_σ , the surface roughness and k , the extinction coefficient.

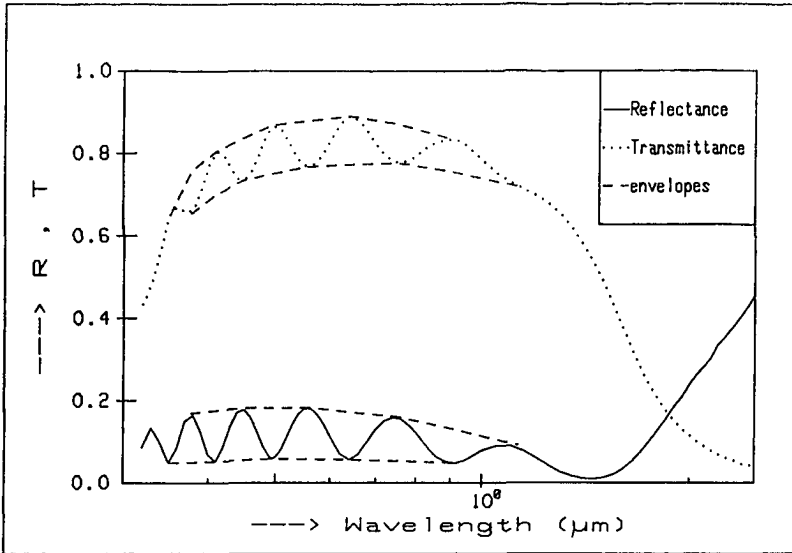


Figure 4.2 Reflectance and transmittance of sample no 187 in the 0.3-2.5 μm spectral range. The envelopes of both spectra, as used in the envelope method, are also drawn.

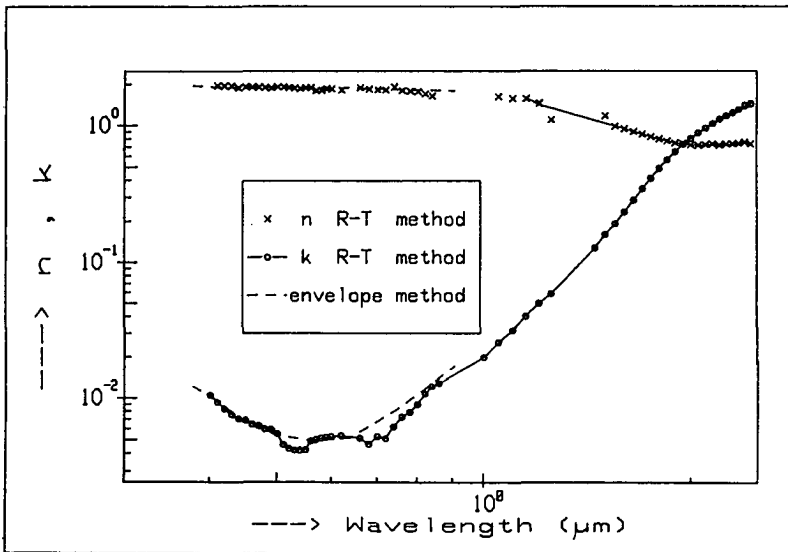


Figure 4.3 Refractive index n and extinction coefficient k of sample no 187 in the 0.3-2.5 μm spectral range as determined with the R-T method and with the envelope method

The $R_{\min}(\lambda)$ etc. functions are obtained by sketching continuous function which connect the minima respectively maxima of the measured transmittance and reflectance, so that envelopes of the transmittance and reflectance curves are formed. The method is given by Szczyrbowski and Czapla (1979), where also the extensive formulary is given. Relative to the R-T method the formulas are simplified as the sine- and cosine terms which appear in the calculations of the reflectance and transmittance (see section 2.2.5) can be put equal to +1 or -1 to obtain a reflectance or transmittance minimum or maximum.

In figure 4.2 the continuous functions $R_{\min}(\lambda)$, $R_{\max}(\lambda)$, $T_{\min}(\lambda)$ and $T_{\max}(\lambda)$ are shown by the dotted lines which connect the extrema of R and T. From these curves, $d_{\sigma} \approx 18 \pm 10$ nm is obtained, which is in accordance with the result of the R-T method. In the 0.3-0.9 μm wavelength region we find that $n_2 \approx n_1 + 0.1$, which indicates a slight inhomogeneity in the coating. In figure 4.3 the average of n_1 and n_2 and k are indicated by the dotted lines. We see that there is a quite good agreement between the results of the envelope method and the results of the R-T method.

The accuracy of the method has been estimated by varying R_{\min} , R_{\max} , T_{\min} and T_{\max} separately by 0.005 (a reasonable estimate for the experimental error) and adding the errors found in $0.5(n_1+n_2)$, k and d_{σ} quadratically. The errors are 0.03 for $0.5(n_1+n_2)$, 0.002 for k and 10 nm for d_{σ} . Compared to the R-T method the determination of n and k is slightly better, but the determination of d_{σ} is less accurate.

The conditions under which this method can be applied limits the spectral area in which it can be used. These conditions are: $k \ll (n - n_{\text{substrate}})$, $k_{\text{substrate}} \approx 0$, the optical constants should change little enough to obtain interference extrema and the coating should be thick enough to give at least two interference minima and maxima in the spectral region where the first three conditions hold. For doped SnO_2 coatings, with $n \approx 2$ for $400 \text{ nm} < \lambda < 900 \text{ nm}$, this means that the thickness must be larger than about 300 nm.

4.3 Application of a Kramers-Kronig relation to the reflectance spectrum

For $\lambda > 2.5 \mu\text{m}$ the R-T method cannot be applied as the substrate becomes absorbing and no transmittance can be measured. However, using reflectance only and by assuming that the coating can be considered as semi-infinite, the complex refractive index can be determined from the reflectance spectrum using a Kramers-Kronig relation.

In general, the Kramers-Kronig relations give the imaginary part of the response of a linear passive system if the real part is known at all frequencies, and vice versa. In this case the complex reflection amplitude r is considered as such a response function and is written in a real and complex part:

$$r = |r| (\cos(\phi) - i \sin(\phi)) = \sqrt{R} \exp(-i\phi) \quad (4.2)$$

The Kramers-Kronig relation between the phase $\phi(\lambda)$ and the reflectance spectrum $R(\lambda)$ is (Stern, 1963):

$$\phi(\lambda) = -\frac{\lambda}{\pi} \mathcal{P} \int_0^{\infty} \frac{\ln(R(\lambda'))}{\lambda^2 - \lambda'^2} d\lambda' \quad (4.3)$$

where \mathcal{P} stands for the Cauchy principal value. The principal value can be omitted by subtracting a constant from $\ln(R(\lambda'))$ which removes the singularity:

$$\phi(\lambda) = -\frac{\lambda}{\pi} \int_0^{\infty} \frac{\ln(R(\lambda')) - \ln(R(\lambda))}{\lambda^2 - \lambda'^2} d\lambda' \quad (4.4)$$

From equations (4.3) and (4.4) it can be observed that in principle the complete reflectance spectrum from zero to infinite wavelength is needed, but the integrand vanishes for $\lambda' \gg \lambda$ and $\lambda' \ll \lambda$. We want to use equation (4.4) in the 2.5 - 40 μm spectral region, so the spectrum needs to be extrapolated beyond this region. The spectrum is extended to lower λ values down to 0.3 μm by calculating $R(\lambda)$ for a semi-infinite medium from the refractive index obtained by the R-T method and/or the envelope method using:

$$R(\lambda) = \frac{(n(\lambda)-1)^2 + k^2}{(n(\lambda)+1)^2 + k^2} \quad (4.5)$$

For $\lambda > 40 \mu\text{m}$ the spectrum is, in the case of a conducting SnO_2 or In_2O_3 coating, extrapolated using the Drude theory where the parameter λ_p is estimated and the parameter λ_γ is fitted to give with equation (4.5) the measured reflectance at $\lambda = 40 \mu\text{m}$. The Drude theory together with (4.5) is then used to extrapolate the reflectance spectrum up to $\lambda = 500 \mu\text{m}$. The reflectance is assumed to be constant for $\lambda < 0.3 \mu\text{m}$ and $\lambda > 500 \mu\text{m}$. For these spectral areas the contribution to the integral of equation (4.4) can be calculated analytically and the integral can be split into three parts:

$$\phi_1(\lambda) = (2\pi)^{-1} \ln \left(\frac{R(0.3\mu\text{m})}{R(\lambda)} \right) \ln \left| \frac{\lambda - 0.3 \mu\text{m}}{\lambda + 0.3 \mu\text{m}} \right| \quad (4.6a)$$

$$\phi_2(\lambda) = -\frac{\lambda}{\pi} \int_{\lambda'=0.3\mu\text{m}}^{\lambda'=500\mu\text{m}} \frac{\ln(R(\lambda')) - \ln(R(\lambda))}{\lambda^2 - \lambda'^2} d\lambda' \quad (4.6b)$$

$$\phi_3(\lambda) = (2\pi)^{-1} \ln \left(\frac{R(500\mu\text{m})}{R(\lambda)} \right) \ln \left| \frac{\lambda + 500 \mu\text{m}}{\lambda - 500 \mu\text{m}} \right| \quad (4.6c)$$

$$\phi(\lambda) = \phi_1(\lambda) + \phi_2(\lambda) + \phi_3(\lambda) \quad (4.6d)$$

The numerical integration of (4.6b) is carried out using the trapezium rule for $2.5 \mu\text{m} < \lambda < 40 \mu\text{m}$. If the coating is considered as semi-infinite (this means that the penetration depth δ (see equation 2.19) is much smaller than the coating thickness), the refractive index is found by combining equations (4.5) and (4.2) yielding:

$$n(\lambda) = n(\lambda) - ik(\lambda) = \frac{1 - R(\lambda) - 2i\sqrt{R(\lambda)} \sin(\phi(\lambda))}{1 + R(\lambda) - 2\sqrt{R(\lambda)} \cos(\phi(\lambda))} \quad (4.7)$$

As thin or poorly reflecting coatings cannot be considered to be semi-infinite, an iterative method has been used to correct the measured spectrum $R_m(\lambda)$ for the substrate influence as to give a corrected spectrum $R_c(\lambda)$ which would be obtained if the coating were semi-infinite and to which equation (4.7) can be applied. The iterative procedure is as follows: as a first estimate of $R_c(\lambda)$ the measured spectrum $R_m(\lambda)$ can be used or, if the electrical properties of the coating are known, a reflectance spectrum can be calculated using the Drude model. This spectrum is called $R_c^0(\lambda)$. It is used to calculate the coating optical constants from equations (4.6) and (4.7). Using these optical constants together with the coating thickness and the substrate optical constants, the reflectance from the film-substrate system can be calculated yielding a spectrum called $R_1(\lambda)$. When this calculated spectrum differs from the measured spectrum, a better estimate for the corrected spectrum $R_c^1(\lambda)$ can be made using:

$$R_c^1(\lambda) = R_c^0(\lambda) \left((1-r) \frac{R_m(\lambda)}{R_1(\lambda)} + r R_c^0(\lambda) \right) \quad (4.8)$$

where r is a relaxation factor which is taken between 0 and 1 to prevent an oscillatory or divergent behaviour of the successive corrections. Now the spectrum $R_c^1(\lambda)$ is used in equations (4.6) and (4.7), which again gives optical constants from which a spectrum $R_1(\lambda)$ can be derived, and a second corrected spectrum $R_c^2(\lambda)$ can be found using equation (4.8) with $R_c^1(\lambda)$ replaced by $R_c^2(\lambda)$ and $R_c^0(\lambda)$ replaced by $R_c^1(\lambda)$. This procedure is repeated until $R_m(\lambda)$ and $R_1(\lambda)$ differ less than 0.0001, which is far within the measuring error of $R_m(\lambda)$, for all wavelengths.

The substrate optical constants have been determined in a similar way by applying equations (4.6) and (4.7) to the reflectance spectra of the bare substrates. Here the extrapolation to long wavelengths consisted of assuming the reflectance to be constant for $\lambda > 40 \mu\text{m}$. The extrapolation in the transparent spectral region ($0.3 \mu\text{m} < \lambda < 3 \mu\text{m}$) was carried out using the optical constants obtained with the R-T method. The extinction coefficients of quartz, pyrex and glass obtained in this way are given in figure 4.4. In this figure the SiO_2 absorptions at $\lambda \approx 9$ and $21 \mu\text{m}$ can clearly be observed. The obtained refractive indexes of glass are in good agreement with the values found by Rubin (1985).

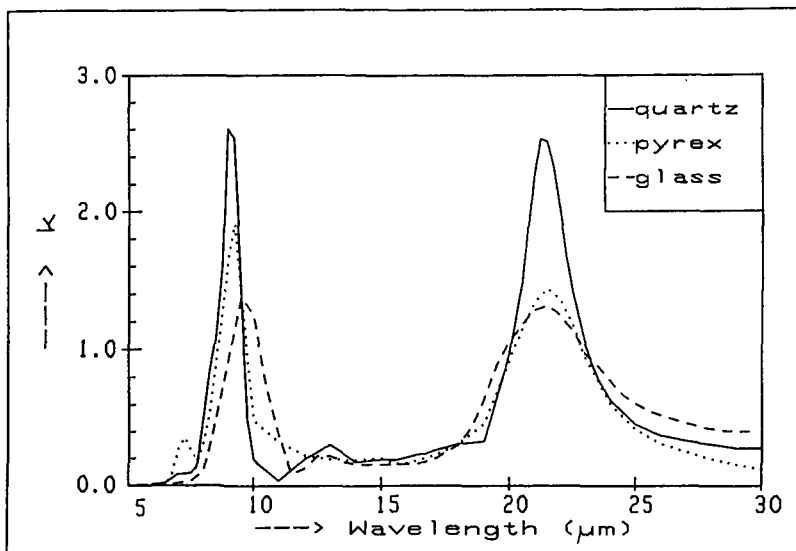


Figure 4.4 Extinction coefficient k of quartz, pyrex and glass obtained from a Kramers-Kronig analysis of the reflectance spectrum.

As an example and to illustrate the errors caused by the numerical integration and by the iterative procedure, the method is applied to the calculated spectrum of a 300 nm coating for which the optical constants are known: the Drude model is used with parameters: $\lambda_p = 2 \mu\text{m}$ and $\lambda_\gamma = 5 \mu\text{m}$. For the substrate optical constants, those of pyrex have been taken. The reflectance of the coating-substrate system is calculated in the 2.5-40 μm spectral region and this spectrum is used as the measured reflectance spectrum $R_m(\lambda)$ to which the method is applied. The Drude model with slightly erroneous parameters ($\lambda_p = 1.9 \mu\text{m}$ and $\lambda_\gamma = 5.5 \mu\text{m}$) is used to obtain a first estimate of $R_c(\lambda)$. The known optical constants are used to extrapolate the reflectance spectrum down to 0.3 μm . The extrapolation to high wavelengths is carried out using a slightly erroneous value for the plasma wavelength: $\lambda_p = 1.9 \mu\text{m}$ and the extrapolation is carried out up to 80 μm instead of 500 μm to simulate an uncertainty in the reflective material properties at long wavelengths. These erroneous assumptions correspond to the uncertainties which are met in practice. As the optical constants and the calculated reflectance spectrum of a semi-infinite coating which should be obtained are known, the spectrum $R_c(\lambda)$ and the optical constants derived using equations (4.6) and (4.7) can be compared directly to the values which have been used as input data to simulate a measured spectrum.

The iteration procedure summarized in equation (4.8) has been carried out using a relaxation factor of $r = 0.5$. The convergence criterion was reached after 20 iterations. In figure 4.5 the calculated reflectance spectrum of the coating-substrate system, the corrected and extrapolated spectrum and the phase angle $\phi(\lambda)$ derived from equation (4.6) are given. The figure shows that the correction procedure leads to a smooth curve $R_c(\lambda)$ while in the $R_m(\lambda)$ curve the substrate influence is clearly visible. The deviations of the calculated $R_c(\lambda)$ and $\phi(\lambda)$ curves from the values they should have according to the Drude theory are too small to be indicated in the figure. Table 4.1 indicates the errors in R_c and ϕ and the influence of these errors on the optical constants are indicated at several wavelengths.

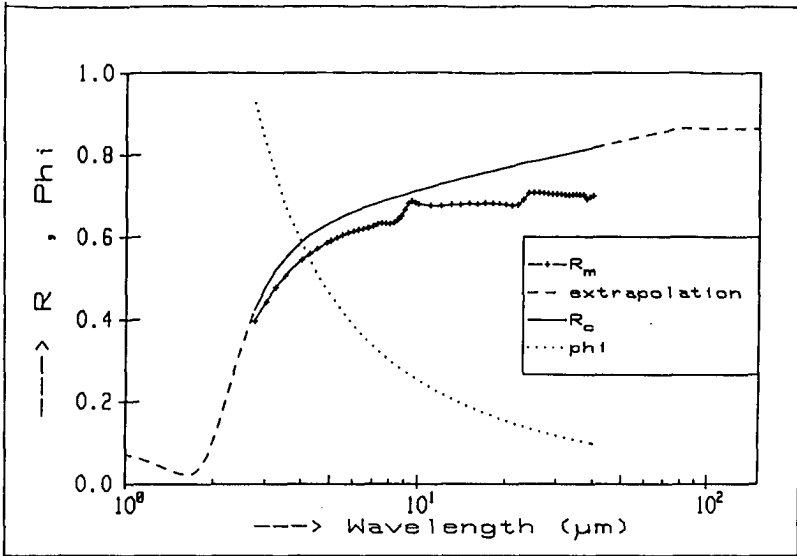


Figure 4.5 'Measured' spectrum together with the corrected spectrum, the extrapolated spectrum and the phase ϕ (phi) calculated from the Kramers-Kronig integration.

Table 4.1 Values of R_c , ϕ , n and k according to the Drude model at different wavelengths and the error imposed by the numerical integration and the correction procedure

λ (μm)	R_c	ΔR_c (%)	ϕ	$\Delta\phi$ (%)	n	Δn (%)	k	Δk (%)
3.0	0.480	1.9	0.797	3.6	1.03	-6.9	1.92	-3.5
5.0	0.636	0.7	0.453	2.0	1.82	-3.9	3.44	-0.6
7.0	0.680	0.3	0.335	1.1	2.63	-2.3	4.41	-0.2
10	0.714	0.0	0.253	0.0	3.68	0.0	5.44	0.0
20	0.774	-0.6	0.159	-2.6	6.19	3.3	7.60	-0.6
30	0.806	-1.0	0.125	-5.5	7.97	6.2	9.16	-3.3
40	0.827	-1.1	0.106	-6.9	9.42	7.2	10.46	-4.8

The table shows that this method can give the optical constants with quite a good accuracy from a measurement of the reflectance spectrum only. The errors are largest at the edges of the $R_m(\lambda)$ spectrum. The errors at low wavelengths are most probably due to the numerical integration procedure. The errors at long wavelengths are due to the extrapolation procedure: these errors disappear when the spectrum is extrapolated up to $\lambda = 500 \mu\text{m}$ using the Drude model. An error due to the numerical integration or to an erroneous extrapolation will also lead to errors in the correction procedure and so to errors in $R_c(\lambda)$. As shown in the table these errors are quite small for this example. An other kind of error due to the correction procedure may occur when the substrate reflectance dominates the reflectance spectrum and a totally erroneous spectrum $R_c^0(\lambda)$ is taken as the first approximation. The correction procedure will always converge to a spectrum $R_c^0(\lambda)$, but it cannot be proved that this is exactly the spectrum which would be obtained from a semi-infinite medium. This can be understood from the limiting case: for a coating being so thin that it does not influence the substrate reflectance this method still leads to some reflectance spectrum $R_c^0(\lambda)$, but this spectrum has no physical significance.

4.4 Ellipsometry

As stated in section 3.6, ellipsometry uses the change in the polarization state of a monochromatic light beam reflected at a surface. From the ellipsometric angles Δ and Ψ obtained at an angle of incidence θ , parameters such as the coating thickness and the optical constants can be derived. For the derivation of optical coating properties at one wavelength, we have used measurements of Δ and Ψ at a number N of different angles of incidence. This kind of ellipsometry is called Multiple Angle of Incidence (MAI) ellipsometry. This measuring method gives an excess of experimental $\Delta(\theta)$ and $\Psi(\theta)$ values relative to the coating parameters which are to be determined. The best estimate for the coating parameters, such as the optical constants, surface roughness etc., is obtained by minimizing the X_r^2 function:

$$X_r^2 = \frac{1}{\nu} \sum_{i=1}^N \left(\frac{\Psi_m(\theta_i) - \Psi_c(n, k, d, d_\sigma, \dots, \theta_i)}{\delta\Psi_m(\theta_i)} \right)^2 + \left(\frac{\Delta_m(\theta_i) - \Delta_c(n, k, d, d_\sigma, \dots, \theta_i)}{\delta\Delta_m(\theta_i)} \right)^2 \quad (4.9)$$

where: N is the number of different angles of incidence θ

Ψ_m, Δ_m are the measured ellipsometric angles

Ψ_c, Δ_c are the calculated angles for a set of coating parameters

$\delta\Psi_m, \delta\Delta_m$ are the experimental errors in Ψ_m and Δ_m

ν is the number of degrees of freedom: $\nu = 2N - p$ with p the number of coating parameters which are varied to give a minimum of X_r^2

The calculation of coating parameters by minimizing X_r^2 and the determination of the error in the parameters has been carried out in an analogous way as in the case of the R-T method (see section 4.1), following the textbook of Bevington (1969).

Maximum information about the coatings studied can be obtained by first determining parameters for a relatively crude model (e.g. a smooth, homogeneous, isotropic coating on a substrate) and then allow more parameters to be determined (e.g. a surface roughness or an anisotropy), until the value of X_r^2 approaches unity. The parameters calculated in this way can be assumed to be physically significant when three conditions are fulfilled:

1. A more detailed model should lead to an appreciable decrease of X_r^2 .
2. The parameters which are determined should have physically acceptable values.
3. The parameters which can be determined by another method should have a value in accordance to the value obtained by ellipsometry.

As an example we use the measurements on sample 342, an Sn-doped In_2O_3 coating on glass. The ellipsometric angles Δ and Ψ have been determined at 7 different angles of incidence at wavelengths between 500 and 2100 nm with 100 nm steps. As each determination of Δ and Ψ requires 4 measurements of the Δ and Ψ in the different zones to eliminate systematic errors, (see section 3.5.4), the complete measurement on this sample required about 450 measurements of Δ and Ψ which take some minutes each. This illustrates the major practical disadvantage of ellipsometry: it is very time consuming.

The coating thickness and an eventual surface roughness have been calculated from the measurements at short wavelengths as at these wavelengths the coating thickness can be obtained with the highest accuracy. The extinction coefficient k of the coating has been fixed to the value as obtained with the R-T method, as k can be determined very accurately with this method. The measurements at $\lambda=600$ nm are, together with the least-squares fit to a model without and a model with an assumed surface roughness, shown in figure 4.6.

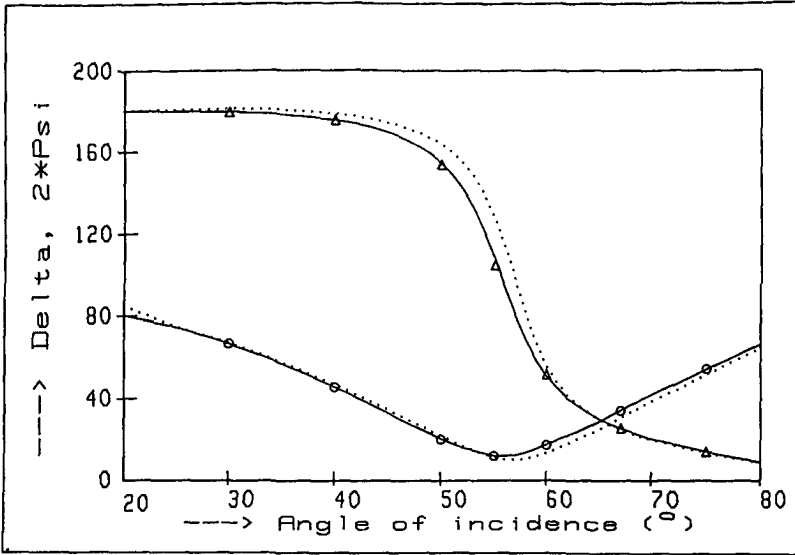


Figure 4.6 Measurements of Δ (Δ) and Ψ (\circ), together with a fit using a model with surface roughness (—) and a model without surface roughness (\cdots).

Table 4.2 Results of the determination of the coating thickness and the surface roughness of sample no 342 by ellipsometry

λ (nm)	model without surface roughness			model with surface roughness			
	n	d	χ_r^2	n	d	d_σ	χ_r^2
500	1.81±0.04	206±12	16	2.02±0.03	156±5	18.5±2.0	0.34
600	> 2.5	123±6	145	2.03±0.09	149±6	20.9±1.9	1.50
700	2.46±0.42	137±34	73	1.92±0.02	153.9±0.7	22.1±1.8	1.88
800	2.02±0.04	169±4	18	1.877±0.007	151±3	23 ±2	0.70
900	1.886±0.004	180±0.8	3.6	1.847±0.007	162±7	15 ±5	1.30

The figure shows that the model with a surface roughness can better be fitted to the measurements. This results in a lower value of χ_r^2 . The resulting parameters of the calculation for a model with and without an assumed surface roughness are presented in table 4.2. In this table it is shown that the assumption of a surface layer describing the surface roughness is necessary to obtain consistent values for n and d at all wavelengths. Also the decrease of χ_r^2 from about 20 to about 1 between the first and the second model shows on one hand that a surface roughness is present and that the thickness of a coating representing this roughness can be determined; on the other hand it shows that it is necessary to take this roughness into account to obtain consistent and acceptable determinations of the coating thickness d and the coating refractive index n .

From table 4.2, using the model with surface roughness, we conclude that the coating thickness is 155 ± 2 nm and the layer representing the surface roughness d_σ has a thickness of 21.5 ± 1.5 nm. These values are now fixed to calculate the optical constants at the other wavelengths. The calculations resulted in accurate values of n and k and χ_r^2 values not deviating very much from unity. This means that for this coating the model of a homogeneous, isotropic film with a surface roughness can be used at all wavelengths.

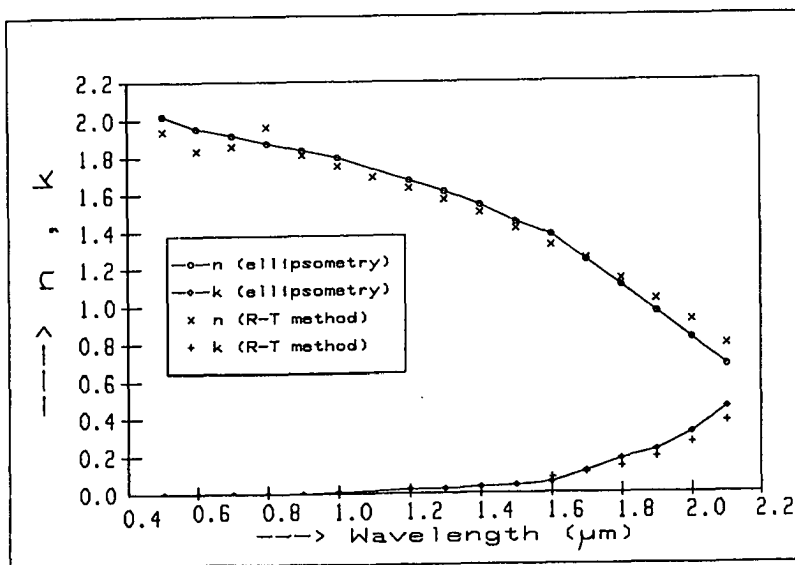


Figure 4.7 n and k of sample no 342 determined with ellipsometry. The values obtained using the R-T method are also shown.

In figure 4.7 the calculated values of n and k as a function of the wavelength are given, together with the values as determined with the R-T method. In this figure it can be observed that both methods give mutually consistent results. The absolute inaccuracy in n and k determined by ellipsometry is about 0.004 at all wavelengths. This is superior to the other methods, except for the determination of k for $\lambda < 1 \mu\text{m}$, which is carried out better by the R-T method or the envelope method.

Non-ideal films

In the example above we have dealt with a film that deviates from the ideal smooth, homogeneous, isotropic film + substrate model as we had to take into account a surface layer to model the surface roughness. The way in which anisotropic and inhomogeneous coatings are treated is discussed in the next two sections.

a. Anisotropy

In an anisotropic model we assume that the n and k values in the direction perpendicular to the substrate (n_e and k_e) are different from those parallel to the substrate (n_o and k_o). The latter determine the normal reflectance and transmittance and can be determined by e.g. the R-T method. The optics for this anisotropic model is given in section 2.2.4. A coating can be assumed to be anisotropic when the application of an isotropic model gives a value for X_r^2 which is much larger than unity, while the application of an anisotropic model gives an appreciable decrease of X_r^2 . As an example we give the results of sample no 200, a 475 nm SnO_2 coating on a quartz substrate at $\lambda = 1523 \text{ nm}$ for an isotropic and for an anisotropic model in table 4.3. From this table it is clear that the anisotropic model gives a much lower X_r^2 and a value for k_o which is more in accordance with the value determined with the R-T method.

Table 4.3 Determination of n and k for an isotropic and for an anisotropic model for sample no 200 at $\lambda = 1523 \text{ nm}$

	n_o	n_e	k_o	k_e	X_r^2
R-T method	1.20 ±0.20	-	0.230±0.008	-	-
ellipsometry (isotropic model)	1.08 ±0.21	-	0.41 ±0.15	-	227
ellipsometry (anisotropic model)	1.117±0.012	1.162±0.012	0.222±0.010	0.197±0.012	4.20

b. Inhomogeneity

The inhomogeneity can be described with a z-dependent refractive index in the coating. To describe the inhomogeneity in the coating exactly an a multiple-film model, it is necessary to model the coating as consisting of an infinite number of sub-layers. However, in calculations using ellipsometric data the number of sub-layers needs to be restricted to two or three, to limit the number of parameters which are to be determined. The optimum position where an interface between two sub-layers can be assumed is found in the following way: the optical constants of a two-layer model (eventually with a third layer representing the surface roughness) are calculated with the interface position fixed in the coating. The value of X_r^2 is recorded as a function of the interface position. Now the points where X_r^2 reaches a minimum are considered to represent the position at which a transition between two sub-layers takes place.

The refractive indexes of the two sub-layers with an interface at a position $z=d_1$ are called $n_{1,1}$ (the coating between $z=0$ and $z=d_1$) and $n_{2,1}$ (the coating between $z=d_1$ and $z=d$). From the refractive indexes calculated with the interface put at an other position d_{1+1} the mean refractive index $\bar{n}_{1,1+1}$ in the sub-layer between $z=d_1$ and $z=d_{1+1}$ can be determined from the change in n_1 as well as from the change in n_2 :

$$\bar{n}_{1,1,1+1} = \frac{n_{1,1+1}d_{1+1} - n_{1,1}d_1}{d_{1+1} - d_1} \quad (4.10)$$

and

$$\bar{n}_{2,1,1+1} = \frac{n_{2,1}(d-d_1) - n_{2,1+1}(d-d_{1+1})}{d_{1+1} - d_1} \quad (4.11)$$

Here it has been assumed that $n_{1,1}$ and $n_{2,1}$ represent the average refractive index in both sub-layers. For a final value of $n_{1,1+1}$ the average of $\bar{n}_{1,1,1+1}$ and $\bar{n}_{2,1,1+1}$ derived from equations (4.10) and (4.11) is taken.

As an example the results are discussed of sample no 218, a 197 nm, undoped SnO_2 - coating on quartz, measured at $\lambda = 632.8$ nm. First the thickness and the surface roughness have been determined, which resulted in $d = 197$ nm and a negligible surface roughness. Application of an anisotropic model showed that the refractive index is not anisotropic at this wavelength. To investigate the inhomogeneity, a two-layer model is applied with a total thickness of 197 nm, in which the interface between

the two sub-layers is shifted with 10 nm steps through the coating. To reduce the number of parameters which are to be calculated at each position of the interface, the extinction coefficient is calculated with the R-T method and is assumed to be constant through the coating. The results of the calculations are shown in figure 4.8, which consists of three parts: figure 4.8a gives the refractive index in each 10 nm sliver of the coating calculated from equations (4.10) and (4.11). Figure 4.8b gives the value of X_r^2 at each measurement, and it shows that minima occur at 10 and at 170 nm from the coating/substrate interface. Figure 4.8c gives the final refractive index 'profile' in the coating, determined from equations (4.10) and (4.11) with the interface put at 10 and 170 nm from the coating/substrate interface.

With the above mentioned method, in principle the inhomogeneity of the refractive index inside the coating can be determined. However, this requires accurate determinations of Δ and Ψ at many (in the example: 12) different angles of incidence.

The errors made with this method can be estimated from the difference in using equations (4.10) and (4.11) in the calculation of a refractive index in a sub-layer. In the example just given this leads to an absolute error of about 0.05 in the determination of n in the three sub-layers. This means that the differences in the sub-layers as sketched in figure 4.8c are just significant.

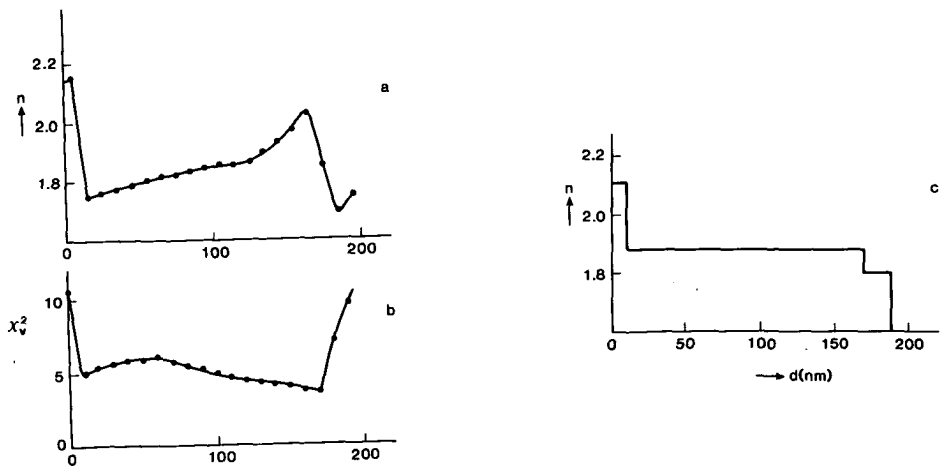


Figure 4.8 a: Refractive index of 10 nm slivers in sample no 218 determined with (4.10) and (4.11). b: Corresponding values of X_r^2 . c: Resulting refractive index profile in the coating.

4.5 Determination of the coating thickness

The coating thickness can be determined by the R-T method and by ellipsometry, as described in sections 4.1 and 4.4. However, even with these methods one needs to have a first estimate of the coating thickness, as the solutions repeat at constant thickness intervals. In this section two more methods to determine the coating thickness are presented. One is related to the R-T method and the other gives a direct measurement of the physical thickness.

4.5.1 Extrema method

The optical thickness, which is defined as $d_{\text{opt}} \equiv n \cdot d$ can be derived from the wavelengths at which reflection minima and maxima occur. Under the assumption that the coating and the substrate are non-absorbing ($k=0$) and n is wavelength-independent, these wavelengths λ_m are given by (Mayer, 1950):

$$\lambda_m = \frac{2d_{\text{opt}}}{N} \quad (4.12)$$

Where λ_m is the wavelength at which a reflection extremum occurs. N is the interference order and is, if the coating refractive index is larger than the substrate refractive index, an integer for a reflection minimum and a half-integer for a reflection maximum. Taking the wavelengths of two successive minima $\lambda_{m,1}$ and $\lambda_{m,2}$, N can be eliminated and the following expression is obtained:

$$d_{\text{opt}} = \left(2 \left(\lambda_{m,2}^{-1} - \lambda_{m,1}^{-1} \right) \right)^{-1} \quad (4.13)$$

This equation is often used to derive the optical thickness. The error due to small uncertainties in the extrema positions and due to a slightly wavelength-dependent coating refractive index is usually about 10 %. However, the error due to a wavelength-dependent refractive index and the error due to an error in the extrema positions can be reduced by at least a factor of five in the following way: The optical thickness found from equation (4.13) is taken as a first approximation. The interference order N of a minimum is calculated from equation (4.12). Now, knowing that N must be an integer, the nearest integer value of N is taken and the inversion of equation (4.12) gives an estimate of the optical thickness at each reflectance minimum.

Table 4.4 Determination of the coating thickness using (4.13) only and the determination using (4.12) with a corrected N .

λ_m (nm) of reflectance minimum	n (envelope method)	$d_{opt} \equiv nd$ (nm) using (4.13)	d_{opt} (nm) corrected with (4.12)	d (nm) using (4.13)	d (nm) corrected
351	1.99		1053		529
408	1.91	1256	1020	644	535
495	1.90	1160	990	609	521
639	1.87	1098	959	583	513
906	1.78	1084	906	592	510

As an example the results for sample no 187 are given in table 4.4. The table shows that the correction procedure gives values which are more consistent at the different wavelengths, and that the values determined with only equation (4.13) are systematically higher, due to the variation of the refractive index, than the values determined with the correction procedure. As a final value for d , the determination at the wavelength where k is smallest is taken (in the example this is at $\lambda = 639$ nm). This leads to $d = 513$ nm, which is in good agreement with the value found using the R-T method. This is not too surprising as fitting the refractive index and thickness to the measured reflectance and transmittance around an extremum implicitly uses an equation like (4.12).

4.5.2 The step method

The most direct way to determine the coating thickness is to remove the coating from part of the substrate and to determine the step at the substrate-with-coating/bare substrate interface with a profilometer.

A SnO_2 or In_2O_3 coating can be partly removed with Zn powder on which a drop of HCl is applied. The height of the step thus formed was measured with a Tencor Alphastep 200 stylus apparatus of the Delft Submicron Technology Center (CST). Figure 4.9 gives a graphical output of the apparatus of a step made in sample no 187. From this figure a coating thickness of 520 ± 20 nm can be derived, which is in good agreement with the results of other methods.

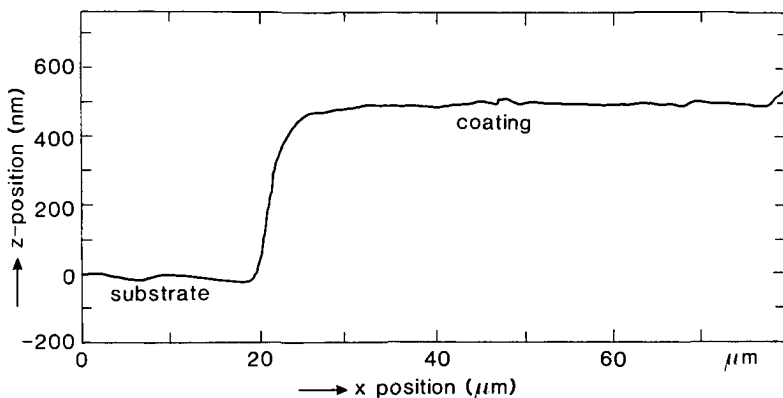


Figure 4.9 Output of the profilometer when crossing the step from the bare substrate to the coating on the substrate of sample no 187.

4.6 Conclusions

In principle the optical constants in the 0.3–40 μm spectral region can be determined with the R-T method and the Kramers-Kronig integration method.

The envelope method gives a slight improvement of the determination of n and k at short wavelengths, but it requires a coating thickness $d > 300$ nm.

The most accurate values can be obtained with ellipsometry and, moreover, it allows also the inhomogeneity and anisotropy in the coating to be determined. With our apparatus, the wavelength range is restricted to 400–2400 nm. Its major drawback is that the method is very time consuming.

The coating thickness can well be obtained from the reflectance and transmittance spectrum using the extrema method or the R-T method. As a check the thickness can be obtained unambiguously with the step method.

5. THE SPRAY PYROLYSIS COATING PROCESS

5.1 Introduction

In this chapter the process and the equipment with which the coatings have been produced are described. The spray pyrolysis process is a process for preparing thin films. The advantages of spray pyrolysis compared to vacuum deposition techniques are the low equipment costs that are involved and the large areas that can be coated. The equipment that has been used to prepare the coatings is described in section 5.2. The principles of the process are discussed in section 5.3. In section 5.4 some coating parameters that are typical for the equipment used are described, including the chemical compounds. Section 5.5 gives the growth rate which is achieved at various process circumstances. The effects of the process parameters on the optical, electrical and structural coating properties are given in chapters 6 and 7.

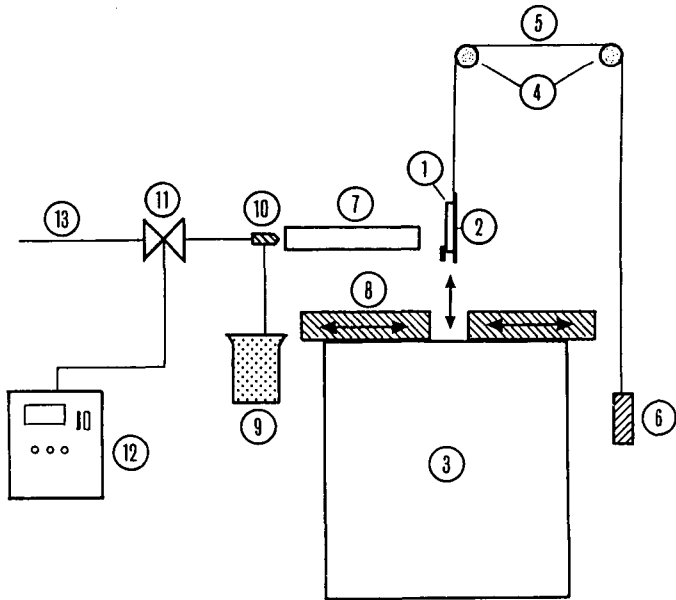
5.2 The spraying equipment

The spraying equipment is schematically sketched in figure 5.1. The substrate is mounted on a metal plate and heated in the oven. When it has reached the oven temperature, the substrate is pulled out of the oven and the solution is sprayed against the substrate. To minimize a large temperature fall of the substrate, the spraying time is limited to a few seconds. To obtain a sufficient coating thickness, the substrate is again put in the oven, heated and sprayed. A number of such heating and spraying cycles has been used in most cases.

Small droplets of the spraying solution are produced with an ultrasonic nozzle (Sonic-Sonicore[®] 125H). The nozzle is depicted in figure 5.2. It is actually an air driven acoustic oscillator that creates a sonic shock wave which shatters the liquid jet, producing very fine droplets in the 5-20 μm diameter range. The carrier gas used is air, nitrogen or oxygen. It is supplied to the nozzle with a pressure between 2 and 10 Bar.

5.3 Film formation by spray pyrolysis

The spray pyrolysis process is basically the thermal/chemical decomposition and oxidation of a dissolved compound which is sprayed against a hot substrate.



1: substrate, 2: metal plate, 3: oven, 4: chain wheels, 5: chain, 6: weight, 7: glazen tube, 8: chain covers, 9: spraying solution, 10: spraying nozzle, 11: valve, 12: timer, 13: gas supply.

Figure 5.1 Schematic lay-out of the spraying equipment.

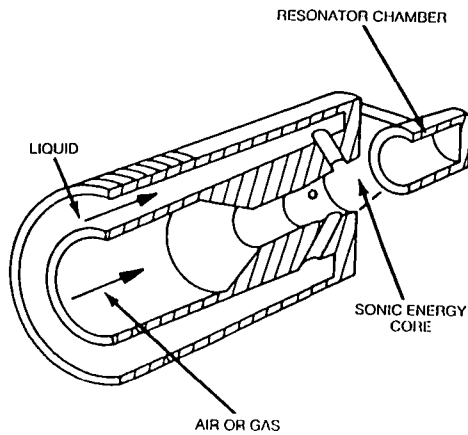


Figure 5.2 Schematic lay-out of the spraying nozzle (Sonicore®)

Little is known of what exactly takes place when a droplet of the solution approaches the hot substrate. It can be assumed that the droplet hits the substrate and evaporates, after which the metal dissolved in the solution precipitates on the surface and oxidizes. Some research into the spray pyrolysis process has been carried out by Siefert (1982, 1984) and by Sears (1988). According to these authors, the 'ideal' process, with an optimum droplet size and substrate temperature would take place as follows:

1. The droplet, containing the coating material dissolved in a solvent, approaches the hot substrate.
2. When reaching the substrate, the droplet does not splash against the substrate, as it is kept away from the substrate by the thermoporetic force and by the vapour which is formed when the droplet is boiling at the substrate side. The temperature of the dissolved material is held almost at the boiling point of the solvent until the solvent is entirely vaporized.
3. The solvent is entirely vaporized short of the substrate, the particle reaches the substrate, is heated up to the substrate temperature and vaporizes.
4. The vaporized particle undergoes the classical Chemical Vapour Deposition (CVD) process, reacts to its final form and is incorporated into the crystal lattice of the coating already present on the surface.

The process can deviate from this ideal case in two ways:

- a. The drop size is too small or the substrate temperature is too high: the reaction already takes place before the substrate is reached and a powdery coating is formed.
- b. The drop size is too large or the substrate temperature is too low: the droplet splashes against the substrate where it locally removes a lot of heat. This temperature decrease adversely affects the reaction kinetics, which results in an inhomogeneous coating.

We have not investigated the process explicitly, but some remarks on this theory can be made:

- A hazy, powdery coating was sometimes obtained in our experiments. We found that this was due to a recirculation of the carrier gas, so material that already reacted to SnO_2 could reach the substrate a second time and form a powdery coating.
- Neither at the highest (650 °C) nor at the lowest temperatures (400 °C) used, a systematical powdery or inhomogeneous coating was formed. This means that a too early reaction (see point a. above) is not observed.

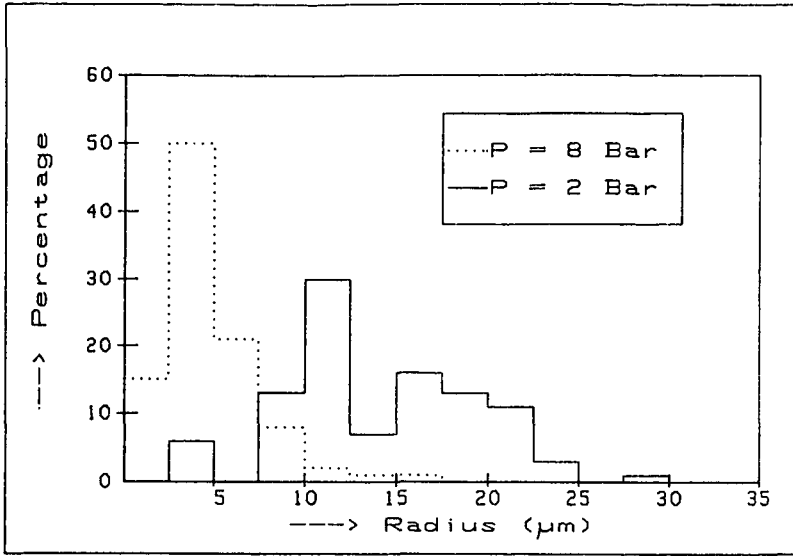


Figure 5.3 Histograms of the droplet radius distribution at two different gas pressures

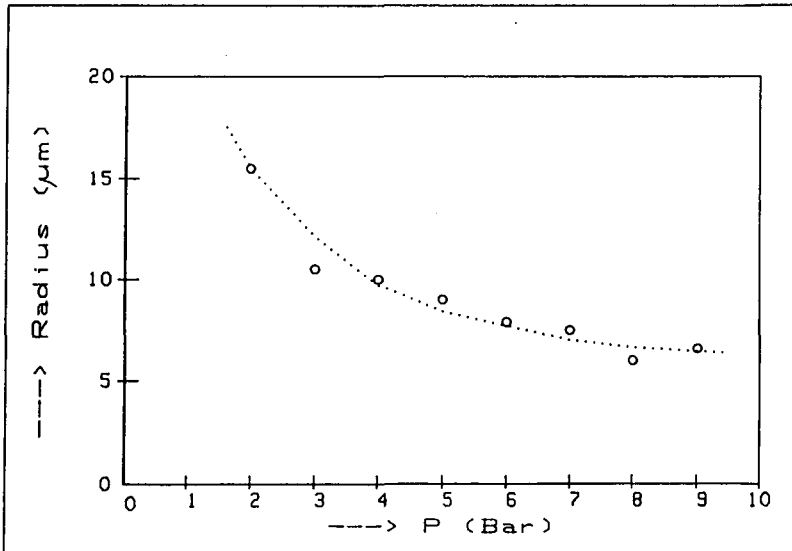


Figure 5.4 Average droplet radius as a function of the gas pressure

This reaction is quite improbable as the evaporation energy needs to be supplied by the substrate, so the reaction cannot take place far away from the substrate. Also a too late reaction (see point b. above) does either not take place, or it does not cause a powdery precipitate on the coating. - When using the ultrasonic spraying nozzle, the coatings were appreciable more homogeneous and reproducible than when using a pneumatic nozzle. This means that the reaction is affected by the drop size and that a narrow drop size distribution favours a homogeneous and reproducible coating.

5.4 The process parameters

5.4.1 Droplet size

The droplet size has been determined by spraying water on a cold glass substrate during a short time (~0.1 sec) and taking a photograph from a short distance. The apparent radii on the photograph are transformed to radii of the initial droplets by assuming a glass/water contact angle of 60° and calculating the radius of the initial droplet. A histogram of the distribution of the droplet radii determined at a gas pressure of 2 and 8 Bar is given in figure 5.3. In this figure it can be observed that the droplet sizes are small (about 10 μm) and are spread in a reasonable narrow distribution around an average value. The dependence of the average droplet size on the gas pressure is illustrated in figure 5.4. In this figure it can be observed that the droplet size tends to decrease with an increasing gas pressure. The droplet sizes and the distributions are similar to the results found by Bladenet (1981), who also investigated the droplet size and the distribution obtained by ultrasonic and pneumatic spraying.

5.4.2 Substrate temperature

A determining factor of the pyrolysis process is the substrate surface temperature during the spraying process. As the temperature at the substrate/air interface is hard to determine with a thermocouple or a Pt-100 element, a Heimann KT-14 radiation thermometer has been used.

As the formation of a coating would change the substrate radiation properties, the substrate surface temperature has been determined while droplets of water are sprayed against the surface. The cold droplets will influence the radiation thermometer output. It has been assumed that a correction can be made for this effect by defining the initial substrate temperature equal to the oven temperature.

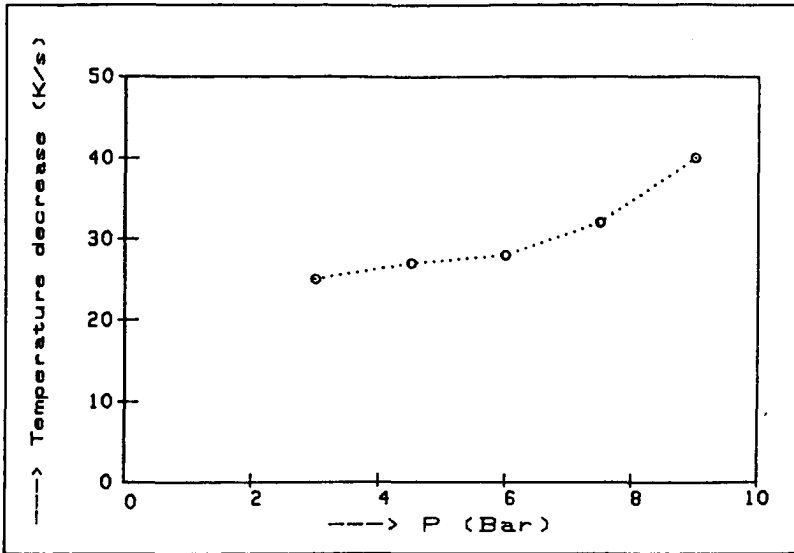


Figure 5.5 Temperature decrease of the substrate as a function of the applied gas pressure

So the radiation thermometer output when the substrate has just left the oven and while it is sprayed, is taken as the output for a substrate at 600 °C. The temperature decrease measured in this way for different gas pressures and for an initial substrate temperature of 600 °C, is given in figure 5.5. In this figure it can be observed that the temperature decrease is about 40 K/s at a maximum flow rate. The reproducibility of these measurements was quite good, but because of the correction for the droplets the error in the values will be about 20 %.

With this method the temperature is not measured exactly at the substrate/air interface, but in the substrate, at a certain distance from the interface. This effective distance δ_{eff} can be estimated by weighting the optical penetration depth $\delta(\lambda)$ (see section 2.2.1, equation (2.19)) with the Planck radiation distribution spectrum $M_b(\lambda, T)$ and the emittance $\epsilon(\lambda) = 1 - R(\lambda)$:

$$\delta_{\text{eff}}(T) = \frac{\int_{\lambda_1}^{\lambda_2} \epsilon(\lambda) \cdot \delta(\lambda) \cdot M_b(\lambda, T) \, d\lambda}{\int_{\lambda_1}^{\lambda_2} \epsilon(\lambda) \cdot M_b(\lambda, T) \, d\lambda} = \frac{\int_{\lambda_1}^{\lambda_2} (1-R(\lambda)) \cdot \frac{\lambda}{4\pi k(\lambda)} \cdot M_b(\lambda, T) \, d\lambda}{\int_{\lambda_1}^{\lambda_2} (1-R(\lambda)) \cdot M_b(\lambda, T) \, d\lambda} \quad (3.1)$$

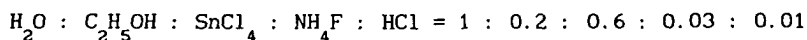
Here $k(\lambda)$ is the extinction coefficient, $R(\lambda)$ is the substrate reflectance spectrum and λ_1 and λ_2 are the lower and upper limit of the spectral sensitivity of the radiation thermometer respectively. For the extinction coefficient the values are taken which are determined at room temperature (see section 4.3, figure 4.4). It is assumed that these values are also valid at 600 °C. The radiation thermometer is sensitive from $\lambda = 2 \mu\text{m}$ to $\lambda = 20 \mu\text{m}$. This gives a value for δ_{eff} of 2 mm. This value is rather high because of the very low extinction coefficient of glass in the 2 - 5 μm spectral region. The effective penetration depth has been greatly reduced by using a filter which only transmits thermal radiation with a wavelength larger than 8 μm . This reduces δ_{eff} to about 3 μm which is fairly close to the surface. The measurements have been performed using this filter, where the radiation thermometer output has been corrected for the missing radiation in the 2-8 μm spectral region.

5.4.3 Chemical solutions used

Four different basic solutions have been used to prepare different coatings: three for the F-doped SnO_2 coatings and one for the Sn-doped In_2O_3 coatings.

1. Tinchloride in water and alcohol with NH_4F as a dopant.

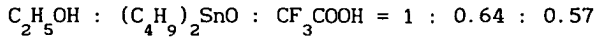
This is the solution used in most of the literature references on tin oxide coatings. Our 'standard' solution of this type is (ratio's by weight):



This gives in the solution an atomic ratio Sn:F of 1:1. The F-doping can be varied by varying the amount of NH_4F in the solution. The advantages of this solution are its cheapness and the easy availability of the components used. Its disadvantages are the fact that an unwanted amount of Cl will be present in the coating and the fact that black enamel is attacked by the HCl which is formed when the SnCl_4 reacts to SnO_2 .

2. Dibutyltin oxide and trifluoroacetic acid in alcohol.

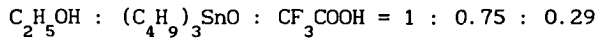
Our standard solution of this type is (ratio's by weight):



This gives an atomic ratio Sn:F of 1:6. The dibutyltin oxide and the trifluoroacetic acid react and in the solution the compound $(\text{C}_4\text{H}_9)_2\text{Sn}(\text{CF}_3\text{COO})_2$ is formed (Peruzzo, 1974). The F-doping may be varied by varying the amount of CF_3COOH , but when this amount is decreased, the ethanol must be replaced by acetic acid as dibutyltin oxide does not dissolve in alcohol.

3. Tributyltin oxide and trifluoroacetic acid in alcohol

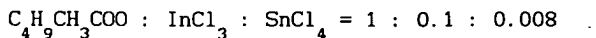
A typical solution of this kind is:



This gives an atomic ratio Sn:F of 1:3 in the solution. The tributyltin oxide and the trifluoroacetic acid react and in the solution the compounds $(\text{C}_4\text{H}_9)_3\text{Sn}(\text{CF}_3\text{COO})$ and water are formed (Peruzzo, 1974). As the reaction is quite exothermic, the tin- and fluorine compounds must be mixed drop by drop. The fluorine content of the solution can be varied by varying the amount of CF_3COOH .

4. Indium chloride in butylacetate with tin chloride as a dopant

The basic solution is:



The doping can be varied by varying the amount of SnCl_4 in the solution. In the literature, often a solution of InCl_3 in water and alcohol is used, but in our attempts to make such solutions the InCl_3 precipitated in the solution, so these solutions have not been used.

5.4.4 The gas and liquid flows in the spraying process

The flow rate of the gas with which the droplets are atomized is about $4.7 \cdot 10^{-3} P$ (m^3/s), where P is the pressure (in Bar) applied to the atomizer. The flow rate of the liquid sprayed is slightly dependent on the applied pressure and the solution used. For solution no 3 it ranges from 0.8 g/s for $P = 2$ Bar to 1.9 g/s for $P = 12$ Bar.

5.5 Film growth

The film growth which actually takes place when producing coatings using the methods as described in the previous section, has been investigated in several ways.

The main factors which determine the film growth are the substrate temperature and the chemical compound which is used. A number of coatings have been produced with the different solutions at different substrate temperatures. The spraying time was 2 seconds per heating/spraying cycle and the gas pressure was 2.5 Bar. The number of spraying cycles varied from two to four between the solutions, but this does not give large differences as the film growth proves to be independent of the coating that is already present on the substrate (see figure 5.8). The film growth is expressed in nm/s and is calculated from the coating thickness divided by the total spraying time (=number of cycles \times the spraying time per cycle). The results are plotted in figure 5.6. The figure shows that the fastest film growth can be achieved with solution no 2, but the temperature dependence of the film growth is also largest when using this solution.

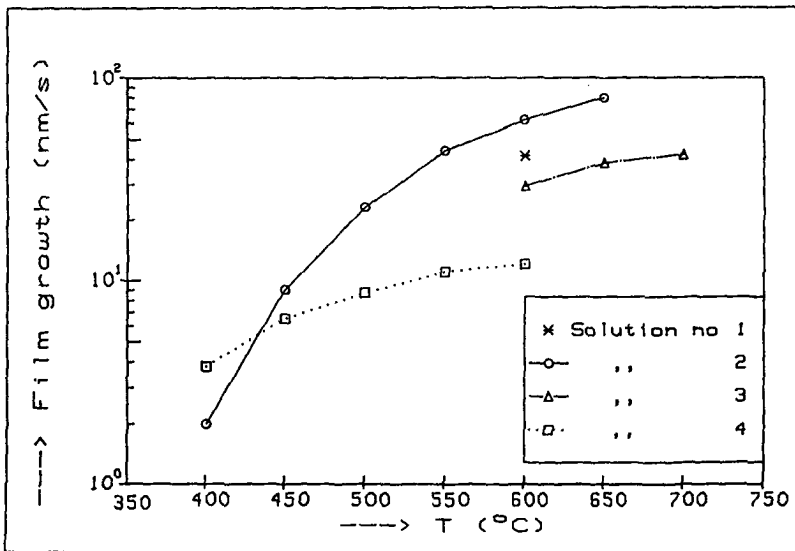


Figure 5.6 Film growth rate as a function of the initial substrate temperature for the different solutions

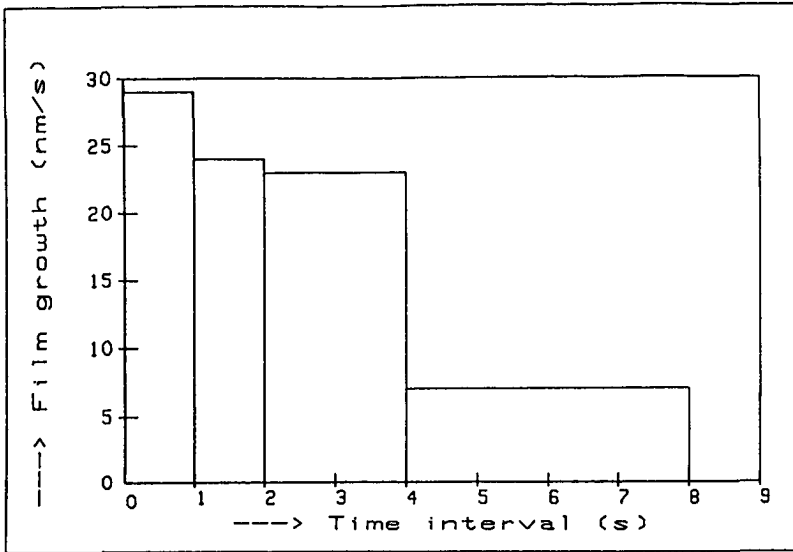


Figure 5.7 Average film growth rate in different time intervals from the beginning of the spraying process

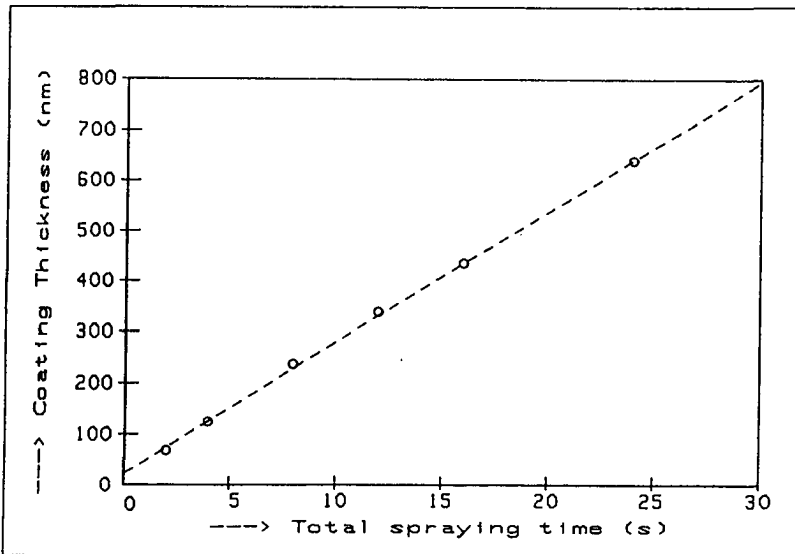


Figure 5.8 Coating thickness as a function of the total spraying time

The time dependence of the film growth during one spraying cycle has been investigated by producing coatings with the same total spraying time (8 seconds), with a different spraying time per cycle, being 1, 2, 4 or 8 seconds. From the difference in thickness between the samples, the average film growth speed in the successive time intervals 0-1, 1-2, 2-4 and 4-8 seconds can be found. The result is given in figure 5.7. In this figure it can be observed that the speed of film growth drops rapidly for a spraying time of more than about 3 seconds. This is caused by the cooling of the substrate during the spraying process (see section 5.4.2), which is determined indirectly in this way.

The dependence of the film growth on the film already present on the substrate has been investigated by producing a series of coatings with an increasing coating thickness. The coatings were produced on pyrex with solution no 3 with nitrogen at a pressure of 2.5 Bar as the carrier gas. The substrate temperature was 600 °C. The coatings were sprayed in cycles of two seconds each; the different coating thicknesses were achieved by variation of the number of cycles from 1 to 12. Figure 5.8 gives the coating thickness as a function of the total spraying time. From this figure it can be derived that during the first spraying cycle, in which the film growth rate is 34 nm/s, the film grows slightly faster than during the following cycles. In these cycles the film grows at a constant rate of (25.9 ± 0.3) nm/s. The latter value is determined from a least-squares fit through the measured points. This fit is also shown in the figure.

5.6 Sample preparation and reproducibility

In most cases the coatings are produced on 10 x 10 cm substrates of quartz, pyrex, black enamelled steel or window pane. The substrate thickness ranges between 1 for the steel, to between 2 and 4 mm for the quartz, pyrex and window pane. The samples of which the properties are determined are discs with a 28 mm radius which are sawn out of the substrate. In order to derive any conclusion on the effects of the spraying conditions, the doping effects, etc., it is necessary that the process shows a good reproducibility, i.e. the sample properties of two coatings produced under equal circumstances should be equal and also independent of the area on the substrate from which the sample is sawn.

The reproducibility of the process has been checked by comparing the properties of samples produced under equal circumstances, as well as the properties of coatings sawn from different areas of the substrate. It proved that the scattering of the sample properties when the coatings are sprayed under equal circumstances is about equal to the scattering of the properties between samples taken from different areas of the substrate. The reproducibility proved to correlate to the temperature-sensitivity of the film formation process (see section 5.4.2) in the sense that a larger temperature-sensitivity leads to a poorer reproducibility. This indicates that the reproducibility is mainly determined by the reproducibility of the substrate temperature during the spraying process. The standard deviation of properties like coating thickness, electron density and electron mobility is about 10% of the average value for solution no 2. For the other solutions, which show a smaller temperature dependence of the properties, the standard deviation is usually 5% or less of the measured values. This standard deviation must be taken into account when comparing coating properties as is done in this chapter and in chapters no 6 and 7.

6. TINDIOXIDE COATINGS

6.1 Introduction

In this chapter the properties of tin dioxide (SnO_2) coatings are discussed. In section 6.2 the more general properties of SnO_2 , with only an indirect impact on the spectrally-selective properties, are described. The physical effects of doping a coating with fluorine are discussed in section 6.3, the effects of varying the coating thickness are discussed in section 6.4 and in section 6.5 the influence of various process parameters, such as the substrate temperature and the carrier gas pressure, is discussed. The effects of annealing and ageing on the coating properties are discussed in sections 6.6 and 6.7. Section 6.8 gives the results of ellipsometric measurements on a number of coatings. In section 6.9 the contribution of lattice oscillations to the dielectric constant is analyzed quantitatively. The results of the former sections are summarized in section 6.10, which gives a full quantitative description of the dielectric constant and where an attempt is made to derive basic relations between the electrical and structural properties of tin oxide coatings. Finally, section 6.11 gives a discussion on the solar absorptance and thermal emittance which can be achieved using tin dioxide coatings.

6.2 General properties of Tin oxide (SnO_2)

Tin oxide has a rutile type crystal structure. Its lattice parameters are: $a = 4.75 \text{ \AA}$ and $c = 3.19 \text{ \AA}$ (Jarzebski, 1983). The unit cell contains six atoms: two Tin and four Oxygen as illustrated in figure 6.1, which is taken from Jarzebski (1976). The specific density is $6.95 \cdot 10^3 \text{ kg/m}^3$, and its hardness on the Moh scale is about 7.8, which is even slightly more than the value of glass. This high hardness is one of the main advantages of tin dioxide coatings over other spectrally selective materials. The melting point is about 1630°C . The refractive indices at $\lambda = 589.3 \text{ nm}$ are 1.997 and 2.093 measured along the a -axis and c -axis respectively (Wheast, 1985). Band structure calculations have been carried out by Robertson (1979). From these calculations a direct band-gap of about 5 eV has been found.

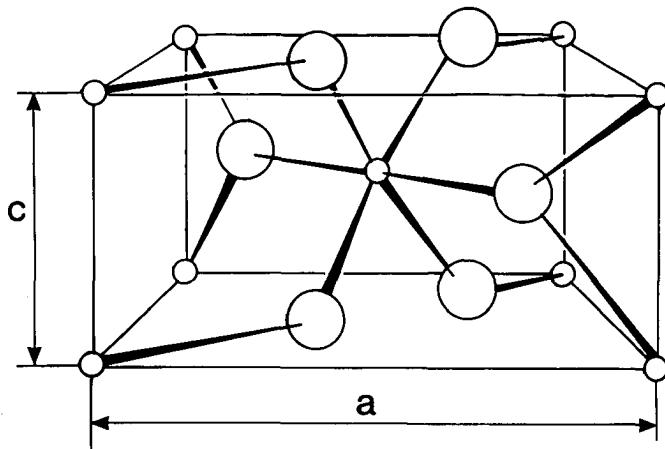


Figure 6.1 Unit cell of the crystal structure of SnO_2 . The large circles indicate Oxygen atoms and the small circles indicate Tin atoms

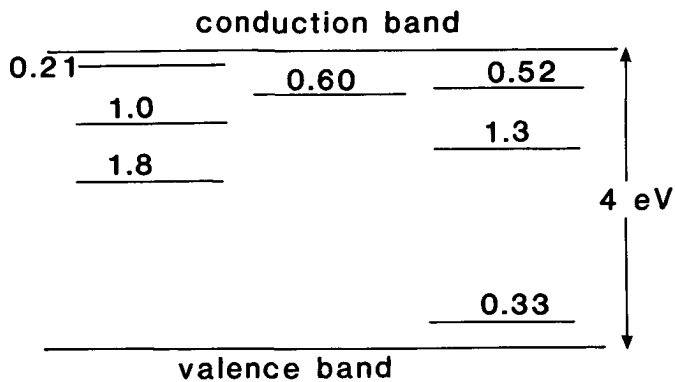


Figure 6.2. Proposed energy level scheme for grown stannic oxide single crystals.

Houston and Kohnke (1965) have analyzed the scheme of energy levels in SnO_2 -single crystals with a photoelectric method. Figure 6.2 is a schematic representation of the distribution of the trapping levels in SnO_2 . The distance of the highest lying trapping level from the bottom of the conduction band for the electrons is 0.21 eV. The band-gap determined by Houston and Kohnke is 4 eV.

The static dielectric constant has been determined by Summitt (1968) and van Daal (1968), who both obtain values of $\epsilon_s = 12$ for \vec{E} parallel to the a-axis and $\epsilon_s = 9.4$ for \vec{E} parallel to the c-axis.

The Debije-temperature, which is an important parameter as it is related to scattering by acoustical phonons, has not been reported in literature, but a reasonable first estimate can be made by taking the literature-value of an oxide with the same crystal structure as SnO_2 : TiO_2 . For TiO_2 , a literature value for θ_D of 760 K has been found (Gray, 1972). An other estimate can be made by using the values for the temperature-dependent heat capacity $c_v(T)$ as given in the handbook of Landolt-Börnstein (1961). For a theoretical curve of $c_v(T)$ the Debije-expression is used with an additional term for the electronic contribution for the specific heat:

$$c_v(T) = 9Nk_B \left(\frac{T}{\theta_D} \right)^3 \int_0^{\theta_D/T} \frac{x^4 e^x}{(e^x - 1)^2} dx + \Theta T \quad (6.1)$$

Here N is the number of ions per mole, k_B is Boltzmann's constant, θ_D is the Debije temperature and Θ is the electronic constant. When fitting θ_D and Θ in (6.1) to the literature-values of c_v , $\theta_D = 720 \pm 20$ K and $\Theta = (9.2 \pm 0.4) \cdot 10^{-3}$ J/Mol K^2 are obtained. Figure 6.3 gives the used literature-values of c_v together with the least-squares fit. This figure shows that equation (6.1) can describe the temperature-dependence of c_v quite well. An exact correspondence should not be expected because of the approximations made in the Debije model. The resulting value of θ_D is reasonably close to the literature value of TiO_2 .

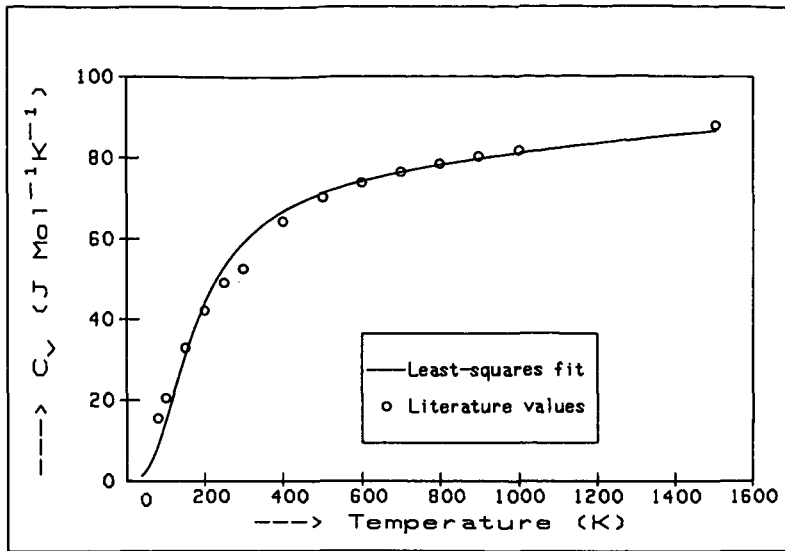


Figure 6.3 Literature-values of the c_v of SnO_2 with a least-squares fit to equation (6.1).

Table 6.1 Preparation conditions of coatings used for studying the effects of doping concentration.

sample no	substrate	substrate temperature ($^{\circ}\text{C}$)	spray cycles	cycle time (s)	solution no	F:Sn ratio in sol.	coating thickness(nm)
310	pyrex	600	4	2	1	1.0	328
312	4	2	1	0.0	370
314	4	2	1	0.70	333
316	4	2	1	0.50	344
318	4	2	1	0.25	353
320	4	2	1	1.50	315
198	quartz	600	4	2	2	4.35	509
200	..	600	4	2	2	9.12	465
202	..	650	4	2	2	0.92	1065
203	..	650	3	2	2	6.33	640
204	..	650	3	2	2	2.67	590
218	..	600	1	2	2	0.0	194
219	..	650	1	1.5	2	6.33	118

6.3 Physical effects of doping with Fluorine.

6.3.1 Preparation conditions

A series of coatings has been produced with solution no 1 (see section 5.4.3), with increasing Fluorine-doping. The coatings were sprayed on 2 mm pyrex substrates at a substrate temperature of 600 °C. This series has been used to study the effect of doping on the infrared-optical constants and on the electrical, structural and morphological properties.

Also a series of coatings on 2 mm quartz substrates has been produced using solution no 2. As quartz is transparent in the near UV-region, this series has been used to study the optical band-gap of SnO₂. Because of the optical flatness of the quartz-substrates, also ellipsometric measurements could be carried out on this series. The spraying conditions are summarized in table 6.1, together with the atomic F:Sn ratio in the solution and the coating thickness obtained.

6.3.2 Infrared optical properties

The measured near-normal reflectance in the 1-25 μm spectral region and the normal transmittance in the 1-2.5 μm spectral region for the samples with a F:Sn ratio of 0, 0.25, 0.50 and 1.00 in the spraying solution are given in figure 6.4. The transmittance for λ > 2.5 μm could not be measured as the substrate becomes opaque for λ > 3 μm. In figure 6.4 it can be observed that the highly-doped coating is more absorbing for λ < 2.5 μm, and is more reflecting in the thermal IR-region as compared to the other samples. As the plasma-wavelength decreases with increasing electron density, this is to be expected considering the discussion as given in sections 2.3 and 2.6.1.

The reflectance peak at λ = 9 μm originates from the substrate; the peaks at λ = 16 μm and λ = 21 μm originate from molecular resonances in the SnO₂ crystal. This will be discussed further in section 6.9.

The optical constants n and k, determined using the combination of the R-T method with a Kramers-Kronig analysis as discussed in chapter 4, are given in figure 6.5 for the coatings with a 0.25 and 1.5 F:Sn ratio in the spraying solution. The similarity of this figure and figure 2.8 can clearly be observed. From the n(λ) and k(λ) values, $\tilde{\epsilon}(\lambda)$ and $\tilde{\rho}(\lambda)$ are calculated using equations (2.16) and (2.58). For ϵ_{∞} a value of 4.0 has been taken. As will be shown in section 6.9 this is a satisfactory estimate in most cases.

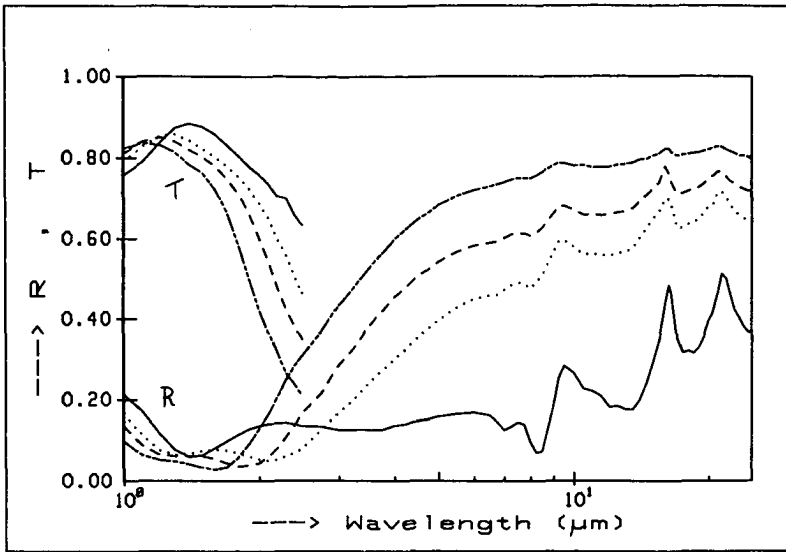


Figure 6.4 Reflectance and Transmittance of samples 312 (with F:Sn ratio 0.0, —), 318 (ratio=0.25, ···), 316 (ratio=0.50, --) and 310 (ratio=1.0, —·—).

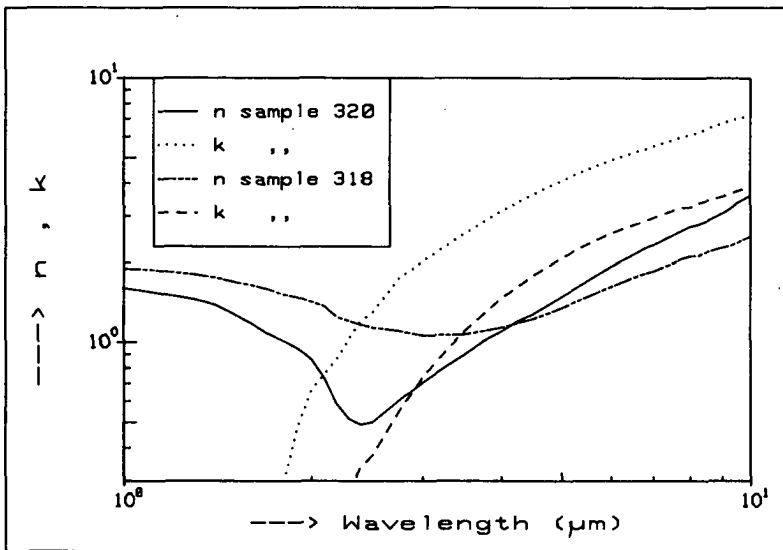


Figure 6.5 Optical constants of samples no 318 and 320

For each sample, the plasma wavelength is calculated from the complex part of $\tilde{\rho}(\lambda)$ in the 3-8 μm spectral region using equation (2.79). The error in the average value is about 5%. The plasma wavelength is an essential parameter when comparing electrical and optical properties, as is done in the next section.

6.3.3 Comparison of optical properties with electrical properties determined at room temperature.

The electrical properties n_- and μ have been determined at room temperature. The effective mass is calculated from the electron density and the plasma wavelength using equation (2.56) :

$$m_{\text{eff}} = \frac{n_-}{\epsilon_0 \epsilon_\infty} \left(\frac{2\pi c e}{\lambda_p} \right)^2 \quad (6.2)$$

The error in m_{eff} is about 10% because of the error in λ_p . We find values for m_{eff} in the range from 0.1 to 0.35 electron mass. The resistivity $\rho_{\text{DC}} = (n_- e \mu)^{-1}$ can be compared directly to the real part of $\tilde{\rho}$. A theoretical calculation of $\tilde{\rho}(\lambda)$ can be made where n_- and m_{eff} are used as input-parameters, based on the modified Gerlach-Grosse theory, as discussed in section 2.4.1. This calculation also gives an upper limit of μ_{DC} which is called μ_{max} . Figures 6.6a, b and c give the measured and calculated values of $\tilde{\rho}$ for the coatings sprayed with solutions having F:Sn ratio's of 1.0, 0.5 and 0.0 respectively. In these figures λ_p and ρ_{DC} are also indicated. In figure 6.6 one can observe that the SnO_2 resonances also affect the ρ_r and ρ_c values around 16 and 21 μm . The measured values of ρ_c follow the calculated curves well for $1 \mu\text{m} < \lambda < 10 \mu\text{m}$. The measured ρ_r accords well with the measured DC-values for samples 310 and 316, but not for the undoped sample 312. The calculated curve of ρ_r is shifted downward relative to the measured curve, which means that the theoretical lower limit for ρ_r has not been achieved. However, this difference is quite small for sample 310. For $\lambda < \lambda_p$, in the measured curves of ρ_r a similar power-law dependence as in the calculated curves, which are calculated according to the theory of ionized impurity scattering, is observed. The Drude-theory predicts a wavelength-independent ρ_r . This power-law dependence has also been observed by Frank (1983), who concludes from this base that ionized impurity scattering is the main damping mechanism.

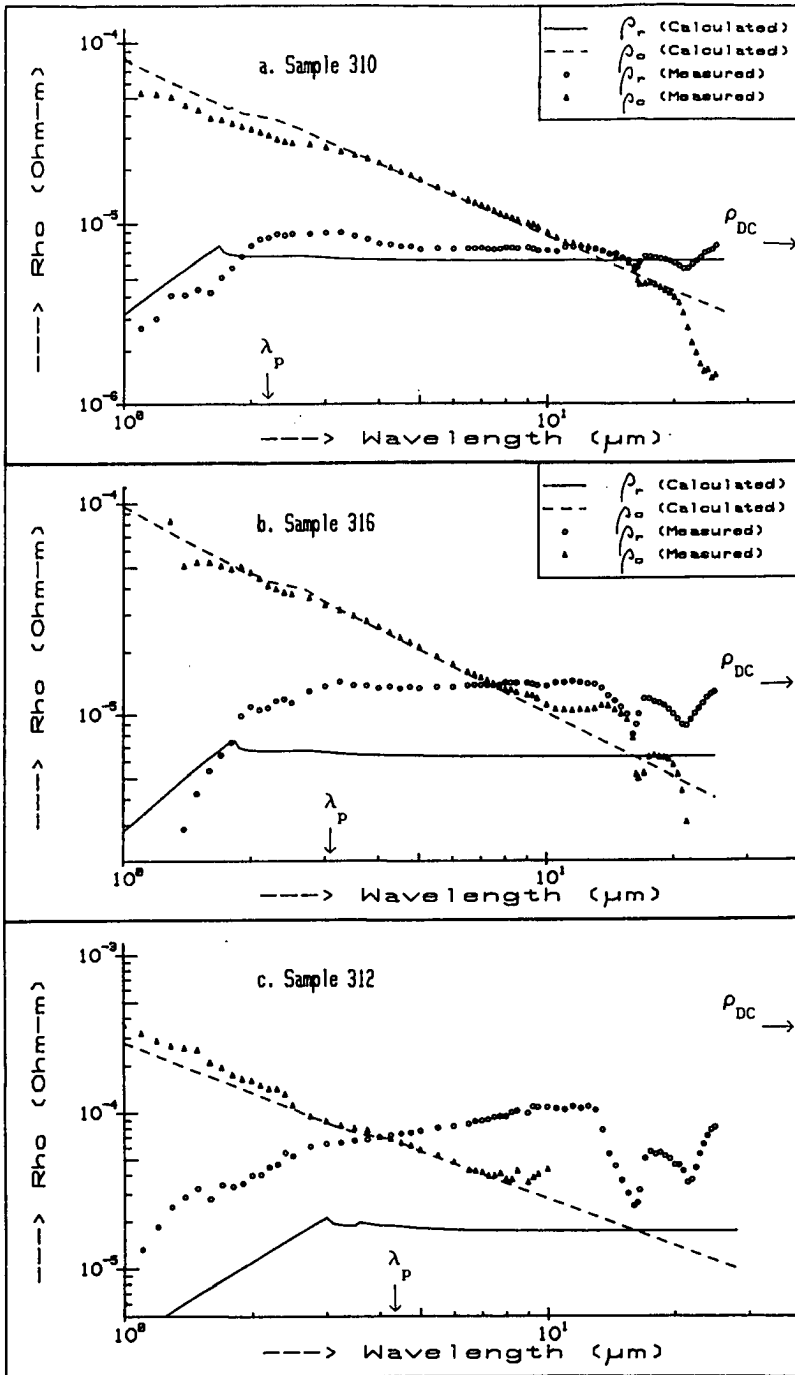


Figure 6.6 Measured and calculated real and complex part of $\tilde{\rho}$
a: F:Sn = 1.0; b: F:Sn = 0.5; c: F:Sn = 0.0 in the solution

The difference between ρ_{DC} and ρ_r can also be expressed by defining an 'optical' mobility :

$$\mu_{opt} = (n_- e \rho_r (\lambda=8\mu m))^{-1} \quad (6.3)$$

ρ_r is taken at $\lambda = 8 \mu m$ for practical reasons: at this wavelength the optical constants can be obtained accurately and from this wavelength region up to $\lambda = \infty$, ρ_r is nearly constant. Table 6.2 gives the electrical properties together with m_{eff} and μ_{opt} as derived from the optical properties. In this table it can be observed that m_{eff} increases with increasing electron density. This increase has also been observed by Shanthi (1980-2), who has found that m_{eff} increases from 0.10 to 0.27 for Sb-doped SnO_2 -films and to 0.33 for F-doped films. The effective mass obtained by other authors is usually in this range. The increase of m_{eff} with increasing n_- indicates that the conduction band will not be parabolic.

For doped coatings, μ_{opt} roughly equals μ_{DC} . This has also been observed by Frank (1983) and, indirectly, by Simonis (1979). For the undoped coating μ_{DC} is much lower. An explanation for this could be the occurrence of grain-boundary scattering which will affect the DC-mobility rather than the optical properties.

Table 6.2 Electrical and optical properties determined at room temperature

sample	n_- ($\cdot 10^{26}/m^3$)	μ_{DC} (cm^2/Vs)	λ_p (μm)	m_{eff} ($\cdot m_e$)	μ_{opt} (cm^2/Vs)	μ_{max} (cm^2/Vs)
312	0.23	6.0	4.3	0.10	~27	319
318	1.04	27.1	3.1	0.22	28	77
316	1.57	28.2	2.6	0.24	29	62
314	2.13	36.1	2.4	0.27	36	50
310	2.33	38.4	2.4	0.30	37	43
320	2.47	37.0	2.2	0.28	36	47

Both n_- and μ_{DC} increase with increasing Fluorine concentration in the spraying solution. The increase in n_- is to be expected, but the increase of μ is the opposite of what is to be expected according to the Gerlach-Grosse theory. This increase of μ with n_- has also been observed by Koch (1963), Fantini (1986) and Agashe (1988), but not by Frank (1983). A further discussion of this effect is given in section 6.10.2.

For the highly doped samples no 310, 314 and 320, μ_{DC} approaches μ_{max} closely. This, together with the wavelength dependence of ρ_r , indicates that in these coatings ionized impurity scattering is the main damping mechanism.

6.3.4 Temperature dependence of electrical properties

The free electron density n_- and mobility μ have been measured from $T = 80$ to $T \cong 450$ K as described in section 3.4.

6.3.4.1 The free electron density

The electron density increased about 7% for the undoped and ~ 1% for the heavily doped samples when the temperature was varied from 80 to 450 K. This small variation has also been found by de Waal (1981) and by Shanthi (1980-2) for Sb-doped tin oxide coatings. The parameters E_d and N_d in the model described in section 2.5 were fitted to the measurements. The resulting donor density N_d and donor energy level E_d are given in table 6.3. In this table it can be observed that N_d and $|E_d|$ increase with increasing electron density. The errors in N_d and E_d are typically 1% or less, but in this calculation a possible systematic error in $n_-(T)$ is not taken into account. The model described in section 2.5 has also been used by Marley (1965) for SnO_2 single crystals with electron densities which are a factor of 1000 smaller than in our case. Marley also finds that the model can successfully be applied to the measurements and finds positive values for E_d , as the electron statistics is non-degenerate at such low doping levels.

Table 6.3 Donor density and donor energy level.

sample number	312	318	316	314	310	320
n_- (T=300 K)	0.237	1.04	1.57	2.13	2.33	2.47
N_d ($\cdot 10^{26}/m^3$)	0.416	2.76	4.13	6.20	7.16	7.68
$- E_d$ (eV)	0.359	0.365	0.436	0.476	0.454	0.506

The model given in section 2.5 proved to describe the temperature dependence of n_- in the 80-450 K temperature range very well in all cases with only two parameters: E_d and N_d . However, because of the crude assumptions made in deriving the model of section 2.5, the physical significance of E_d and N_d is questionable. This is also because the E_d values are negative, which means that the energy levels are inside the conduction band. The E_d values proved to be close to the Fermi energy. This is because E_d needs to be about equal to E_F (see equation 2.98) to obtain only a slight temperature dependence of $n_-(T)$. This leads to $N_d \approx 3n_-$, as is observed in table 6.3.

6.3.4.2 The mobility

Figure 6.7 gives a plot of the mobility as a function of temperature for the different samples. In this figure it can be observed that the mobility of the doped coatings decreases with temperature, but the mobility of the undoped sample 312 increases with temperature.

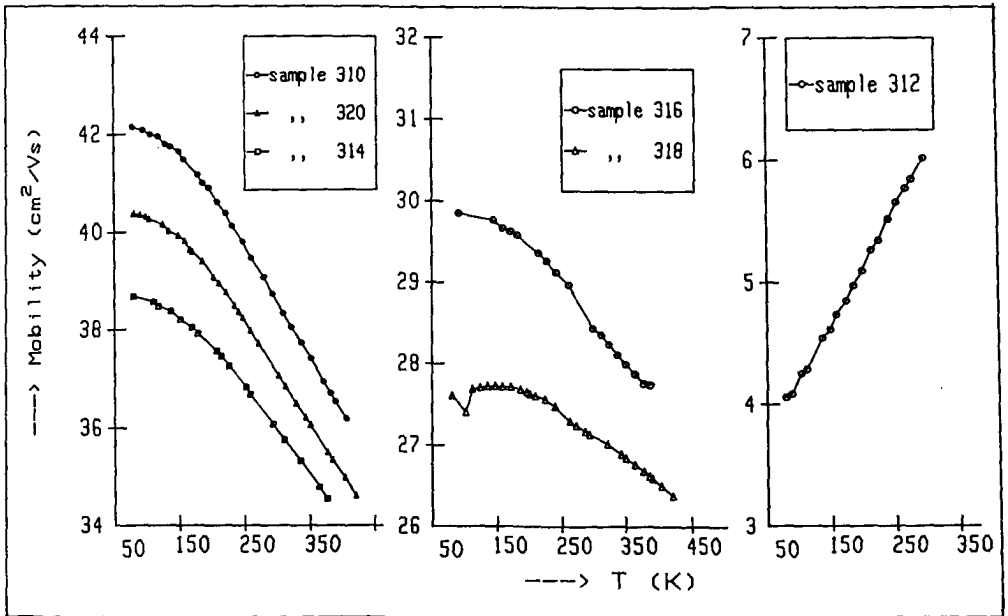


Figure 6.7 Mobility as a function of temperature

The temperature dependence of the samples having a high mobility cannot be explained by ionized impurity scattering as, according to equation (2.72), the only temperature dependent factor is n_- , which is nearly constant as shown in the previous section. The scattering mechanisms which may account for the temperature dependence are the scattering by acoustical phonons and the scattering by optical phonons. When using equation (2.97) for combining a constant mobility μ_0 with a mobility as is found for optical or acoustical phonon scattering, the following equations hold for the resulting mobility μ_{eff} :

$$\mu_{eff}^{-1} = \mu_0^{-1} + \frac{c_a}{\theta_R} \left(\frac{T}{\theta_R} \right)^5 \int_0^{\theta_R/T} \frac{z^5}{(e^z - 1)(1 - e^{-z})} dz \quad (6.4)$$

with c_a a constant and θ_R the characteristic temperature of acoustical phonon scattering, and

$$\mu_{eff}^{-1} = \mu_0^{-1} + c_{10} T^{-1} \sinh^{-2} \left(\frac{\theta_{10}}{2T} \right) \quad (6.5)$$

with c_{10} a constant and θ_{10} the characteristic temperature for longitudinal optical phonon scattering. When fitting the values of μ_0 , θ_R and c_a in (6.4), and μ_0 , θ_{10} and c_{10} in (6.5) to the measured mobilities, it appears that both (6.4) and (6.5) can be fitted about equally well to the measured data. However, the value of θ_R should have about the same magnitude as the Debye-temperature θ_D of SnO_2 . The values for θ_R obtained from the fit are 1096 ± 9 , 1106 ± 17 and 1084 ± 6 K for sample 310, 314 and 320 respectively. These values are internally consistent, but differ considerably from the value of θ_D as obtained in section 6.2. Therefore the occurrence of only acoustical phonon scattering is rejected, but it should be noted that a combination of acoustical and optical phonon scattering can not be excluded fully. A further argument might be that, according to Marley (1965), acoustical lattice scattering would be negligible because the structure of SnO_2 is centrosymmetric.

Figure 6.8 shows the measured mobility of samples 310, 320 and 314, together with the theoretical curves according to (6.5). The figure shows that the fit follows the measurements perfectly.

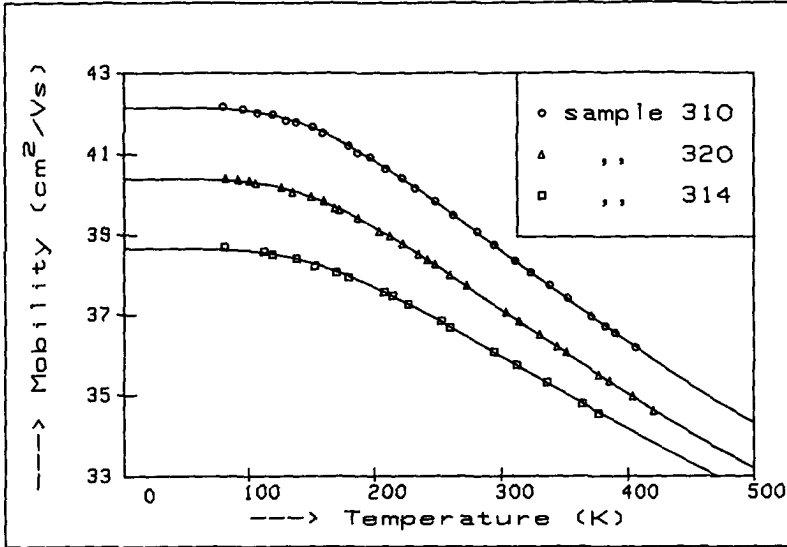


Figure 6.8 Measured mobilities with fits to equation (6.5)

Table 6.4 gives the parameters in equation (6.5) resulting from a least-squares fit to the measurements for the samples with a decreasing mobility with temperature. The constants derived from the measurements of samples 316 and 318 are less accurate, because the temperature dependence becomes less when μ_0 decreases. This makes the determination of θ_{10} and c_{10} more sensitive to experimental errors and to a possible temperature dependence of the Hall scattering factor r , which might deviate from unity for slightly doped samples. The values of θ_{10} are higher than the value obtained by Marley (1965), who obtains $\theta_{10} \approx 500$ K for single crystal tindioxide.

Table 6.4 Constants describing the temperature-dependence of the mobility

sample number	310	320	314	316	318
μ_0 (cm ² /Vs)	42.16±0.11	40.33±0.13	38.62±0.15	29.8±0.2	27.7±0.2
θ_{10} (K)	842±6	836±6	839±12	896±43	1200±500
c_{10} (10 ⁴ VsK/m ²)	2.36±0.04	2.31±0.04	2.08±0.08	2.37±0.1	5.4±0.5

The values of μ_0 in table 6.4 should be compared to the theoretical upper limit given in table 6.2, rather than the mobility measured at room temperature which is also given in this table. This gives a difference in the sense that μ_0 from table 6.4 closer approaches the theoretical limit; in the case of sample 310 the theoretical limit even seems to have been reached.

The increasing mobility with temperature of the undoped sample 312 can be explained by grain boundary scattering, which is in agreement with the observed difference between electrical and optical properties. As the mobility of sample 312 will also be determined by impurity and lattice scattering, the mobility due to grain boundary scattering μ_{gb} can be obtained by correcting for the mobility due to impurity- and optical phonon scattering μ_{i+lo} in the following way:

$$\mu_{gb}^{-1} = \mu_{\text{measured}(312)}^{-1} - \mu_{i+lo}^{-1} \quad (6.6)$$

For μ_{i+lo} the mobility of sample 318, with a low dopant concentration, has been taken, as this mobility about equals the optical mobility of sample 312 and it can be assumed that the temperature-dependence of μ_{i+lo} of sample 312 is equal to that of the electrical mobility of sample 318. This correction has no large effects on the temperature dependence of μ_{gb} compared to the uncorrected mobility of sample 312.

The models for grain boundary scattering as discussed in section 2.4.4 leads to a temperature dependence of the form :

$$\mu_{gb} = c_g \cdot T^{-1/2} \cdot \exp(-\phi_g/kT) \quad (6.7)$$

for the model which is often used in the literature, and

$$\mu_{gb} = c_g \cdot T^{-1} \cdot \exp(-\phi_g/kT) \quad (6.8)$$

for the model where a correction has been made for the degeneracy of the electron statistics. In equations (6.7) and (6.8), c_g is a constant and ϕ_g is the grain boundary potential. In figure 6.9 $\ln(\mu_{gb} \sqrt{T})$ is plotted against T^{-1} (to check whether equation 6.7 applies) and in figure 6.10 $\ln(\mu_{gb} T)$ is plotted against T^{-1} (to check whether equation 6.8 applies). In the case of a constant ϕ_g , figure 6.9 or 6.10 should show a straight line, which is clearly not observed.

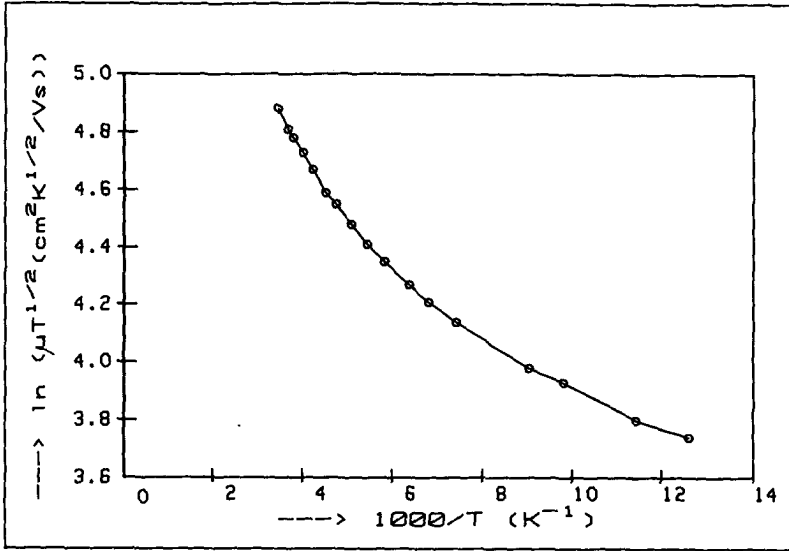


Figure 6.9 Plot of $\ln(\mu_{gb} \sqrt{T})$ against T^{-1} for sample 312.

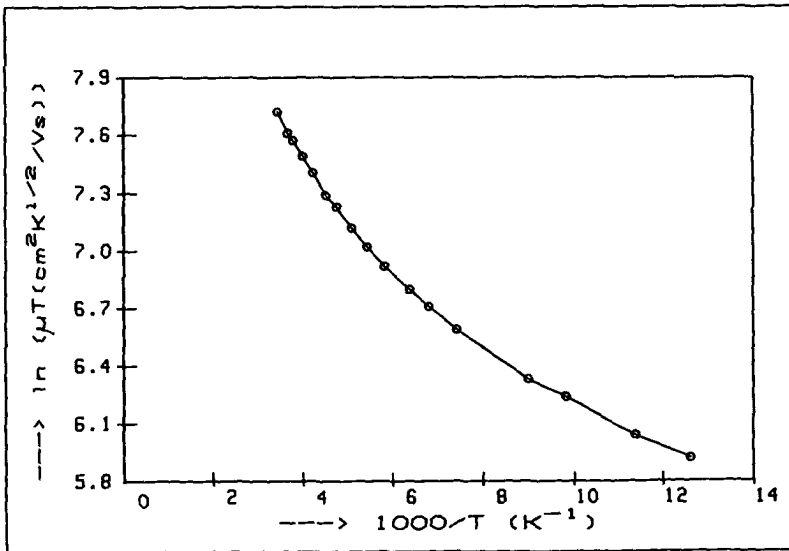


Figure 6.10 Plot of $\ln(\mu_{gb} T)$ against T^{-1} for sample 312.

When assuming that equation (6.7) is valid with a temperature-dependent ϕ_g , a decrease of ϕ_g with decreasing temperature is observed, which is to be expected considering the discussion as given in section 2.4.4. However, as the \sqrt{T} term influences the product $\mu_{gb}\sqrt{T}$ as much as the change in μ_{gb} over the temperature range, we think that (6.7) is too inaccurate to derive quantities such as the barrier gap height and the grain size. The same applies to equation (6.8) and figure 6.10.

Nevertheless, the increase of μ with temperature, together with the difference between 'optical' and electrical mobility are sufficient arguments to conclude that grain boundary scattering is the main damping mechanism for the electrical mobility in the undoped sample 312.

6.3.5 X-ray diffraction measurements

In table 6.5 the results of X-ray diffraction measurements are given.

Table 6.5 results from X-ray diffraction measurements.

sample no	Relative Intensity						randomly oriented SnO ₂
	312	318	316	314	310	320	
crystal plane							
(110)	19	18	21	20	34	21	100
(101)	<5	<5	<6	<5	9	<6	80
(200)	100	100	100	100	100	100	25
(211)	8	8	9	7	12	9	65
(002)	<5	<5	<6	<5	<7	<6	8
(310)	21	19	23	18	24	21	14
(301)	6	8	12	7	13	10	16
Grain size (nm)							
(110)	20	20	23	18	23	23	
(101)					18		
(200)	33	33	33	33	33	37	
(211)	25	25	25	25	30	25	
(310)	21	19	23	18	24	21	
(301)	6	8	12	7	13	10	

The intensity measurements are given relative to the highest peak in each diffractogram, which is defined as '100'. The intensity of the (200) peak varied a little between the diffractograms, according to the thickness differences between the coatings. The intensity measurements indicate a strong orientation in the (200) direction of the crystallites for all samples. In terms of the unit cell shown in figure 6.1, this means that more crystallites than expected from a random orientation distribution are oriented with the a-axis perpendicular to the substrate.

A preferential orientation in the (200) direction has been observed by several authors (Iida, 1988; Bélanger, 1985; Agashe, 1988; Hecq, 1973; Fantini, 1986 and Srinivasa Murty, 1983), but we, as well as some of the mentioned authors, find that the occurrence of this preferential orientation is dependent on the preparation method and the substrate temperature. Results of coatings having a different microstructure are e.g. shown in table 6.10.

The grain sizes in the different orientation directions have been determined from the diffraction peak widths. The grain size derived from the (200) peak is largest, which means that the crystallites are largest in the a-axis direction. This, together with the preferential orientation, indicates that the crystallites are column-like orientated perpendicular to the substrate. This column-like orientation is also apparent on SEM pictures taken perpendicular to the coating surface. Such a picture is given in figure 6.11.



Figure 6.11 SEM picture of a cleaved SnO₂ coating

A striking result is that the microstructure is about the same for all samples, independent of the Fluorine doping. This is not found by most other authors. However, there is much confusion on this topic. Fantini (1986) finds a decrease of the (200) intensity with increasing doping level, Saxena (1985) finds the opposite, and Agashe (1988), finds an increase of the (200) intensity at low doping levels and a decrease at high doping levels. These differences must be attributed to differences in preparation methods and conditions.

The importance of our result is that differences in electrical and optical properties between the samples are not influenced by a difference in microstructure and must be explained by other factors. An attempt for such an explanation is made in section 6.10.2, where also the results of other samples are taken into account.

6.3.6 Elemental composition

The elemental compositions of the samples have been determined with electron microprobe analysis. Besides the elements O, F and Sn, in the samples also a small amount, typically 0.24 at% of Cl relative to Sn, has been detected. If it is assumed that each F or Cl atom replaces an O atom in the coating, it is to be expected that each F or Cl atom in the coating gives rise to one free electron. In figure 6.12 the free electron density measured at room temperature is plotted against the fluorine concentration plus the chlorine concentration. In this figure it is observed that the electron density is only about 1/3 of the value expected from the donor concentration. This discrepancy between the free electron density and the amount of F actually present in the coating, has also been observed by Frank (1983). It can be due to the fact that part of the F atoms occupies interstitial positions in the lattice.

The Oxygen/Tin ratio is plotted in figure 6.13. In this figure we see that the ratio decreases with increasing doping concentration. However, when the fluorine and the chlorine concentration are added to the oxygen concentration, the $[F + O + Cl]/[Sn]$ ratio remains 2 within the error of 0.5%, independent of the doping concentration. This means that the fluorine replaces the oxygen in the coating, so it is reasonable to presume that the fluorine atoms occupy oxygen positions in the lattice. The results from the model for the temperature dependence of the electron density, as given in table 6.3, are in notable agreement with this hypothesis, as this model predicts a donor density of about three times the free electron density.

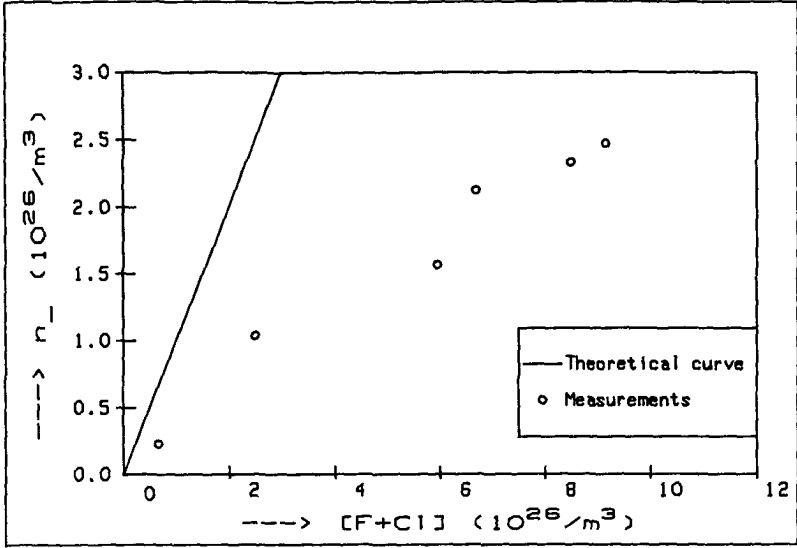


Figure 6.12 Free electron density vs. the Fluorine and Chlorine concentration

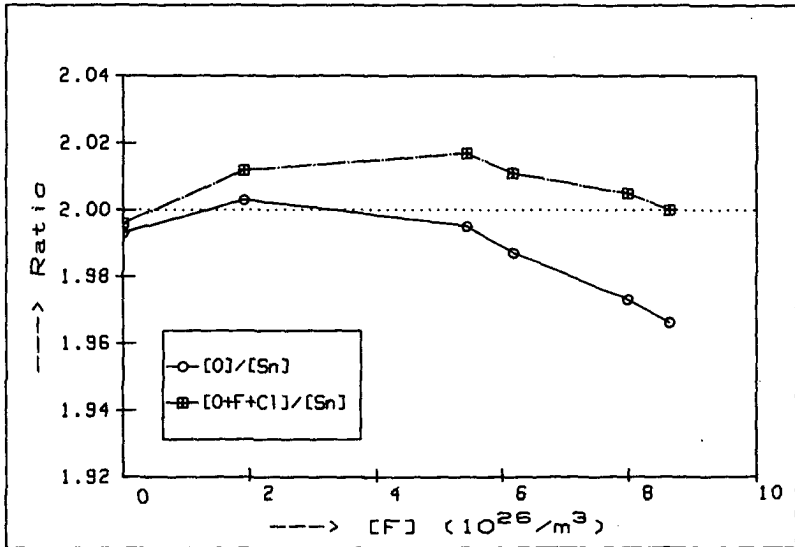


Figure 6.13 O/Sn atomic ratio vs. the Fluorine concentration.

6.3.7. Optical properties near the fundamental band-gap.

In the UV region, where the free electron properties hardly affect the dielectric constant, the coating becomes absorbing due to band-gap absorption. In the vicinity of the band-gap, the following empirical relations hold for the absorption coefficient $\alpha = 4\pi k/\lambda$ (Johnson, 1967; Harbeke, 1972) :

$$\alpha = \alpha_1 (h\nu - E_g)^{1/2} \quad \text{for } h\nu > E_g \quad (6.9)$$

with $h\nu$ being the photon energy, E_g the direct band-gap and α_1 a constant for direct transitions, and :

$$\alpha = \alpha_2 (h\nu - E_g)^2 \quad \text{for } h\nu > E_g \quad (6.10)$$

with E_g being the indirect band-gap and α_2 a constant for indirect transitions. For photon energies smaller than the band gap, it is assumed that the spectral dependence of the absorption coefficient follows the empirical Urbach rule (Melsheimer, 1985) given by :

$$\alpha = \alpha_3 \exp \left(\frac{h\nu - E_1}{E_0} \right) \quad (6.11)$$

with α_3 a constant, E_0 the Urbach energy and E_1 the band gap energy E_g or, if an indirect transition is present, the indirect band-gap E_g .

The direct band gap, as determined from (6.9) is in a first order approximation (Hamberg, 1984) dependent on the electron density and the so-called band-band effective mass $m_{eff,bb}$:

$$E_g = E_{g0} + \frac{h}{4\pi m_{eff,bb}} (3\pi^2 n_-)^{2/3} \quad (6.12)$$

where E_{g0} is the fundamental direct band gap. The second term in (6.12) is called the Burstein-Moss shift. A more comprehensive theory, which also accounts for band gap shifts due to electron interaction and impurity scattering, is given by Hamberg (1984).

The optical constants of the coatings sprayed on quartz have been determined in the wavelength range from 220 to 400 nm, which corresponds to a photon energy between 3 and 5.7 eV. The absorption coefficient α , derived from the extinction coefficient k which is determined with the R-T method, is shown as a function of the photon energy for three samples in figure 6.14.

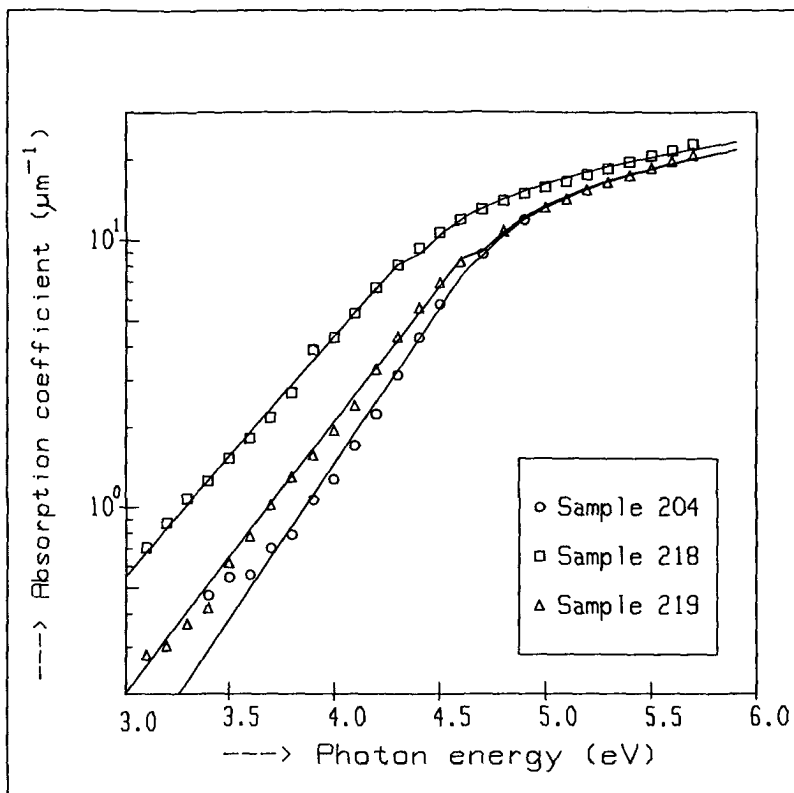


Figure 6.14 Absorption coefficients of samples 204, 218 and 219.
The lines show the fits to equations (6.8) and (6.10).

The absorption coefficients of the other samples showed a similar behaviour as those plotted in figure 6.14. In this figure different slopes for $\alpha < 8 \mu\text{m}^{-1}$ and $\alpha > 8 \mu\text{m}^{-1}$ are observed. The parameters of the theoretical curves, given in equations (6.9), (6.10) and (6.11), have been fitted to the measurements in the two different regions. It proved that for $\alpha < 8 \mu\text{m}^{-1}$, equation (6.11) can be applied best, and that for $\alpha > 8 \mu\text{m}^{-1}$ equation (6.9) holds. The fits according to equations (6.9) and (6.11) are also shown in figure 6.14. The values of α_1 , α_3 , E_g and E_0 , resulting from the least-squares fit, are given for four samples in table 6.6. Unfortunately, only the electrical properties of samples 218 and 219 could be determined.

Table 6.6 Constants describing the dependence of the absorption coefficient on the photon energy

sample number	198	204	218	219
α_1 ($\mu\text{m}^{-1}\sqrt{\text{eV}}$)	18.3 \pm 0.2	18.2 \pm 0.4	17.6 \pm 0.2	18.1 \pm 0.1
α_3 (μm^{-1})	5.45 \pm 0.15	5.1 \pm 0.3	5.89 \pm 0.07	5.95 \pm 0.09
E_g (eV)	4.36 \pm 0.01	4.47 \pm 0.02	4.145 \pm 0.005	4.447 \pm 0.006
E_0 (eV)	0.396 \pm 0.005	0.372 \pm 0.005	0.483 \pm 0.007	0.428 \pm 0.007

In the other samples sprayed on quartz, small cracks appeared some days after deposition, due to a different thermal expansion coefficient of quartz and tin oxide. The electron density n_e of samples 198 and 204 have been derived from the plasma wavelength λ_p , where a same effective mass ($m_{\text{eff}} = 0.225$) as determined in sample 219 has been assumed.

To determine the band-band effective mass, the energy gap is plotted against $n_e^{2/3}$ in figure 6.15. For comparison the results obtained by Shanthi (1982) are also shown. Assuming that equation (6.12) is valid, our results give : $E_{g0} = (4.04 \pm 0.04)$ eV and $m_{\text{eff,bb}} = (0.33 \pm 0.04)$ m_e . Shanthi's results lead to : $E_{g0} = (3.95 \pm 0.04)$ eV and $m_{\text{eff,bb}} = (0.43 \pm 0.05)$ m_e . The differences between the results are not large and are most probably due to the fact that we have determined α up to higher energies than Shanthi, which gives more accurate results for E_g .

Further values of E_g are reported by Demichelis (1985) for F-doped SnO_2 coatings, by Shanthi (1982) for Sb-doped SnO_2 coatings and by Abass (1988) for I-doped SnO_2 coatings. These values are all between $E_g = 4$ eV and $E_g = 4.5$ eV, as in figure 6.15.

To determine the 'real' band gap and band-band effective mass of SnO_2 , the measurements have to be corrected for electron-electron and electron-impurity scattering according to the method as given by Hamberg (1984) for In_2O_3 coatings. This method has not yet been applied to SnO_2 coatings. As this is a very tedious task, we have not carried out this correction. In the case of In_2O_3 , the correction leads to an increase of E_g of about 0.10 eV and to an increase of $m_{\text{eff,bb}}$ with 30 to 50 % relative to the uncorrected case, and it can be expected that an analysis for SnO_2 will give similar results.

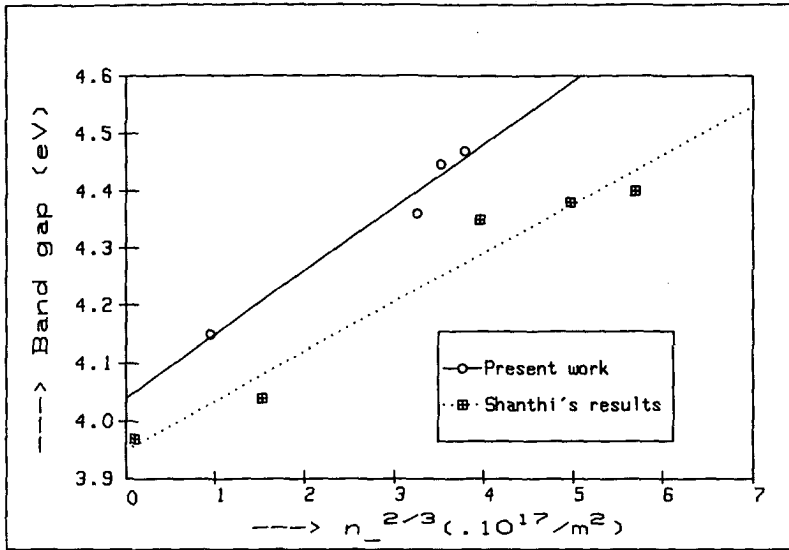


Figure 6.15 Energy gap as a function of $n_2^{2/3}$

From our work it can be concluded that the direct band gap absorption is well described by equations (6.9) and (6.12) with the parameters as given above and in table 6.6.

An indirect band gap has been reported by several authors: Melsheimer (1985) gives E_g -values between 3.3 and 3.5 eV, Demichelis (1985) gives $E_g = 2.80$ and Abass (1988) gives $E_g = 2.58$. We, however, find no region of photon energies where a dependence according to equation (6.10) occurs. This is most probably due to the fact that E_g is usually obtained from a plot of $\alpha^{1/2}$ against the photon energy. In such a plot always a region can be found where the dependence appears to be linear, but the choice of this region is rather arbitrary and a different region on the $\alpha^{1/2}$ scale leads to different results. So we conclude that no indirect band-gap is present in SnO_2 coatings.

The E_g values found in table 6.6 are about twice as high as the values obtained by Melsheimer (1985). The values of α_3 are reasonably constant, while they vary with a factor of 100 in Melsheimer's results. This may be due to the fact that Melsheimer applies equation (6.11) to energies below 3 eV, where the free electron absorption will also affect the determination of α which will lead to erroneous results.

6.4 Coating Thickness Effects.

6.4.1 Spraying conditions.

A series of coatings having a different thickness have been produced. For this series the solution no 3 has been used (see section 5.4.3), the substrate temperature was 600°C , and the coatings were sprayed on polished pyrex substrates during 2 seconds per cycle. The number of cycles was 1, 2, 4, 6, 8 and 12 for the different coatings. The obtained coating thickness ranged from 55 to 633 nm and varied linearly with the number of spraying cycles, as has been shown in figure 5.8.

6.4.2 Optical properties

The reflectance and transmittance of the coating having thicknesses of 55, 102, 205 and 633 nm are shown in figure 6.16. A similarity between this figure and the calculated curves in figure 2.20 can clearly be observed. In figure 6.16 it can also be observed that the transmittance in the 1-2.5 μm spectral region decreases with the coating thickness due to absorption in the coating.

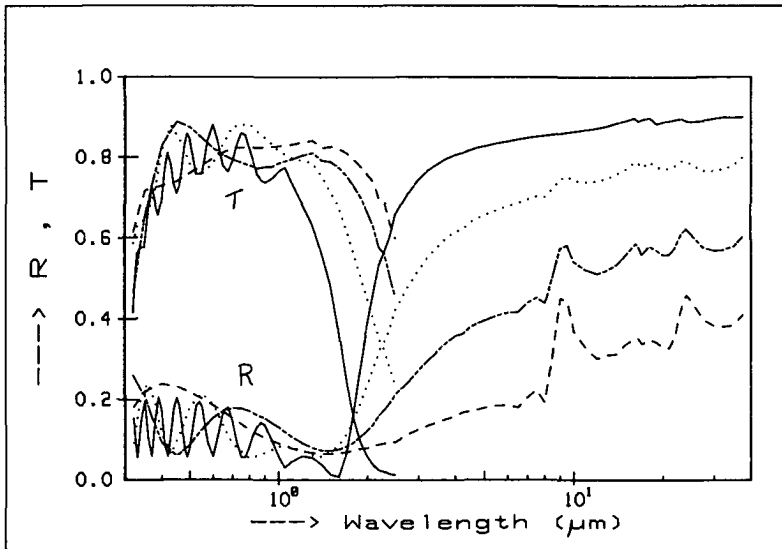


Figure 6.16 reflectance and transmittance in the 0.3 - 40 μm region of samples with a different coating thickness
(—: 633 nm, \cdots : 205 nm, ---: 102 nm, -·-: 55 nm.).

6.4.3 Electrical properties

The electron density n_- and the mobility μ have been determined at room temperature. Under the assumption that the subsequent coatings deposited at each cycle do not influence the coatings deposited at previous cycles, and under the assumption that the coatings can be reproduced accurately, the measurements of n_- and μ as a function of coating thickness can be used to determine a profile of n_- and μ inside the coating. Equations (3.17) and (3.18) can be rewritten in terms of the mobility and electron density effectively measured at different coating thicknesses:

$$n_-(d, d+\Delta d) = \frac{[\Delta(n_- \mu d)]^2}{\Delta d \cdot \Delta(n_- \mu^2 d)} \quad (6.13)$$

and

$$\mu(d, d+\Delta d) = \frac{\Delta(n_- \mu^2 d)}{\Delta(n_- \mu d)} \quad (6.14)$$

where d is the coating thickness and Δ denotes the difference between a quantity before and after the deposition of a coating of thickness Δd . These equations give an average electron density and mobility in the thickness interval from d to $d+\Delta d$. The electron density determined for different coating thicknesses is plotted together with the profile as determined with (6.14) in figure 6.17.

In this figure, the different values for n_- at one thickness indicate measurements on different samples taken out of one piece of coated pyrex. For the derivation of the profile, the average of the measurements at each thickness has been taken. The errors in the profile are about 10% due to the limited reproducibility of the coatings, and due to the fact that small errors in n_- , μ and d have a large effect on the determined profile, as in equation (6.14) differences are taken. Figure 6.17 shows that the electron density is nearly constant through the coating, except for the first 50 nm. This can probably be attributed to a fitting of the crystal structure to the amorphous substrate surface. The measurements of μ are plotted analogously in figure 6.18. In this figure it is shown that the mobility is nearly constant inside the coating for $d > 100$ nm. These results indicate that the film structure and -composition will be about constant for a thickness larger than about 100 nm. Inside this first 100 nm the film will grow to a structure which it maintains for larger thicknesses.

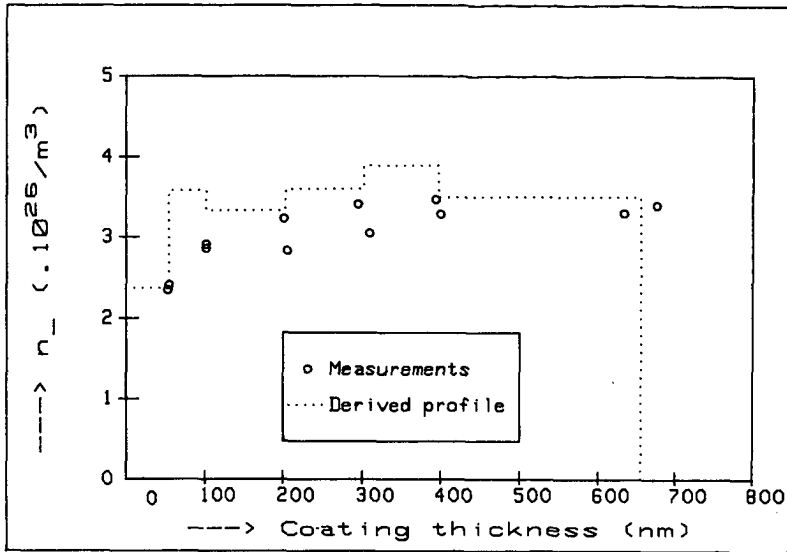


Figure 6.17 Electron density as a function of coating thickness and the profile derived from these measurements.

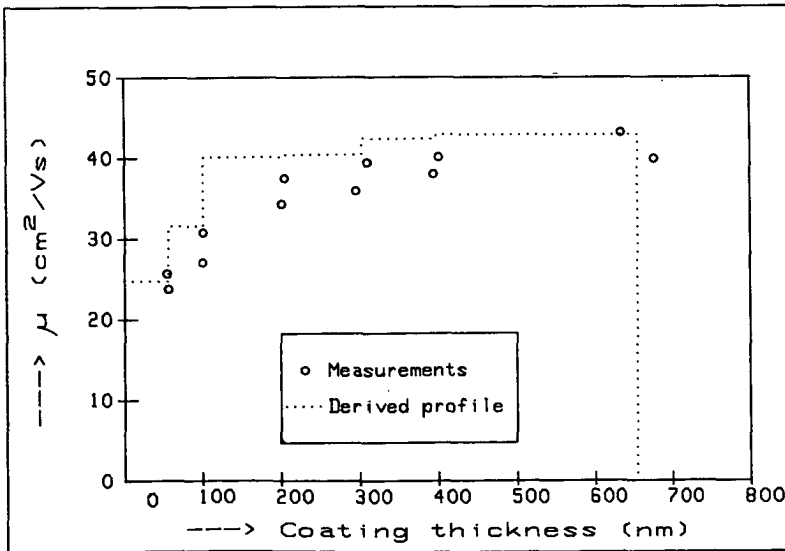


Figure 6.18 Mobility as a function of coating thickness and a profile derived from the measurements.

6.4.4 Comparison of electrical and optical properties

The optical and electrical properties have been compared in an analogous way as in section 6.3.3. As an example the result for the sample of 433 nm thickness is discussed. The effective mass has been calculated to be 0.26 for this sample. The results showed small differences between the optical, electrical and maximal mobility, for which the values are 36.2, 38.0 and 46.7 cm²/Vs respectively. The fact that the optical and electrical mobility are close to the maximum mobility indicates that in this coating the theoretical maximum mobility, as predicted by the Gerlach-Grosse theory (see section 2.4.1), has almost been reached.

When the maximum attainable mobility is corrected for optical phonon scattering as observed in section 6.3.4., the maximum becomes 42.9 cm²/Vs, which is even closer to the measured DC-value. The other coatings with a thickness \geq 200 nm showed similar results. For the 55 and 102 nm coatings the calculation of the optical constants for $\lambda > 2.5 \mu\text{m}$ failed because of the dominating substrate influence on the reflectance of the coating /substrate system.

In these calculations the inhomogeneity in the sample, as shown in the previous section, has not been taken into account. This will cause different effects in the different wavelength regions: at small wavelengths, where the coating is transparent, the reflectance and transmittance will be determined by the whole coating, i.e. an effective refractive index is observed which is determined by the refractive indexes in the different sub layers. At wavelengths of about 10 μm , the skin depth δ , calculated from the measured extinction coefficient using equation 2.19, is about 100 nm, so only the properties of the upper 200 nm (twice the skin depth) of the coating determine the reflectance. This will not cause large errors as the coatings are rather homogeneous except for a small lower part (see figures 6.17 and 6.18), in our case probably some percents.

6.4.5 X-ray diffraction measurements

In table 6.7 the results of X-ray diffraction measurements are given. The intensity measurements are scaled against the (200) peak in the 633 nm coating. As in table 6.5, also in this series a strong preferential orientation in the (200) direction is observed in the samples. The intensity of the (200) peak increases with increasing sample thickness, as is to be expected from coatings having a same microstructure.

Table 6.7 results from X-ray diffraction measurements on samples with different thickness.

thickness(nm)	103	205	309	397	633
crystal plane					
	Relative intensity				
(110)	6	5	5	6	6
(101)	4	5	5	5	4
(200)	11	27	45	61	100
(211)	6	9	13	14	12
(002)	3	3	3	3	3
(310)	-	7	7	7	8
(301)	6	9	14	23	42
	Grain size (nm)				
(110)	9	13	15	15	18
(101)	10	9	12	13	13
(200)	24	34	33	37	39
(211)	25	28	33	35	35
(002)	20	20	15	17	17
(310)	-	13	15	17	16
(301)	15	21	26	27	31

The same applies to the (211) and the (301) intensities, but not for the intensities in the other orientations. For the intensities in the (110), (101), (002) and (310) directions, the conclusion must be that also in the thickest coatings, the intensities in these directions originate from the first 100 nm of the coating. This means that for coatings thicker than 100 nm, in the sub-layer up to 100 nm all crystallite orientations are present to some extent, but in the rest of the coating only the (200), (211) and (301) orientations are present.

The largest grain size is about 40 nm in the (200) direction. This indicates, like in section 6.3.5., that the crystallites are column-like oriented perpendicular to the substrate. An other striking result is that the grain size in the (110) direction increases with increasing coating thickness. As this orientation is only present in the first 100 nm of each coating, this is not a thickness effect, but this must be due to the heating of the coating between two spraying cycles.

This causes a re-orientation of the grains in the first 100 nm. However, as the basic orientation seems to remain the same inside the first 100 nm, it can be presumed that measurements on a 100 nm coating also can be applied to the first 100 nm of thicker samples. This hypothesis has been used in the derivation of the profiles of n_* and μ in section 6.4.3.

6.4.6 Elemental composition

The elemental compositions of the samples having a thickness between 200 and 633 nm has been determined with electron microprobe analysis. The composition was: 32.9% Sn, 65.6% O and 1.5% F in all samples and was not significantly different between the samples. As 99% of the emitted X-rays originate from the upper 0.13 μm of the coating for each element, this shows that the elemental composition is constant for a distance larger than about 100 nm from the substrate. Unfortunately the 55 and 103 nm samples were too thin to be analyzed with this method. The Fluorine concentration corresponds to a density of $1.3 \cdot 10^{27}$ Fluorine atoms per m^3 , which is, as also observed in section 6.3.6, about three times the free electron density determined in the coatings.

6.4.7 Scanning Electron Micrographs

Scanning electron micrographs have been taken from the surface of the samples. Figure 6.19 gives the pictures of the 101 nm and 394 nm coatings.

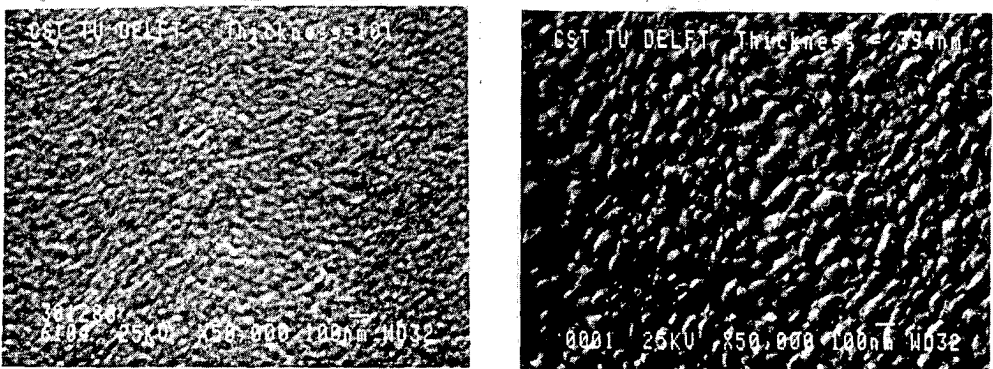


Figure 6.19 SEM pictures of the surface of a 101 nm coating (left) and a 394 nm coating (right)

These and pictures of the other coatings of this series show that the surface structures which can be observed visually on the micrographs increase with the coating thickness, but these structures are much larger than the grain size as determined from the X-ray diffraction measurements. So it must be concluded that the structures shown on the micrographs are not the SnO₂ crystallites, but these must be coagulations of grains of which the size increases with the coating thickness.

6.5 Influence of the process parameters

6.5.1 Influence of the substrate temperature

The substrate temperature during the coating process has a large influence on the coating properties. The influence on the growth speed of the coating has already been discussed in section 5.4.2. In this section the influence on the optical, electrical and structural properties will be discussed.

A series of coatings has been produced at different substrate temperatures, while it has been tried to keep the coating thickness about constant. The required spraying time at the different temperatures has been derived from a preliminary coating series. Solution no 2 (see section 5.4.3) has been used as the spraying solution and the coatings were produced on pyrex substrates.

6.5.1.1 Electrical and optical properties

The spraying conditions and the obtained electrical properties are summarized in table 6.8. The Hall coefficient could hardly be determined in the coatings sprayed at 450 °C and 500 °C, but the measured specific resistivity is given.

Table 6.8 Spray conditions and electrical properties of samples produced at different substrate temperatures

Substrate temperature (°C)	450	500	550	600	625
Spraying cycles	13	5	4	3	3
Spraying time per cycle	5	4	2.5	2.2	1.5
Coating thickness (nm)	560	470	436	410	340
ρ_{DC} ($\cdot 10^{-6} \Omega m$)	750	510	105	7.5	6.0
n_- ($\cdot 10^{26} / m^3$)	~0.2	~0.4	1.2	3.4	3.5
μ (cm^2 / Vs)	~3.5	~3.5	4.6	24	30

As can be observed in table 6.8, the coating thicknesses vary quite a lot between the samples. However, they differ less than a factor of two, which would not have been obtained if all coatings had been sprayed an equal time. The longer spraying time used at lower substrate temperatures will cause the substrate temperature to decrease more during each spraying cycle. This will exaggerate the influence of the substrate temperature on the coating properties. An equal spraying time per cycle would have necessitated a very large number of spraying cycles as the growth rate is very low at low substrate temperatures.

In table 6.8 it can be observed that the electrical properties improve rapidly for a substrate temperature larger than 550 °C. This is also shown from the optical properties: figure 6.20 gives the transmittance and reflectance for the samples in the 0.3-40 μm region. For the sake of clarity, the reflectance and transmittance in the 0.3-2.5 μm spectral region are shown for three of the five coatings only. The optical constants of the SnO₂ coatings have been determined with the R-T method combined with a Kramers-Kronig analysis as discussed in section 4.4. The resulting real and complex part of the resistivity are plotted for the coatings sprayed at 550 °C and 625 °C in figure 6.21. From the complex resistivity and the free electron density, the effective mass and the optical mobility have been derived following the method discussed in section 6.3.3.

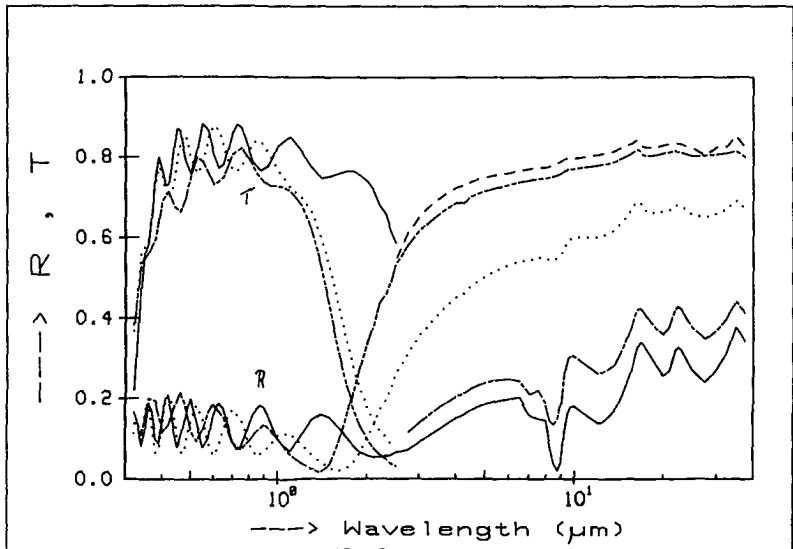


Figure 6.20 Reflectance and Transmittance of coatings prepared at different temperatures: — 450 °C; --- 500 °C, ... 550 °C, --- 600 °C, --- 625 °C

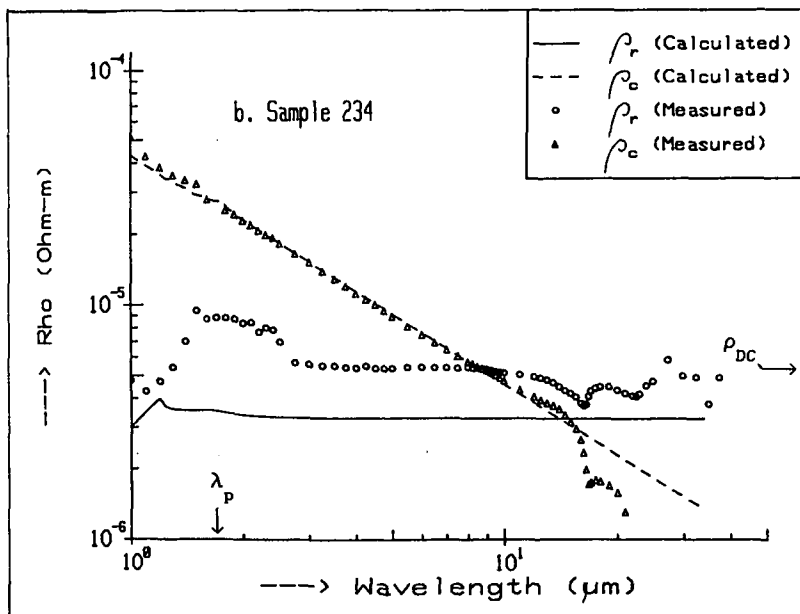
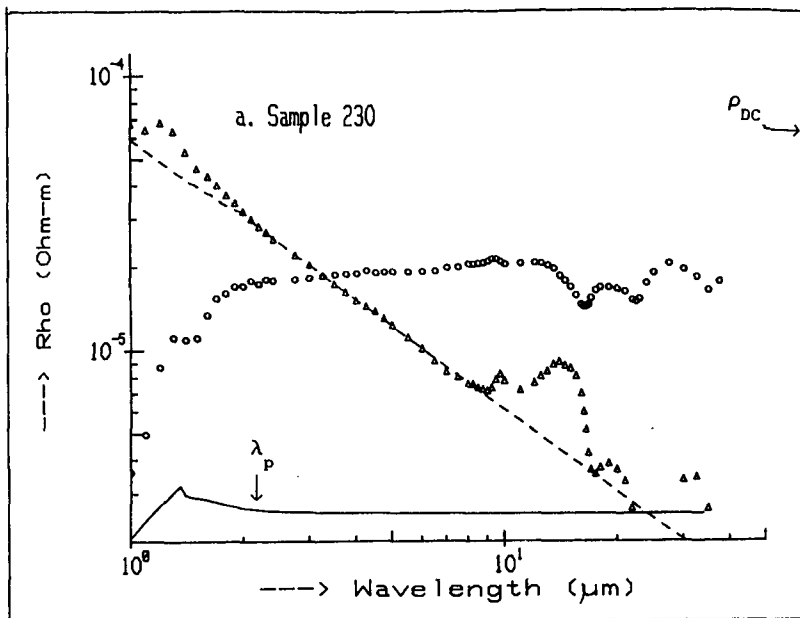


Figure 6.21 Real and Complex part of the resistivity of a sample sprayed at 550 °C (a) and of a sample sprayed at 625 °C (b)

The theoretical complex resistivity, calculated from the free electron density and the effective mass according to the modified Gerlach-Grosse theory, is also drawn in figure 6.21. In figure 6.21 it is shown that for the sample sprayed at 550 °C the DC-resistivity is much higher than the optical resistivity. The theoretical real part of the resistivity is much lower than measured, indicating that the theoretical lower limit has by far not been reached. For the sample sprayed at 625 °C the DC-resistivity about equals the optical resistivity. In this case the difference between the theoretical and measured ρ_r is much smaller.

Table 6.9 gives the electrical and optical properties as derived from the free electron density and the complex resistivity. As discussed in sections 6.3.3 and 6.3.4, the difference between the optical and electrical mobility at the samples sprayed at 500 and 550 °C, must be attributed to grain boundary scattering. At 600 and 625 °C the optical and electrical mobility are about equal and approach the theoretical limit within 50 %.

Table 6.9 Electrical and optical properties of samples prepared at different substrate temperatures

Substrate temperature (°C)	500	550	600	625
Plasma wavelength (μm)	~3	2.1	1.9	1.75
Effective mass ($\cdot m_{e1}$)	-	0.12	0.28	0.23
μ_{DC} (cm^2/Vs)	~3.5	4.6	24	30
μ_{opt} (cm^2/Vs)	~20	24	26	33
μ_{max} (cm^2/Vs)	-	181	44	58

6.5.1.2 X-ray diffraction measurements

In table 6.10 the results of X-ray diffraction measurements are given. The intensity measurements are calibrated against the (200) peak in the coating sprayed at 625 °C, and corrected for the thickness differences. This table -again- shows the apparent (200) preferential orientation present in well conducting coatings. The coatings sprayed at 450 and 500 °C show no preferential orientation compared to the intensity distribution of randomly oriented SnO_2 (see table 6.5). The grain size in the (200), (211) and (301) orientations increase with the preparation temperature.

Table 6.10 Results of X-ray diffraction measurements on coatings sprayed at different substrate temperatures

T substrate (°C)	Relative intensity				
	450	500	550	600	625
crystal plane					
(110)	41	51	19	14	22
(101)	38	39	24	13	17
(200)	14	22	5	28	100
(211)	16	22	35	29	23
(002)	6	5	7	6	12
(310)	-	-	-	3	12
(301)	-	-	22	15	18
Grain size (nm)					
(110)	5	4	8	11	7
(101)	4	4	4	6	9
(200)	5	5	14	30	30
(211)	8	7	14	20	25
(002)	17	26	20	20	17
(310)	-	-	-	40	13
(301)	-	-	7	15	15

The coating prepared at the highest substrate temperature shows a similar microstructure as obtained in tables 6.5 and 6.7, though a different spraying solution has been used in these three cases. This indicates that the microstructure is mainly sensitive to the thermal preparation conditions. The effect of the substrate temperature on the structural properties of SnO₂ coatings has been investigated by several authors. Lou (1983) reports that between 200 and 550 °C only the (111) and (301) planes are observed; at 600 °C also the (310), (211), (200), (101) and (110) lines appear in the diffraction spectrum with a largest intensity in the (211) direction. Kim (1986) observes an amorphous film structure at 300 °C, at 400 °C the orientation directions as given in table 6.10 appear with largest intensities in the (301) and (211) directions. At 700 °C the largest intensities are in the (211), (101) and (301) directions. Karlsson (1982) finds amorphous films at 200 °C and polycrystalline films at T_s = 380 °C with a preferential orientation in the (211) direction.

Srinivasa Murty (1983) observes polycrystalline coatings with no preferential orientation at 400 °C and 450 °C, and with a preferential (200) orientation at 500 °C. Agashe (1988) finds a preferential orientation in the (200) direction which increases with the deposition temperature between 400 °C and 500 °C.

The general trend which can be observed in our coatings as well as in some of the literature results is that the coatings show no preferential orientation when they are prepared at low temperatures. When the temperature is raised, first a preferential (211) orientation appears and a preferential (200) orientation appears at the highest temperatures. The mutual differences between the various authors and the differences of our results with some of the results obtained in the literature illustrate the dependence of the microstructure in the coatings on the exact preparation conditions.

6.5.1.3 Elemental composition

The elemental compositions of the samples have been determined with electron microprobe analysis. Table 6.11 gives the elemental composition of the coatings resulting from these measurements. In this table it can be observed that the amount of fluorine in the coating is smaller at 450 and 500 °C than at higher temperatures. This effect might be connected to the low growth rate at 450 and 500 °C which enables the fluorine to escape to the atmosphere before it can be incorporated in the coating. The increase of the fluorine concentration at higher temperatures corresponds with a decrease of the oxygen in the coating. This has also been observed in section 6.3.6 and indicates that the fluorine replaces the oxygen in the coating. The ratio $[O+F]/[Sn]$ is about 2.1 for all samples. This means that, relative to pure SnO_2 , there is an excess of oxygen in the coatings.

Table 6.11 Elemental composition of coatings sprayed at different substrate temperatures

T _{substrate} (°C)	450	500	550	600	625
[O] (at.%)	66.9	66.1	64.2	64.1	63.9
[Sn](at.%)	31.6	32.1	32.2	32.2	32.5
[F] (at.%)	1.42	1.72	3.61	3.77	3.60
n _o /[F] ratio	0.02	0.03	0.04	0.10	0.11

This is also observed in the samples discussed in section 6.4.5, but not in the samples discussed in section 6.3.6. An other striking result in table 6.11 is the low $n_{\parallel}/[F]$ ratio which is about 0.30 in sections 6.3.6 and 6.4.5, but is much lower in table 6.11 especially at a substrate temperature below 600 °C. This effect might be connected to the grain size in the (200) orientation. It will be further discussed in section 6.10.2.

These differences must be due to the difference in chemical composition of the spraying solution used as the other preparation conditions were similar. The samples discussed in section 6.4.5 were prepared using solution no 3 (tributyltin oxide and trifluoric acid in alcohol), the samples discussed in section 6.3.6 were prepared using solution no 1 (SnCl_4 and NH_4F in water and alcohol) and those listed in tables 6.10 and 6.11 were prepared using solution no 2 (dibutyltin oxide and trifluoric acid in alcohol).

6.5.1.4 Scanning Electron Micrographs

SEM-pictures have been taken of the surfaces of the coatings sprayed at different temperatures. These pictures show that the surface structures increase in size with increasing spraying temperature. This is illustrated in figure 6.22, which gives the SEM-pictures of the coatings sprayed at 500 °C and 600 °C. The more smooth surfaces at lower substrate temperatures are probably due to the lower growing speed or to the more random distribution of the crystallite orientations. As also found in section 6.4.6, there is no direct correspondence between the observed surface structure and the grain size.

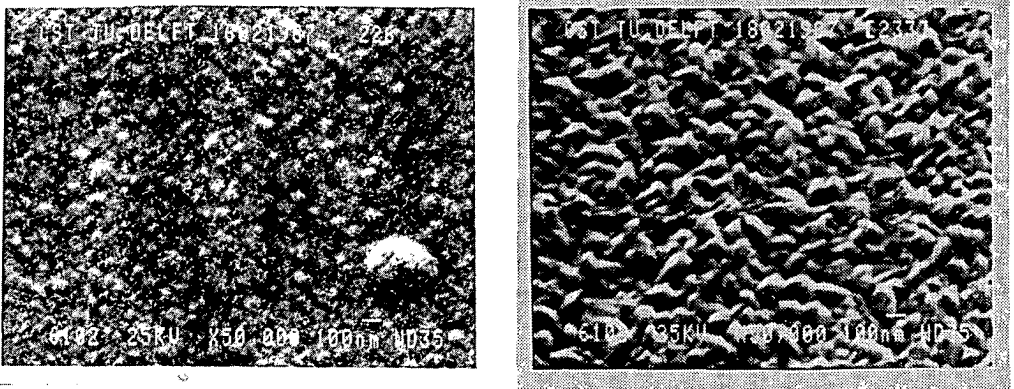


Figure 6.22 SEM-pictures of the surface of coatings sprayed at 500 (left) and 600 °C (right) substrate temperature

6.5.1.5 Other substrate/solution combinations

Also coatings on black enameled steel have been produced using solutions no 2 and 3 (see section 5.4.3). Here temperatures up to 700 °C can be applied, which is higher than when preparing coatings on pyrex, where the maximum temperature which can be used is 625 °C. As the only purpose of these series was to find the optimum substrate temperature (i.e. the substrate temperature at which the coating with the lowest resistivity can be obtained), only the thickness and the electrical resistivity have been determined. Table 6.12 gives the results for solution no 3. The coatings have been sprayed with nitrogen as the carrier gas with a pressure of 6 Bar during one cycle of 6 seconds.

Table 6.12 Results of solution no 3 on black enamelled steel

Substrate temperature (°C)	600	650	700
Thickness (nm)	176	230	253
Resistivity (Ωm)	7.4	6.0	8.5

In the table it is shown that this substrate/solution combination is not very temperature sensitive for a substrate temperature larger than 600 °C. The optimum temperature is in the 600-650 °C range, when the probable thickness dependence of the resistivity is taken into account (see section 6.4).

The results for solution number 2 are summarized in table 6.13. The number of spraying cycles has been taken such as to give about a same coating thickness at different temperatures. The coatings were sprayed during 2 seconds per cycle with nitrogen as a carrier gas at a pressure of 3 Bar. The coatings of this series have become quite thin, probably due to a fault in the spraying nozzle.

Table 6.13 Results of solution no 2 on black enamelled steel

Substrate temperature (°C)	600	650	700	750
Spraying cycles	6	4	3	2
Coating thickness (nm)	150	154	153	173
Resistivity ($\cdot 10^{-5} \Omega m$)	14.9	10.6	10.1	26.6

In table 6.13 it can be observed that the optimum substrate temperature for solution no 2 is between 650 and 700 °C. From the results given in table 6.8 for the same solution sprayed on pyrex it already could be observed that the optimum spraying temperature could be larger than the maximum temperature which can be applied to pyrex (about 625 °C).

6.5.1.6 Effect of the spraying time

The effect of the spraying time per cycle is discussed here as it is essentially a temperature effect: during spraying of a coating the substrate temperature decreases which affects the coating properties. A series has been produced using solution number 3 on pyrex at 600 °C. The carrier gas was nitrogen at a pressure of 6 Bar. The spraying time per cycle was varied while keeping the total spraying time constant. The results are summarized in table 6.14.

In table 6.14 it can be observed that the electrical properties improve when a shorter spraying time per cycle is taken. This is to be expected as the electrical properties deteriorate when the substrate temperature decreases, which also takes place when the coating is sprayed for a longer time. The decrease of the film growth speed as a function of the spraying time has already been given in figure 5.7. The major change of the properties, in figure 5.7 as well as in table 6.14, takes place when the coating is sprayed 1x8 seconds instead of 2x4 seconds. So with this substrate/coating/temperature combination the best results are obtained when spraying only one second per cycle. When it is desirable to obtain fairly thick coatings in a minimum of spraying cycles, the spraying time can be taken 4 seconds without affecting the optimum properties too much.

Table 6.14 Effect of spraying time on electrical properties

Spraying time per cycle (s)	8	4	2	1
Number of cycles	1	2	4	8
Coating Thickness (nm)	130	200	214	232
$n_$ ($\cdot 10^{26}/m^3$)	2.04	2.92	3.01	2.75
μ (cm^2/Vs)	19.5	29.7	33.1	39.7
ρ_{DC} ($\cdot 10^{-6} \Omega m$)	15.7	7.2	6.3	5.7

6.5.1.7 Optimum temperature found in literature

In literature different values for the optimum spraying temperature are found. When spraying a solution like our solution number one (see section 5.4.3), Fantini (1986) finds an optimum substrate temperature of 350 °C; Shanthi (1982) and Karlsson (1985) find 400 °C; Agashe (1988) finds 425 °C; Mavrodiev (1984) finds 430 °C; Manificier (1981) finds 450/500 °C and Simonis (1979) finds 500/600 °C. These differences are most probably due to differences in the flow with which the droplets are applied to the substrate. When the flow is made small enough, the substrate can be maintained at a constant temperature during the spraying process, and the resulting optimum temperature will be lower than in the case in which the substrate is severely cooled down during the spraying process, which is the case in our process. Frank (1983) finds an optimum spraying temperature of 650 °C for a spraying solution consisting of butylacetate with tin chloride with HF as a dopant. Simonis (1987) finds an optimum spraying temperature of 700 °C when using solution no 2 ((C₄H₉)₂SnO and CF₃COOH in alcohol; see section 5.4.3), which accords with our result in section 6.5.1.5. This is not surprising as the same spraying equipment was used in both cases.

6.5.2 Influence of the carrier gas

The influence of the carrier gas has been investigated by spraying coatings with oxygen and nitrogen, keeping the other process parameters constant. Solution no 3 ((C₄H₉)₃SnO and CF₃COOH in alcohol) has been sprayed on pyrex substrates at 600 °C substrate temperature and solution no 2 has been sprayed on black enameled steel at a substrate temperature of 700 °C. The spraying time was 2 seconds per cycle in all cases. The resulting coating thickness, electrical properties and the reflectance at $\lambda = 25 \mu\text{m}$ are summarized in table 6.15.

Table 6.15 Influence of carrier gas on electrical/optical properties

Carrier gas	substrate	cycles	d(nm)	n ₋ (·10 ²⁶ /m ³)	μ (cm ² /Vs)	ρ_{DC} (·10 ⁻⁶ Ωm)	R
O ₂	pyrex	7	329	3.35	38.8	4.78	0.860
N ₂	pyrex	7	290	2.98	38.8	5.43	0.832
O ₂	enamel	4	530	2.56	25.6	9.74	0.816
N ₂	enamel	4	510	2.08	24.0	13.1	0.776

At a first sight it might seem unexpected that a coating is formed when using N_2 gas, as oxygen is needed for the oxidation of tin to tin oxide. However, though N_2 gas is used for the atomization flow, the process takes place in an air atmosphere, so some oxygen will be present when the coating is formed. The fact that the coating has become somewhat thicker when O_2 has been used as the carrier gas, indicates that there might be a slight lack of oxygen when N_2 is used as the carrier gas. In the table it is also shown that the carrier gas type has the largest influence on the electron density in the coatings. Coatings with a smaller resistivity and a larger infrared reflectance are obtained when oxygen instead of nitrogen is used as a carrier gas.

The microstructure of the coatings prepared on pyrex, as determined from X-ray diffraction measurements, shows some small but interesting differences. Both coatings show a preferential orientation and a largest grain size in the (200) direction. The grain size in the (200) direction ($d_g = 40$ nm) and the intensity (defined as $I_{(200)} = 100\%$) are somewhat larger for the coating sprayed with oxygen relative to the coating sprayed with nitrogen ($d_g = 36$ nm and $I_{(200)} = 73\%$). This indicates that an oxygen-rich environment during the spraying process leads to a large grain size and a strong preferential (200) orientation of the crystallites, which causes a larger electron density and so a larger infrared reflectance. The effect of the microstructure on the electrical properties will be further discussed in section 6.10.2.

6.5.3 Influence of droplet size

An attempt has been made to determine the influence of the droplet size on the coating properties. Unfortunately this effect cannot be determined unambiguously as a smaller droplet size is connected to a higher gas flow which affects both the liquid flow and the decrease of the substrate temperature. The temperature effect has been eliminated to some extent by varying the spraying time per cycle in such a way that the cooling of the substrate (see section 5.4.2) during one spraying cycle remains constant. The effect of a larger liquid flow on the coating thickness has been compensated by using the same amount of spraying solution (no 3) for each sample. The coatings have been sprayed on pyrex substrates at a substrate temperature of 600°C . About 5 cycles were needed in all cases to spray the fixed amount of the solution (15 g) on the substrate.

Table 6.16 Influence of gas pressure and droplet size on coating properties

Gas pressure (Bar)	3	4.5	6	7.5	9
Average droplet size (μm)	11	9.5	8	7.5	6.3
Spraying time/cycle (s)	1.7	1.5	1.3	1.1	0.9
Coating thickness (nm)	171	148	136	139	137
Resistivity ρ_{DC} ($\cdot 10^{-6} \Omega\text{m}$)	5.87	6.93	6.91	8.05	8.07

Table 6.16 gives the resulting thickness and specific resistivity of the coatings. The average droplet size has been determined as described in section 5.4.1. In this table it can be observed that the coating thickness decreases with increasing gas pressure in the 3-6 Bar range and the specific resistivity increases over the 3-7.5 Bar gas pressure range. It is not certain to what mechanism this has to be attributed. Possibly the larger droplets have a larger chance to reach the substrate as they have a larger impulse towards the substrate. The smaller droplets tend to follow the gas stream which moves along the substrate. This causes a smaller film growth and different coating properties.

Anyhow it can be concluded that for obtaining a minimum resistivity it is advantageous to apply a low gas pressure in the spraying process as has been used in this study.

6.6 Annealing

From the literature (e.g. Grosse, 1982) it is known that the electrical properties of tin dioxide coatings can be improved by giving them a heat treatment of about one hour at about 500 °C in vacuum or in a reducing gas like hydrogen or carbon monoxide.

Several samples have been annealed using the Cryostat/Vacuum chamber which is described in section 3.4. A typical result of an annealing procedure is sketched in figure 6.23. In this figure the resistance $R_{\text{AB,CD}}$ as defined in (3.13) is given as a function of temperature during the heating and cooling, indicated by arrows, of the undoped sample no 312 (see section 6.3) in vacuum. In the figure it is shown that the resistance first decreases when the temperature is increased, and remains about constant when the sample is cooled down to room temperature. The result of this irreversible behaviour is that the resistivity of the sample is decreased with about a factor of three.

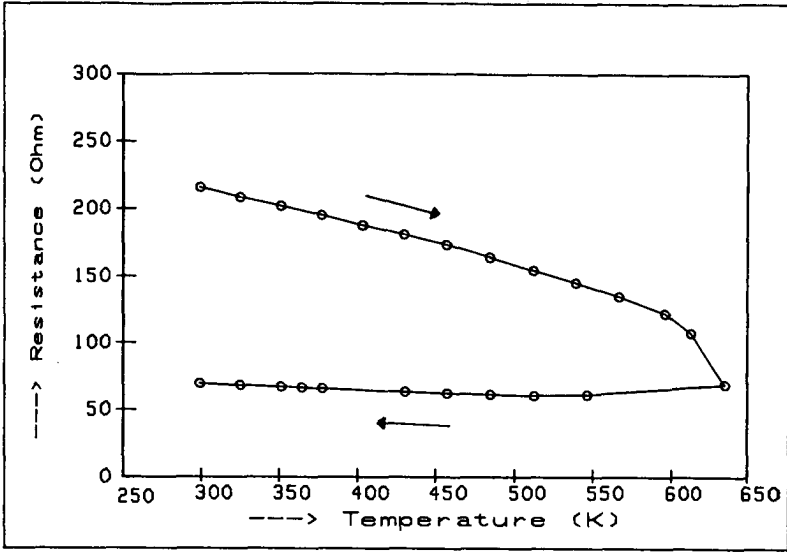


Figure 6.23 Resistance of sample 312 during the annealing process

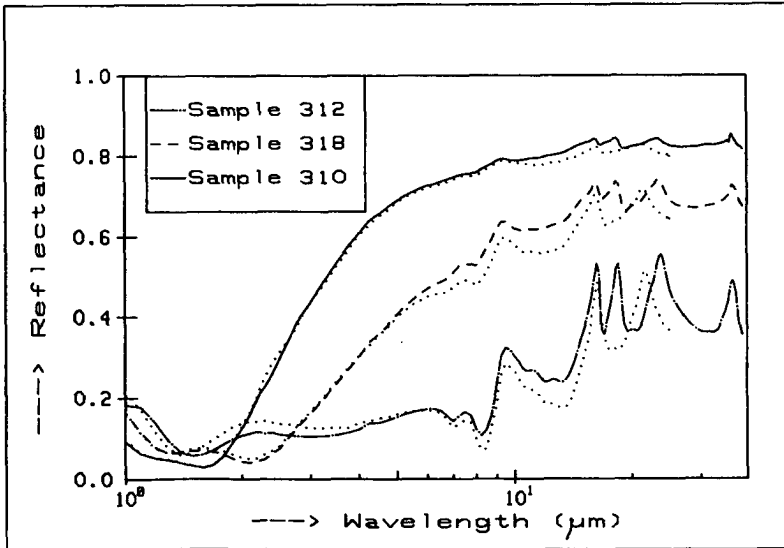


Figure 6.24 Reflectance before (···) and after (—) annealing

In general, we find that annealing has a large effect on poorly conducting samples. However it has little effect on heavily doped, well conducting coatings as is further discussed in the next sections.

6.6.1 Electrical and optical properties

The electrical and optical properties have been determined in a similar way as in section 6.3.3. Figure 6.24 gives the infrared reflectance of the undoped sample no 312 and the doped samples no 318 and 310 before and after the annealing.

The figure shows no drastic changes as a result of the annealing, though the reflectance has increased somewhat. The structure of the molecular oscillation peaks at $\lambda \approx 20 \mu\text{m}$ changes. This effect will be discussed in section 6.9. The electrical properties and the characteristic optical properties are summarized in table 6.17.

When comparing these results to those given in table 6.2, it proves that for the heavily doped sample 310 there is little change, for the slightly doped sample 318 the electron density and the electrical mobility increase, the plasma wavelength also increases somewhat, so the effective mass increases. The most drastic changes take place in the electrical properties of the undoped sample 312: the electron density increases with a factor 1.5 and the electrical mobility increases with a factor of two. As the optical properties change less, the calculation of the effective mass from the plasma wavelength and the electron density results in a larger value; this leads to a much smaller difference between the optical and electrical mobility than before the annealing process.

Table 6.17 Electrical and optical properties at room temperature before and after annealing

Sample number	312		318		310	
	before	after	before	after	before	after
μ_{DC} (cm^2/Vs)	6.0	14.4	27.1	34.9	38.4	39.0
n_- ($\cdot 10^{26}/\text{m}^3$)	0.23	0.36	1.04	1.11	2.33	2.43
λ_{p} (μm)	4.3	4.5	3.1	3.2	2.4	2.4
m_{eff} ($\cdot m_0$)	0.10	0.16	0.22	0.27	0.30	0.30
μ_{opt} (cm^2/Vs)	25	27	28	31	37	38

In section 6.3.3 the difference between the electrical and optical mobility has been attributed to grain boundary scattering. Following this hypothesis it appears that annealing diminishes the influence of the grain boundaries on the electrical properties. As the reflectance has hardly changed, it must be concluded that the properties of the bulk of the SnO_2 coating have not changed. However, the electron density, as determined from the Hall effect, seems to have changed as a result of the annealing. This can be explained assuming that the determination of the Hall coefficient is also affected by the grain boundaries. This would imply that one of the conditions given by equations (2.87) and (2.88) is not fulfilled. An estimate of the electron free range gives $\ell \approx 6$ nm which is not much smaller than the grain size $d_g \approx 20$ nm (see table 6.5). If it is nevertheless assumed that condition (2.87) is met, this means that condition 2.97 is not fulfilled, i.e. the density of trapped electrons in the grain boundaries is about $n_t \approx n_- \cdot d_g \approx 7 \cdot 10^{17}/\text{m}^2$. These trapped electrons might originate from an oxygen excess in the grain boundaries. The decrease of the influence of the grain boundaries when the sample is annealed can be explained by assuming that oxygen is removed from the grain boundaries when the coating is heated in vacuum or in a reducing atmosphere. This is supported by the fact that the resistivity increases when annealing takes place in an oxygen or air atmosphere. The fact that grain boundaries do not affect the electrical properties of the doped coatings can be explained when considering the fact that the Fermi energy, which is proportional to $n_-^{2/3}$, is much higher for the doped samples. So the free electrons in the doped samples will more easily skip the inter-grain barriers. Another possibility is that the grain boundaries are passivated by the Fluorine when the coating is doped.

6.6.2 Temperature dependence of electrical properties

After annealing, the electron density n_- and mobility μ have been determined from $T = 80$ K to $T \approx 450$ K, and the results have been compared to the results before annealing. Just like in section 6.3.4, the parameters E_d and N_d in the model described in section 2.5, have been fitted to the measurements of the electron density as a function of temperature. The results are summarized in table 6.18, together with the results obtained before annealing, which are given for comparison. In the table it is observed that N_d and E_d are only slightly affected as a result of the annealing of the doped samples 310 and 318.

Table 6.18 Parameters describing the temperature dependence of the electron density before and after annealing

sample no	312		318		310	
	before	after	before	after	before	after
N_d ($\cdot 10^{26}/m^3$)	0.416	0.611	2.76	2.91	7.16	7.60
$-E_d$ (eV)	0.359	0.273	0.365	0.317	0.454	0.470

In the case of the undoped sample no 312 the changes are large, which is in agreement with the changes in the electron density determined at 300 K.

The temperature dependence of the mobility changed little as a result of the annealing for the doped samples 310 and 318. In the case of the undoped sample 312 the mobility after annealing changes from $11.2 \text{ cm}^2/\text{Vs}$ to $14.4 \text{ cm}^2/\text{Vs}$ when the temperature is changed from 80 to 300 K. This increase of the mobility with temperature indicates that grain boundary scattering still governs the electrical mobility. The temperature dependence has become less when compared to the unannealed case, where the mobility increases 50 % in the same temperature range (see figure 6.7). This indicates that the influence of grain boundary scattering has decreased, which is in accordance with the decrease of the difference between the optical and electrical mobility as discussed in section 6.6.1.

6.6.3 Structural properties

The X-ray diffraction patterns measured after the annealing of samples 310, 312 and 318 showed no changes as compared to the results before annealing which are given in table 6.5. This means that annealing of the coatings has no effects on the crystal structure. This result further confirms the conclusions drawn in sections 6.6.1 and 6.6.2 that annealing mainly affects the properties in the grain boundaries.

6.6.4 Comparison with literature

The results found in sections 6.6.1 and 6.6.2 regarding the annealing properties of the undoped coating are in accordance with results found in literature (Viscrian, 1969; Shanthi, 1980-1; Islam, 1986). Viscrian has annealed undoped tin dioxide coatings in vacuum and oxygen and observes an irreversible decrease of the resistivity when the coating is annealed in vacuum, and an increase when the coating is annealed in oxygen.

Shanthi (1980-1) observes a nearly equal change as in our sample 312 in the electrical properties at room temperature of an undoped tin oxide sample due to annealing in vacuum; Islam (1986) obtains similar results. Shanthi also observes that the effects of annealing on the electrical properties at room temperature are less when the coating is doped with antimony. Grosse (1982) finds an increase of both n_- (about a factor 1.1) and μ (about a factor 1.4) in doped samples with an initial mobility of about $10 \text{ cm}^2/\text{Vs}$.

None of these authors determine the influence of annealing on the optical properties as is done in section 6.6.1. As is shown by our results, the determination of both electrical and optical properties enables to distinguish between grain boundary scattering and other scattering mechanisms. In this way the assumption that an oxygen excess determines the grain boundary scattering (Viscristian, 1969; Shanthi, 1980; Islam, 1986) can be confirmed and it is shown that an increase of the oxygen vacancies in the bulk of the coating, which has been supposed by Grosse (1982), hardly takes place. In our work it is shown that the optical and electrical properties of doped coatings having a mobility $\mu > 20 \text{ cm}^2/\text{Vs}$ are not affected by the electrical conduction in the grain boundaries. This means that the assumption of Shanthi (1980-2) and Chopra (1983) that grain boundary scattering is the main damping mechanism in doped tin oxide coatings can be rejected.

When comparing the results regarding the change in structural properties due to annealing to results obtained in literature, it should be noted that in literature only the change in crystal structure is determined of coatings which are deposited in vacuum at low temperatures. In these coatings large changes in the crystal structure are observed due to the oxidation of SnO to SnO₂ (Banerjee, 1987; Beensh-Marchwicka, 1984; Geurts, 1984). The presence of the SnO phase has not been observed in X-ray diffractograms of any of our samples.

6.7 Ageing

The ageing properties of tin oxide coatings are important in connection to the durability of these coating when applied in solar collectors, as discussed in section 1.4. An ageing test consists of keeping the coating at a high temperature for a long time (some days or weeks). In the literature, several investigations into the ageing properties of tin oxide coating have been carried out (Simonis, 1979, 1987; de Waal, 1981; van der Ley, 1979).

The result of these investigations is that the electrical and optical properties hardly change if the coatings are aged for a long time in an air atmosphere up to 400 °C and in vacuum up to 250 °C. At higher temperatures the optical and electrical properties deteriorate, where the increase of the thermal emittance is less than would be expected from the decrease of the electrical resistivity. We have carried out some ageing tests to investigate the physical mechanisms which cause these ageing effects. Three samples were taken out of one piece of pyrex on which a coating was deposited. This coating was prepared at a substrate temperature of 600 °C using solution no 3 in 10 cycles of two seconds each. The resulting coating thickness was about 580 nm. One sample was kept as a reference, one sample was aged in air at 500 °C for 10 days and one sample was aged in vacuum at 500 °C for 10 days. These ageing conditions were chosen such that, according to the literature, a large deterioration of the properties was to be expected. The results are discussed in the next sections.

6.7.1 Optical and electrical properties

The spectral transmittance and reflectance of the reference coating and the coating aged in air showed no differences exceeding 0.003 units of transmittance/reflectance. The spectral transmittance and reflectance of the reference coating and the coating after ageing in vacuum are shown in figure 6.25. The figure shows some apparent differences: the aged coating has a lower transmittance in the 0.3-2.5 μm spectral region and a lower reflectance in the 8-40 μm spectral region. The lower transmittance results in a higher value for the extinction coefficient k when the optical constants are calculated. Figure 6.26 shows the results of the calculation of k using the R-T method. Also a curve is drawn based on the Drude theory where the electrical properties of the reference coating have been used. The deviation of the values of the reference coating from those obtained using the Drude theory in the 0.9-1.8 μm spectral region can be attributed to the influence of ionized impurity scattering. The aged coating has a higher k value relative to the reference coating in the 0.3-2.4 μm spectral region, as is to be expected regarding the lower transmittance. In the visible spectral region (0.4-0.8 μm) the values of k of the aged coating are even a factor of four higher than the values of the reference coating. Moreover, in the reflectance spectrum of the aged coating strong absorption peaks appear in the reflectance spectrum at $\lambda = 13.8, 18.5, 29.7$ and $38.3 \mu\text{m}$ (wavenumbers: 727, 541, 337 and 261 cm^{-1}).

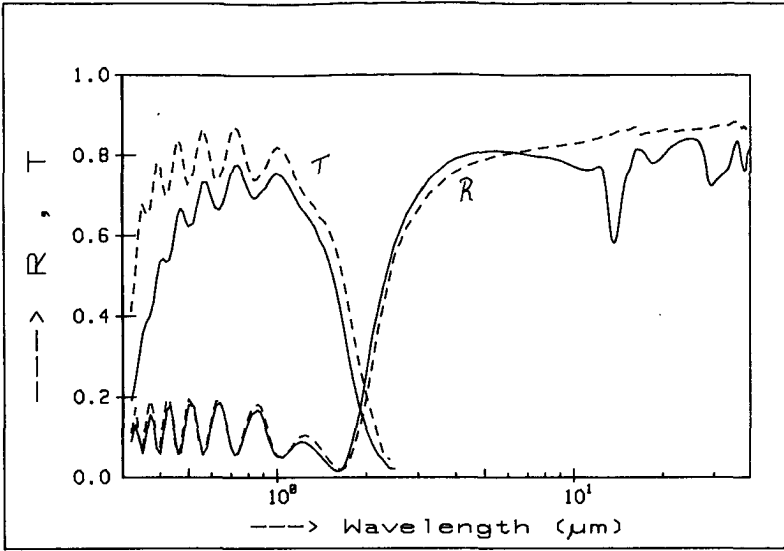


Figure 6.25 Reflectance and transmittance of the coating aged in vacuum (—) and of the unaged coating (---)

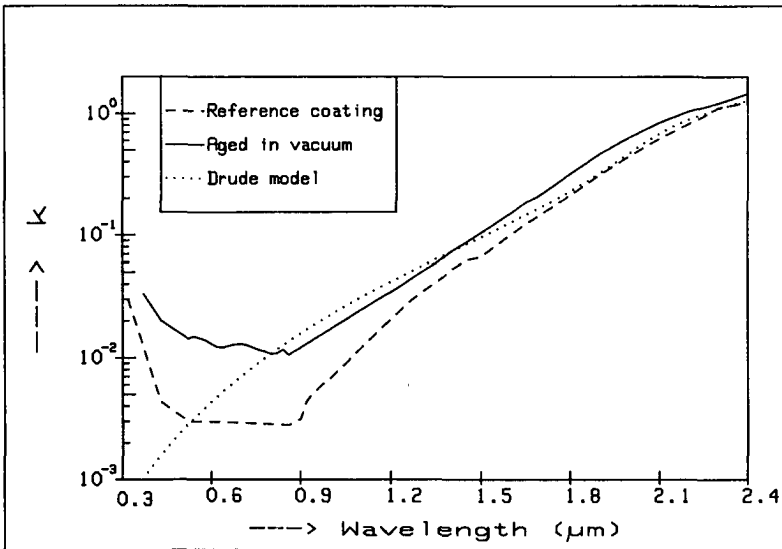


Figure 6.26 Extinction coefficient k for an unaged coating, a coating aged in vacuum and according to the Drude-theory.

Some characteristic optical and electrical properties are given in table 19. The measured hemispherical emittance ϵ_h is derived from the optical reflectance spectrum, while the calculated value of ϵ_h is derived from measured electrical properties. The electrical resistivity of the coating aged in vacuum had increased so much (a factor of 400) that the Hall coefficient could not be determined, so of this coating the mobility and the electron density are not given in the table.

Regarding the properties of the coating aged in vacuum the table shows what also can be derived from the reflectance spectra: the increase of the resistivity with a factor of 400, which would theoretically lead to a poor infrared reflectance and a thermal emittance of 0.82, does by far not affect the reflectance spectrum in the expected extent. Considering the optical properties, it can be derived from the reflectance spectrum in the 1.5-5 μm spectral region that the electron density and the optical mobility must have remained about the same, as the position of the reflectance edge and the steepness of the reflectance increase remain basically the same. This indicates that the occurrence of grain boundary scattering must cause the large increase of the electrical resistivity. On the other hand the decrease of the transmittance in the 0.3-2.5 μm spectral region and the occurrence of the absorption peaks in the reflectance spectrum indicate that a compound different from SnO_2 has been formed in the coating. We have not succeeded to identify the absorption spectrum to that of one of the compounds given in some handbooks on infrared spectra (Nyqvist, 1971; Szemanski, 1970). This excludes the formation of SnO , of many compounds containing tin or fluorine, and also of many compounds containing iron, sodium or silicon, which might have been formed by diffusion from the substrate. Some remaining possibilities are the formation of Sn_2O_3 or SnF_2 , of which the infrared absorption spectra are not given in these handbooks.

Table 6.19 Characteristic optical and electrical properties of the unaged and the aged coatings

	n_e ($\cdot 10^{26}/\text{m}^3$)	μ_{DC} (cm^2/Vs)	ρ_{DC} (Ωm)	λ_p (μm)	ϵ_h (meas.)	ϵ_h (calc.)
Reference coating	3.0	43	$4.9 \cdot 10^{-6}$	2.02	0.162	0.173
Aged in air	2.3	48	$5.7 \cdot 10^{-6}$	2.09	0.161	0.190
Aged in vacuum	-	-	$2.1 \cdot 10^{-3}$	2.08	0.221	0.821

The results concerning the thermal emittance indicate that for ageing in air the emittance is not affected by temperatures up to 500 °C; when ageing at this temperature in vacuum the emittance increases somewhat, though not dramatically.

The solar absorptance, when defined as the radiation which is not reflected in the coating, does not change by the annealing process. This means that a spectrally selective tin oxide coating will survive a stagnation temperature of 500 °C in air very well and in vacuum reasonably well. This is a very good compared to other spectrally selective materials.

The amount of solar radiation which is absorbed in the coating itself increases when the coating is annealed in vacuum (from 0.11 to 0.22). This may be of importance when the solar transmitting property of the coating is relevant, e.g. in applications on solar cells or on windows.

6.7.2 X-ray diffraction and Electron Microprobe analysis

From the X-ray diffractograms a similar preferential orientation in the (200) direction and similar grain sizes were obtained as in the case of the 633 nm coating discussed in section 6.4.5, with no significant differences between the reference coating and the both aged ones.

The determination of the elemental composition gave as an average result for the three samples (in atomic %): 0.56% F, 32.5 % Sn and 66.9 % O. The fluorine content was within the error of 0.03% the same in the three coatings. Also the O/F ratios did not differ significantly.

These results show that major changes in the structural properties and major changes in the elemental composition are not the cause of the effects on the optical and electrical properties of the coating aged in vacuum.

The results on the structural, optical and electrical properties make it most probable that at the grain boundaries oxygen is removed and compound is formed in such a quantity that it does not affect the crystal structure and the chemical composition of the bulk, but which is absorbing in the 0.3-2.5 spectral region and which has a characteristic infrared absorption spectrum.

6.8 Determination of anisotropy and inhomogeneity with ellipsometry

The ellipsometer described in section 3.5.2 has been used to determine the optical properties of the coatings sprayed on quartz at $\lambda = 632.8$ and 1523 nm. The coatings on quartz have been selected because the smooth surface of quartz is not affected by temperatures of about 650 °C.

The spraying conditions of the samples are summarized in table 6.1. (in short: sample no 218 is undoped, 202 and 204 are slightly doped, 200, 203 and 219 are heavily doped). One sample, no 203, has been polished with 0.25 μm diamond grains. The removal of subsequent sub-layers of the coating enables a check of the inhomogeneity determined from measurements of the total layer. Two lasers, giving a wavelength of 632.8 and 1523 nm respectively, have been used as a light source to enable an accurate determination of the ellipsometric parameters Δ and Ψ as a function of the angle of incidence θ (see section 3.5). The measurements of Δ and Ψ have been performed at about 8 different angles of incidence θ between $\theta = 30^\circ$ and $\theta = 80^\circ$. The methods described in section 4.4 have been used to determine the coating thickness, the complex refractive index and the eventual anisotropy and inhomogeneity of the complex refractive index.

6.8.1 Results at $\lambda = 632.8$ nm

6.8.1.1 Coating thickness and refractive index

The coating thickness has been calculated using a model of a single film with and without surface roughness. The extinction coefficient k did not deviate significantly from zero in all cases, so $k=0$ has been taken in the final calculations. The assumption of a hypothetical layer representing the surface roughness (see section 2.2.6) leads to a decrease of the X_r^2 (chi-square) -value of about a factor of four, except when the resulting surface roughness does not deviate from zero significantly.

Table 6.20 Refractive index, film thickness and surface roughness determined at $\lambda = 632.8$ nm

Sample no ^a	n	d	σ	X_r^2
200	1.87 \pm 0.04	476 \pm 25	12 \pm 7	9
202	1.97 \pm 0.03	1030 \pm 18	14 \pm 2	12
203	1.87 \pm 0.05	632 \pm 31	17 \pm 5	8
203 (6)	1.875 \pm 0.01	602 \pm 4	≤ 0	0.92
203 (45)	1.94 \pm 0.03	536 \pm 10	2.4 \pm 1.2	2.1
203 (225)	1.899 \pm 0.016	125.6 \pm 0.8	≤ 0	2.5
203 (240)	1.96 \pm 0.02	53.8 \pm 0.4	≤ 0	1.3
204	1.83 \pm 0.04	581 \pm 20	6 \pm 2	2.6
218	1.85 \pm 0.06	196 \pm 9	2 \pm 5	11
219	1.95 \pm 0.01	112 \pm 3	2 \pm 4	31

^aNumerals in parenthesis represent the polishing time (minutes)

This means that the surface roughness has to be taken into account to obtain correct values for the thickness d and the refractive index n (see also section 4.4, table 4.2). The results are summarized in table 6.20.

6.8.1.2 Anisotropy

The anisotropy has been determined by calculating the ordinary and extraordinary components of the complex refractive index n (see section 2.2.4) : n_o, n_e, k_o and k_e . The values of n_o and n_e on the one hand and k_o and k_e on the other hand differed not significantly from each other. The values of n and k were also in agreement with the values obtained with the R-T method. So it can be concluded that the tested coatings show no significant anisotropy at $\lambda = 632.8$ nm.

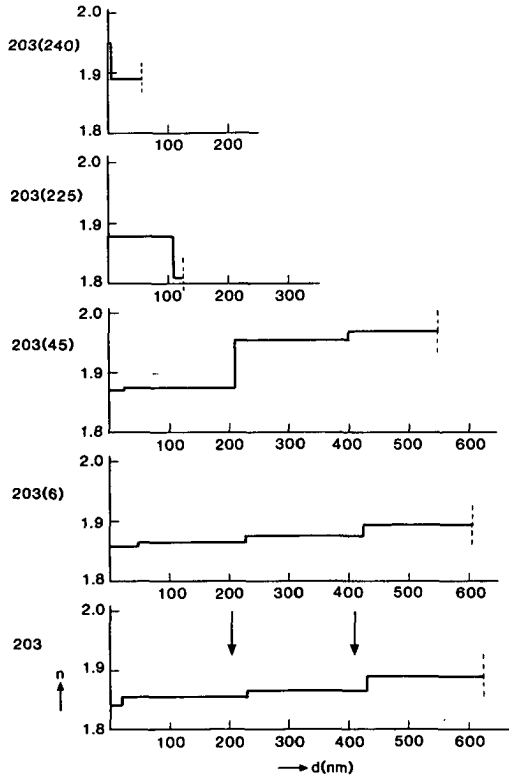


Figure 6.27 Refractive index profiles at $\lambda = 632.8$ nm of sample 203 and the samples obtained by polishing

6.8.1.3 Inhomogeneity

The inhomogeneity of the heavily doped sample 203 and its polished versions has been analyzed with the method discussed in section 4.4. The results are given in figure 6.27. The arrows indicate the positions at which a transition to another sublayer could occur considering that the coating has been sprayed three times, during which the spray conditions may have changed slightly. The figure shows that the absolute values of the refractive index in the specific sublayers are not the same for the different measurements. This might be due to a small error in the coating thickness which will occur as the precise inhomogeneity cannot be taken into account when the thickness is calculated. The positions of the transitions, however, remain about the same for each determination.

6.8.2 Results at $\lambda = 1523$ nm

6.8.2.1 Coating thickness and refractive index with a single layer model

The thicknesses determined at $\lambda = 1523$ nm proved to be less accurate than those determined at $\lambda = 632.8$ nm, though they did not conflict. An apparent surface roughness could not be ascertained. These effects will have two reasons: the refractive index is much lower at this wavelength, and the dimensionless thickness d/λ , which enters into the equations (see section 2.2), is much smaller than unity. Moreover, the inhomogeneity and anisotropy which are observed at this wavelength (we come to this in the next sections) will influence the thickness determination. Therefore the thickness and surface roughness from table 6.20 are used in the further calculations.

The determination of the complex refractive index using an isotropic, homogeneous film model yielded X_r^2 values between 10 and 1700 and values of k which were very high compared to the values determined with the R-T method. So it is concluded that the model of a homogeneous isotropic film is not valid here, though it is valid at $\lambda=632.8$ nm. This difference will be caused by the conduction electrons, which affect the optical constants at $\lambda=1523$ nm (where $\lambda \approx \lambda_p$) much more than at $\lambda=632.8$ nm (where $\lambda < \lambda_p$).

6.8.2.2 Anisotropy

An anisotropic film model was applied to the measurements, which gave results as presented in table 6.21.

Table 6.21 Refractive index parallel (o) and perpendicular (e) to the surface at $\lambda = 1523$ nm

Sample no	n_o	n_e	k_o	k_{R-T}^a	k_e	X_r^2
200	1.117±0.006	1.162±0.006	0.222±0.005	0.23	0.197±0.006	4.2
202	1.358±0.008	1.318±0.007	0.100±0.009	0.07	0.013±0.009	56
203 (45)	1.000±0.010	1.060±0.001	0.180±0.005	-	0.171±0.003	2.1
203 (225)	1.09 ±0.13	1.16 ±0.10	0.12 ±0.10	-	0.07 ±0.08	3.7
204	1.003±0.009	1.119±0.009	0.297±0.012	0.20	0.227±0.010	2.1
218	1.987±0.006	1.94 ±0.09	0.087±0.021	0.08	0.10 ±0.15	0.58
219	1.23 ±0.05	1.28 ±0.05	0.202±0.041	0.20	0.13 ±0.05	0.78

^a k_{R-T} denotes the value of k_o obtained with the R-T method

The values of X_r^2 are considerably reduced compared to the isotropic model, and the complex refractive indexes in the ordinary and extraordinary direction are significantly different from each other. The values of k_o agree well with the values obtained from the R-T method. Therefore it is clear that the coatings exhibit anisotropy at $\lambda = 1523$ nm. This is in agreement with X-ray diffraction measurements which indicate preferential orientations in the (200) (sample 200) and (211) (sample 202) directions.

Interpretation in terms of electrical transport properties

The Drude theory, as given in section 2.3, enables the determination of the plasma wavelength λ_p and the relaxation wavelength λ_γ when the complex refractive index is known at one wavelength. From the values given in table 6.21 the plasma wavelength and relaxation wavelength can be calculated normal and parallel to the surface. Table 6.22 gives the results of these calculations. As has been shown in sections 6.3 and 6.4, λ_γ becomes wavelength dependent for $\lambda < \lambda_p$, so the values listed in table 6.22 will be different from the DC-value of λ_γ which is usually obtained for $\lambda > \lambda_p$. The table shows that $\lambda_{\gamma,e}$ is in most cases larger than $\lambda_{\gamma,o}$. This means that the mobility will be largest perpendicular to the surface. The small differences between $\lambda_{p,o}$ and $\lambda_{p,e}$ might be caused by differences in the effective mass parallel and perpendicular to the surface.

As an example the effective mass of sample 219, which has an electron density of $3.05 \cdot 10^{26} \text{ m}^{-3}$ has been calculated. For $m_{\text{eff},o}$ and $m_{\text{eff},e}$ we find 0.240 and 0.261 electron mass respectively.

Table 6.22 Plasma wavelength λ_p and relaxation wavelength λ_γ derived from the refractive indices given in table 6.21

Sample no	$\lambda_{p,o}$	$\lambda_{p,e}$	$\lambda_{\gamma,o}$	$\lambda_{\gamma,e}$
200	1.792±0.004	1.831±0.005	8.6 ± 0.2	8.9 ± 0.3
202	2.054±0.010	2.025±0.008	12.1 ± 1.0	100 ± 100
203 (45)	1.734±0.003	1.774±0.002	12.8 ± 0.4	12.2 ± 0.2
203 (225)	1.80 ±0.10	1.86 ±0.09	16 ± 10	25 ± 20
204	1.703±0.007	1.791±0.007	7.9 ± 0.4	8.4 ± 0.4
219	1.88 ±0.05	1.96 ±0.05	7.7 ± 1.4	11 ± 6

We observe that, though small differences are present and can be determined, the electrical transport properties parallel and perpendicular to the surface are not too different. Probably ellipsometry is the only way in which this can be established in thin films.

6.8.2.3 Inhomogeneity

The determination of the inhomogeneity at $\lambda = 1523$ nm is complicated because the refractive index is both complex and anisotropic, which requires the determination of 8 parameters when a two-layer model is applied. Calculations with this model failed because the parameters showed a strong correlation, which means that, for example, for each value of k_{1e} a value for the other parameters can be found which gives the same minimum value of X_r^2 . This problem only can be circumvented by reducing the number of parameters. We assumed the layers to be isotropic, thus reducing the number of parameters to four. Therefore the absolute values of n and k determined in this way will not be fully correct, as the anisotropy could not be taken into account.

The resulting profiles of n and k of sample 203 (45) are shown in figure 6.28. In this figure we see that the sample shows a strong inhomogeneity in both n and k . The interface positions are found at about the expected positions considering that the layer has been sprayed three times (indicated by arrows in the figure). The inhomogeneity inside the first 200 nm from the substrate indicates substrate-film interaction and is in accordance with the results found on the thickness dependence in section 6.4. Figure 6.29 gives the plasma wavelength λ_p and the relaxation wavelength λ_γ as a function of the position in the coating. This figure shows that λ_γ varies through the sample, while λ_p remains nearly constant.

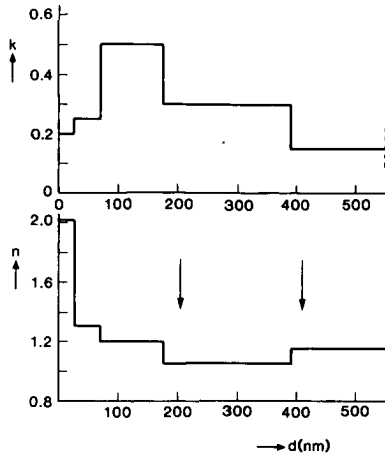


Figure 6.28 Profile of the refractive index and the extinction coefficient in coating no 203(45).

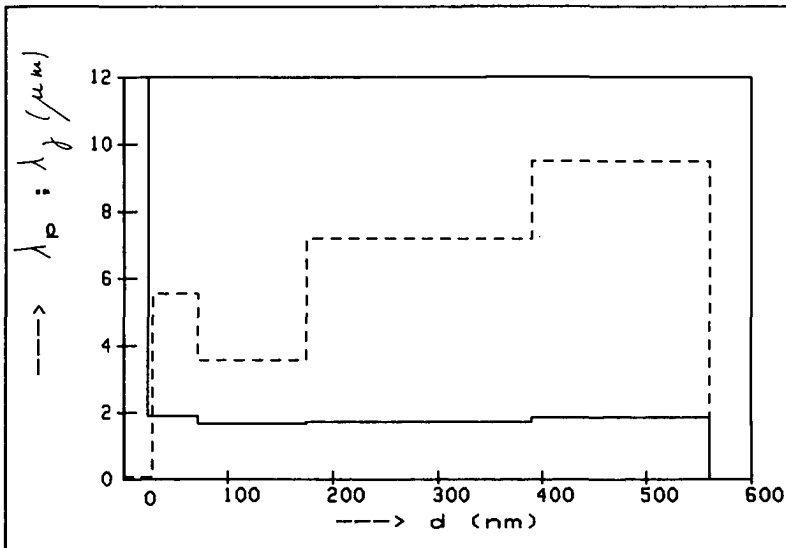


Figure 6.29 Profile of the plasma wavelength (λ_p , --) and the relaxation wavelength (λ_γ , —) derived from the refractive indexes given in figure 6.28.

This means that the electron density will be approximately constant through the layer, while the mobility varies between the different sublayers. The error resulting from the assumption of an isotropic coating can be estimated by comparing the average λ_p and λ_γ in figure 6.29 to the values given in table 6.22. This comparison shows that the value of λ_p deviates about 5% and the value of λ_γ deviates about 30% from the correct value. Near the substrate, as also observed in several other films investigated, a small, about 20 nm, non-conducting layer is present. This indicates that between the amorphous substrate and the polycrystalline film a thin transition layer is formed.

The profile given in figure 6.29 can be compared to the profiles given in section 6.4.3 for the electron density and the mobility. As $\lambda_p \sim n_-^{1/2}$ and $\lambda_\gamma \sim \mu$ the figures 6.17 and 6.18 on one hand and 6.29 on the other hand show some similarity, but the samples analyzed in section 6.4.3 seem to be more homogeneous than the sample investigated by ellipsometry. The difference between these two sample series is the spraying compound: the samples discussed in section 6.4.3 have been prepared using solution no 3 and the samples discussed in this section have been prepared using solution no 2 (see section 5.4.3).

6.9 Effects of lattice resonances

In the reflectance spectra of SnO_2 coatings, some peaks are present for $\lambda > 10 \mu\text{m}$, which cannot be attributed to the substrate. In this section it will be investigated whether this can be attributed to resonance oscillations in the SnO_2 lattice.

In general, one may represent the contribution of the oscillations to the dielectric constant by a sum of m damped Lorentz oscillators (Hamberg, 1983, 1986-1) :

$$\chi^{\text{PH}} = \sum_{j=1}^m \frac{S_j}{\lambda_j^{-2} - \lambda^{-2} - i\Gamma_j/\lambda} \quad (6.15)$$

where S_j denotes the oscillation strength, λ_j the resonance wavelength, Γ_j the damping constant and χ^{PH} is the phonon dielectric susceptibility (cf eq. 2.61). Equation (6.15) implies that oscillations result in peaks at $\lambda = \lambda_j$ in the complex part of the dielectric constant $\epsilon_c(\lambda)$. To check whether this also appears in doped SnO_2 coatings, the spectrum of $-\epsilon_c = 2 \cdot n \cdot k$ has been plotted for the three annealed samples no 310, 312 and 318 in figure 6.30.

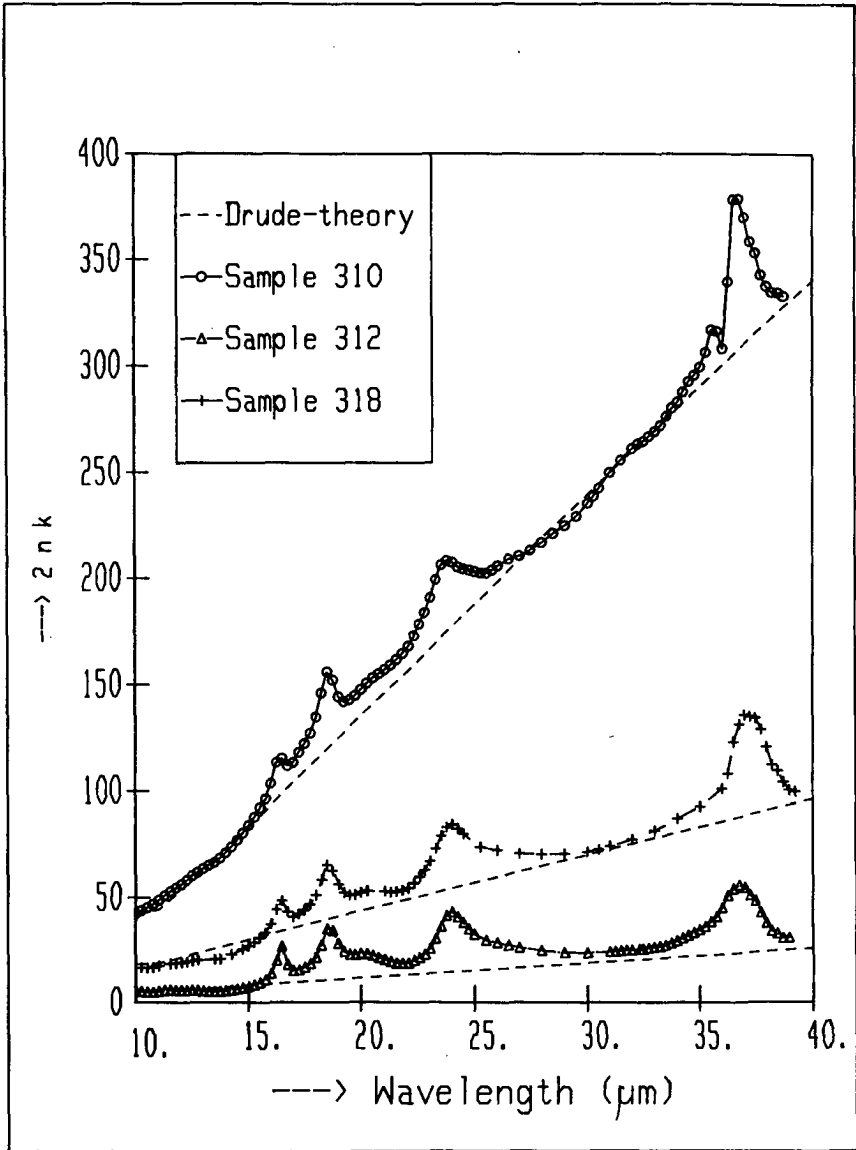


Figure 6.30 Complex part of dielectric constant as a function of wavelength for three samples compared with results as predicted by the Drude-theory

In this figure it is clearly shown that peaks are present superimposed on the free electron behaviour according to the Drude theory, where the parameters λ_p and λ_g are derived from the optical constants in the 1 - 10 μm spectral region. The peaks appear at the same wavelength and have about the same magnitude for the three samples, which means that they are independent of the Fluorine doping and must be attributed to properties of the SnO_2 crystallites.

The phonon susceptibility has been determined by subtracting ϵ_c as calculated from the Drude-theory from the measured value:

$$\chi_c^{\text{PH}}(\lambda) = \epsilon_c(\lambda)_{\text{measured}} - \epsilon_c(\lambda)_{\text{free electrons(Drude)}} \quad (6.16)$$

As shown in figure 6.24 and already mentioned in section 6.6.1, different reflectance spectra are found for samples 310, 312 and 318 before and after annealing. This is not due to the annealing itself, as an unannealed sample of the same series showed exactly the same oscillation peaks when measured at the same date as the annealed samples. It must be concluded that the infrared reflectance peak structure has changed in due course. As the electrical and structural properties of the unannealed samples have not changed we have no explanation for this effect.

Equation 6.15 has been applied to four different samples: sample 318 before annealing (sample A), sample 318 after annealing (sample B), the sample sprayed at 550 °C listed in table 6.8 (sample C) and the 633 nm coating of which the reflectance is shown in figure 6.14 (sample D). Application of equation (6.16) to samples no 310 and 312 gave nearly the same results as for sample B.

The resulting complex part of χ^{PH} of samples A, B and C is shown in figure 6.31. Sample D showed a similar behaviour as sample B, but has not been drawn in the figure for the sake of clarity. The figure shows that the different samples all give the same peak at $\lambda = 16.5 \mu\text{m}$, but the magnitude and size of the other peaks are quite different for the different samples. It can be checked whether the peaks indeed originate from the SnO_2 lattice by comparing the peak positions to measurements on SnO_2 single crystals (Summitt, 1968; van Daal, 1968) and SnO_2 powder (Szemanski, 1970). Table 6.23 gives a listing of the wavelengths at which reflectance or absorptance peaks are found according to our measurements and the literature results.

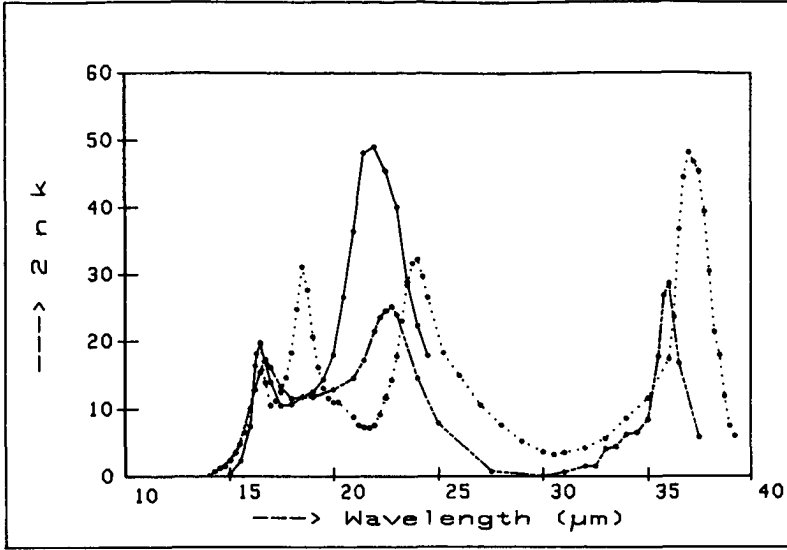


Figure 6.31 Complex part of χ'' for samples A (—), B (···) and C (— · —) (see text).

Table 6.23 Positions of reflectance or absorption peaks of tin oxide
 - : no peak found; = : no measurements

	λ_1 (μm)	λ_2 (μm)	λ_3 (μm)	λ_4 (μm)	λ_5 (μm)	λ_6 (μm)	λ_7 (μm)
Summitt (1968)	16.5	-	21.5	27.1	35.2	36.6	41.1
van Daal (1968)	16.5	-	22.0	28.0	36.0	37.0	43.5
Szemanski (1970)	16.1	18.2	-	-	-	-	-
sample A	16.5	-	21.9	=	=	=	=
sample B	16.5	18.5	24.0	-	-	37.2	=
sample C	16.8	-	22.5	-	36.0	-	=
sample D	16.4	18.2	23.4	-	-	37.8	=

The table shows that our samples show reflectance peaks at wavelengths which are also found in literature. As the reflectance of sample A has only been determined up to $\lambda = 25 \mu\text{m}$, the peak at $\lambda = 36 \mu\text{m}$ is not observed for this sample. The table also shows that the coatings can be split into two types: one type showing a reflectance peak at $\lambda = 18 \mu\text{m}$ (samples B and D) and one type which does not show a peak at this wavelength (samples A and C). As already discussed, this could not be related to any other coating property. Peaks at $\lambda \approx 42 \mu\text{m}$ could also be observed in our reflectance spectra, but they could not clearly be distinguished from the spectrophotometer noise which increases rapidly for $\lambda > 40 \mu\text{m}$.

The parameters S_j , λ_j and Γ_j in the model for χ^{PH} , could well be fitted to the measurements shown in figure 6.31. The results are summarized in table 6.24. The error in λ_j is about $0.2 \mu\text{m}$; the relative errors in S_j and Γ_j are about 10%.

Table 6.24 Parameters describing χ^{PH} for different samples

sample	A		B				C		
$\lambda_j (\mu\text{m})$	16.5	21.9	16.5	18.5	24.0	37.2	16.8	22.5	36.0
$S_j (\cdot 10^{-2} \mu\text{m}^{-2})$	0.42	1.51	0.30	0.61	0.57	0.18	0.32	0.73	0.11
$\Gamma_j (\cdot 10^{-2} \mu\text{m}^{-1})$	0.43	0.71	0.31	0.41	0.46	0.14	0.36	0.73	0.16

The determination of the parameters λ_j , S_j and Γ_j enables a refinement of the Drude-model for the complex dielectric constant. From the reflectance spectra (e.g. figure 6.4) it can be expected that the lattice oscillations have a noticeable effect on the thermal emittance only when the coating is poorly infrared reflecting. The physical reason for this is that the complex part of the dielectric constant becomes larger when the coating is more conducting, while the influence of the lattice oscillation remains the same. So the influence of the lattice oscillations on the optical properties becomes relatively less when the coating is more conducting and more infrared reflecting. Table 6.25 shows the calculations on a 500 nm coating on pyrex using the Drude model with and without the contributions of lattice oscillations. For the parameters in (6.15), the values given in table 6.24 for sample C have been taken. The table shows that the correction results in a decrease of the emittance with 0.06 for coatings showing a high emittance. The decrease of ϵ_h becomes nearly negligible (0.003) for coatings showing a low emittance.

Table 6.25 Hemispherical emittance according to the Drude-model with and without a correction for lattice oscillations

λ_p (μm)	λ_γ (μm)	ϵ_h (uncorrected)	ϵ_h (corrected)
2.0	15.0	0.146	0.143
2.0	5.0	0.309	0.299
5.0	5.0	0.692	0.636

6.10 General discussion

In this section the results obtained in the previous sections of this chapter are used to propose models which connect the optical, electrical and structural properties. A model for the dielectric constant of tin oxide coatings is discussed in section 6.10.1. In section 6.10.2 the relations between the electrical and structural properties are discussed.

6.10.1 Model for the optical properties of tin oxide coatings in the 0.25 - 50 μm spectral region

In this section the results obtained in the previous sections on the modelling of the dielectric constant of tin oxide coatings will be summarized into one equation from which the dielectric constant can be obtained in the 0.25 - 40 μm spectral region. This is the complete spectral region of interest when solar absorptance and thermal emittance are concerned. The model can be written in the form of equation (2.52) as :

$$\tilde{\epsilon}(\lambda) = \epsilon_\infty - \frac{i \lambda}{\epsilon_0 \tilde{\rho}(\lambda) 2\pi c} - \frac{i \lambda \alpha_g \sqrt{\epsilon_\infty}}{2\pi} + \sum_{j=1}^m \frac{S_j}{\lambda_j^{-2} - \lambda^{-2} - i\Gamma_j/\lambda} \quad (6.16)$$

valence electrons

free electrons

band-gap absorption

lattice oscillations

The four terms will be discussed separately below

Valence electron contribution

The valence electron contribution to the dielectric constant has not been determined explicitly. An estimate of ϵ_{∞} can be made using the refractive index of single crystal tin dioxide (see section 6.2). This gives $\epsilon_{\infty} \cong n^2 \cong 4.20$. The value for a polycrystalline coating will be lower because of a lower specific density compared to a single crystal which gives a lower average refractive index in the coating .

ϵ_{∞} has been derived for several coatings from the refractive index in the 0.6 - 1 μm spectral region. In this spectral region, n can be approximated by (see eq (2.79)) :

$$n(\lambda) = \left[\epsilon_{\infty} \left(1 - \left(\frac{\lambda}{\lambda_p} \right)^2 \right) \right]^{1/2} \quad (6.17)$$

Fitting of the parameters ϵ_{∞} and λ_p to the measured values of $n(\lambda)$ yielded values for ϵ_{∞} of 4.08 ± 0.05 for heavily doped coatings and 3.95 ± 0.05 for undoped coatings. The uncertainty in ϵ_{∞} has little effect on most calculated quantities such as the effective mass and the complex resistivity at long wavelengths. This means that the assumption that $\epsilon_{\infty} = 4$, which has been used in the preceding sections, does not introduce large errors for long wavelengths ($\lambda > 1.2 \mu\text{m}$). For short wavelengths, $\lambda < 1.2 \mu\text{m}$, the effect of the error on the complex resistivity is considerable as $\tilde{\epsilon}$ approaches ϵ_{∞} and the error in the factor $(\epsilon_{\infty} - \epsilon_r)$, which appears in the definition of the real and complex part of the resistivity, becomes large.

Free electron contribution

In figures 6.6a, b and c it is shown that $\tilde{\rho}(\lambda)$ follows the Drude model for $\lambda > \lambda_p$, and $\rho_r(\lambda)$ becomes wavelength-dependent for $\lambda < \lambda_p$, with the power-law as predicted by the modified Gerlach-Grosse theory given in section 2.4.1. This behaviour is also observed in other coatings investigated. This leads to the following expressions for $\tilde{\rho}(\lambda)$:

$$\begin{aligned} \tilde{\rho}(\lambda) &= \frac{\lambda_p^2}{2\pi c \epsilon_0 \epsilon_{\infty}} \left(\lambda_{\gamma}^{-1} - i \lambda^{-1} \right) && \text{for } \lambda > \lambda_p \\ &= \frac{\lambda_p^2}{2\pi c \epsilon_0 \epsilon_{\infty}} \left(\left(\frac{\lambda}{\lambda_p} \right)^{1.7} \lambda_{\gamma}^{-1} - i \lambda^{-1} \right) && \text{for } \lambda < \lambda_p \end{aligned} \quad (6.18)$$

Here λ_p and λ_γ are the wavelengths corresponding to the plasma frequency and the relaxation frequency which are defined by equations (2.56) and (2.59). These parameters are established when n_-, μ, m_{eff} and ϵ_∞ are known. The maximum mobility which can be obtained for a given n_-, m_{eff} and ϵ_∞ can be calculated using equations (2.71) and (2.80) for the contribution of ionized impurity scattering, which must be combined using equation (2.97) with the temperature dependent mobility given by equation (6.5), using the constants given in table 6.4.

Band gap absorption

The band gap absorption coefficient α_g in equation (6.16) is given by equation (6.8) for $h\nu > E_g$ and by equation (6.10) for $h\nu < E_g$. For α given in μm^{-1} , the photon energy $h\nu$ and the band gap energy E_g in electron volts this gives:

$$\alpha = 18.1 \cdot (h\nu - E_g)^{1/2} \quad \text{for } h\nu \geq E_g \quad (6.19)$$

and

$$\alpha = 5.6 \exp \left(\frac{hc/\lambda - E_g}{0.419} \right) \quad \text{for } h\nu < E_g \quad (6.20)$$

with

$$E_g = 4.04 + \frac{h}{4\pi \cdot 0.33m_e} (3\pi^2 n_-)^{2/3} \quad (6.21)$$

According to this model, the only electrical parameter which determines the band gap absorption is the electron density n_- which appears in equation (6.21). In this model, the effect of the band gap absorption on the refractive index n has been neglected. In practice, n increases from 2 at $\lambda \approx 400 \text{ nm}$ to 2.2 when $hc/\lambda \approx E_g$ ($\lambda \approx 300 \text{ nm}$) and decreases to 2.0 for smaller wavelengths. This effect slightly increases the reflectance at $\lambda \approx 300 \text{ nm}$ (Melsheimer, 1983).

Lattice oscillations

The contribution of lattice oscillations to the dielectric constant has been discussed in section 6.9. For the constants λ_j, S_j and Γ_j the values given in table 6.24 for samples B or C can be taken.

The effect of the extension of the model used in section 2.6 to the extended model given by equation (6.16) has little effect on the calculations of the solar absorptance and thermal emittance as carried out in section 2.6. The wavelength dependence of ρ_r and the band gap absorption mainly affect the transmittance of the coating which is not important for the application as a spectrally selective coating on a black substrate as it is indifferent whether the radiation is absorbed by the coating or by the substrate. The lattice oscillations diminish the emittance for poorly infrared reflecting coatings, but for well infrared reflecting coatings, which are of most interest, the effect of the lattice oscillations become negligible, as shown in section 6.9. This means that the model calculations carried out in section 2.6 can be assumed to be valid for fluorine doped tin dioxide coatings.

The extended model as given by equation (6.16) is of importance for applications where also the transmittance of the coating is of interest, such as the use of tin oxide as a heat-reflecting coating on window glass. Moreover, the extended model gives a good insight in the physical principles which determine the optical constants of tin dioxide coatings.

6.11.2 Relations between the electrical and structural properties

In this section an attempt is made to derive basic relations between the electrical properties of tin dioxide coatings and the structural and morphological properties, without reference to the process parameters during spraying, the spraying solution, etc. At first this problem can be split into two parts:

1. The dependence of n_2 on the amount of Fluorine and on the structural properties
2. The relation between μ and the structural properties

These problems are treated separately in the next two sections.

6.10.2.1 The free electron density

A theory for the dependence of the free electron density on the structural properties of SnO_2 has been given by Bélanger (1985) and is recapitulated here briefly. In figure 6.32 the charge distribution is sketched for crystallites along different orientation directions. At the boundaries of crystallites oriented along the (110), (211) and (301) plane, the Sn(IV) atoms are partly reduced to Sn(II).

The Sn(II) surface states behave as trapping centers for the free electrons originating from the Fluorine doping. This means that in coatings consisting of large crystallites or crystallites which are mainly oriented along the (200) direction, the effect of the Sn(II) surface states is minimized and the electron density will be about equal to the fluorine concentration.

The above, ideal case has not been observed in our coatings. From the analysis of the structural properties of a number of coatings, the $n_-/[F]$ ratio proved to depend on two factors: the grain size in the (200) direction and the oxygen excess. This is illustrated in figure 6.33. In this figure it is shown that the $n_-/[F]$ ratio is largest when the crystallite size in the (200) direction is large and when the oxygen excess is small.

The dependence on the grain size in the (200) direction is in marked agreement with the qualitative model of Bélanger. The dependence on the oxygen excess may be explained by assuming that when an excess of oxygen is present in the coating, the oxygen atoms may compensate the free electrons originating from the Fluorine atoms. Bélanger also gives a quantitative model on the free electron density, based upon the assumption that first all Sn(II) surface states must be compensated by donor electrons before free electrons occur in the coating. This predicts a constant difference between n_- and $[F]$ for the same micro structure, while we observe a constant ratio between n_- and $[F]$ (see figure 6.12). Therefore we confine ourselves to the qualitative explanation of the dependence of the $n_-/[F]$ ratio on the grain size and the oxygen excess.

The remaining question is why the $n_-/[F]$ ratio never becomes larger than about 0.30. One possibility is that the fluorine is only ionized when it is positioned in two out of the six possible oxygen positions it can occupy in a unit cell (see figure 6.1). Another possibility is that the model for the electron density as given in section 2.5, based upon the model of a single donor level in a degenerate semiconductor, is valid, in spite of the major objections which can be made against the validity of this model. When considering equation (2.98) and assuming that the donor energy is about equal to the Fermi level, equation (2.98) gives that $N_d = 3 n_-$, which is about the observed maximum for n_- . This result is also found from the temperature dependence of n_- (see table 6.3).

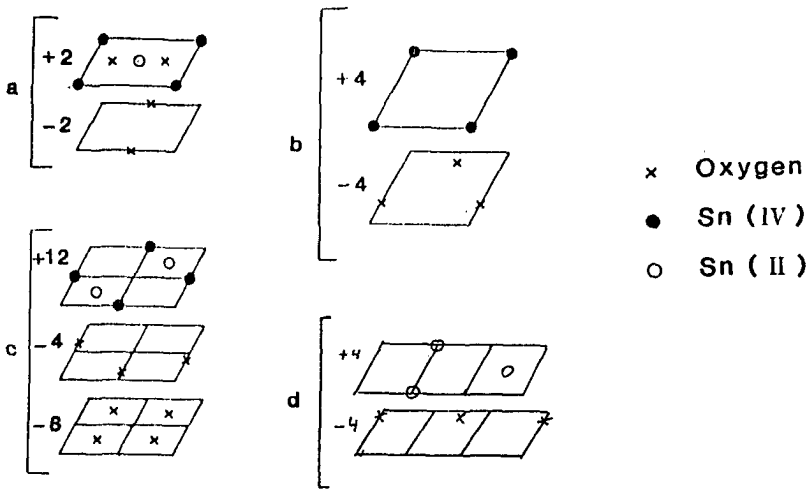


Figure 6.32 Crystallite surfaces of SnO_2 grown according to the (110) plane (a), the (200) plane (b), the (211) plane (c) and the (301) plane (d).

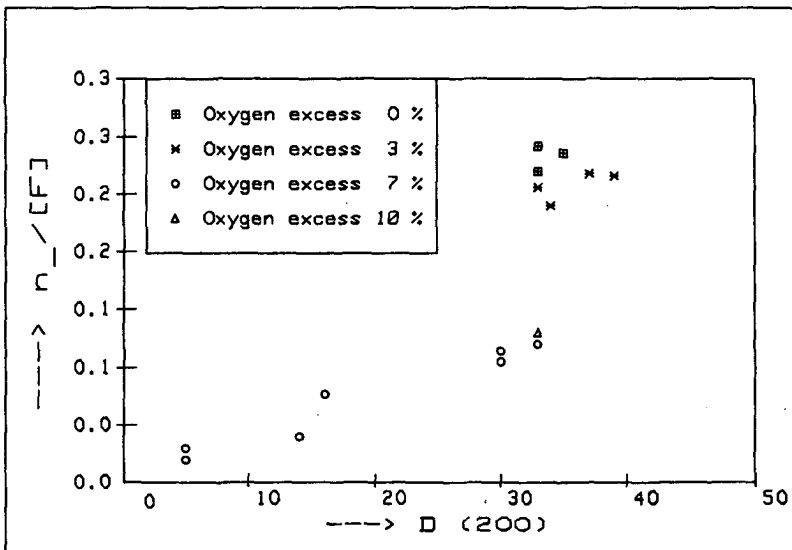


Figure 6.33 The $n_{200}/[F]$ ratio as a function of the grain size in the (200) direction.

6.10.2.2 The electron mobility

The maximum mobility which can be obtained is limited, mainly by ionized impurity scattering, as has been shown theoretically in section 2.4.1 and by measurements in section 6.3.3. In most cases this theoretical maximum is not achieved. From the analysis of a number of coatings two quantities proved to be most important in determining the mobility: the electron density and the grain size in the (200) direction. Also the presence of a preferential orientation in the (200) direction, which is correlated to a large grain size in the (200) direction in most cases, proved to be of importance. The mobility seems not to be directly influenced by an oxygen excess in the coating. The dependence of the mobility on the grain size in the (200) direction is plotted in figure 6.34. In this figure a division has been made between samples having a larger and samples having a smaller free electron density than $2 \cdot 10^{26} / \text{m}^3$. The figure shows a reasonable linear dependence for both cases with an exception for the undoped sample no 312 (see section 6.3.3).

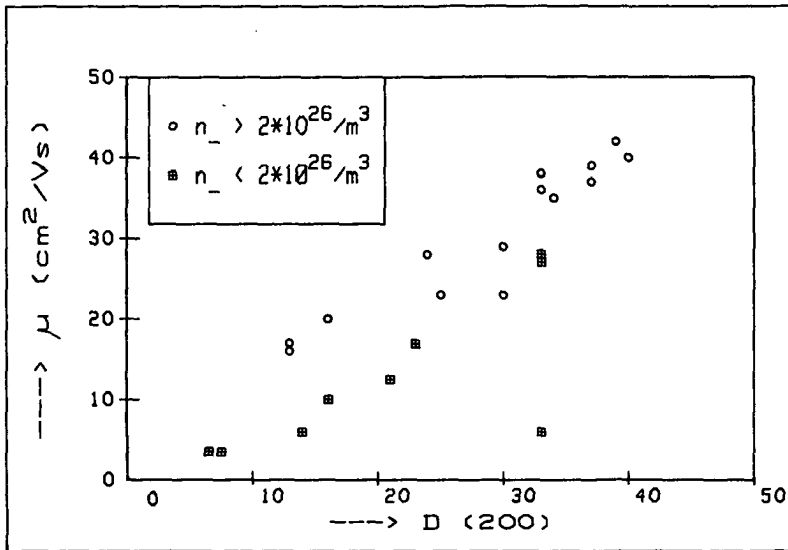


Figure 6.34 Dependence of the mobility on the grain size in the (200) direction. The point right below indicates the result for sample no 312.

A complicating factor in this analysis is that only the electrical mobility could be used. The optical mobility has been determined for a few samples only. If the optical mobility is considered it can be expected that some points in figure 6.34 with a low electron density will move upward, as is anyhow the case with sample no 312 (see table 6.2).

As stated in section 6.10.2.1, the (200) orientation direction is a trap-free orientation. This means that along a crystallite oriented in the (200) direction, charge carriers originating from donor atoms are not trapped at the surface, but can contribute to the conductivity. This also means that no potential barrier is present between grains which are both oriented in the (200) direction. If it is assumed that electrons can freely move between neighbouring grains with a (200) orientation, it is clear that a strong preferential orientation and a large grain size in the (200) direction will diminish the scattering of the free electrons in the grains against grain boundaries. Following this approach it can also be understood why a high electron density is favourable for obtaining a high mobility: when the electron density is high, the electrons have a high Fermi energy and will more easily skip the potential barriers between the grains. It should be noted that the scattering against grain boundaries discussed here is essentially an effect differing from the grain boundary scattering as discussed in section 2.4.4. In section 2.4.4. it is assumed that the electrical mobility is limited by the electrical properties of the regions between the grains, while in this section the effect of grain boundaries on the free electron inside the grains is considered. This kind of grain boundary scattering will affect the DC- as well as the optical mobility. The scattering will be nearly temperature independent as the Fermi energy of the electrons is nearly temperature independent.

Scattering of free electrons in a grain against grain boundaries becomes significant when the free range ℓ is of the same order of magnitude as the grain size. Though the grain size in the (200) direction is about 40 nm for the coatings having the largest grain size and mobility, the grain size in the other directions is usually smaller. When considering the reflection of an electromagnetic plane wave on a coating consisting of crystallites with a (200) preferential orientation, the electric field acts on the electrons parallel to the surface. This means that for this case the grain size in the (002) direction is decisive when comparing the electron free range to the grain size. As shown in tables 6.7 and 6.10, the grain size in the (002) direction is about 20 nm, which gives an average free range of about 10 nm for the free electrons in the grain.

This implies a maximum mobility of $80 \text{ cm}^2/\text{Vs}$. Combining this with a maximum mobility of $45 \text{ cm}^2/\text{Vs}$ due to ionized impurity scattering this gives an effective mobility of $27 \text{ cm}^2/\text{Vs}$.

Experimentally, this is about the value which is found for the optical mobility when the electron density is low (table 6.2) or when there is no preferential orientation in the (200) direction (table 6.8). In these cases the electrical mobility may be even lower due to a poor conduction in the inter granular regions.

The discussion above can be summarized into the following hypotheses:

- when the optical mobility is lower than the theoretical maximum, this is due to scattering of free electrons in the grains against grain boundaries.
- a preferential orientation and a large grain size in the (200) direction favour a high mobility and a high electron density, as electrons are not trapped in the grain boundaries and so between grains having a (200) orientation no potential barriers due to trapped electrons are present.
- a large electron density favours a high mobility as the Fermi energy increases with the electron density and electrons with a high energy will less be influenced by potential barriers between the grains.

These effects are well illustrated by the coating series with increasing thickness (see figures 6.17 and 6.18 and table 6.7). Inside the first 100 nm of the coating, several crystal orientations are present, the electron density is lower than in the rest of the coating and the mobility is less than the theoretical maximum of about $45 \text{ cm}^2/\text{Vs}$. In the rest of the coating mainly the (200) orientation is present, the electron density is higher and the mobility approaches the theoretical maximum (see figure 6.18).

For obtaining a heavily doped coating with large grains and a preferential orientation in the (200) direction, the most important process conditions are a spraying solution containing a sufficient amount of fluorine and a high substrate temperature ($600 \text{ }^\circ\text{C}$ or more, depending on the spraying solution).

6.11 Conclusions for application in solar collectors

On basis of the results obtained we will discuss in the next sections the application as a spectrally selective coating for solar collectors. First the solar absorptance is considered, then the thermal emittance.

6.11.1 The solar absorptance

As the coating thickness and the mobility have little influence on the solar absorptance α (see section 2.6.2), variation of these parameters is not useful to affect the solar absorptance. This is because the reflective properties of the coating in the solar spectral region are mainly governed by the value of ϵ_{∞} which is a material constant which cannot be changed.

The main possibilities to improve α are surface roughing and application of an anti reflection coating.

The coating surface has an intrinsic roughness due to the polycrystalline structure. This roughness is maximal when the coating is deposited at a high temperature (see figure 6.22) with a large thickness (see figure 6.19). These are also the conditions at which a minimum ϵ_n is obtained. The effect of this intrinsic roughness has been determined by polishing the coatings. This caused the solar absorptance to increase by about 0.01 (from 0.91 to 0.92), so the roughness improves the solar absorptance with 0.01 relative to a smooth coating for which the calculations in section 2.6.2 have been made. This corresponds to a 25 nm coating which represents the surface roughness according to the model given in section 2.2.6. This is also about the maximum surface roughness which is determined using the R-T method (see section 4.1) and ellipsometry (see table 6.20). It has been tried to improve the solar absorptance further by grinding the coating by very fine grinding powder. This was not successful: either no effect was observed, either the complete coating was removed. The other possibility, application of an additional anti-reflection coating, has been tried in literature (Frank, 1981) and leads to about a result as calculated in section 2.7 ($\alpha = 0.96$). However, it is questionable whether this method can be cost-effective.

6.11.2 Coating with lowest emittance obtained

The best heat-reflecting coating has been obtained using solution no 3 as the spraying solution and pyrex as the substrate. The coating has been sprayed using air as a carrier gas at a pressure of 2.5 Bar at a substrate temperature of 600 °C in 11 cycles of 2 seconds, resulting in a 620 nm coating with electrical properties: $n = 3.2 \cdot 10^{26} / \text{m}^3$, $\mu = 51 \text{ cm}^2 / \text{Vs}$ and $\rho = 3.8 \cdot 10^{-6} \Omega \text{m}$. The reflectance and transmittance of this coating are given in figure 6.35. The hemispherical emittance, determined with the apparatus described in section 3.3, is 0.145 and the value obtained from the optical constants is 0.151.

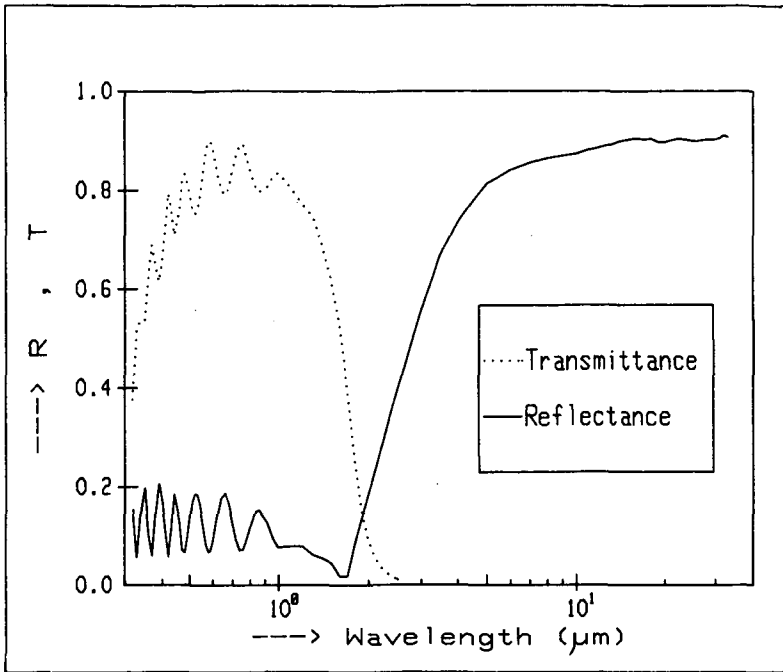


Figure 6.35 Reflectance and transmittance of the best heat-reflecting tinoxide coating obtained

The solar absorptance of this layer, defined by equation (2.5), is 0.888. When correcting this value for the reflectance at the backside of the substrate, a solar absorptance of 0.92 can be expected when applying this coating on black enamel. The fraction of the solar radiation transmitted by the coating is 0.757. This means that 13.1 % of the solar radiation is absorbed by the coating itself. This is no problem when the coating is used on black enameled steel, but it may be of importance when the coating is used on a glass cover of a solar collector, or on window glass. In these cases it may be advantageous to apply a thinner coating which is less heat-reflecting, but transmits more solar radiation.

The hemispherical emittance of 0.15 is comparable to the best values found in literature (Simonis, 1979, 1987) and is close to the theoretical minimum of about 0.13 which can be obtained (see figure 2.26).

7. INDIUMOXIDE COATINGS

In this chapter the properties of indiumoxide (In_2O_3) coatings are discussed. Some properties of indiumoxide coatings have been studied already exhaustively in the literature; we did not find it useful to repeat these investigations. These properties are the fundamental bandgap absorption and the infrared lattice oscillations, which are fully discussed in the review paper by Hamberg and Granqvist (1986-1).

The general properties of In_2O_3 coatings are described in section 7.1. In section 7.2 the physical effects of doping an In_2O_3 coating with tin are discussed. The effects of annealing these coatings is discussed in section 7.3. Effects of varying the coating thickness are discussed in section 7.4 and in section 7.5 the influence of the substrate temperature is analyzed. Section 7.6 gives a discussion of the best coating obtained and a final discussion of the results is given in section 7.7.

7.1 General properties of indiumoxide (In_2O_3)

At normal pressure In_2O_3 crystallizes in a cubic structure of the bixbyite Mn_2O_3 (I) type (also called the C-type rare-earth oxide structure). The lattice parameter is 10.12 Å and the density is 7.18 g/cm³ (Wheast, 1985). The complicated crystal structure (a unit cell contains 80 atoms) has precluded band structure calculations. The fundamental optical bandgap is 3.75 eV as has been determined from measurements on single-crystal plates of In_2O_3 (Weiher and Ley, 1966).

7.2 Effects of tin doping

A series of coatings has been produced using solution no 5 (see section 5.4.3) with a tin/indium atomic concentration fraction in the solution of 0, 1, 2, 4, 6, 8 and 12 % respectively. The coatings were sprayed with air as the carrier gas on glass substrates at a substrate temperature of 550 °C in 4 cycles of 2 seconds each. The resulting coating thickness and the electrical properties are summarized in table 7.1. In this table it is shown that the electron density and the mobility increase with the tin/indium fraction up to a fraction of 4%, after which they decrease somewhat. The optical and the temperature dependent electrical properties are more conveniently discussed in connection with the properties after annealing, as is done in the next section.

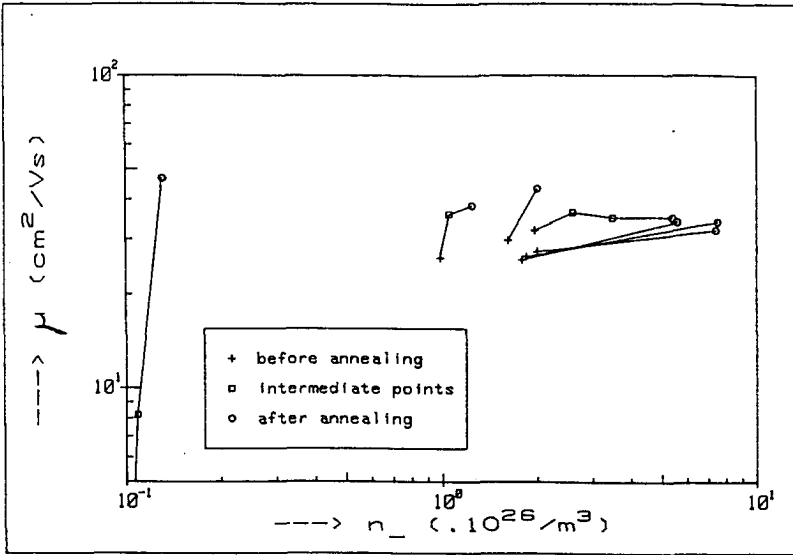


Figure 7.1 Mobility and electron density of coatings before and after annealing

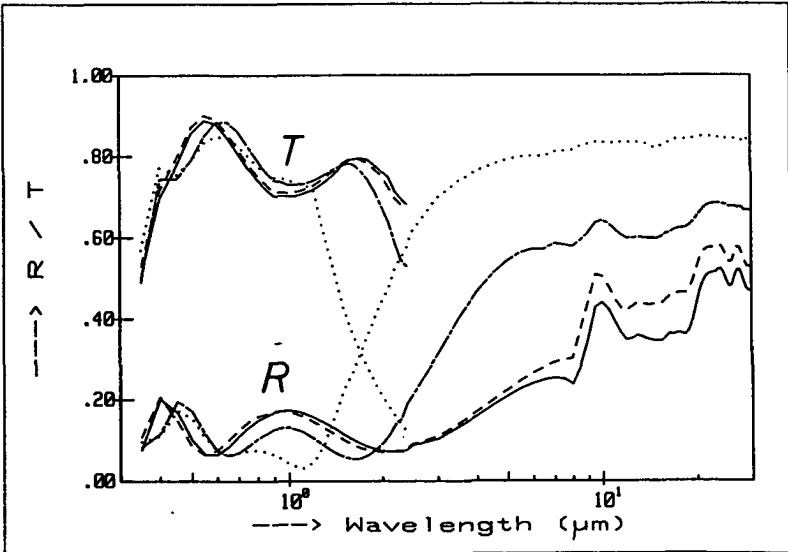


Figure 7.2 Reflectance (R) and transmittance (T) of coatings doped with 1% tin before (—) and after (---) annealing and doped with 12 % tin before (—) and after (···) annealing

Table 7.1 Thickness and electrical properties of coatings with a different tin/indium fraction

Sn/In fract. (%) in solution	thickness d (nm)	n_{-} ($\cdot 10^{26}/m^3$)	μ (cm^2/Vs)	ρ (Ωm)
0	142	-	-	$9.6 \cdot 10^{-2}$
1	142	0.98	26.1	$2.44 \cdot 10^{-5}$
2	143	1.61	29.8	$1.30 \cdot 10^{-5}$
4	147	1.96	32.0	$9.95 \cdot 10^{-6}$
6	138	1.78	25.8	$1.36 \cdot 10^{-5}$
8	166	1.84	26.4	$1.29 \cdot 10^{-5}$
12	175	2.00	27.4	$1.14 \cdot 10^{-5}$

7.3 Annealing effects

Annealing the coatings in vacuum or in a hydrogen atmosphere proved to have a large influence on the electrical properties of the coatings. In general, of coatings having a low electron density particularly the mobility increases when they are annealed, while of coatings having a high electron density particularly the electron density increases. This has also been observed by Frank and Köstlin (1982). It is illustrated in figure 7.1, where the mobility and the electron density of the samples listed in table 7.1 are shown before and after annealing. Annealing has the largest effect on the undoped sample, where the conductivity increases with a factor of 1000. Also on the heavily doped samples having a tin doping of 6, 8 and 12 %, where the conductivity increases with a factor of 5, the effect of annealing is considerable.

7.3.1 Electrical and optical properties

The optical properties also change when the coatings are annealed. This is illustrated in figure 7.2, where the reflectance and the transmittance of the coatings with 1 and 12 % tin doping are given. In this figure it is shown that the infrared reflectance increases according to the increase in mobility for the coating with 1 % tin doping. For the coating with 12 % tin doping the infrared reflectance increases and the reflection edge shifts to a lower wavelength, according to the increase of the electron density in this coating.

The real and complex part of the resistivity $\hat{\rho}(\lambda)$ have been determined in the same way as for SnO₂ coatings in section 6.3.2. This enables a comparison between the optical and electrical properties, which has been carried out in an analogous way as in section 6.3.3. Figures 7.3 and 7.4 give the values of $\hat{\rho}(\lambda)$ for the unannealed and annealed case respectively for the cases of doping with 1, 2 and 12 % tin. Theoretical curves are drawn based on the ionized impurity scattering theory given in section 2.4.1. Also the plasma wavelengths and the DC-resistivities are indicated in the figures. In the figures it is shown that in the measured curves a similar power-law dependence of $\rho_r(\lambda)$ is observed for $\lambda < \lambda_p$ as in the calculated curves. The measured $\rho_r(\lambda)$ accords well with the measured DC-values in all cases. In the case of the 2 and 12 % tin-doped, annealed coatings the measured and calculated curves of $\rho_r(\lambda)$ almost overlap, which means that for these coatings the maximum attainable mobility due to ionized impurity scattering has almost been achieved.

The power-law dependence of $\rho_r(\lambda)$ for $\lambda < \lambda_p$ has also been observed by Frank (1983). A similar agreement between the measured and calculated curves of $\rho_r(\lambda)$ as in the case of the 2 and 12% tin-doped, annealed coatings has been obtained by Hamberg (1984, 1986-1,2) for heavily doped ($n_> 5 \cdot 10^{26}/\text{m}^3$) coatings prepared by reactive electron-beam evaporation.

The optical and electrical properties of the coatings doped with 1, 2 and 12 % tin before and after annealing are summarized in table 7.2.

Table 7.2 Electrical and optical properties determined at room temperature

% Sn/In	before/after annealing	$n_>$ $10^{26}/\text{m}^3$	μ cm^2/Vs	λ_p μm	m_{eff} m_{el}	μ_{opt}	μ_{max}
1	before	0.99	27.4	3.10	0.21	29	82
	after	1.29	38.0	3.04	0.27	33	57
2	before	1.60	29.5	2.44	0.21	34	75
	after	2.06	43.6	2.45	0.28	40	49
12	before	2.14	28.1	2.09	0.21	32	72
	after	6.56	33.6	1.52	0.30	32	36

In the table some interesting effects are observed. The effective mass m_{eff} increases due to annealing, which causes the maximum mobility μ_{max} to decrease. An other effect is that the optical mobility μ_{opt} , as defined by equation (6.3), is generally slightly larger than the DC-value for unannealed coatings and smaller for the annealed coatings.

The effects of annealing can be explained by presuming that the excess oxygen present in the coating is removed by the annealing process. This excess oxygen, which is originally present in the coating reduces the conductivity in two ways:

- a. It reduces the free electron density by acting as a trapping center for the electrons originally induced by the dopant.
- b. It reduces the mobility by acting as a scattering center for the remaining electrons.

This hypothesis, proposed by Frank (1983), explains the effects of annealing on the mobility and the electron density as shown in figure 7.1 and in table 7.2. As the optical and the DC-mobility do not differ much, the grain boundaries do not play an important role, but because of the change in the difference between optical and DC-mobility it can be assumed that part of the excess oxygen is present at the grain boundaries.

The effective masses listed in table 7.2 are of the same magnitude as found in the literature. Clanget (1973) finds a value of 0.28 when the electron density is low which increases with increasing n_- to 0.32 for $n_- \approx 5.5 \cdot 10^{26} / \text{m}^3$. This trend is also observed for the annealed coatings in table 7.2, though the absolute values are somewhat smaller. This supports the suggestion of Weiher and Ley (1966) that the conduction band is not parabolic. Other values found in the literature are 0.24 (Singh, 1986), 0.30 (Müller, 1968) and 0.35 (Köstlin, 1975).

7.3.2 Tin concentration and free electron density

The tin content of some coatings has been determined by electron microprobe analysis. It proved that the tin content in the coating was about 1/2 to 1/3 of the tin content in the solution. This is not in agreement with the results of some authors who find that the tin content of the coating is about the same as in the spray solution (Köstlin, 1975; Frank, 1982). The free electron density is plotted against the tin density in the coating in figure 7.5. In this figure also a theoretical curve, based on the assumption that each tin atom gives rise to one free electron, has been drawn.

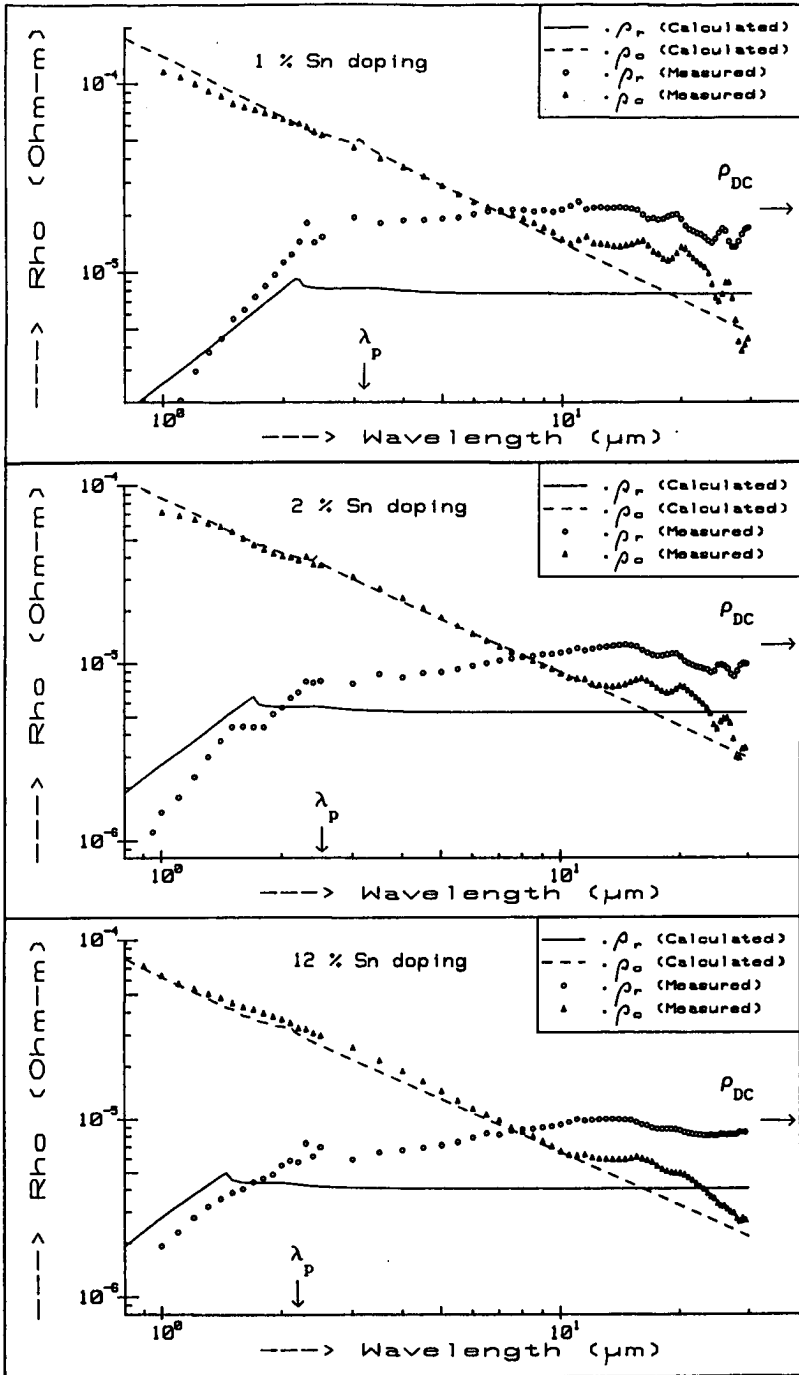


Figure 7.3 Real and complex part of the resistivity of coatings doped with 1, 2 and 12 % of tin before annealing. Curves calculated from the modified Gerlach-Grosse theory are also shown.

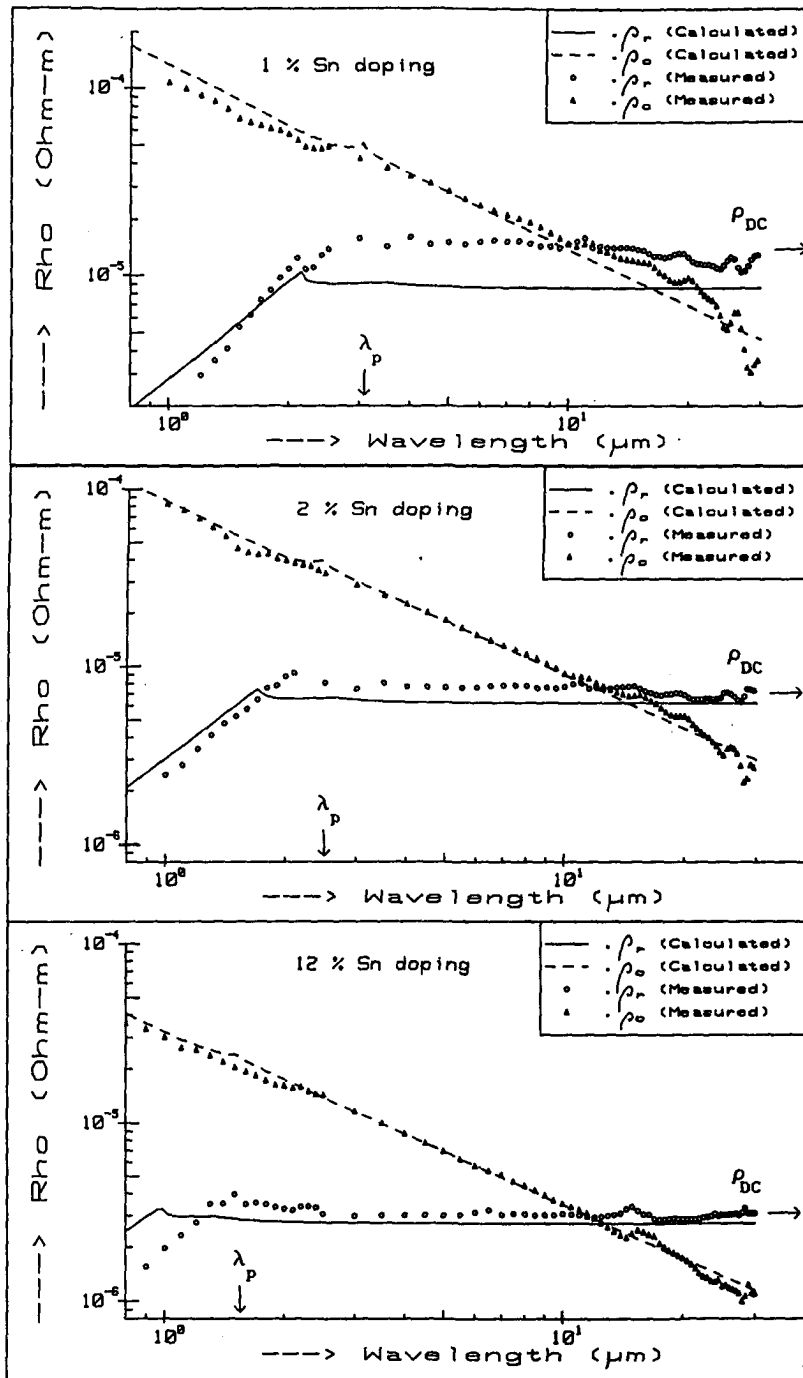


Figure 7.4 Real and complex part of the resistivity of coatings doped with 1, 2 and 12 % of tin after annealing. Curves calculated from the modified Gerlach-Grosse theory are also shown.

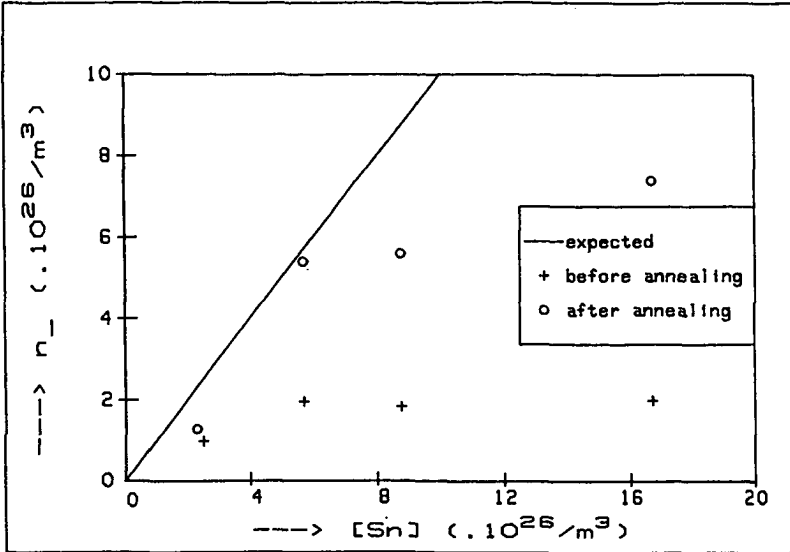


Figure 7.5 Free electron density vs. the tin concentration

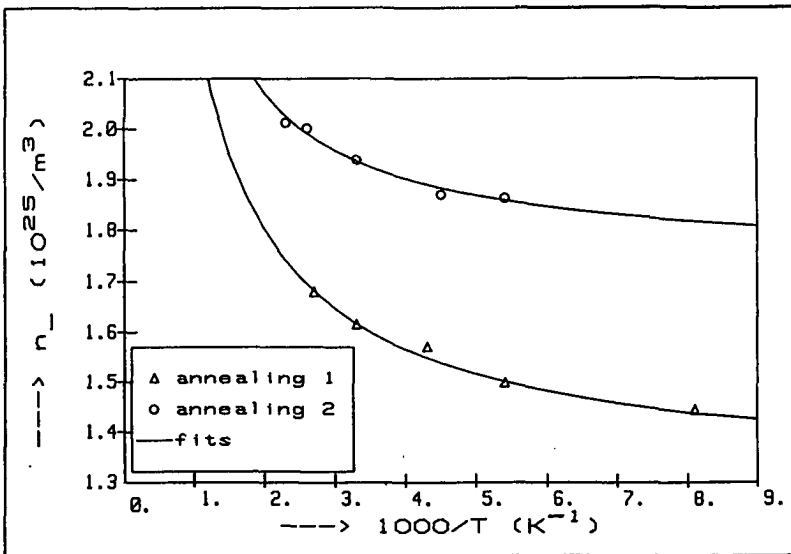


Figure 7.6 Temperature dependence of the electron density of the 0.2% doped coating after one (Δ) and after two (o) annealing stages. The fits to the theoretical model are also shown.

The figure shows that in one case, the annealed coating with a 4% Sn/In fraction in the spraying solution, the expected electron density has been achieved. In the other cases the free electron density is less, especially in the unannealed cases. These results are quite different from the results for fluorine doped SnO_2 coatings, where a maximum electron density of about one third of the donor concentration is found.

According to Frank (1982), a smaller electron density than the tin concentration can be attributed to additional oxygen which is still present in the coating. Frank claims that the free electron density equals the tin concentration when the coating is annealed at 500°C at a partial oxygen pressure of less than 10^{-20} bar. The maximum electron density found in his determinations is $1.5 \cdot 10^{27}/\text{m}^3$, which corresponds to a 5 % tin doping of the coating. This tin doping corresponds to the solubility limit of about 5% tin in In_2O_3 (Frank, 1979).

We have annealed our coatings at a lower temperature (350°C), where the partial oxygen pressure has been reduced by evacuation to about 10^{-6} bar and by introducing H_2 gas in the vacuum chamber. Probably in our case this annealing procedure was not in all cases sufficient to achieve the highest possible electron density .

7.3.3 Temperature dependence of the electrical properties

The temperature dependence of the electron density n_- and the mobility μ have been determined for two samples at different stages of annealing. These different stages have been achieved by slowly raising the sample temperature in vacuum until a certain decrease of the resistivity has been achieved, after which the sample is cooled down quickly. Two coatings have been used for these measurements: the coating doped with 4% tin of which some measurements have been given in the previous sections, and a coating doped with about 0.5 % tin. The latter coating has been prepared to obtain a coating with a low mobility before annealing.

7.3.3.1 Electron density

The electron density increased about 15 % for the 0.5 % doped coating in the first annealing stage and less than 1% for the 4% doped coating in the (final) second annealing stage. The parameters E_d and N_d in the model described in section 2.5 were fitted to the measurements. In figure 7.6 it is shown that this model describes well the temperature dependence of the electron density in the case of partly annealed In_2O_3 coatings.

Table 7.3 Donor density and donor energy level

doping	annealing stage	n_- (T=300 K) ($\cdot 10^{26}/m^3$)	m_{eff}^\dagger ($\cdot m_e$)	N_d ($\cdot 10^{26}/m^3$)	$-E_d$ (eV)
0.5 %	0	0.214	0.15	0.744 [†]	0.157
0.5 %	1	0.183	0.15	0.786	0.135
0.5 %	2	0.219	0.15	0.744	0.163
0.5 %	3	0.329	0.15	0.774	0.232
0.5 %	4	0.482	0.15	1.311	0.294
0.5 %	5	0.495	0.15	1.346	0.297
0.5 %	0	2.07	0.21	5.70 [†]	0.559
0.5 %	1	3.49	0.25	10.4	0.721
0.5 %	2	5.50	0.28	17.1	0.805

† estimated values

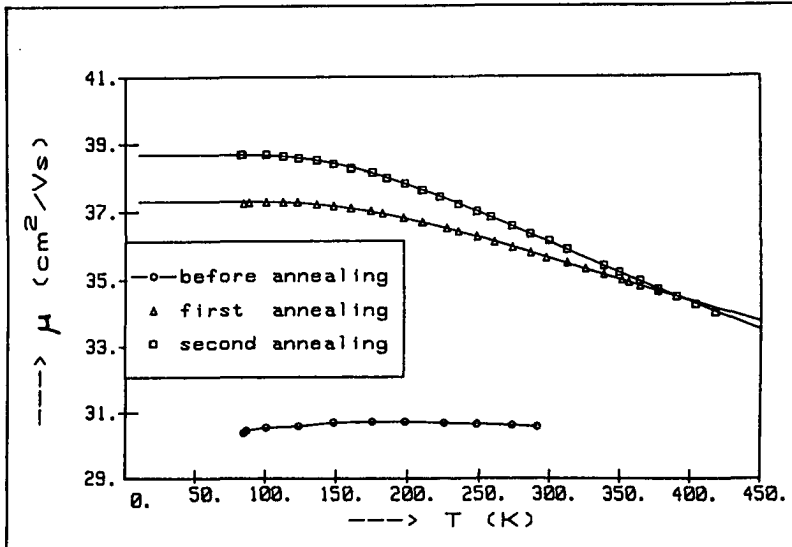


Figure 7.7 Mobility of the 4% tin-doped coating for the unannealed case and after one and two annealing stages as a function of temperature

Table 7.3 gives the resulting donor density N_d and donor energy level E_d . In some cases one of the parameters had to be estimated as the measurements were not accurate enough to determine both parameters. Table 7.3 shows that N_d and $|E_d|$ increase with increasing electron density. It is found that $N_d \approx 3 \cdot n_-(300 \text{ K})$ which has also been obtained in section 6.3.4.1. However, in the case of the annealed coatings with $n_- > 2 \cdot 10^{26} / \text{m}^3$, n_- proved to be totally temperature-independent, i.e. the variation was less than 0.01% in the 80-400 K temperature range. In these cases a model with $E_d = -\infty$ and $N_d = n_-$ can as well be fitted to the measurements. This means that here the model can no longer be used unambiguously and it can also be assumed that the free electron density about equals the donor density. This agrees with the results found in section 7.3.2 in the sense that the annealed coatings have an electron density which is larger than one third of the donor concentration.

7.3.3.2 Mobility

The mobility as a function of temperature determined for the 4 % doped coating is shown in figure 7.7 and for the 0.5 % doped coating in figure 7.8. In these figures it is observed that the mobility increases with temperature when the mobility is low, while it decreases with temperature when the mobility is high. This has also been observed in the case of SnO_2 coatings in section 6.3.4.2, so we can repeat the conclusions derived for SnO_2 that also in the case of In_2O_3 coatings grain boundary scattering determines the mobility when the mobility is low and phonon scattering determines the temperature dependence of the mobility when the mobility is high.

Equation (6.5), which predicts the mobility for a combination of longitudinal optical phonon scattering and neutral or ionized impurity scattering, has been used to fit the measured data of the samples having a decreasing mobility with temperature. The resulting constants in eqn. (6.5) are shown in table 7.4.

Table 7.4 Constants describing the temperature dependence of the mobility

Tin doping	annealing stage	μ_0 (cm^2/Vs)	θ_{10} (K)	C_{10} ($\cdot 10^4 \text{ VsK}/\text{m}^2$)
0.2 %	2	20.30	930 ± 50	2.9 ± 0.5
0.2 %	3	26.71	890 ± 150	1.5 ± 0.5
0.2 %	4	47.47	873 ± 13	2.79 ± 0.09
0.2 %	5	59.72	824 ± 10	2.92 ± 0.11
4 %	1	37.30	916 ± 20	1.85 ± 0.06
4 %	2	38.68	867 ± 15	2.26 ± 0.03

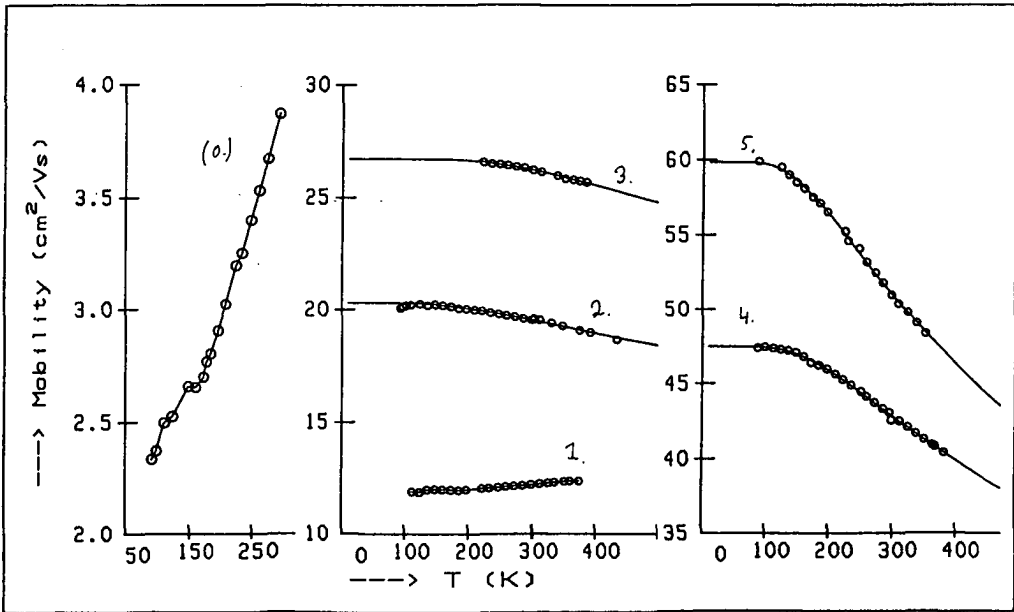


Figure 7.8 Mobility of the 0.2% tin-doped coating for the unannealed case and after up to five annealing stages as a function of temperature

The fits are also drawn in figure 7.7 and in figure 7.8 for annealing stages 2, 3, 4 and 5. In the figures it is observed that the measurements can well be represented by eqn. (6.5). Table 7.4 shows that the constants θ_{10} and c_{10} are not too different between the samples but the differences are larger than in the case of SnO_2 (see table 6.4). A striking result is that the constants θ_{10} and c_{10} in tables 6.4 and 7.4 have about the same magnitude. This means that the temperature dependence of the mobility in SnO_2 and In_2O_3 coatings is about equal.

7.4 Coating thickness effects

7.4.1 Preparation conditions

A series of coatings having a different thickness has been produced. The solution no 3 (see section 5.4.3) with a 4% tin/indium ratio has been used. The coatings have been produced on pyrex substrates using nitrogen as the carrier gas at a pressure of 3 Bar and a substrate temperature of 600 °C. The spraying time was 5 seconds per cycle and the number of spraying cycles was 1, 2 and 4 for the different samples respectively. This resulted in coatings of 80, 160 and 300 nm thickness.

7.4.2 Optical and electrical properties

The reflectance and transmittance of the three coatings are shown in figure 7.9. The transmittance decreases and the infrared reflectance increases with increasing coating thickness, as expected.

The characteristic electrical and optical properties are listed in table 7.5. The table shows that the optical and electrical properties tend to improve with the coating thickness. It is also observed that the electron density and the mobility which are achieved without annealing are higher than in the coatings prepared with an equal tin doping described in section 7.2. The difference is that in this case the coatings have been prepared using nitrogen as the carrier gas instead of air in the case discussed in section 7.2. This will cause less excess oxygen to be incorporated in the coating.

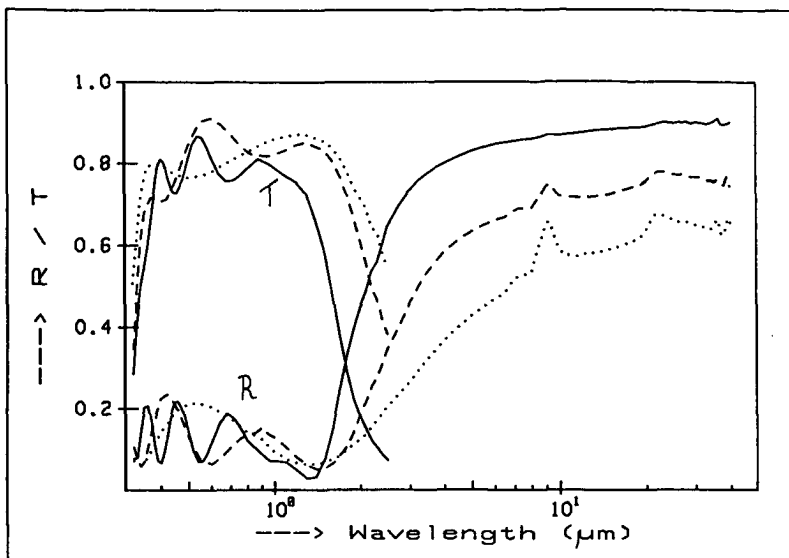


Figure 7.9 Reflectance and transmittance of coatings of 80 nm (···), 160 nm (---) and 300 nm (—) thickness.

Table 7.5 Electrical and optical properties determined at room temperature

thickness (nm)	n_{-} ($\cdot 10^{26}/m^3$)	μ_{DC} (cm^2/Vs)	λ_p (μm)	m_{eff} ($\cdot m_e$)	μ_{opt} (cm^2/Vs)	μ_{max} (cm^2/Vs)
80	3.65	37.6	1.87	0.28	37	48
160	3.21	38.3	1.89	0.26	37	55
300	4.22	47.7	1.72	0.28	45	47

7.4.3 X-ray diffraction measurements

In table 7.6 the results of X-ray diffraction measurements are given. The intensity measurements are calibrated against the (400) peak in the 300 nm sample. In the table a strong preferential orientation in the (400) direction is observed for the 160 nm and 300 nm coatings. The intensity and the grain size of the (222) peak slightly decrease with the thickness. This indicates that a re-orientation in the first 80 nm of the coating takes place when subsequent layers are deposited during the spraying process. In the literature, a preferential (400) orientation is observed by nearly all authors (Hecq, 1973; Köstlin, 1975; Singh, 1983; Ratcheva, 1986) with Mammana (1981), who finds a (222) preferential orientation, as the only exception. The latter result might be related to the small grain size of 3-10 nm in the coatings.

The conclusion of Fan (1977), that the electrical and optical properties appear to be independent of the orientation effects, is confirmed by our results. The crystal orientations in the 80 and the 300 nm coating are very different, but the difference in optical and electrical properties of these coatings (table 7.5) is much less dramatic.

Table 7.6 Results of X-ray diffraction measurements on coatings with different thicknesses

thickness (nm)	80	160	300	randomly oriented In_2O_3
crystal plane				
	Relative Intensity			
(211)	< 2.8	< 2.8	3.1	14
(222)	9.0	7.6	6.2	100
(400)	8.0	28	100	30
(431)	< 2.8	< 2.8	< 2.8	10
(440)	< 2.8	< 2.8	< 2.8	35
(622)	< 2.8	5.8	9.0	25
	Grain size (nm)			
(211)	-	-	23	
(222)	23	23	18	
(400)	31	31	37	
(622)	-	25	25	

7.4.4 Scanning electron micrographs

Scanning electron micrographs have been taken from the sample surface. Figure 7.10 gives the pictures of the 80 nm and the 300 nm coatings. Just like in the case of tin oxide coatings the grain size observed at the surface increases with the coating thickness. When comparing the grain size to the 100 nm bar on the pictures it can be observed that the grains are about 30 nm when the coating thickness is 80 nm and about 100 nm when the coating thickness is 300 nm. The first value corresponds well to the grain size obtained from X-ray diffraction in table 7.6. The second value is much larger than the value obtained in table 7.6. This indicates that in this case the grains observed at the coating surface consist of coagulations of grains as they are observed by X-ray diffraction.

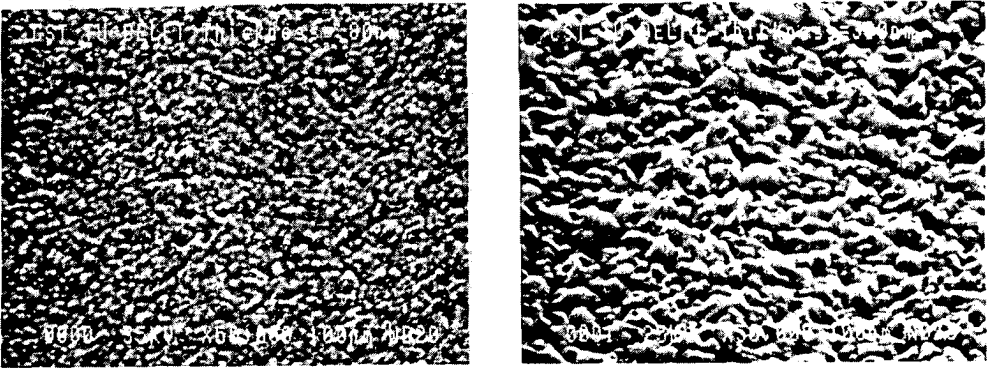


Figure 7.10 Scanning electron micrographs of a 80 nm (left) and of a 300 nm In_2O_3 coating (right)

7.5 Influence of the substrate temperature

A series of coatings has been produced at a different substrate temperature during the spraying process. Solution no 4 (see section 5.4.3) with a tin/indium ratio of 0.02 has been used as the spraying solution. The coatings were produced on window pane using air as the carrier gas at a pressure of 2.5 Bar in 4 cycles of 2 seconds each. The thickness and the electrical properties of the coatings are given in table 7.7. In this table it is shown that the thickness, electron density and the mobility increase with the substrate temperature. The increase of the electron density and the mobility may be a combined effect of the increasing coating thickness and the increasing substrate temperature.

Table 7.7 Thickness and electrical properties of coatings prepared at different substrate temperatures

Substrate temperature (°C)	400	450	500	550	600
Thickness d (nm)	30	52	70	88	96
n_{-} ($\cdot 10^{26}/m^3$)	1.1	1.9	2.1	2.0	2.1
μ_{DC} (cm^2/Vs)	11	12	25	29	32

In the 500 - 600 °C range the electrical properties do not change much, particularly not when compared to the preparation of tin oxide coatings (see section 6.5, table 6.9).

Using the same spraying solution as we do, Frank (1982) uses a substrate temperature of 500 °C. Siefert (1984) concludes that the In_2O_3 coatings are polycrystalline when the substrate temperature is larger than 350 °C.

Most authors use an alcoholic solution of $InCl_3$. Of these authors, Kulaszewicz (1981) finds that amorphous films are formed when the substrate temperature is 400 °C or lower. The optimum spraying temperatures obtained with this solution are 450 °C (Pommier, 1981) to 500 °C (Manificier, 1979; Ratcheva, 1986). An more extensive analysis of the influence of the preparation conditions on the coating properties has not been carried out in the literature, probably because the coating properties do not change much when the preparation conditions are about optimal.

7.6 Best coating obtained

The best coating obtained with respect to the thermal emittance is the 300 nm coating discussed in section 7.4. The hemispherical emittance, calculated from the optical constants, $\epsilon_{h,400K}$ is 0.150. The solar absorptance, defined by equation (2.3), is 0.866. When correcting this value for the reflectance at the backside of the substrate, a solar absorptance of 0.90 can be expected when applying this coating on black enamel. The solar transmittance of the coating/substrate system is 0.733. The solar absorptance and transmittance are less than in the case of the best tin oxide coating, because the plasma wavelength is so low ($\lambda_p = 1.72 \mu m$) that part of the near-infrared solar spectrum is reflected (see also the calculations in section 2.6.2, figure 2.22).

When preparing a 500 nm coating with the same optical properties, the hemispherical emittance would become 0.132. The emittance can be reduced further by using a more heavily doped coating, but a larger electron density causes the plasma wavelength to decrease, so the solar absorptance will decrease rapidly when the emittance is reduced in this way.

7.7 Final discussion

The tin-doped indiumoxide coatings behave very similar to fluorine doped tin oxide coatings. The equation which gives the dielectric constant has the same form as equation (6.16), where only the band-gap absorption and the lattice oscillations are to be modelled with different constants (see Hamberg and Granqvist, 1986-1). The terms ϵ_{∞} and $\tilde{\rho}(\lambda)$ can be modelled exactly as in section 6.9, and even constants such as the effective mass and the constants describing the temperature dependence of the mobility have the same magnitude as in the case of a doped tin oxide coating.

The coating properties are slightly dependent on the spraying conditions where, besides the substrate temperature which must be high enough to obtain a polycrystalline coating, the composition of the atmosphere in which the coating is prepared seems to be the most critical. An excess of oxygen in the coating influences the free electron density and the mobility in a negative way.

When the maximum obtainable mobility due to ionized impurity scattering is not achieved in a sprayed coating, it will probably be achieved after annealing the coating in a reducing gas at 350 °C at minimum. The electron density also increases as a result of the annealing procedure. At maximum, a free electron density about equal to the tin concentration can be achieved. This is more than in the case of a fluorine doped SnO₂ coating, where the free electron density is at maximum one third of the fluorine concentration.

A relation between the structural and electrical/optical properties could not be established. This relation, if present, is much less strong as in the case of tin oxide coatings.

The best coating obtained has a hemispherical emittance of 0.150 and will have a solar absorptance of about 0.90 when applied to black enamelled steel. The emittance can be further reduced, but this will also reduce the solar absorptance. This means that the optimum properties for application as a spectrally selective layer are about equal to those of an optimized fluorine doped tin oxide coating.

8. CONCLUDING REMARKS

In this chapter the main conclusions of the preceding chapters will be restated briefly and commented.

8.1 Theoretical investigations

In chapter 2, some theoretical investigations have been carried out. It is shown that the matrix formalism for optical calculations on isotropic planar structures can be extended to the case of anisotropic films, very thick layers and, within some limits, to surface roughness.

Calculations, based on the assumption that the coating behaves optically according to an extended Drude-model, show that the solar absorptance is hardly affected by the coating properties as long as the plasma wavelength is larger than $1.8 \mu\text{m}$ and the coating thickness is larger than 150 nm. The solar absorptance can be improved from 0.90 to about 0.93 when roughing the surface and to 0.96 by application of an additional SiO_2 anti-reflection coating.

Calculations on the emittance show that, when the electron mobility is limited by ionized impurity scattering, the minimum infrared emittance which can be achieved depends on the plasma wavelength and on the electron effective mass. For the case of SnO_2 and In_2O_3 coatings with a plasma wavelength of $2 \mu\text{m}$ and an effective mass of at least 0.20 this gives a minimum hemispherical emittance of about 0.13 at 400 K. This means that already on a theoretical base, it should not be expected that, without decreasing the solar absorptance, an emittance lower than 0.13 can be achieved.

8.2 Characterization methods

In chapters 3 and 4 it is shown that, using two spectrophotometers which can determine the normal-hemispherical reflectance and transmittance in the $0.25\text{--}2.5 \mu\text{m}$ spectral range and the normal specular reflectance in the $0.3\text{--}40 \mu\text{m}$ spectral range, all basic optical properties of SnO_2 and In_2O_3 coatings could be derived:

- the solar absorptance is obtained from an integration of the normal-hemispherical reflectance in the $0.3\text{--}2.5 \mu\text{m}$ spectral range

- the coating thickness is obtained from the interference minima in the 0.4-1.0 μm spectral region
- the optical constants and the surface roughness in the 0.3-2.5 μm spectral region are obtained from the spectral reflectance and transmittance using the R-T method or the envelope method
- the optical constants in the 2.5-40 μm spectral region are obtained from a Kramers-Kronig integration of the reflectance spectrum. A correction method, which corrects for the substrate optical constants and leads to the reflectance of a semi-infinite medium to which the Kramers-Kronig integration can be applied, proves to give correct results.
- the hemispherical emittance of the coating-substrate system can be calculated straightforward once the coating and substrate optical constants are known in the 2.5-40 μm spectral region.

Further optical analysis has been carried out by determining the normal-hemispherical reflectance in the 2.0-15 μm spectral region. Using ellipsometry, the inhomogeneity and the anisotropy of the coating can be determined. The angular thermal emittance can also be determined directly with the apparatus described in section 3.3.2.

The electrical properties, i.e. the resistivity and the Hall coefficient, can be well determined as a function of the temperature using the apparatus as described in section 3.4.

8.3 The spray pyrolysis coating process

The spray pyrolysis process, as it is described in section 5, can well be used to prepare spectrally selective SnO_2 and In_2O_3 coatings. In most cases the coating must be deposited in several preparation cycles to obtain a sufficient thickness. This is due to the fast decrease of the substrate temperature when the coating is deposited, combined with the high temperature sensitivity of the deposition process.

The spectrally selective coating properties of tin oxide, which are described in chapter 6, improve with the substrate temperature up to a temperature of 650 à 700 $^\circ\text{C}$ for all chemical spraying solutions used. The best coating is produced at the shortest spraying time per cycle. This spraying time should not exceed 4 seconds. Somewhat better coating properties are obtained when using oxygen instead of nitrogen as the carrier gas. It has been tried to examine the influence of the droplet size and the gas pressure, but as these quantities are very related in the used equipment, these influences could not clearly be distinguished.

In our equipment, a carrier gas pressure of 3 Bar can be used at best. At this pressure, the used ultrasonic nozzle produces droplets with an average diameter of about 12 μm .

8.4 Results on SnO_2 coatings

Chapter 6 gives the results on SnO_2 coatings. It is shown that doping SnO_2 coatings with fluorine increases the electron density and the mobility in the coating. The free electron/fluorine ratio in the coating increases with the crystallite grain size in the (200) direction and decreases with the excess of oxygen. The dependence on the crystalline size is qualitatively in accordance with the theory of Bélanger which predicts that free electrons are trapped at grain boundaries when crystallites are oriented different from the (200) direction. At maximum an electron density of 1/3 of the fluorine concentration in the coating has been obtained. The maximum electron density which can be obtained is about $4 \cdot 10^{26}/\text{m}^3$. The plasma wavelength decreases with an increasing electron density according to an effective mass of about $0.25m_e$ and is about 1.8 μm at a maximum electron density.

The real part of the complex resistivity ρ_r derived from the optical constants behaves as $\rho_r \sim \lambda^{1.7}$ for $\lambda < \lambda_p$ where λ and λ_p are the wavelength and the plasmawavelength respectively, as is predicted by the modified Gerlach-Grosse theory for ionized impurity scattering. When the mobility is larger than about 20 cm^2/Vs , ρ_r is constant for $\lambda > \lambda_p$ and corresponds to the DC-resistivity. For $\lambda > \lambda_p$, the optical properties accord to the classical Drude theory. The maximum mobility of about 45 cm^2/Vs which has been obtained, roughly equals the maximum mobility predicted by the theory for ionized impurity scattering. This means that for these coatings the maximum attainable heat reflectance, leading to an emittance $\epsilon_{h, T=400\text{K}}$ of about 0.15, has been obtained. The mobility slightly decreases with the temperature. This temperature dependence can conveniently be described by a theory of optical phonon scattering.

When the maximum mobility has not been reached, this can be due to two factors: a too weak preferential orientation in the (200) direction or a too small electron density in the coating. This dependence is qualitatively in accordance with the theory of Bélanger when it is considered that electrons trapped at grain boundaries of crystallites which are oriented different from the (200) direction, form potential barriers which reduce the mobility.

In coatings having a very low doping level, or having a very weak preferential orientation, the electrical mobility may be further limited by the poorly conducting intergranular regions. This case is characterized by a small electrical mobility relative to the optical mobility, and by a mobility which increases with the temperature. The models which are commonly used to describe the temperature dependence for this case, give unsatisfactory results when applied to our coatings.

The fundamental absorption in the UV spectral region is well described by a direct band gap absorption and a logarithmic band edge (also called Urbach tail). The fundamental band gap has been determined to be 4.08 eV. With increasing electron density the bandgap shifts to smaller wavelengths according to a Burstein-Moss shift with a 'band-band' effective mass of 0.33 m_e . A model for the dielectric constant is further completed with describing the infrared reflectance peaks using three or four damped Lorentz oscillators.

The relatively low solar absorptance of 0.91 of a smooth coating on an absorbing glass-like substrate is mainly caused by the refractive index in the visible spectrum, which is about 2 and is inherent to the crystal structure. The intrinsic surface roughness of a coating may enhance the absorptance with 0.01. A SiO_2 anti reflection coating will increase it further up to 0.96.

The spectrally selective properties of the coatings prove to be little affected by an ageing test where they are kept at 500 °C during ten days. The coating aged in air showed no change at all. However, the coating aged in vacuum shows a decrease of the optical transmittance, a considerable loss of electrical conductivity and an increase in the emittance from 0.16 to 0.22 due to the ageing process. The increase of the emittance is due to the appearance of infrared absorption bands, of which the exact origin could not be identified. The solar absorptance is not affected in all cases.

These results indicate that tin oxide coatings can withstand stagnation temperatures up to 500 °C. This, together with the mechanical hardness, makes them very suitable for the use as a spectrally selective coating in a solar collector.

8.5 Results on indium oxide coatings

The results on indium oxide coatings are given in chapter 7. In this chapter it is shown that the dielectric function of tin-doped indium oxide coatings can be modelled analogous as in the case of tin oxide coatings. Only the band-gap absorption and the lattice oscillations are to be modelled with different constants.

Annealing the coating in a reducing gas at 350 °C enhances the free electron density and the mobility, as far as the maximum obtainable mobility due to ionized impurity scattering was not achieved. At maximum, a free electron density about equal to the tin concentration can be achieved. The maximum free electron density obtained is about $7 \cdot 10^{26}/\text{m}^3$, which is apparently larger than in the case of tin oxide coatings.

A relation between the structural and electrical/optical properties could not be established. This relation, if present, is much less strong as in the case of tin oxide coatings.

The optimum spectrally selective coating properties are similar to those of a fluorine doped tin oxide coating. The hemispherical emittance of 0.15 and the solar absorptance of about 0.90 when applied on a glass-like absorbing substrate are the limits for the same reasons as in the case of tin oxide coatings.

8.6 Final conclusions

An extensive insight has been obtained in the relations between the optical, electrical and structural coating properties. In this thesis, they can be related to the spray pyrolysis process we have used, but they are generally applicable to SnO_2 and In_2O_3 coatings. When preparing SnO_2 or In_2O_3 coatings under optimum conditions, a thermal emittance of about 0.15 and a solar absorptance of 0.92 can be achieved. It could be shown that it is not possible to decrease the emittance further as in the optimum case the electron mobility, and so the thermal infrared reflectance, is mainly limited by ionized impurity scattering which is inherent to the presence of ionized donor atoms.

The solar absorptance can be further enlarged to 0.96 by an additional SiO_2 anti reflection coating. Because of the good spectrally selective properties and the very good thermal, mechanical and chemical stability, tin oxide coatings are very attractive for use as a spectrally selective coating.

As In_2O_3 coatings are much more expensive and do not have better properties in this respect, they are not attractive for this purpose. The In_2O_3 coatings can achieve a higher conductivity as a higher doping level can be achieved. For this reason they may be more attractive for applications where the reflectance in the near-infrared solar spectrum is no problem or is even desired.

PRINCIPAL SYMBOLS

Complex latin symbols are printed in bold, e.g. n : the complex refractive index. Complex greek symbols are denoted with a '~', e.g. $\tilde{\rho}$: the complex resistivity.

Latin symbols:

symbol	meaning	dimension (in basic SI units)
a	absorption coefficient	m^{-1}
a_0^*	effective Bohr radius	m
A	area	m^2
A	ellipsometric analyzer angle	-
B	magnetic field strength	$kg\ s^{-2}\ A^{-1}$
c	light velocity	$m\ s^{-1}$
c_v	specific heat at constant volume	$kg\ m^2\ s^{-2}\ mol^{-1}\ K^{-1}$
C	ellipsometric compensator angle	-
d	coating thickness	m
D	electric displacement	$kg\ m\ s^{-3}\ A^{-1}$
e	elementary charge	$s\ A$
E	electric field strength	$kg\ m\ s^{-3}\ A^{-1}$
E_d	donor energy level	$kg\ m^2\ s^{-2}$
E_o	Urbach energy	$kg\ m^2\ s^{-2}$
E_s	solar irradiant energy	$kg\ s^{-3}$
h	heat loss coefficient	$kg\ s^{-3}\ K^{-1}$
h	Planck constant	$kg\ m^2\ s^{-1}$
\hbar	$h/(2\pi)$	$kg\ m^2\ s^{-1}$
I	radiant intensity	$kg\ m^{-1}\ s^{-2}\ sr^{-1}$
I	electric current	A
k	extinction coefficient	-
k_o	ordinary extinction coefficient	-
k_e	extraordinary extinction coefficient	-
\underline{k}	electron wavevector	m^{-1}
k_F	electron Fermi wavenumber	m^{-1}
k_B	Boltzmann constant	$kg\ m^2\ s^{-2}\ K^{-1}$

symbol	meaning	dimension (in basic SI units)
ℓ	electron free range	m
m	mass	kg
m_e	electron mass	kg
m_{eff}	electron effective mass	kg
M_b	Planck radiant intensity	$\text{kg m}^{-1} \text{s}^{-3}$
n	refractive index	-
n_o	ordinary refractive index	-
n_e	extraordinary refractive index	-
n_t	trapped electron density	m^{-2}
n_-	electron density	m^{-3}
N	interference order	-
N_c	quantum concentration	m^{-3}
N_i	ion density	m^{-3}
N_d	donor atom density	m^{-3}
P	dipole moment	A s m^{-2}
P	gas pressure	$\text{kg m}^{-1} \text{s}^{-2}$
P	ellipsometric polarizer position	-
q	heat current density	kg s^{-3}
r	amplitude reflectance	-
R	reflectance	-
R	resistance	$\text{kg m}^2 \text{s}^{-3} \text{A}^{-2}$
R_H	Hall coefficient	$\text{m}^3 \text{A}^{-1} \text{s}^{-1}$
S	oscillation strength	m^{-2}
t	time	s
t	amplitude transmittance	-
T	transmittance	-
T	temperature	K
v_F	electron fermi velocity	m s^{-1}
V	potential difference	$\text{kg m}^2 \text{s}^{-3} \text{A}^{-1}$
z	z-axis coordinate	m
Z	number of elementary impurity charges	-

Greek symbols

α	absorption coefficient	m^{-1}
α_g	band gap absorption coefficient	m^{-1}

symbol	meaning	dimension (in basic SI units)
α_a	absorber solar absorptance	-
α_s	solar absorptance	-
β	phase shift	-
β^{-1}	spin degeneracy factor	-
γ	relaxation frequency	s^{-1}
Γ	Gamma function	-
Γ	damping constant	m^{-1}
δ	skin depth	m
Δ	ellipsometric phase shift angle	-
ϵ	relative dielectric permittivity	-
ϵ	thermal emittance	-
ϵ_0	free space permittivity	$kg^{-1} m^{-3} s^4 A^2$
ϵ_∞	relative permittivity at $\omega=\infty$	-
ϵ_h	hemispherical thermal emittance	-
ϵ_a	absorber thermal emittance	-
ϵ_c	cover thermal emittance	-
ϵ_d	dimensionless donor energy	-
ϵ_s	relative permittivity at $\omega=0$	-
θ	polar angle	-
θ_D	Debye temperature	K
θ_R	characteristic temperature	K
θ_{lo}	characteristic temperature	K
κ	wavenumber	m^{-1}
λ	wavelength	m
λ_p	plasma wavelength	m
λ_γ	relaxation wavelength	m
μ	magnetic permeability	$kg m s^{-2} A^{-2}$
μ	electron mobility	$kg^{-1} s^2 A$
ν	photon frequency	s^{-1}
ρ	resistivity	$kg m^3 s^{-3} A^{-2}$
σ	Stefan-Boltzmann constant	$kg s^{-3} K^{-4}$
σ	surface roughness standard deviation	m
σ	conductivity	$kg^{-1} m^{-3} s^3 A^2$
σ_s	sheet conductivity	$kg^{-1} m^{-2} s^3 A^2$
τ	relaxation time	s
τ_c	cover solar transmittance	-

symbol	meaning	dimension (in basic SI units)
ϕ	azimuthal angle	-
ϕ	phase shift angle	-
ϕ_b	grain boundary potential	$\text{kg m}^2 \text{s}^{-2}$
ϕ_F	Fermi level	$\text{kg m}^2 \text{s}^{-2}$
ϕ_p	pseudo activation energy	$\text{kg m}^2 \text{s}^{-2}$
Φ	ellipsometric amplitude ratio angle	-
χ	dielectric susceptibility	-
χ_r^2	reduced chi-square value	-
ω	circular frequency	s^{-1}

REFERENCES

- Abass, A.K. et.al., "Electrical and optical properties of chemically deposited SnO : I coatings". *Solar Energy Materials* **17** (1988) pp 425 - 453.
- Agashe, C. et.al., "Structural properties of Sn₂O :F films deposited by spray pyrolysis". *Solar Energy Materials* **17** (1988) pp 99 - 118.
- Agnihotri, O.P. and B.K. Gupta, *Solar selective surfaces*.
John Wiley & Sons, New York, 1981.
- Alonso, M. and E.J. Finn, *Fundamental University Physics III: Quantum and Statistical Physics*. Addison Wesley, Reading, 1975.
- Ashcroft, N.W. and N.D. Mermin, *Solid State Physics*. Holt, Rinehart and Winston, New York, 1976.
- Azzam, R.M.A. and N.M. Bashara, *Ellipsometry and polarized light*, North-Holland, Amsterdam, 1977.
- Banerjee, R. and D. Das, "Properties of tin oxide films prepared by reactive electron beam evaporation". *Thin Solid Films* **149** (1987) pp 291 - 301.
- Beensh-Marchwicka, G., L. Król-Stepniewska and A. Misiuk, "Influence of annealing on the phase composition, transmission and resistivity of SnO_x thin films". *Thin Solid Films* **113** (1984) pp 215 - 224.
- Bélanger, D. et.al., "Thickness dependence of transport properties of doped polycrystalline tin oxide films". *J. Electrochem. Soc.* **132** (1985) pp 1398 - 1405.
- Bevington, P.R., *Data reduction and error analysis for the Physical Sciences*. Mc-Graw Hill, New York, 1969.
- Blakemore, J.S., *Semiconductor statistics*. Pergamon Press, Oxford, 1962.
- Blandenet, G., M. Court and Y. Lagarde, "Thin layers deposited by the pyrosol process". *Thin Solid Films* **77** (1981) pp 81 - 90.
- Blatt, F.J., *Physics of electronic conduction in solids*, Mc Graw-Hill, New York, 1968.
- Bruggeman, D.A.G., "Berechnung verschiedener physikalischer Konstanten von heterogenen Substanzen". *Ann. Phys.* **24** (1935) pp 636 - 664.
- Chopra, K.L., S. Major and D.K. Pandya, "Transparent conductors, a status review". *Thin Solid Films* **102** (1983) pp 1 - 46.
- Clanget, R., "Ionized impurity scattering in degenerate In₂O₃". *Applied Physics* **2** (1973) pp 247 - 256.

- Daal, H.J. van, "The static dielectric constant of SnO_2 ". J. Appl. Phys. **39** (1968) pp 4467 - 4479.
- Demichelis, F. et.al., "Physical properties of chemically sprayed tin oxide and indium tin oxide conductive films". J. Phys. D: Appl. Phys. **18** (1985) pp 1825 -1832.
- Drummeter, L.F. and G. Hass, in: Physics of Thin Films (G. Hass and R.E Thun (eds)), p 305. Academic Press, New York, 1964.
- Duffie, J.A. and W.A. Beckman, Solar Engineering of Thermal Processes, John Wiley & Sons, New York, 1980.
- Elich, J., E.C. Boslooper and H. Haitjema, "Electrical properties of sprayed tin oxide layers". Thin Solid Films **177** (1989)
- Erginsoy, C., "Neutral impurity scattering in semi-conductors". Phys. Rev. **79** (1950) pp 1013 - 1014.
- Fan, J.C., F.J. Bachner and G.H. Foley, "Effect of O_2 pressure during deposition on properties of rf-sputtered Sn-doped In_2O_3 films". Applied Physics Letters **31** (1977) pp 773 - 775.
- Fantini, M. and I. Torriani, "The compositional and structural properties of sprayed SnO_2 :F thin films". Thin Solid Films **138** (1986) pp 255 - 265.
- Frank, G., H. Köstlin and A. Rabenau, "X-ray and optical measurements in the In_2O_3 - SnO_2 system". Phys. Stat. Sol. (a) **52** (1979) pp 231 - 238.
- Frank, G., E. Kauer and H. Köstlin, "Transparent heat-reflecting coatings based on highly doped semiconductors". Thin Solid Films **77** (1981) pp 107 - 117.
- Frank, G. and H. Köstlin, "Electrical properties and defect model of tin-doped indium oxide layers". Applied Physics **A27** (1982) pp 197 - 206.
- Frank, G. et.al., "Transparent heat-reflecting coatings for solar applications based on highly doped tin oxide and indium oxide". Solar energy materials **8** (1983) pp 387 - 398.
- Gainsbury, M.J., "Industrial production of low emissivity coatings". in: Solar Optical Materials, M.G. Hutchins (ed.), Pergamon Press, Oxford, 1988.
- Gerlach, E. and P. Grosse, "Scattering of free electrons and dynamical conductivity". Festkörperprobleme **17** (1977) pp 157 - 193.
- Geurts, J. et.al., "SnO films and their oxidation to SnO_2 : Raman scattering, IR reflectivity and X-Ray diffraction studies". Thin Solid Films **121** (1984) pp 217 - 225.

- Granqvist, C.G., "New functional window coatings for automotive applications". in: M.G. Hutchins (ed), Solar Optical Materials, Pergamon Press, Oxford, 1988.
- Gray, D.E. (ed.), American Institute of Physics handbook. Mc. Graw Hill, New York, 1972.
- Grosse, P. et.al., "Preparation and growth of SnO₂ thin films and their optical and electrical properties". Thin Solid Films 90 (1982) pp 309 - 315.
- Groth, R. and E. Kauer, "Warmte-isolatie van natriumlampen". Philips Technisch Tijdschrift 26 (1965) pp 270 - 276.
- Haitjema, H. and J. Elich, "Investigations on Fluorine-doped tin dioxide films". in : Proceedings SPIE 653, C.-G. Granqvist (ed.) (1986) pp 137 - 141.
- Haitjema, H. and J. Elich, "The physical properties of fluorine-doped tin dioxide films and the influence of ageing and impurity effects". Solar Energy Materials 16 (1987) pp 79 - 90.
- Haitjema, H., J. Elich and C.J. Hoogendoorn, "The physical properties of Fluorine-doped tin dioxide coatings for Solar Collectors". in : Advances in Solar Energy Technology, W.H. Bloss and F. Pfisterer (ed.) pp 677 - 681, Pergamon Press, Oxford, 1988.
- Haitjema, H., "The physical properties of pyrolytically sprayed tin dioxide coatings". in: Solar Optical Materials, M.G. Hutchins (ed.) pp 69-76, Pergamon Press, Oxford, 1988.
- Haitjema, H. and G.F. Woerlee, "Analysis of tin dioxide coatings by Multiple Angle of Incidence ellipsometry". Thin Solid Films 169 (1989) pp 1 - 16.
- Haitjema, H., J. Elich and C.J. Hoogendoorn, "The optical, electrical and structural properties of Fluorine-doped, Pyrolytically sprayed tin dioxide coatings". Solar Energy Materials 18 (1989) pp 283 - 297.
- Hamberg, I. and C.G. Granqvist, "Dielectric function of "undoped" In₂O₃". Thin Solid Films 105 (1983) pp L83 - L86.
- Hamberg, I. et.al., "Band-gap widening in heavily Sn-doped In₂O₃". Phys. Rev. B30 (1984) pp 3240 - 3249.
- Hamberg, I. and C.-G. Granqvist, "Evaporated Sn-doped In₂O₃ films : Basic optical properties and applications to energy-efficient windows". J. Appl. Phys. 60 (1986-1) pp R123 - R160.
- Hamberg, I. and C.G. Granqvist, "Theoretical model for the optical properties of In₂O₃:Sn films in the 0.3-50 μm range" Solar Energy Materials 14 (1986-2) pp 241 - 256.

- Hamberg, I. and C.-G. Granqvist, "Optical properties of transparent and heat-reflecting indium-tin-oxide films: Refinements of a model for ionized impurity scattering". *J. Appl. Phys.* 59 (1986-3) pp 2950 - 2952.
- Harbeke, G., "Optical Properties of Semiconductors". in : *Optical properties of Solids*, F. Abelès (ed.), North Holland, Amsterdam, 1972.
- Heavens, O.S., *Optical Properties of thin solid films*, Dover Publications, New York, 1965.
- Hecq, M., A. Dubois et J. van Cakenberghe, "Étude par diffraction de rayons X de films à base d'oxydes d'étain et d'indium". *Thin Solid Films* 18 (1973) pp 117 - 125.
- Heereveld, A.A.M.T. van, *Surface roughness and spectral selectivity*, PhD. Thesis. Van Denderen, Groningen, 1988.
- Hjortsberg, A., "Determination of optical constants of absorbing materials using transmission and reflection of thin films on partially metallized substrates: analysis of the new (T, R_m) technique". *Applied Optics* 20 (1981) pp 1254 - 1263.
- Houston, J.E. and E.E. Kohnke, "Photoelectric analysis of imperfections in grown stannic oxide crystals". *J. Appl. Phys.* 36 (1965) pp 3931 - 3938.
- Howarth, D.J. and E.H. Sondheimer, "Scattering by optical phonons". *Proc. Roy. Soc.* A219 (1953) pp 53 - 71.
- Iida, H. et.al., "Sb-doped SnO_2 films deposited by the CMD (Chemical Mist Deposition) method". *Solar Energy Materials* 17 (1988) pp 407 - 424.
- Islam, M.N. and M.O. Hakim, "Post-deposition heat treatment of polycrystalline SnO_2 thin films prepared by the pyrosol process". *J. Phys. D : Appl. Phys.* 19 (1986) pp 615 - 621.
- Jackson, J.D., *Classical Electrodynamics*, 2nd ed. Wiley, New York, 1975.
- Jarzebski, Z.M., *Oxide Semiconductors*. Pergamon Press, Oxford, 1983.
- Jarzebski, Z.M. and J.P. Marton, "Physical properties of SnO_2 materials". *J. Electrochem. Soc.* 123 (1976) pp 199C - 205C.
- Johnson, E. J., "Absorption near the fundamental edge". in: *Semiconductors and Semimetals*, Vol. 3, R.K. Willardson and A.C. Beer (ed.), Academic Press, New York, 1967.
- Justus, C.G. and M.V. Paris, *Modelling solar spectral irradiance and radiance at the bottom and top of a cloudless atmosphere*, Georgia institute of technology, Georgia, 1987.

- Karlsson, T., A. Roos and C.-G. Ribbing, "Optical selectivity and crystallization in pyrolytic SnO₂-Films". *Physica Scripta* 25 (1982) pp 772 - 774.
- Karlsson, T., A. Roos and C.-G. Ribbing, "Influence of spray conditions and dopants on highly conducting tin dioxide films". *Solar Energy Materials* 11 (1985) pp 469 - 478.
- Kim, K.H. and J.S. Chun, "X-ray studies of SnO₂ prepared by chemical vapour deposition". *Thin Solid Films* 141 (1986) pp 287 - 295.
- Koch, H., "Elektrische Untersuchungen an "zusatzfreien" Zinndioxydschichten hoher Elektronenkonzentration im Temperaturbereich zwischen 90 °K bis etwa 290 °K". *Phys. Stat. Sol.* 3 (1963) pp 1059 - 1071.
- Köhl, M., K. Gindele and M. Mast, "Accelerated ageing testing of copper-oxide and Ni-MgF₂-cermet solar absorber coatings". *Solar Energy Materials* 16 (1987) pp 155 - 166.
- Köstlin, H., R. Jost and W. Lems, "Optical and electrical properties of doped In₂O₃ Films". *Phys. Stat. Sol. (a)* 29 (1975) pp 87 - 93.
- Kruidhof, W. and M. van der Ley, "Cobalt oxide as a spectrally selective material for use in solar collectors". *Solar Energy Materials* 2 (1979) pp 69 - 79.
- Kulaszewicz, S., "Electrical, optical and structural properties of thin films of In₂O₃:Sn deposited by hydrolysis". *Thin Solid Films* 76 (1981) pp 89 - 95.
- Kumar, S.N., M.L. Malhotra and K.L. Chopra, "Low cost electroless nickel black coatings for photothermal conversion". *Solar Energy Materials* 3 (1980) pp 519 - 546.
- Lampert, C.M., "Coatings for enhanced photothermal energy collection I, selective absorbers". *Solar Energy Materials* 1 (1979) pp 319 - 341.
- Landolt-Börnstein, *Zahlenwerte und Funktionen*, 4. Teil, II. Band. Springer, Berlin, 1961.
- Ley, M. van der, "The possibility of black Zinc-oxide as spectrally selective coating for low temperature solar collectors". *J. Electrochem. Soc.* 125 (1978) pp 1361 - 1364.
- Ley, M. van der, *Spectral-selective surfaces for the thermal conversion of solar energy*, PhD. thesis, 1979, Delft University Press.
- Ley, M. van der and C.J. Hoogendoorn, "Influence of the direct spectral solar energy distribution on the normal total absorptivity of spectral selective surfaces". *Solar Energy* 19 (1977) pp 575 - 577.

- Linhard, J., "On the properties of a gas of charged particles". Kgl. Danske Videnskab. Selskab. Mat. Fys. Medd. 28 (1954) pp 1 - 66.
- Linthorst, S.J.M., Natural convection suppression in solar collectors, PhD Thesis TU Delft, Dutch Efficiency Bureau, Pijnacker, 1985.
- Lou, J.C. et al., "Process study of chemically vapour-deposited SnO_x ($x \approx 2$) films". Thin Solid Films 106 (1983) pp 163 - 173.
- Mammana, A.P. et al., "Structural characterization of transparent semiconducting films of SnO_2 and In_2O_3 ". Thin Solid Films 85 (1981) pp 355 - 359.
- Manificier, J.-C. et al., " In_2O_3 :(Sn) and SnO_2 :(F) films-application to solar energy conversion". Mat. Res. Bull. 14 (1979) pp 109 - 119.
- Manificier, J.C., J.P. Fillard and J.M. Bind, "Deposition of In_2O_3 - SnO_2 layers on glass substrates using a spraying method". Thin Solid Films 77 (1981) pp 67 - 80.
- Marley, J.A and R.C. Dockerty, "Electrical properties of stannic oxide single crystals". Physical Review 140 (1965) pp A304 - A310.
- Mavrodiev, G., M. Gajdardziska and N. Novkovski, "Properties of SnO_2 :F Films prepared on glass substrates by the spraying method". Thin Solid Films 113 (1984) pp 93 - 100.
- Mayer, H., Physik dünner Schichten I. Wissenschaftliche Verlagsgesellschaft, Stuttgart, 1950.
- McCrackin, F.L. et al., "Measurement of the thickness and refractive index of very thin films and the optical properties of surfaces by ellipsometry". J. Res. Natl. Bur. Std. 67A (1963) pp 363 - 377.
- Meaden, G.T., Electrical resistance of metals. Plenum Press, New York, 1965.
- Melsheimer, J. and D. Ziegler, "Thin tin oxide film of low conductivity prepared by chemical vapour deposition". Thin Solid Films 109 (1983) pp 71 - 83.
- Melsheimer, J. and D. Ziegler, "Band-gap energy and Urbach tail studies on amorphous, partially crystalline and polycrystalline tin dioxide". Thin Solid Films 129 (1985) pp 35 - 47.
- Müller, H.K., "Electrical and Optical Properties of Sputtered In_2O_3 Films". Phys. Stat. Sol. 27 (1968) pp 733 - 740.
- Nilsson, P.O., "Determination of optical constants from intensity measurements at normal incidence". Applied Optics 7 (1968) pp 435 - 442.
- Nyquist, R.A. and R.O. Kagel, Infrared spectra of inorganic compounds. Academic Press, New York, 1971.

- Orton, J.W. and M.J. Powell, "The Hall effect in polycrystalline and powdered semiconductors". Rep. Prog. Phys. Vol. 43 (1980) pp 1263 - 1307.
- Pauw, L.J. van der, "Meting van de soortelijke weerstand en van de Hall-coëfficiënt aan schijfjes van willekeurige vorm". Philips Technisch Tijdschrift 20 (1958-1) pp 221 - 225.
- Pauw, L.J. van der, "A method of measuring specific resistivity and Hall-effect of discs of arbitrary shape". Philips Research Reports 13 (1958-2) pp 1 - 9.
- Perruzzo, V. and G. Tagliavini, "The cleavage of tin-allyl bonds in $R_2(CH_2=CH-CH_2)_2Sn$ substrates as a route to organostannoxanes". Journal Organometallic Chem. 66 (1974) pp 437 - 445.
- Pettit, R.P. and C.J. Brinker, "Use of sol-gel thin films in solar energy applications". Solar Energy Materials 14 (1986) pp 269 - 287.
- Pommier, R., C. Gril and J. Marucchi, "Sprayed films of indium tin oxide and fluorine-doped tin oxide of large surface area". Thin Solid Films 77 (1981) pp 91 - 97.
- Putley, E.H., The Hall-effect and semi-conductor physics. Dover Publications, New York, 1968.
- Ratcheva, T.M. et al., "Properties of $In_2O_3:Te$ films prepared by the spraying method". Thin Solid Films 139 (1986) pp 189 - 199.
- Robertson, J., "Electronic structure of SnO_2 , GeO_2 , PbO_2 , TeO_2 and MgF_2 ". J. Phys. C. 12 (1979) 4767 - 4776.
- Roos, A. and M. Georgson, "Solar selective properties of tin oxide on pigmented aluminium oxide". in: C.G. Granqvist et al. (ed.), Proceedings SPIE 653 (1986) pp 196 - 201.
- Roth, A.P. and D.F. Williams, "Properties of zinc oxide films prepared by the oxidation of diethyl zinc". J. Appl. Phys. 52 (1981) pp 6685 - 6692.
- Rubin, M., "Optical properties of soda lime silica glasses". Solar Energy Materials 12 (1985) pp 275 - 288.
- Saxena, A.K. et al., "Characterization of fluorine-doped SnO_2 films prepared by chemical vapour deposition". Thin Solid Films 131 (1985) pp 121 - 129.
- Schopper, H., "Zur Optik dünner doppelbrechender und dichroitischer Schichten". Zeitschr. für Ph. 132 (1952) pp 146 - 170.
- Sears, W.M. and M.A. Gee, "Mechanics of film formation during the spray pyrolysis of tin oxide". Thin Solid Film 165 (1988) pp 265 - 277.

- Sella, C. et al., "Low cost selective absorber based on a Fe-Al₂O₃ cermet film". Solar Energy Materials 16 (1987) pp 143 - 154.
- Seraphin, B.O. (ed.), Solar Energy Conversion: Topics in Applied Physics. Vol. 31, Springer-Verlag, Berlin, 1979.
- Shanthi, E. et al., "Annealing Characteristics of tin oxide films prepared by spray pyrolysis". Thin Solid Films, 71 (1980-1) pp 237 - 244.
- Shanthi, E. et al., "Electrical and optical properties of undoped and antimony-doped tin oxide films". J. Appl. Phys. 51 (1980-2) pp 6243 - 6251.
- Shanthi, E., A. Banerjee and K.L. Chopra, "Dopant effects in sprayed tin oxide films". Thin Solid Films 88 (1982) pp 93 - 100.
- Siefert, W., "Entwicklung eines Spray Pyrolyse Beschichtungsverfahren mit erheblich gesteigertem Abscheidegrad", PhD. Thesis. Alfred Schütz Verlag, Lahr, 1982.
- Siefert, W., "Properties of thin In₂O₃ and SnO₂ films prepared by corona spray pyrolysis, and a discussion of the spray pyrolysis process". Thin Solid Films 121 (1984) pp 275 - 282.
- Siegel, R. and J.R. Howell, Thermal radiation heat transfer, Mc Graw-Hill, New York, 1972.
- Sievers, A.J., "Thermal radiation from metal surfaces". J. Opt. Soc. Am. 68 (1978) pp 1505 - 1518.
- Sikkens, M., Spectrally selective solar energy materials. PhD. Thesis, R.U. Groningen, 1980.
- Sikkens, M., "Physical background of spectral selectivity". Solar Energy Materials 5 (1981) pp 55 - 70.
- Sikkens, M., "Properties of spectrally selective Ni-C films produced by reactive sputtering". Solar Energy Materials 6 (1982) pp 403 - 428.
- Simonis, F., M. van der Ley and C.J. Hoogendoorn, "Physics of doped tin dioxide films for spectral-selective surfaces". Solar Energy Materials 1 (1979) pp 221 - 231.
- Simonis, F., A.J. Faber and C.J. Hoogendoorn, "Porcelain enamelled absorbers, coated by spectral selective tin oxide". J. Sol. En. Eng. 109 (1987) pp 22 - 25.
- Singh, S.P. et al., "Characterization of Fluorine-doped In₂O₃ films synthesized by spray pyrolysis". Thin Solid Films 105 (1983) pp 131 - 138.
- Singh, S.P., L.M. Tiwari and O.P. Agnihotri, "Optical investigations of In₂O₃:F films". Thin Solid Films 139 (1986) pp 1 - 7.

- Singwi, K.S. et al., "Electron correlations at metallic densities".
Phys. Rev. **176** (1968) pp 589 - 599.
- Srinivasa Murty, N., and S.R. Jawalekar, "Structural studies of chemically vapour-deposited tin oxide films". Thin Solid Films **100** (1983) pp 219 - 225.
- Stern, F., Elementary theory of the Optical Properties of Solids. in: Solid State Physics, Vol. 15, F. Seitz and D. Turnbull (eds). Academic Press, New York, 1963.
- Summitt, R., "Infrared absorption in single-crystal stannic oxide : optical lattice-vibration modes". J. Appl. Phys. **39** (1968) pp 3762 - 3767.
- Szczyrbowski, J., and A. Czapla, "On the determination of optical constants of films". J. Phys. D : Appl. Phys. **12** (1979) pp 1737 - 1751.
- Szczyrbowski, J., K. Schmalbauer and H. Hoffmann, "Optical properties of rough thin films". Thin Solid Films, **130** (1985) pp 57 - 73.
- Szemanski, H.A. and R.E. Erickson, Infrared band handbook.IFI/Plenum Data Corporation, New York, 1970.
- Tabor, H., "Selective Radiation: I. Wavelength discrimination and II. Wavefront discrimination ". Bull. Res. Council. of Israel **5A** (1956) pp 119 - 134.
- Tal-Tarlo, I. and Y. Zvirin, "The effects of radiation properties of surfaces and coatings on the performance of solar collectors". J. Sol. En. Eng. **110** (1987) pp 217 - 225.
- Thomas, L.K. et al., "Properties of solar selective absorbing Cr-SiO cermet after high temperature treatment". Solar Energy Materials **16** (1987) pp 133 - 142.
- Vashista, P. and K.S. Singwi, "Electron correlations at metallic densities V". Phys. Rev. **B6** (1972) pp 875 - 887.
- Viscrican, I. and V. Georgescu, "Contributions to the study of tin oxide films". Thin Solis Films **3** (1969) pp R17 - R22.
- Vogelzang, E., A.A.M.T. van Heereveld and M. Sikkens, "Thin transition-metal nitride films with surface roughness for application as selective absorbers in evacuated solar collectors" in: Proc. SPIE **401** (1983) pp 368 - 375.
- Waal, H. de and F. Simonis, "Tin oxide coatings: Physical properties and applications". Thin Solid Films **77** (1981) pp 253 - 258.
- Warkusz, F., "The scattering of electrons on grain boundaries: electrical conductivity". Thin Solid Films **161** (1988) pp 1 - 11.

- Weiher, R.L. and R.P. Ley, "Optical properties of indium oxide". J. Appl. Phys. 37 (1966) pp 299 - 302.
- Wheast, H. (ed.), Handbook of Chemistry and Physics, 65th ed. CRC-Press, Boca Raton, 1985.
- Wieder, H.H., "Electrical and galvanomagnetic measurements on thin films and epilayers". Thin Solid Films 31 (1976) pp 123 - 138.
- Wieder, H.H., Laboratory notes on electrical and galvanomagnetic measurements. Elsevier Scientific Publishing Company, Amsterdam, 1979.
- Wilson, A.H., The theory of metals. Cambridge University Press, 1965.

SUMMARY

In the process of photothermal conversion of solar energy, as it takes place in a flat-plate collector, heat losses occur due to heat conduction, natural convection and radiation. This thesis is about a method to reduce the radiation losses by using a spectrally selective absorber. A spectrally selective absorber combines a high absorption factor for solar radiation to a low emittance for thermal radiation. Of the many methods to prepare a spectrally selective surface and the many materials of which a surfaces which can be composed (see chapter 1), we have investigated the properties of doped tin oxide and indium oxide coatings. When these coatings are prepared properly, they are transparent for solar radiation, while they have a low thermal emittance. When applying such a coating on a black absorber surface, e.g. on black enamelled steel, the substrate+coating combination forms a spectrally selective absorber.

A fluorine-doped tin oxide coating is an attractive spectrally selective coating because of the mechanical, thermal and chemical stability. This leads to a very good durability and the coating can withstand the high temperatures which occur when a stagnation in the water flow through the collector occurs.

These coatings are thoroughly investigated in this thesis to determine the physical properties which govern the spectrally selective behaviour and to determine the limits of the selectivity which can be achieved in theory as well as in practice. Tin-doped indium oxide coatings are investigated to determine their suitability as a spectrally selective coating and also because a comparison of the physical properties of indium oxide and tin oxide may enhance the physical understanding of both.

The theory of the spectrally selective behaviour of SnO_2 and In_2O_3 coatings is given in chapter 2. After the definitions of the various radiation quantities, this theoretical chapter further gives the thin film optics used, the Drude model which relates electrical and optical properties, the various scattering mechanisms which might limit the conductivity in the coatings and a model for the free electron density in a semiconductor with a degenerate electron statistics.

Based upon this theory, various model calculations have been carried out.

These calculations show that the solar absorptance is hardly affected by the thermal emittance which is fully related to the electrical properties. The solar absorptance can be improved from 0.90 to about 0.93 when roughing the surface and to 0.96 by application of an additional SiO_2 anti reflection coating.

Calculations on the emittance show that, when the electron mobility is limited by ionized impurity scattering, which will always be the case in our coatings as these impurities are necessary to generate free electrons, the minimum hemispherical emittance which can be achieved for the case of SnO_2 and In_2O_3 coatings is about 0.13 at 400 K.

The measuring techniques which have been used to determine the coating properties are described in chapter 3. These techniques include spectrophotometry, Hall-effect determinations, ellipsometry, and the determination of the angle-dependent thermal emittance. The determinations which have been carried out for us by other groups (e.g. X-ray diffraction and electron microprobe analysis) are briefly discussed.

In chapter 4 the various methods in which the optical constants and the thickness of the coatings have been determined are given and mutually compared. Knowledge of the optical constants is essential for the physical modelling of the coatings. The optical constants and the surface roughness in the 0.3-2.5 μm spectral region are calculated from the spectral reflectance and transmittance using the R-T method or the envelope method. A method is developed to derive the eventual inhomogeneity and/or anisotropy of the coating coating optical constants from ellipsometric measurements. The optical constants in the 2.5-40 μm spectral region are obtained from a Kramers-Kronig integration. A correction method for the substrate influence proves to work conveniently.

Chapter 5 describes the pyrolysis process with which the coatings have been produced. The influence of the carrier gas, the spraying time, the spraying temperature and the spraying solution on the coating properties are determined. It has been tried to examine the influence of the droplet size and the gas pressure, but as these quantities are very related in the used equipment, these influences could not clearly be distinguished. The chemical solutions which have been used in the spray pyrolysis process are also described in this chapter.

The results on tin oxide coatings are given in chapter 6. These results include the effects of fluorine doping, coating thickness and the process parameters.

It is shown that doping SnO_2 coatings with fluorine increases the electron density and the mobility in the coating. Both effects reduce the thermal emittance. At maximum an electron density of 1/3 of the fluorine concentration in the coating is obtained. The maximum electron density which can be obtained is about $4 \cdot 10^{26}/\text{m}^3$. The optical plasma wavelength decreases with an increasing electron density according to an effective mass of about $0.25m_e$ and is about $1.8 \mu\text{m}$ at a maximum electron density.

The real part of the complex resistivity ρ_r , as derived from the optical constants, behaves as $\rho_r \sim \lambda^{1.7}$ for $\lambda < \lambda_p$, where λ and λ_p are the wavelength and the plasma wavelength respectively, as is predicted by the modified Gerlach-Grosse theory for ionized impurity scattering. When the mobility is larger than about $20 \text{ cm}^2/\text{Vs}$, ρ_r is constant for $\lambda > \lambda_p$ and corresponds to the DC-resistivity as it is measured electrically. This means that for $\lambda > \lambda_p$, the optical properties accord to the classical Drude theory. The maximum mobility of about $45 \text{ cm}^2/\text{Vs}$ which is obtained experimentally, roughly equals the maximum mobility predicted by the theory for ionized impurity scattering. This means that for these coatings the maximum attainable heat reflectance, leading to an emittance $\epsilon_{h, T=400\text{K}}$ of about 0.15, has been obtained. The slight decrease mobility with the temperature can conveniently be described by a theory of optical phonon scattering.

In coatings having a very low doping level, or having a very weak preferential orientation, the electrical mobility may be further limited by the poorly conducting intergranular regions. This case is characterized by a small electrical mobility relative to the optical mobility, and by a mobility which increases with the temperature. The models which are commonly used to describe the temperature dependence for this case, give unsatisfactory results when applied to our coatings.

The relatively low solar absorptance of 0.91 of a smooth coating on an absorbing glass-like substrate is mainly caused by the refractive index in the visible spectrum, which is about 2 and is inherent to the crystal structure. The intrinsic surface roughness of a coating may enhance this value with 0.01. An additional SiO_2 anti reflection coating will increase the solar absorptance up to 0.96.

The optimization of the spectrally-selective properties by varying the process parameters leads to the following recommendations:

- a. The substrate temperature should be 550°C to 700°C , dependent on the solution used.
- b. The spraying time should be 4 seconds per cycle at maximum.

- c. As a carrier gas, oxygen can be used at best.
- d. The pressure of the carrier gas should be about 3 Bar; at a higher pressure, finer droplets are produced, but the coating quality decreases.

At the end of the chapter these results are summarized in a model for the optical properties and in a discussion on the relation between the structural and electrical properties. In the model for the dielectric constant, which describes the optical properties, also terms which describe the band gap absorption in the UV spectral region and the lattice oscillations in the thermal infrared region are incorporated. The relations which are observed experimentally between the electrical and structural properties are in qualitative agreement with the theory of Bélanger. This theory predicts that when the crystallites are oriented different from the (200) direction, free electrons are trapped at the grain boundaries which will decrease the free electron density and the electron mobility. Optically, this results in an increase of the emittance.

Chapter 7 gives the results obtained for indiumoxide coatings. The effects of tin doping, annealing and the coating thickness are determined and compared to the results found in chapter 6 for tin oxide coatings. It is shown that annealing the indiumoxide coating in vacuum, may considerably enhance the free electron density and the mobility, as far as the maximum obtainable mobility due to ionized impurity scattering was not achieved. At maximum, a free electron density about equal to the tin concentration can be achieved. The maximum free electron density obtained is about $7 \cdot 10^{26} / \text{m}^3$, which is apparently more than in the case of tin oxide coatings.

The optimum spectrally selective coating properties are similar to those of a fluorine doped tin oxide coating. The hemispherical emittance of 0.150 and the solar absorptance of about 0.90 when applied on a black, glass-like, absorbing substrate are the limits for the same reasons as in the case of tin oxide coatings.

The thesis is concluded with a summary of the main theoretical and experimental results and conclusions in chapter 8. The main conclusion is that a thermal emittance combined with a solar absorptance of 0.92 is the limit which can be achieved when preparing doped SnO_2 or In_2O_3 coatings under optimum conditions. These results have also been obtained by others before this investigation was started.

It is not surprising that we have not succeeded to decrease the emittance further as in the optimum case the electron mobility, and so the thermal infrared reflectance, is mainly limited by ionized impurity scattering which is inherent to the presence of ionized donor atoms. The solar absorptance can be further enlarged to 0.96 by an additional SiO_2 anti reflection coating.

Because of the good spectrally selective properties and the very good thermal, mechanical and chemical stability, tin oxide coatings still are very attractive for use as a spectrally selective coating. As In_2O_3 coatings are much more expensive and do not have better properties in this respect, they are not attractive for this purpose. The In_2O_3 coatings may be more attractive for applications where the reflectance in the near-infrared solar spectrum is no problem and where a maximum conductivity is needed.

SAMENVATTING

In het fothermische omzettings proces van zonne-energie, zoals dat plaatsvindt in een vlakke-plaat collector, treden warmteverliezen op door warmtegeleiding, warmtestraling en door natuurlijke convectie. Dit proefschrift gaat over een methode om de verliezen door warmtestraling te beperken door gebruik te maken van een zgn. spectraal-selectieve absorber. Een spectraal-selectieve laag combineert een hoge absorptiefactor voor zonnestraling met een lage emissiefactor voor warmtestraling. Van de vele typen spectraal selectieve lagen -een overzicht staat in hoofdstuk 1- hebben we gedoteerde tinoxide en indiumoxyde coatings nader onderzocht. Wanneer deze lagen op de juiste manier vervaardigd worden, zijn ze transparant voor zonnestraling en reflecteren ze thermische warmtestraling, wat tot een lage thermische emissiecoëfficiënt leidt. Door een dergelijke laag op een zwart, zonne-straling absorberend oppervlak aan te brengen, bijvoorbeeld op zwart geëmailleerd staal, vormt het geheel van coating en substraat een spectraal-selectief oppervlak.

Een fluor-gedoteerde tinoxide coating is een aantrekkelijke spectraal-selectieve coating vanwege de goede mechanische, thermische en chemische stabiliteit. Deze leidt tot een goede duurzaamheid, en de coatings zijn dan ook bestand tegen de hoge temperaturen die in een collector kunnen voorkomen wanneer de watertoe- of afvoer van de collector stagneert.

Een groot deel van het proefschrift is gewijd aan het onderzoek naar deze coatings, dat is uitgevoerd met als doel te komen tot een beter begrip van de fysische eigenschappen die de spectraal-selectieve eigenschappen bepalen en het vaststellen van de limieten van deze eigenschappen die theoretisch en in de praktijk kunnen worden bereikt. Tin gedoteerde indiumoxyde coatings worden onderzocht, niet alleen vanwege hun mogelijke toepasbaarheid als spectraal-selectieve laag, maar ook om de fysische eigenschappen met die van tinoxide te kunnen vergelijken, hetgeen het fysisch inzicht in beide typen lagen verder kan vergroten.

De theorie van het spectraal-selectieve gedrag van tinoxide (SnO_2) en indiumoxyde (In_2O_3) coating wordt in hoofdstuk 2 beschreven. Na de definitie van de diverse relevante stralingsgrootheden staat in dit theoretische hoofdstuk de gebruikte dunne-film optica beschreven, het zgn. Drude-model, dat een relatie legt tussen elektrische en optische eigenschappen, de diverse verstrooiingsmechanismen die de geleidbaarheid in

een coating zouden kunnen beperken, en een model voor de vrije-elektronen dichtheid in een halfgeleider met een gedegenererde elektronenstatistiek, waarmee we in ons geval te maken hebben.

Op basis van deze theorie zijn diverse modelberekeningen uitgevoerd. Deze berekeningen laten zien dat de zonne-absorptiefactor α nauwelijks wordt beïnvloed door de elektrische eigenschappen, die wel volledig de thermische emissiefactor ϵ bepalen. De zonne-absorptiefactor kan worden verbeterd tot ca. 0.93 wanneer het oppervlak van de coating op een bepaalde manier ruw gemaakt kan worden. Een verbetering tot $\alpha = 0.96$ kan worden bereikt door een extra SiO_2 (kwarts) anti-reflectie coating.

Berekeningen aan de emissiecoëfficiënt ϵ laten zien dat, wanneer de elektronenmobiliteit wordt beperkt door verstrooiing aan geïoniseerde onzuiverheden -wat het geval is in onze coatings omdat deze onzuiverheden de noodzakelijke vrije elektronen leveren- de minimum waarde voor ϵ die theoretisch kan worden bereikt ca. 0.13 bedraagt voor SnO_2 en In_2O_3 coatings.

De gebruikt meettechnieken om de coatings te karakteriseren worden in hoofdstuk 3 beschreven. Deze technieken zijn o.a. spectrofotometrie, Hall-effect metingen, ellipsometrie en de bepaling van de hoek-afhankelijke emissiecoëfficiënt. Ook de bepalingen die elders ten behoeve van dit onderzoek zijn uitgevoerd (o.a. Röntgendiffractie, Röntgenmicroanalyse) worden kort beschreven.

In hoofdstuk 4 worden de methoden die zijn gebruikt om de optische constanten van de coatings te bepalen beschreven en onderling vergeleken. Kennis van de optische constanten is essentieel wanneer modellen voor het optische gedrag van de coating moeten worden opgesteld of gecontroleerd. De optische constanten en de oppervlakteruwheid in het spectraal gebied van 0.3 tot 2.5 μm worden berekend uit de spectrale reflectie- en transmissiecoëfficiënten, waarbij de zgn. R-T methode of de 'omhullende' methode wordt gebruikt. Ook de ontwikkelde methode om een eventuele anisotropie en/of inhomogeniteit in de optische constanten met behulp van ellipsometrie te bepalen wordt beschreven. De optische constanten in het spectraal gebied van 2.5 tot 40 μm worden bepaald door middel van een Kramers-Kronig analyse van het reflectiespectrum. Een ontwikkelde correctiemethode voor de substraat- invloed blijkt goed te werken.

Hoofdstuk 5 beschrijft het pyrolyseproces waarmee de coatings worden vervaardigd. Dit proces houdt in dat een vloeistof wordt verneveld en naar het verhitte substraat wordt geleid. Op dit substraat vindt een chemische reactie plaats waardoor de coating wordt gevormd. De invloed van het

drijfgas, de vernevelingstijd en de gebruikte vloeistof op de substraattemperatuur en de filmgroei wordt in dit hoofdstuk bepaald. Ook de invloed van de druppelgrootte en de gasdruk zijn bepaald, maar omdat deze effecten sterk gecorreleerd zijn konden ze niet duidelijk worden gescheiden. Ook de vloeistoffen die in het pyrolyseproces zijn gebruikt worden in dit hoofdstuk beschreven.

De onderzoeksresultaten betreffende de tinoxide coatings worden in hoofdstuk 6 beschreven. Deze betreffen o.a. de invloed van de fluor dotering, de coatingdikte en de procesparameters. Het blijkt dat het doteren van de coatings niet alleen de vrije-elektronendichtheid doet toenemen, maar ook de mobiliteit. Beide eigenschappen verlagen de thermische emissiecoëfficiënt. Een vrije-elektronendichtheid van maximaal 1/3 van de fluorconcentratie in de coating kan worden bereikt. De maximum elektronen dichtheid die kan worden bereikt bedraagt $4 \cdot 10^{26}/m^3$. De optische plasmagolfengte, die ruwweg de scheiding tussen lichtdoorlatend en reflecterend gedrag van de coating aangeeft, neemt af met een toenemende elektronendichtheid overeenkomstig een effectieve massa van ca 0.25 elektronmassa. De plasmagolfengte bedraagt ca 1.8 μm bij een maximale elektronendichtheid.

Het reële deel van de complexe weerstand, ρ_r , zoals afgeleid uit de optische constanten, neemt af met de golflengte volgens $\rho_r \sim \lambda^{1.7}$ voor $\lambda < \lambda_p$, waar λ_p staat voor de plasmagolfengte en λ voor de golflengte. Dit is ook het resultaat van de aangepaste Gerlach-Grosse theorie -beschreven in hoofdstuk 2-, die ρ_r voorspelt als functie van de golflengte wanneer de mobiliteit wordt beperkt door verstrooiing aan geïoniseerde onzuiverheden. Experimenteel blijkt dat wanneer de mobiliteit hoger is dan ca. 20 cm^2/Vs , ρ_r constant blijft voor $\lambda > \lambda_p$ en overeenkomt met de DC-soortelijke weerstand zoals deze elektrisch wordt gemeten. Dit betekent dat voor $\lambda > \lambda_p$ de klassieke Drude-theorie geldt. De maximum mobiliteit van ca. 45 cm^2/Vs die experimenteel wordt gevonden komt ruwweg overeen met de waarde die gegeven wordt door de theorie voor verstrooiing aan geïoniseerde onzuiverheden. Deze verstrooiing is niet te vermijden omdat deze geïoniseerde onzuiverheden juist de vrije elektronen leveren die voor de elektrische geleiding, en dus voor de thermische infrarood-reflectie, zorgen. Dit betekent dat voor deze coatings de maximale infrarood-reflectie, die leidt tot een emissiecoëfficiënt $\epsilon_{h,400K}$ van 0.15, is bereikt. De geringe afname van de mobiliteit bij toenemende temperatuur kan goed worden verklaard uit de verstrooiing van elektronen aan optische fononen.

In laag gedoteerde coatings en in coatings waarin de kristallieten weinig voorkeursoriëntatie vertonen, kan de elektrische mobiliteit nog verder worden beperkt door het slecht geleidende gebied tussen de korrelgrenzen. Hierdoor ontstaat een geringe elektrische mobiliteit ten opzicht van de optische mobiliteit en een elektrische mobiliteit die toeneemt met een stijgende temperatuur. De modellen die in de literatuur gebruikt worden om de temperatuursafhankelijkheid voor dit geval te voorspellen geven echter onbevredigende resultaten wanneer ze op onze metingen worden toegepast.

De relatief lage zonne-absorptiefactor van 0.91 van een coating op een absorberend, glasachtig substraat wordt voornamelijk veroorzaakt door de brekingsindex in het zichtbare spectrum. Deze is ongeveer 2 en is inherent aan de kristalstructuur. De intrinsieke oppervlakteruwheid van een coating verhoogt deze waarde met ca. 0.01. Een extra kwarts anti-reflectiecoating zal de zonneabsorptie verhogen tot ca. 0.96.

De optimalisatie van de spectraal-selectieve eigenschappen door middel van parametervariëaties in het pyrolyseproces leidt tot de volgende richtlijnen voor de produktie van een optimale coating:

- a. De substraattemperatuur dient 550 à 700 °C te zijn, afhankelijk van de gebruikte vloeistof.
- b. Er dient niet langer dan 4 seconden op het substraat gespoten te worden; indien na deze tijd de noodzakelijke laagdikte van 0.5 à 0.6 μm nog niet is bereikt dient meer dan een keer gespoten te worden.
- c. Als drijfgas kan het best zuurstof worden gebruikt
- d. De druk van het drijfgas dient 2 à 3 bar te zijn; bij hogere spuitdruk wordt een fijnere verneveling van de vloeistof bereikt, maar de coatingkwaliteit neemt af.

Aan het eind van hoofdstuk 6 worden de verkregen resultaten samengevat in een compleet model voor de optische eigenschappen en in een discussie omtrent de relatie tussen de elektrische en de structurele eigenschappen. In het model voor de diëlektrische constante die de optische eigenschappen vastlegt, zijn ook experimenteel bepaalde termen opgenomen die de band-afstandsabsorptie in het ultraviolet gebied en de roostertrillingen in het thermisch-infraroodgebied beschrijven. De relaties die experimenteel gevonden worden tussen de elektrische en structurele eigenschappen komen kwalitatief overeen met de theorie van Bélanger. Deze theorie voorspelt dat, wanneer de kristallieten anders dan in de (200) richting georiënteerd zijn, vrije elektronen aan de korrelgrenzen zullen worden ingevangen.

Dit veroorzaakt een afname van zowel de vrije-elektronendichtheid als van de mobiliteit. Optisch gezien veroorzaakt dit een toename van de emissiecoëfficiënt.

De onderzoeksresultaten betreffende de indiumoxyde coatings worden in hoofdstuk 7 beschreven. De effecten van het doteren met tin en het uitstoken van de coatings, en de invloed van de dikte zijn bepaald en vergeleken met de resultaten zoals die in hoofdstuk 6 voor de tinoxide coatings zijn gevonden. Het blijkt dat de eigenschappen van de coating flink kunnen verbeteren door uitstoken van de coatings in vacuüm, voorzover de maximum bereikbare eigenschappen nog niet bereikt waren. Maximaal kan een vrije-elektronendichtheid gelijk aan de tinconcentratie worden bereikt. De maximum vrije-elektronendichtheid die kan worden gehaald is $7 \cdot 10^{26} / \text{m}^3$, hetgeen aanzienlijk meer is dan wat met fluor-gedoteerde tinoxide coatings kan worden gehaald.

De geoptimaliseerde spectraal-selectieve eigenschappen zijn ongeveer gelijk aan die van tinoxide coatings. De hemisferische emissiecoëfficiënt van 0.15 en de zonne-absorptiefactor van 0.90, wanneer de coating op een zwart, glasachtig substraat wordt aangebracht, vormen de limiet om dezelfde redenen als in het geval van tinoxide coatings.

Het proefschrift wordt in hoofdstuk acht besloten met een samenvatting van de voornaamste theoretische en praktische resultaten. De voornaamste conclusie is dat een thermische emissiecoëfficiënt van 0.15 gecombineerd met een zonne-absorptiefactor van 0.92 onder optimale procesomstandigheden gehaald kan worden. De emissiecoëfficiënt kan niet verder worden verlaagd, zoals wel onze opzet was, omdat de elektronenmobiliteit in het optimale geval beperkt wordt door de verstrooiing aan geïoniseerde onzuiverheden die inherent is aan de dotering die nodig is om vrije elektronen te genereren. De zonne-absorptie-factor kan verder verhoogd worden door een extra kwarts anti-reflectie coating. Vanwege de redelijk tot goede spectraal-selectieve eigenschappen en de zeer goede thermische, chemische en mechanische stabiliteit, zijn tinoxide coatings aantrekkelijk voor gebruik als spectraal-selectieve laag.

Vanwege de veel hogere kostprijs van In_2O_3 coatings, en de spectraal-selectieve eigenschappen die analoog zijn aan die van tinoxide, zijn deze niet aantrekkelijk voor dit doel. Indiumoxyde coatings kunnen aantrekkelijk zijn voor toepassingen waar extra reflectie in het nabij-infrarood gebied geen probleem is en waar een maximale geleidbaarheid van de laag een eerste vereiste is.

CURRICULUM VITAE

23 februari 1958	Geboren te Ommen
1964-1970	Openbare lagere school te Ommeren
1970-1976	Atheneum B aan de Rijksscholengemeenschap Tiel
1976-1985	Universitaire studie experimentele natuurkunde aan de Rijksuniversiteit Utrecht
14 januari 1985	Doctoraalexamen experimentele natuurkunde
1 februari 1985 - 1 februari 1989	Promotieplaats bij de Stichting FOM, werkgroep TFII aan de TU Delft, Faculteit der Technische Natuurkunde, groep Warmtetransport
vanaf 1 juli 1989	Wetenschappelijk medewerker fysische standaarden bij het Van Swinden Laboratorium van het Nederlands Meetinstituut te Delft

NAWOORD

Dit proefschrift zou nooit tot stand zijn gekomen zonder de hulp en initiatieven van een groot aantal personen en instanties, waarvan ik er hier een aantal wil noemen en bedanken.

Professor Hoogendoorn dank ik voor zijn kundige begeleiding en voor zijn opbouwende kritiek op eerdere versies van het proefschrift. Mijn directe begeleider Jack Elich ben ik dankbaar voor zijn hulp bij bijna alles, met name voor het organiseren van de opstelling voor de elektrische metingen, het altijd beschikbaar zijn en het altijd mee willen denken. Waar in dit proefschrift 'we' wordt gebruikt betekent dit vaak 'Jack en ik'.

Erik Boslooper, Gerard de Jong, Martin van de Pol, Bob Schulte, Jack Simons, Luc van Vugt en Geert Woerlee hebben in het kader van hun natuurkundestudie aan het project meegewerkt en wezenlijke bijdragen geleverd. Als stagière hebben Karin Bruynings-Ingenhoes, Artur Magiera en Gorazd Planinšič gedurende korte tijd meegewerkt.

Bovenstaande personen en de andere studenten en collega's van de vakgroep warmtetransport dank ik bijzonder voor het in stand houden van de gezellige en typerende sfeer binnen WT.

Buiten de groep WT bedank ik de groep Glas van de TPD voor de plezierige samenwerking en het ruimhartig beschikbaar houden van de spuitopstelling en de spectrofotometers. De optische slijperij bedank ik voor het uitboren van de ruim 500 glazen rondjes waarop dit proefschrift is gebaseerd. Jan Toth van het centrum voor submicrontechnologie (CST) maakte diverse SEM opnamen. De Röntgenmicroanalyses zijn uitgevoerd door medewerkers van de afdeling metaalkunde. De Röntgendiffractieopnamen zijn gemaakt door Ed Sonneveld van de TPD bij de vakgroep vaste stof.

Het onderzoeksproject is tot stand gekomen op initiatief van ISES-Nederland. Met steun van het PEO/NOVEM en de ministeries van EZ en O&W heeft het als een FOM/STW project gestalte gekregen. Deze instanties bedank ik voor hun initiatieven en vooral voor het beschikbaar stellen van de broodnodige financiële middelen.

Mijn ouders bedank ik voor de gelegenheid die ze mij hebben geboden mijn universitaire studie te volgen. Mijn vrouw Margreeth bedank ik voor haar niet aflatende steun en voor het overnemen van veel taken waardoor ik de inspiratie en de grote hoeveelheid tijd kon vinden die voor het schrijven van een proefschrift een eerste voorwaarde zijn.

Stellingen

behorende bij het proefschrift

'Spectrally selective tinoxide and indiumoxide coatings'

1. De thermische emissiecoëfficiënt van gedoteerde tinoxyde en indiumoxyde coatings kan niet beneden 0,13 worden gebracht zonder dat de reflectie van het nabij-infrarode deel van het zonnenspectrum toeneemt.

Dit proefschrift

2. De gangbare vuistregel dat de hemisferische emissiecoëfficiënt voor metalen of voor metaal-achtige materialen een factor 1,2 à 1,3 hoger is dan de loodrechte emissiecoëfficiënt zou voor emissiecoëfficiënten tussen de 0,1 en 0,3 te vervangen moeten worden door de vuistregel dat de hemisferische emissiecoëfficiënt 0,02 hoger is dan de loodrechte emissiecoëfficiënt.

Dit proefschrift

3. Bij de afwezigheid van magnetoweerstand kan in een configuratie met vier contacten op de rand van het te meten object bij een aanwezig magneetveld loodrecht op dit object het Hall-effect worden bepaald terwijl de sterkte en de richting van het magneetveld ten opzichte van het object niet veranderen.
4. Dat de Fresnelcoëfficiënten voor de polarisatierichting parallel aan het grensvlak voor een overgang tussen twee uniaxiaal anisotrope media zoals gegeven door o.a. Azzam en Bashara onjuist moeten zijn kan worden ingezien door van deze uitdrukking de limiet voor isotrope media te nemen.

Azzam en Bashara, Ellipsometry and Polarized Light, 1977, p. 358.

5. De door Kane en Schweizer met ellipsometrie waargenomen variatie in de brekingsindex van tinoxyde coatings - er werden waarden tussen de 1,75 en 2,3 gevonden bij een golflengte van 546 nm - is het gevolg van het negeren van de oppervlakteruwheid.

Kane and Schweizer, J. Electrochem. Soc 122 (1975) p. 1144.

Dit proefschrift

6. Het beschouwen van korrelgrenzen in polykristallijn materiaal als quantummechanische potentiaalbarrières geeft een meer bevredigende beschrijving van de elektrische transportgrootheden dan de beschrijving op grond van thermionische emissie [1]. Dit model zou ook toegepast moeten worden op de gas-film interactie in zuurstofsensoren op basis van tinoxyde, waarvan de gebruikelijke beschrijving steeds meer in twijfel wordt getrokken [2].

1. F. Warkusz , Thin Solid Films 161 (1988) p 1.
2. J. N. Zemel, Thin Solid Films 163 (1988) p 189.

7. De opgegeven waarde voor de statische diëlectrische constante van tinoxyde doet vermoeden dat het veelgebruikte 'Handbook of Chemistry and Physics' al tientallen jaren steeds weer wordt uitgegeven zonder te zijn bijgewerkt.

8. De ontwikkelingen op het gebied van de 'Scanning Tunnelling Microscope' maken het enerzijds mogelijk geadsorbeerde atomen op het oppervlak van een standaard kilogram te onderzoeken en zo de huidige vastlegging van de kilogram te verbeteren, anderzijds openen ze via de nauwkeurige bepaling van interatomaire afstanden perspectieven op vervanging van de huidige kilogramdefinitie door een definitie als bijvoorbeeld een aantal mol van het atoom ²⁸Si.

K. Carneiro, DFM publikatie, 1989.

9. Een betere vergelijking tussen conventionele en alternatieve energiebronnen kan tot stand komen wanneer in de kostprijs van een energiebron de kosten om de belasting voor het milieu van deze energiebron teniet te doen of te compenseren worden opgenomen.

10. Het laatste pianostuk uit Schumann's 'Kinderszenen' is nauw verwant aan het gelijknamige deel uit Heine's gedicht 'Aus einem Briefe'.

11. Zolang kinderopvang wordt ervaren als een vrouwenprobleem zal er niet serieus aan een oplossing worden gewerkt.

12. Een originele stelling is zelden juist en een juiste stelling is zelden origineel.